

https://dspace.org/

Internal Cooling at the Trailing-Edge of a High- Pressure Gas Turbine Blade

Schekman, Sjouke W.

2024

University of the Witwatersrand, Johannesburg

https://hdl.handle.net/10539/46278

Schekman, Sjouke W. . (2024). Internal Cooling at the Trailing-Edge of a High- Pressure Gas Turbine Blade [PhD thesis, University of the Witwatersrand, Johannesburg]. WIReDSpace. https://hdl.handle.net/10539/46278

Downloaded from a DSpace repository. https://dspace.org/

Internal Cooling at the Trailing-Edge of a High-Pressure Gas Turbine Blade

Sjouke W. Schekman

School of Mechanical, Industrial and Aeronautical Engineering
University of the Witwatersrand
Johannesburg, South Africa

A thesis submitted to the Faculty of Engineering and the Built Environment, University of the Witwatersrand, in fulfilment of the requirements for the degree of Doctor of Philosophy.

DECLARATION

I, Sjouke Schekman, declare that this thesis is my own unaided work. It is being submitted to the Degree of Doctor of Philsophy to the University of the Witwatersrand, Johannesburg. It has not been submitted before for any degree or examination to any other University.

24th day of April 2024

ABSTRACT

The efficiency of a gas turbine engine tends to be increased when its turbine blades are operated at higher temperatures. In turn, this requires the adequate cooling of these turbine blades (for both rotors and stators, collectively termed "airfoils"). Of specific concern in this study is the cooling at the trailing-edge of the airfoils. However, there exists limited space for cooling due to a requirement for a thin trailing-edge. A combination of perforated blockage plates and a pin-fin array (a "blockage pin-fin" configuration) is particularly focused on here. Such a configuration has been previously discounted due to a presumed poor thermal performance ($\eta_{TP} < 1.0$). This thesis demonstrates that the thermal performance has been misrepresented in part due to a misunderstanding of flow behaviours present in the configuration. To this end, a series of experimental tests are undertaken using particle image velocimetry, oil-dye flow visualization, and thermochromic liquid crystal paints. The new results show that a thermal performance greater than one (i.e., $\eta_{TP} > 1.0$) can be achieved for a blockage pin-fin configuration. Despite previous studies concluding otherwise there may be merit in the use of a blockage pin-fin configuration for internally cooling the trailing-edge of a turbine blade. Further, a unique flow topology, present in a blockage pin-fin configuration was revealed. Such a flow, termed as a "jet-pin" flow, and its interactions has been previously unidentified or misinterpreted.

LIST OF CONTENTS

Declaration ..... **i**
Abstract ..... **ii**
List of Contents ..... **iii**
List of Figures ..... **vi**
Nomenclature ..... **xiii**
1. Introduction **1**
2. A Review of Gas Turbine Cooling technologies **4**
2.1. Thermal loads on gas turbine airfoils 4
2.1.1. Local surface characteristics at the mid-span 5
2.1.2. Local surface characteristics at the root and tip 7
2.2. Requirement for cooling 8
2.3. External cooling at the trailing-edge 9
2.4. Internal cooling at the trailing-edge 11
2.4.1. Background 11
2.4.2. Pin-fin cooling at the trailing-edge 15
2.4.3. Perforated blockages at the trailing-edge 22
2.4.4. Pin-fins cooled by blockage jet 30
2.4.5. Knowledge areas requiring elucidation 32
2.5. Research questions and objectives 38
2.5.1. Research questions 38
2.5.2. Objectives 38
3. Experimental Approach and Methodology **39**
3.1. Experimental approach 39
3.1.1. A singular pin-fin subjected to a singular impinging jet 39
3.1.2. The effect of perforated blockages 39
3.1.3. The thermal performance of a full blockage pin-fin configuration 40
3.2. Experimental measurements to be considered 40
3.3. End-wall surface flow visualization using an oil-dye mixture technique 40
3.3.1. Processing of images 42
3.3.2. Interpretation of the image 42
3.4. Mainstream flow measurement techniques 45
3.4.1. Data reduction parameters 46
3.4.2. Measurement uncertainties 46
3.5. Flow field mapping using particle image velocimetry (PIV) 47
3.6. Surface temperature measurements 50

3.6.1. End-wall surface heating 50
3.6.2. End-wall surface temperature mapping using infrared thermography 50
3.6.3. Surface heat transfer mapping using thermochromic liquid crystal (TLC) 51
3.6.4. Data reduction parameters and uncertainties for surface temperature measurements 56
4. A Pin-Fin Subjected To An Impinging Tube Jet 59
4.1. Objective 59
4.2. Test setup 59
4.2.1. Rationale for specifications 60
4.2.2. Consideration of the distances between jet exit and pin-fin leading-edge 61
4.3. Flows around pin-fin subjected to an impinging tube jet 62
4.3.1. Flows at the end-wall surface 62
4.3.2. Flows in the vertical plane 63
4.3.3. Flows away from the end-wall 65
4.3.4. Heat transfer on the end-wall surface 67
4.4. Effect of the jet exit-to-pin-fin leading-edge distance 68
4.4.1. Flows away from the end-wall 68
4.4.2. Flows in the vertical plane 70
4.4.3. Flows at the end-wall surface 72
4.4.4. Heat transfer on the end-wall surface 73
4.5. Summary 74
5. Effects of Perforated Blockages and neighbouring pin-fins 77
5.1. Objectives 77
5.2. Test setup 77
5.2.1. General setups 77
5.2.2. Rationale for additional specifications 78
5.3. The effect of perforated blockages for a singular pin-fin 80
5.3.1. Consideration of the distances between perforation exit and pin-fin leading-edge 80
5.3.2. Flows at the end-wall surface 80
5.3.3. Flows in the vertical plane 82
5.4. The effect of multiple jets interacting with multiple pin-fins 84
5.4.1. Flows in the mid-height of an empty channel 84
5.4.2. Flows in the channel mid-height with downstream pin-fins 88
5.4.3. Flows at the end-wall surface with multiple pin-fins 95
5.5. Summary 100
6. Thermal Performance of a Blockage Pin-Fin Configuration 102
6.1. Objective 102
6.2. Test setup 102

6.2.1. General setups 102
6.2.2. Rationale for specifications 103
6.3. Flows in the channel mid-height 104
6.3.1. Without pin-fins 104
6.3.2. With pin-fins 106
6.4. Flows at the end-wall surface 108
6.5. End-wall heat transfer 110
6.6. Heat transfer on perforated blockage surfaces 113
6.7. Pin-fin heat transfer 115
6.8. Thermal performance 116
6.9. Summary 117
7. Conclusions 119
8. Recommendation for future work 122
8.1. Further development of a more optimal blockage pin-fin configuration 122
8.2. Numerical studies 122
8.3. Consideration of additional parameters 123
9. References 124

LIST OF FIGURES

Figure 1.1. Cross-section of a representative gas turbine engine as used in commercial aviation applications. (a) Overall engine layout of a turbofan type, (b) The stator and rotor terminology, and (c) An example of cooling paths for stators and rotors. 1

Figure 2.1. Thermodynamic and fluid dynamic properties of hot gas flow through a representative turbine. (a) Trends in power, temperature, pressure and velocity over the axial length of a turbine, (b) absolute velocity distributions along the span just upstream of each airfoil, (c) static pressure distributions in the radial direction at stator input, rotor input and rotor output, and (d) total temperature distributions in the radial direction. 5

Figure 2.2. Local distributions over the pressure and suction surfaces of stators (s) and rotors (r). (a) Heat transfer, (b) Heat flux and (c) Static pressure. 6

Figure 2.3. Variation in airfoil profiles investigated previously. (a) Mark II stator (Hylton et al., 1983), (b) E3 stage-1 stator (Halila et al., 1982), (c) NASA C3X stator (Hylton et al., 1983), (d) E3 stage-2 stator (Halila et al., 1982), (e) E3 stage-1 rotor (Halila et al., 1982), (f) E3 stage-2 rotor (Halila et al., 1982), (g) Rotor by Bunker (2008), and (h) rotor by Azad et al. (2002). 6

Figure 2.4. Three-dimensional flow field near the tips and roots of a turbine airfoils. (a) Based on Goldstein and Spores (1988) and (b) Based on Gladden et al. (1988). 8

Figure 2.5. Overheated turbine rotors (Rolls Royce, 1996). 9

Figure 2.6. Example of turbine airfoils with external cooling schemes. (a) Stator vane showing pressure surface and trailing-edge (Cleynen, 2013), (b) A rotor blade showing leading-edge, trailing-edge, and suction surface (Parsons et al., 2011), and (c) A first stage rotor blade showing leading-edge, trialing-edge and pressure surface (Sulzer, 2019). 10

Figure 2.7. Trailing-edge cooling averaged in spanwise direction: (a) Schematic of trailing-edge cutback and (b) Variation of film effectiveness with blowing ratio M (Horbach et al., 2011). 11

Figure 2.8. Examples of internal structure layouts of turbine airfoils for internal cooling purposes: (a) Vertical cross section from US patent 4,753,575, (b) Vertical cross section from European patent 1,420,142B1, (c) Vertical cross section from US patent 7,377,746, (d) Profile cross section from European patent 1,420,142B1, (e) Annotated close up of trailing edge from European patent 1,420,142B1, and (f) Profile cross section from Stage 1 vane of E^3 engine (Halila et al., 1982) ... 12

Figure 2.9. Schematic of internal cooling schemes used in the trailing edge of a turbine airfoil: (a) Gas turbine airfoil design, (b) A scheme employing a pin-fin array subjected uniform-like coolant stream, (c) A scheme employing perforated blockages plates, and (d) A combination of schemes into a blockage pin-fin configuration. 13

Figure 2.10. Trailing-edge cooling scheme terminology. (a) For a pin-fin array, and (b) For a perforated blockage configuration. 14

Figure 2.11. Flow topology of a laminar horseshoe vortex system around a circular short aspect ratio pin-fin (not drawn to scale, certain features are exaggerated for illustrative purposes). 16
Figure 2.12. Near end-wall streamline patterns in pin-fin near wakes at y/H = 0.05, based on Laser-Doppler Velocimetry by Sahin et al. (2008) at Re_D = 6,150. 17
Figure 2.13. Schematic illustrating interaction between end-wall surface horseshoe vortex flows for multiple pin-fins exposed to a uniform flow field. 18
Figure 2.14. Variation of end-wall heat transfer around pin-fins with increasing pin-fin aspect ratio (H/D) reproduced from (Brigham & VanFossen, 1984). 18
Figure 2.15. Cooling performance of pin-fin array with various spacings, reproduced from Lawson et al. (2011). (a) Thermal performance variation with Reynolds number and (b) End-wall heat transfer variation along length of pin-fin array. 20
Figure 2.16. Sample of pin-fin profiles, configurations and orientations in the x-z and x-y planes where the flow direction is from left to right. (a) Circular profile, (b) Oblong profile, (c) Elliptical profile, (d) Cubic or diamond profile, (e) Staggered layout, (f) Inline layout, (g) Vertical straight, (i) vertical with stepped cross section, (j) Vertical with end fillets, and (k) Inclined. 22
Figure 2.17. Flow patterns considering perforated blockages based on prior publications. (a) For jet impingement on a flat solid surface, (b) For jet impingement on a second perforated surface in the x-y plane, and (c) For jet impingement on a second perforated surface in the x-z plane. 24
Figure 2.18. End-wall heat transfer contours between perforated blockages with spot Nu/Nu_0 values at Re_{Dh} = 10,000 adapted from (Moon & Lau, 2003). 25
Figure 2.19. Variations in trailing edge blockage perforations configurations. (a) With circular perforations, (b) With slotted or square perforations, (c) With perforations not aligned with the channel mid-height, (d) With multiple rows of perforations, (e) With perforations at end-wall, and (f) With inclined perforations. 26
Figure 2.20. Schematic of characteristic turbulent jet and select flow properties. 28
Figure 2.21. Blockage jet characteristics based on results from Liu et al. (2022): (a) Variation of potential core length (l_p) with t/D_j with shaded region indicating a more practical range of t/D_j for internal cooling at leading edge of gas turbine blades and (b) Radial profile at jet exit. 29
Figure 2.22. Radial heat transfer distributions on target plate at Re_j = 20,000 for both blockage jets (t/D_j = 2.0 and 5.0), with H/D_j =: (a) 1.0, and (b) 2.0. (Liu et al., 2022). 30
Figure 2.23. Distinction for a combination of perforated blockages and pin-fins. (a) With jets perpendicular to pin-fin axis and (b) With jets parallel pin-fin with parallel and perpendicular jets. 31
Figure 2.24. Sample of end-wall heat transfer contours adapted from Kan et al. (2014). (a) with 7 perforations and a blockage ratio of 11.45% and (b) With 4 perforations and a blockage ratio of 11.06%. 31

Figure 2.25. Velocity contours from numerical simulations for a pin-fin array near the end-wall (y/D = 2.5×10^{-4}) by Kan et al. (2014). (a) With a uniform-like upstream flow field and (b) With an upstream perforated blockage and close up (inset).....33
Figure 2.26. Envisaged flow patterns considering perforated blockages. (a) In the plane of symmetry (*x*-*y* plane) and (b) On the end-wall (*x*-*z* plane). 34
Figure 2.27. Velocity contours in the mid-height plane through a pin-fin array from previous studies. (a) With uniform-like upstream flow field and upstream flow in the x-direction (Kan et al., 2014), (b) With upstream perforated blockage and upstream flow in the x-direction (Kan et al., 2014) (c) With uniform-like upstream flow field and upstream flow in the y-direction (Kim et al., 2019) and (d) With upstream perforated blockage and upstream flow in the y-direction (Kim et al., 2019)..35
Figure 2.28. Flow schematics regarding blockage jet curvature. (a) For a blockage jet exhibiting curvature and off-axis impingement on a pin-fin, (b) Mutual entrainment and symmetrical flow curvature, and (c) Symmetrical entrainment preventing curvature.....36
Figure 3.1. Summary of setups to be assessed. (a) With a single tube jet impinging on a single pin-fin, (b) Considering the effects of perforated blockages and multiple pin-fins, and (c) With a full blockage pin-fin configuration. 39
Figure 3.2. Example of residual oil-dye splatter on lid of test section following a test. 41
Figure 3.3. Processing transition of oil dye flow visualization technique including closeup for a pin-fin exposed to a uniform flow field at Re_D = 35,000. (a) Original raw image and (b) Processed final image. 42
Figure 3.4. Oil-dye flow visualization for a uniform-like flow around a short circular pin-fin at Re_D = 3.5×10^{4}, showing an end-wall flow topology image (upper part) and corresponding interpreted schematic (lower part). (a) With the typical mixture ratio of oil and dye and (b) With a larger ratio of dye in the mixture. 44
Figure 3.5. Oil-dye end-wall flow visualization for a tube jet exiting into an empty narrow channel (Re_j = 17,500). (a) Jet schematic in the *x*-*y* plane, (b) At the end-wall (*x*-*z* plane) with flow schematic (top), processed oil-dye image (bottom) and full oil-dye image (inset), and (c) Schematic explaining shape of end-wall patterns.....45
Figure 3.6. Test configurations for a particle image velocimetry (PIV). (a) With light sheet aligned with the *x*-*z* plane, (b) With the light sheet aligned with the *x*-*y* plane, and (c) Setup employing an isotropic planar illumination of the *x*-*y* plane. 47
Figure 3.7. Particle image velocimetry (PIV) measurement windows in the *x*-*y* and *x*-*z* planes for various setups. (a) With a single tube jet impinging on a single pin-fin, (b) For considering the effect of perforated blockages on a single row of pin-fins, and (c) With a full blockage pin-fin configuration. 48
Figure 3.8. Instantaneous image from PIV demonstrating perspective along height of the pin-fins. 49

Figure 3.9. Sample image taken by infrared thermal camera for a tube jet impinging on a circular pin-fin. 51
Figure 3.10. Specifications for setup utilising thermochromic liquid crystals in a full blockage pin-fin configuration. 52
Figure 3.11. Calibration curves for the present thermochromic liquid crystal (TLC) for $\alpha = 90°$ and $\alpha = 30°$ inclined viewpoints. 53
Figure 3.12. End-wall of empty channel upstream of first perforated blockage coated with TLC's with no flow through the channel and a constant heat input. (a) Raw image showing TLC colours and (b) the calibrated temperature contours. 54
Figure 3.13. Preliminary TLC image processing approach using patchwork splicing of images for complete capture of end-wall. (a) Raw images taken from two perspectives with overlay of pin-fins, (b) Schematic showing regions masked by pin-fins (top and bottom) and spliced schematic (centre), (c) Resulting end-wall compilation image, and (d) Image capture regions used. 55
Figure 3.14. Preliminary TLC image processing approach for straightening the surfaces of the perforated blockages. (a) The raw image, (b) The isolated blockage surface, and (c) The final straightened image. 56
Figure 3.15. Points on TLC images of pin-fins where measurements were taken. (a) Of the upstream surface, (b) Of the downstream surface, (c) Of the top of the pin-fin from overhead, and (d) Schematic of camera positions. 56
Figure 4.1. Test section schematic for consideration of a single tube jet impinging on a single pin-fin. 59
Figure 4.2. Jet centreline velocity variation with increasing distance from the exit for tube jet with Re_j = 17,500. 61
Figure 4.3. End-wall flows around a short circular pin-fin subjected to an impinging jet for Re_j = 17,500 (Re_D = 35,000). (a) Oil-dye flow visualization and (b) Combination of PIV velocity contours (top) and corresponding oil-dye flow visualization (bottom). 63
Figure 4.4. Flow fields in the x-y plane at z/D_j = 0.0 for Re_j = 17,500 (Re_D = 35,000). (a) Velocity contours from PIV and (b) Closeup of the velocity contours from PIV at the corner between the lower end-wall and pin-fin base. 64
Figure 4.5. Flow field schematics for the development of the end-wall jet stream-lines: (a) For radial end-wall jets and (b) For tangential end-wall jets. 65
Figure 4.6. Flow features from PIV in the x-z plane for Re_j = 17,500 (Re_D = 35,000). (a) PIV at the mid-height of the channel (y/H = 0.5), (b) PIV at the quarter height of the channel (y/H = 0.25). 66
Figure 4.7. End-wall heat transfer for for a short pin-fin subjected to a jet impingement at l/D_j = 2.0 from the pin-fin leading edge for $Re_D = 3.5\times10^4$. (a) Temperature contour from infrared thermography on the end-wall surface (top) with corresponding end-wall flow pattern and (b) Nusselt number distribution in the plane of symmetry. 67

Figure 4.8. Velocity contours from PIV in the *x-z* plane at the mid-height of the channel ($y/H = 0.5$) for Re_j = 17,500 (ReD = 35,000). (a) For $l/D_j = 2.0$, (b) For $l/D_j = 4.0$, and (c) For $l/D_j = 8.0$. 69
Figure 4.9. Velocity contours from PIV in the *x-z* plane at $y/H = 0.25$) for Re_j = 17,500 (ReD = 35,000). (a) For $l/D_j = 2.0$, (b) For $l/D_j = 4.0$, and (c) For $l/D_j = 8.0$. 69
Figure 4.10. Flow distributions along the z-axis at $x'/D = -0.75$ for the l_2, l_4 and l_8 cases for Re_j = 17,500 (ReD = 35,000). (a) Velocity magnitude at $y/H = 0.5$, (b) Velocity magnitude at $y/H = 0.25$, (c) flow directions at $y/H = 0.5$, and (d) Flow directions at $y/H = 0.25$..... 70
Figure 4.11. Velocity contours from PIV in the vertical (*x-y)* plane at $z/D_j = 0.0$ for Re_j = 17,500 (Re_D = 35,000). (a) For $l/D_j = 2.0$, (b) For $l/D_j = 4.0$, (c) For $l/D_j = 8.0$, (d) closeup of pin-fin and end-wall interface for $l/D_j = 4.0$, and (e) Closeup of pin-fin and end-wall interface for $l/D_j = 8.0$. 72
Figure 4.12. Flow distributions along the *y*-axis at $x'/D = -1.0$ for the l_2, l_4 and l_8 cases for Re_j = 17,500 (Re_D = 35,000). (a) Velocity magnitude distributions and (b) Flow direction distributions. 72
Figure 4.13. End-wall flow field with velocity contours from PIV (top) and flow visualization from oil-dye (bottom) for Re_j = 17,500 (Re_D = 35,000). (a) For $l/D_j = 2.0$, (b) For $l/D_j = 4.0$, and (c) For $l/D_j = 8.0$. 73
Figure 4.14. End-wall heat transfer for for a short pin-fin subjected to a jet impingement at l/D_j=2.0 from the pin-fin leading edge for Re_j = 17,500 (Re_D = 35,000). (a) For $l/D_j = 2.0$, (b) For $l/D_j = 4.0$, and (c) For $l/D_j = 8.0$. 74
Figure 4.15. Schematics of flow topologies in the vertical (*x'-y*) plane and on the end-wall surface, and corresponding end-wall heat transfer distribution for a pin-fin subjected to an impinging jet. 75
Figure 5.1. Test section schematic for consideration of perforated blockages with multiple pin-fins. 77
Figure 5.2. Terminology applied to jet configurations used in Chapter 5. (a) With only direct impingement on the pin-fins and (b) With flanking jets. 79
Figure 5.3. Jet centreline velocity variation with increasing distance from the exit for a tube jet at Re_j = 17,500 and a blockage jet ($t/D_j = 0.5$) at Re_j = 22,000. 80
Figure 5.4. End-wall flows from oil-dye visualization around a single pin-fin subjected to an impinging blockage jet at Re_j = 22,000. (a) For $l/D_j = 1.0$, (b) For l/D_j =2.0, (c) A closeup of the outer leading edge of the pin-fin for $l/D_j = 1.0$, (d) Flow schematic for flow interaction between radial streamlines and blockage plate, and (e) For $l/D_j = 4.0$. 82
Figure 5.5. Flow field in the vertical (*x-y*) plane of a single pin-fin subjected to an impinging jet. (a) For $l/D_j = 2.0$ for a tube jet at Re_j = 17,500, (b) For l/D_j =4.0 for a tube jet at Re_j = 17,500, (c) For $l/D_j = 1.0$ with a blockage jet at Re_j = 22,000, (d) For $l/D_j = 2.0$ with a blockage jet at Re_j = 22,000, and (e) For $l/D_j = 4.0$ with a blockage jet at Re_j = 22,000. 83
Figure 5.6. Extracted distributions in the mid-height plane ($y/H = 0.5$) along the *y*-axis at $x'/D_j = -1.25$ for a tube jet flows at Re_j = 17,500 and blockage jet flows at Re_j = 22,000. (a) Velocity distribution for tube jet flows, (b) Velocity distribution for blockage jet flows, (c) Flow direction distribution for tube jet flows, and (d) Flow direction distribution for blockage jet flows. 84

Figure 5.7. Velocity contours from PIV for jets exiting into an empty channel in the mid-height plane (y/H = 0.5) comparing three configurations of blockage jets at Re_j = 22,000. (a) For a 1-jet configuration (b) For a 3-jet configuration, and (c) For a 7-jet configuration. 85
Figure 5.8. Extracted jet centreline velocity distribution along the x-axis for 1-jet, 3-jet, and 7-jet configurations at Re_j = 22,000 86
Figure 5.9. Distribution of flow velocity magnitude along the jet axis for the centre jet (at z/D_j = 0.0) and outer jet (at z/D_j = -4.0) for x/D_j = 0.75, 1.75 and 3.75 for blockage jets exiting into empty channel at Re_j = 22,000. 87
Figure 5.10. Distribution of flow direction along the jet axis for the centre jet (at z/D_j = 0.0) and outer jet (at z/D_j = -4.0) for x/D_j = 0.75, 1.75, and 3.75 for blockage jets exiting into empty channel at Re_j = 22,000. 88
Figure 5.11. Velocity contours in the mid-height plane (y/H = 0.5) from PIV at Re_j = 22,000. (a) For a 3-jet configuration at l/D_j = 1.0, (b) For a 7-jet configuration at l/D_j = 1.0, (c) For a 3-jet configuration at l/D_j = 2.0, (d) For a 7-jet configuration at l/D_j = 2.0, (e) For a 3-jet configuration at l/D_j = 4.0, and (f) For a 7-jet configuration at l/D_j = 4.0. 90
Figure 5.12. Extracted distributions in the mid-height plane (y/H = 0.5) along the z-axis at x'/D_j = -1.25 without downstream pin-fins (empty) and with the pin-fins at l/D_j = 1.0 for 3-jet and 7-jet configurations at Re_j = 22,000 91
Figure 5.13. Extracted velocity distributions at l/D_j = 2.0 and 4.0 in the mid-height plane (y/H = 0.5) along the z-axis at x'/D_j = -1.25 upstream of the pin-fin at Re_j = 22,000 for 3-jet and 7-jet configurations. 92
Figure 5.14. Extracted flow direction distributions at l/D_j = 2.0 and 4.0 in the mid-height plane (y/H = 0.5) along the z-axis at x'/D_j = -1.25 upstream of the pin-fin at Re_j = 22,000 for 3-jet and 7-jet configurations. 93
Figure 5.15. Centreline velocity decay of the flanking jet exiting at z/D_j = ±2.0 without pin-fins (empty) and with pin-fins at l/D_j = 2.0 and 4.0. 94
Figure 5.16. End-wall flow fields from oil-dye with 3 pin-fins subjected to a uniform like flow field for Re_D = 44,000. (a) Overview of all three pin-fins and (b) Closeup of end-wall around C and L pin-fins. 95
Figure 5.17. End-wall flow fields from oil-dye with 3 pin-fins for Re_j = 22,000 (Re_D = 44,000) with overviews for l/D_j = 1.0. (a) For a 3-jet configuration and (b) For a 7-jet configuration. 96
Figure 5.18. Schematic illustrating interaction between end-wall surface jet pin flows for multiple pin-fins exposed to multiple impinging blockage jets. 97
Figure 5.19. End-wall flow fields from oil-dye with 3 pin-fins for Re_j = 22,000 (Re_D = 44,000) with overviews for l/D_j = 2.0. (a) For a 3-jet configuration and (b) For a 7-jet configuration. 99
Figure 5.20. End-wall flow fields from oil-dye with 3 pin-fins for Re_j = 22,000 (Re_D = 44,000) with overviews for l/D_j = 4.0. (a) For a 3-jet configuration and (b) For a 7-jet configuration. 99

Figure 6.1. Test section schematic for consideration of a complete blockage pin-fin configuration. 103
Figure 6.2. Velocity contours from PIV at the channel mid-height ($y/H = 0.5$) for a perforated blockage configuration, without downstream pin-fins at Re_j = 13,000 (Re_{Dh} = 10,000). (a) A standard result and (b) An anomalous result. 105
Figure 6.3. Centreline velocity decay for blockage jets ($t/D_j = 0.5$) in various configurations at Re_j = 22,000 for 1- and 7-jet configurations and Re_j = 13,000 for 10-jet configurations. 106
Figure 6.4. Mid-height velocity contours with pin-fins from PIV at Re_D = 26,000 (Re_{Dh} = 10,000). (a) With upstream perforated blockages as a blockage pin-fin configuration and (b) Without upstream perforated blockages as a conventional pin-fin array configuration. 107
Figure 6.5. Velocity variations along the x-axis through perforated blockage (PB), blockage pin-fin (BPF) and pin-fin (PF) array configurations at Re_D = 26,000 (Re_j = 13,000, Re_{Dh} = 10,000). (a) From $z/D_j = 0.0$ and (b) From $z/D_j = 1.0$..... 108
Figure 6.6. End-wall surface flow patterns by oil-dye flow visualization at Re_D = 26,000 (Re_{Dh} = 10,000). (a) Between perforated blockage plates in blockage pin-fin configuration with closeup on the left, (b) Around a pin-fin array in a blockage pin-fin configuration, and (c) Section of end-wall around a pin-fin array in a conventional pin-fin array. 109
Figure 6.7. End-wall surface heat transfer contours measured by TLC for the BPF configuration at Re_D = 26,000 (Re_{Dh} = 10,000). Between perforated blockage plates and (b) Around a pin-fin array. 110
Figure 6.8. Local end-wall heat transfer variation along the length of a pin-fin array in a blockage pin-fin configuration for at Re_D = 26,000 (Re_j = 13,000, Re_{Dh} = 10,000). (a) At $z/D_j = 0.0$ and (b) At z/D_j = 2.0. 111
Figure 6.9. End-wall heat transfer averaged in the transverse (z) direction for the blockage pin-fin (BPF) and conventional pin-fin (CPF) configurations at $Re_{Dh} \approx 10{,}000$. (a) Between perforated blockages and (b) Around the pin-fin array. 113
Figure 6.10. Heat transfer contours measured using TLC on the surface of the perforated blockages of a blockage pin-fin configuration at Re_{Dh} = 10,000: (a) The first blockage and (b) The second blockage. 114
Figure 6.11. Pin-fin surface heat transfer measured using TLC at $Re_{Dh} \approx 10{,}000$. (a) Individual pin-fin surface heat transfer for a blockage pin-fin configuration and (b) Spanwise-averaged pin-fin heat transfer for a blockage pin-fin (BPF) and conventional pin-fin (CPF) configurations. 116
Figure 6.12. Comparisons of cooling performance with conventional pin-fin arrays (CPF), blockage pin-fin configurations (BPF) and perforated blockages (PB) at $Re_{Dh} \approx 10{,}000$. (a) Heat transfer, (b) Friction factor, and (c) The thermal performance (η) with different cooling configurations. 117

NOMENCLATURE

A	Area
Cp	Specific heat of air
D	Pin-fin diameter
Dj	Jet or orifice diameter
f	Moody friction factor
H	Height of the channel / cylinder
h	Heat transfer
k	Thermal conductivity
l	Distance between jet exit and pin-fin leading edge
lp	Potential Core length
$\dot{m}$	Mass flow rate
Nu	Nusselt number
p	static pressure
Pr	Prandtl number
Q	applied heat
q''	heat flux
r	radial length extending from a pin-fin surface
r	reference length from pin-fin surface
Re	Reynolds number
S	relative spacing distance / separation point
T	temperature
t	thickness of perforated blockage
Tin	temperature at inlet of channel
U	velocity along streamwise direction
W	channel width
x	streamwise axis with origin at the exit of the jet
x'	streamwise axis with origin at the centre of the pin-fins base
y	vertical axis with origin at the lower end-wall surface
z	spanwise axis with origin at the centre of the channel

Greek symbols

α	inclination of r vector
μ	dynamic viscosity
ρ	air density
η	thermal performance

Subscripts

0	baseline value
amb	ambient air conditions
avg	average

b	blockage
bulk	local bulk air value
c	jet centreline
D	pin-fin
Dh	hydraulic diameter
e	jet exit
h	heater
in	inlet
ins	insulation board
j	jet
s	surface condition
x	streamwise direction
z1	spanwise direction with respect to pin-fins
z2	spanwise direction with respect to jet centrelines

1. INTRODUCTION

Gas turbine engines, a form of internal combustion engine, are used broadly in aviation, maritime, and land-based power generation applications. Such engines are favoured in aviation and shipbuilding for high power to weight ratios, smaller size factors, and greater reliability than common alternatives such as reciprocating engines. The engines are also advantageous in land-based power generation for relatively fast start-up times and the ability to run on a variety of fuels. They will see continued use into the foreseeable future (Carter et al., 2023) and further research into improving their designs is thus required.

Figure 1.1(a) shows a turbofan-type variant of a gas turbine used to produce thrust for an aircraft as an example. There the working gaseous fluid (e.g., air) is brought into the engine, through a large fan section, and compressed through a series of compressor stages. The compressed air is then mixed with the fuel in the combustor and ignited, producing high temperature and momentum gas streams. The hot gases expand through a turbine before being discharged into the atmosphere. The turbine is responsible for converting a portion of the energy of the expanding gases into mechanical energy, which can then be used to maintain the rotation of the engines' components and generate power for systems external to the engine. Thrust is generated both by the exhaust of the hot gases leaving the engine and from the front fan, that utilises power extracted from the turbine.

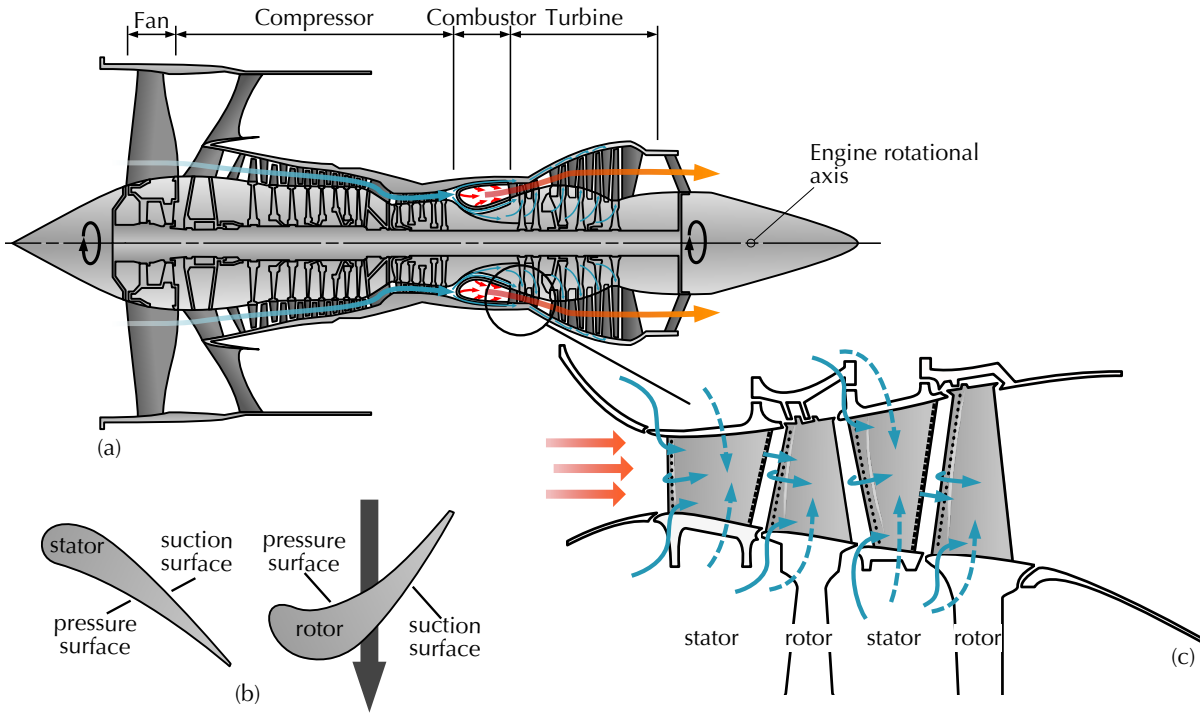

Figure 1.1. Cross-section of a representative gas turbine engine as used in commercial aviation applications. (a) Overall engine layout of a turbofan type, (b) The stator and rotor terminology, and (c) An example of cooling paths for stators and rotors.

The overall efficiency of a gas turbine engine relies on the efficiency of subsidiary components (i.e. compressor, combustor and turbine). Of note is the temperature of exhaust gas streams from the combustor section leading into the turbine section. The so-called "turbine inlet temperature (TIT)," plays an important role in determining the overall efficiency – the higher the TIT, the greater the energy in expanding gases moving through gas turbine stages and the higher the gas turbine efficiency. It has been previously reported (Johnke & Mast, 2002; Ni et al., 2005) that an increased TIT of 100 K may lead to a 6~7% reduction of fuel consumption and a 20%~25% increase in output power. Further, with engine size unchanged, a 55 K increase in TIT leads to a 10% increase in engine thrust. Therefore, numerous efforts have been made to increase the TIT of gas turbine engines that can operate at temperatures of 1600 ºC to nearly 2000 ºC (Han, 2018; Langston, 2007; Yuri et al., 2013). These operating temperatures, however, are far above the permissible temperatures of the typical material used in the turbine stage, being approximately 777 ºC to approximately 1420 ºC (Han, 2018; Langston, 2007; Shaikh, 2018). Higher TITs are possible using higher quality materials such as nickel-based alloys. The nickel-based alloys are nonetheless heavier and hence, while allowing for higher TITs, there is an increase in centrifugal stresses at turbine blade root. Therefore, of equal or higher importance in the development of gas turbines with higher TIT's has been the use of active cooling of the airfoils.

These airfoils are categorised as either stator vanes or rotor blades (shown in Figure 1.1(b)). Each turbine stage, in an axial turbine, is comprised of a ring of stationary stator vanes and a ring of rotating blades. The stator vanes are also referred to as nozzle guide vanes, stator blades or simply stators, nozzles or vanes in some texts. The first stage stator vanes are often specifically referred to as inlet guide vanes (IGVs). The rotor blades are, similarly, also referred to as rotors or blades. The more turbine stages in a gas turbine, the more energy that is possible to be extracted.

Thus far, various techniques of cooling stator vanes and rotor blades (or "airfoils" collectively for both as they will hereon be referred) have been proposed. These include air cooling, water cooling and steam cooling. Among these, air cooling appears to be the most prevalent technique, predominantly adopted by contemporary gas turbine blades for aero-propulsion and will be focused on here. This is likely due to the lower weight compared to water or steam cooling techniques as the coolant is sourced from the ambient air and does not need to be taken onboard the aircraft separately. In a modern gas turbine engine, around 20% (Han, 2013) of the compressed air, from the compressor section, is known to be bled off before entering the combustor and used for cooling and sealing purposes. An example of the internal coolant path is schematically illustrated in Figure 1.1(c) – dashed lines representing flows internal to the turbine structures and solid lines representing flows ejecting into the mainstream flow. The coolant is fed through the internal structure of the engine and then to the turbine airfoils. The coolant is either passed internally through the airfoils before being returned to the mainstream passage in the turbine section or ejected at root or tips of the airfoils. Cooling technologies are then broken down into internal and external cooling. Internal cooling considers the usage of the coolant through the

internal structure while external cooling considers the usage of the coolant external to the airfoils.

An increase in the pumping power required to supply the coolant results in a reduction in engine performance (Han, 2013, Boyce, 2012). Therefore, during the design process of the turbine stages, a compromise is needed to minimize the amount of coolant that is bled from compressors while maximizing the cooling. This ensures that the maximum airfoil surface temperatures and temperature gradients during operation are compatible with the maximum airfoil thermal stress for the life of the design, under the highest possible turbine inlet temperature for the maximum efficiency of gas turbine engines. This forms the primary challenge when developing cooling configurations for turbine airfoils. The thermal loads on gas turbine airfoils are notoriously difficult to accurately predict under operating conditions. Inaccurate predictions have significant implications on factors such as turbine airfoil life, which can be reduced by 50% if the temperature prediction is off by only 10 K (Han et al., 2012). To compensate for this, gas turbines are designed non-optimally to use more coolant than may be necessary in case of higher temperatures. This, in turn, results in the engine operating in a non-optimal state. An improved understanding and design of gas turbine airfoil cooling techniques then enables designs that require less coolant overall or designs that prevent local hot spots that may reduce airfoil life.

Given the large scope encompassed in turbine cooling research, a focus on specific areas and technologies becomes necessary. Here, the focus will be on the internal air-cooling at the trailing-edge of the airfoils. Specifically, the performance of a cooling configuration involving both perforated blockages and a pin-fin array will be assessed. The rationale for this focus and the consequent research question will be elucidated in the following chapters.

2. A REVIEW OF GAS TURBINE COOLING TECHNOLOGIES

2.1. Thermal loads on gas turbine airfoils

Before considering cooling schemes, how the hot gases from the combustor stage interact with gas turbine airfoils, needs to be understood. These interactions explain the thermal and fluid dynamics to which the airfoils are exposed. Such loads are the basis for understanding what cooling schemes may be necessary. Here, as an example, a two-stage turbine as shown in Figure 1.1(c) and Figure 2.1(a) is considered. The thermal loads shown in Figure 2.1 are summarized based on those from literature (Dunn, Martin, et al., 1986; Han, 2013; Rolls-Royce, 1996; Suo, 1978).

When analyzing the mainstream flow characteristics through gas turbine stages, the primary parameters are the static and total pressure (P_s and P_0), the static and total temperature (T_s and T_0) and the flow velocity magnitude (V_{abs}). The variation of these parameters through the turbine are qualitatively shown in Figure 2.1(a), following Boyce (2012). From the combustor, the static pressure and temperature decrease through the stators (including the inlet guide vanes (IGV's)) as the flow accelerates and the mainstream flow begins to cool. The total pressure, total temperature and stagnation enthalpy (H_o) are considered to be constant since there is no energy being extracted by the IGVs or stators from the mainstream flow. Since energy is extracted by the rotors, the total pressure, total temperature and stagnation enthalpy all decrease across the rotors. The static pressure and temperature continue to decrease although at a different rate to that through the IGV's or stators. In contrast, the velocity magnitude increases across a stator and decreases across a rotor (Figure 2.1(a)). At the entrance to the first stage rotors, the absolute velocity is in the order of 750 m/s (Rolls-Royce, 1996), which is considered close to the speed of sound due to high temperatures of the gaseous stream. This velocity is 2 to 3 times higher than that at the entrance to the IGVs (Han, 2013).

Along the span of the airfoil (from root to tip), the absolute velocities (Figure 2.1(b)), static pressure (Figure 2.1(c)) and static temperature (Figure 2.1(d)) vary. The variation in absolute velocity is designed to be uniform leading into the IGVs and stators to limit loads near the root and tips (Rolls-Royce, 1996). After an IGV or stator the velocity becomes skewed towards the root. Geometric twisting of the rotor along its span then ensures a uniform velocity distribution leading into the next stator or the exhaust. The static pressure (Figure 2.1(c)) is skewed towards the tip downstream of an IGV or stator (Dunn, Martin, et al., 1986; Rolls-Royce, 1996). The total temperature (T_o in Figure 2.1(d)) is similarly skewed towards the tip, which is attributed to the rotation of the rotors. By design, it is intended that the peak temperatures occur away from the root or tip to minimize the thermal loads there (Han, 2013).

The variation in thermodynamic and fluid dynamic characteristics through the turbine section, shown in Figure 2.1, leads to local variations of flow characteristics on the surface of each airfoil. Due to the variations along the airfoil span (Figure 2.1(b-d)), characteristics at the mid-span are typically considered independently to those at the roots and/or tips.

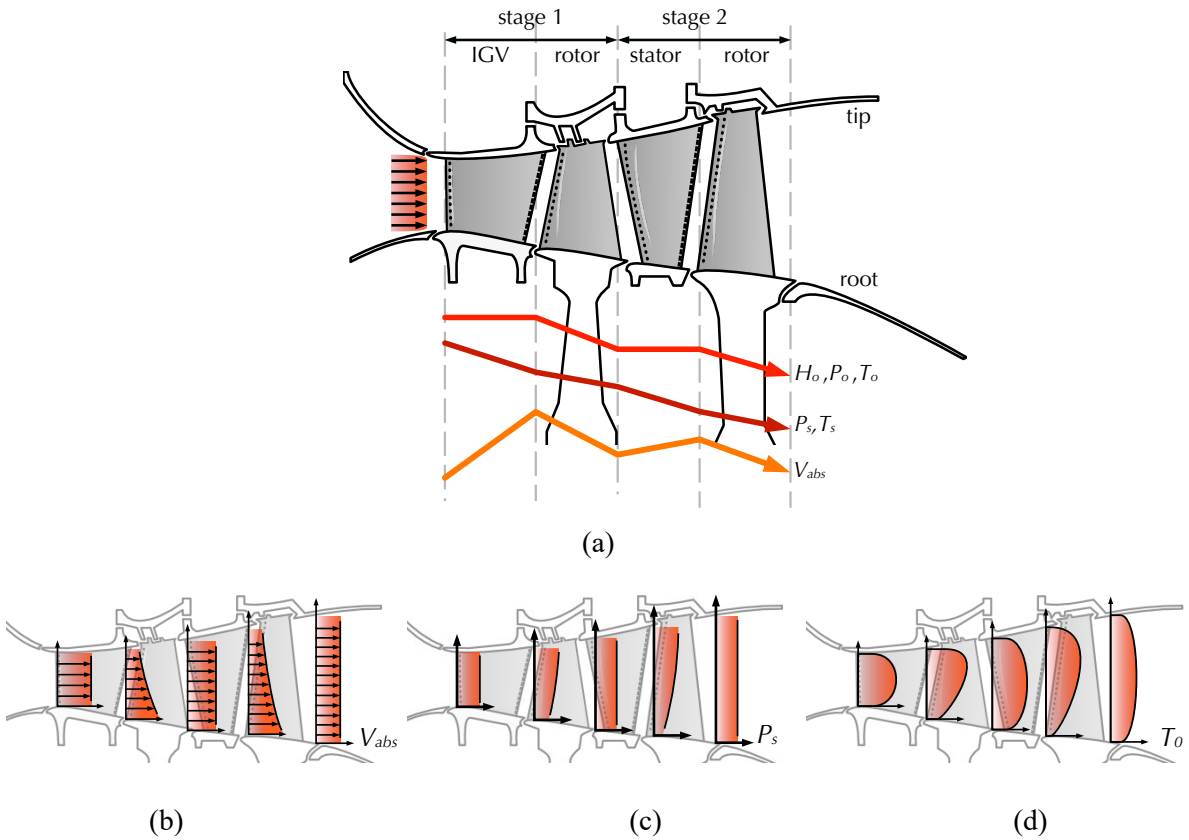

Figure 2.1. Thermodynamic and fluid dynamic properties of hot gas flow through a representative turbine. (a) Trends in power, temperature, pressure and velocity over the axial length of a turbine, (b) absolute velocity distributions along the span just upstream of each airfoil, (c) static pressure distributions in the radial direction at stator input, rotor input and rotor output, and (d) total temperature distributions in the radial direction.

2.1.1. Local surface characteristics at the mid-span

The local flow characteristics for stators and rotors in the mid-span of the airfoils, away from root and tip effects, are shown in Figure 2.2. Quantitative trends and variations of the local flow characteristics for stators and rotors are subjected to numerous parameters including gas stream properties (such as those in Figure 2.1), the specific airfoil shapes (a sample of which is shown in Figure 2.3), and the local introduction of cooling flows ejected into the mainstream (as shown by solid lines in Figure 1.1(c)). Qualitative trends can, however, be generated and are summarized in Figure 2.2. These have been obtained from a combination of studies on operating gas turbine engines and simulated turbine stages.

The three primary parameters of interest are heat transfer (Figure 2.2(a)), heat flux (Figure 2.2(b)) and static pressure (Figure 2.2(c)). The pressure and suction surfaces of both stators and rotors are considered. Static pressure distributions were adapted from (Blair et al., 1989; Guenette et al., 1989; Nealy et al., 1984). These distributions are governed predominantly by the cross-sectional profile of a given airfoil with the static pressure on the suction surface being more susceptible to changes in the

airfoil profile. For example, an airfoil with a blunter leading-edge as seen for the NASA C3X airfoil (Figure 2.3(c)), results in a smoother variation of static pressure on the suction surface. The noticeable dip in static pressure on the stator in Figure 2.2(c), would be less distinct for a blunter leading-edge (Nealy et al., 1984). The heat transfer and heat flux distributions are similarly dependent on the surrounding flow features and airfoil shape. The distribution of heat transfer is not typically presented in this manner but is shown here for completeness, based on a compilation of results from multiple publications (Blair et al., 1989; Camci & Arts, 1990; Dunn, George, et al., 1986; Martinez-Botas et al., 1995). The heat flux distribution was adapted from (Han & Wright, 2006).

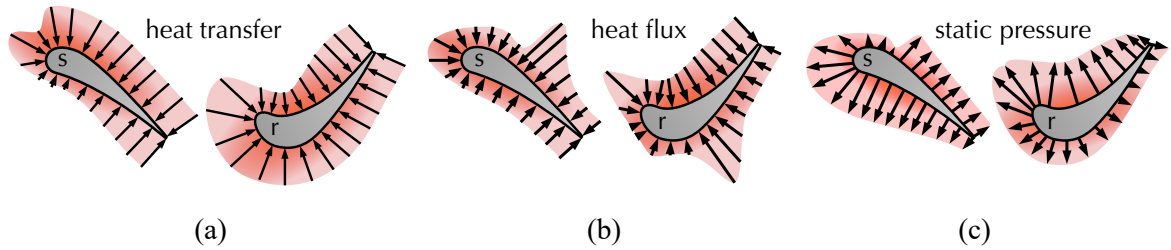

Figure 2.2. Local distributions over the pressure and suction surfaces of stators (s) and rotors (r). (a) Heat transfer, (b) Heat flux and (c) Static pressure.

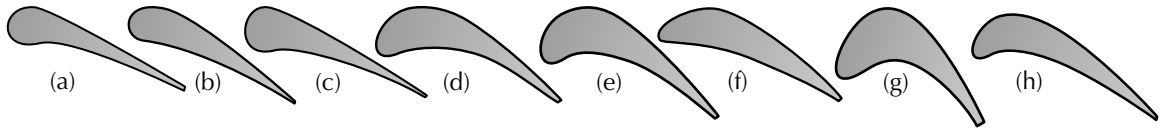

Figure 2.3. Variation in airfoil profiles investigated previously. (a) Mark II stator (Hylton et al., 1983), (b) E3 stage-1 stator (Halila et al., 1982), (c) NASA C3X stator (Hylton et al., 1983), (d) E3 stage-2 stator (Halila et al., 1982), (e) E3 stage-1 rotor (Halila et al., 1982), (f) E3 stage-2 rotor (Halila et al., 1982), (g) Rotor by Bunker (2008), and (h) rotor by Azad et al. (2002).

For a given airfoil profile, variations in static pressure and temperature are, based on prior studies, attributed to changes in (1) Reynolds number (Blair et al., 1989; Nealy et al., 1984), (2) Mach number (Nealy et al., 1984), (3) free stream turbulence (Ames, 1997; Ames & Plesniak, 1997), (4) unsteady wakes (Ashworth et al., 1985; Doorly and Oldfield, 1985; Dullenkopf et al., 1991; Guenette et al., 1989; Han et al., 1993; Lorenz et al., 2010; Mayle and Dullenkopf, 1991; O'Brien and Capp, 1989; Priddy and Bayley, 1988; Schobeiri and Pardivala, 1992), and (5) surface roughness (Abuaf et al., 1998; Boyle & Senyitko, 2005; Erickson et al., 2012; Hoffs et al., 1996; Lorenz et al., 2010). These properties tend to have an effect either on the leading-edge, suction surface or trailing-edges of the airfoils. For example, the Reynolds number governs where boundary layer transition to turbulence occurs. The transition to turbulence is responsible for the sharp increase in heat flux on the suction side surface as seen in Figure 2.2(b). An increase in the Reynolds number causes the boundary layer transition to move

towards the leading-edge and, as a result, overall higher levels of heat transfer across the surface of the airfoil are encountered (Blair et al., 1989; Nealy et al., 1984).

While important to note and understand, these properties (from Reynolds number to surface roughness) are difficult to consider in experimental studies. Numerical simulations can address some of these constraints but in turn large computational processing is expected. As such the thermal loads that airfoils are exposed (as shown in Figure 2.2) should be seen as a guide. Specifically, a guide of where to focus cooling technologies and what areas, such as the trailing edge of the airfoils, require more cooling than others.

2.1.2. Local surface characteristics at the root and tip

In addition to the surfaces of stators and rotors in the mid-span, distinct flows and associated heat transfer feature at the roots and tips of the airfoils. The flow structures featured are shown in Figure 2.4. The end-wall surfaces are seen to be dominated by horseshoe vortex-type flows. Secondary flows towards the end-wall on the pressure surface and away from the end-wall on the suction surface exist, causing vortices to detach from the end-wall. The horseshoe vortices that detach from the end-wall, specifically the passage and suction side vortices, enhance heat transfer along the suction surface of the airfoil (Goldstein et al., 1994; Graziani et al., 1980). The region of enhanced heat transfer extends over a significant portion of the trailing-edge of the suction surface of the airfoil. Heat transfer on the pressure surface is not enhanced to any significant degree, due to lack of surface vortices, with only a small enhancement very close to the end-wall (Goldstein et al., 1994).

Due to the high rotational speed of the rotors, a high blade loading is generated, causing a large pressure difference between the pressure side and the suction side of the rotors. As a result, some hot exhaust gases leak from the pressure side via a tip gap to the suction side. This tip flow is the primary cause of turbine tip failure, as hot gases passing through the narrow gap lead to increased heat transfer near the tip of the pressure and suction side of the rotors. Further, as the hot gaseous stream moves through the gap, it forms a vortex near the trailing-edge tip of the suction side, which would be expected to increase the heat transfer further. These effects on heat transfer are not applicable to typical stators, because there is no need to design for a gap, as the structure is not required to rotate relative to stationary parts of the gas turbine. For the rotors, however, it is difficult to eliminate the tip gap as the clearance is used to account for thermal expansion of the blade during operation.

The root and tip gas streams contribute to a further variation in thermal load along the span of the trailing-edge of the airfoil. This variation is not accounted for in studies of internal cooling technologies, likely to simplify the measurements or isolate its effect. This same logic will be continued here and no further consideration of these root and tip external flows will be made. The flow characteristics do, however, serve to highlight the importance of cooling at the trailing-edge.

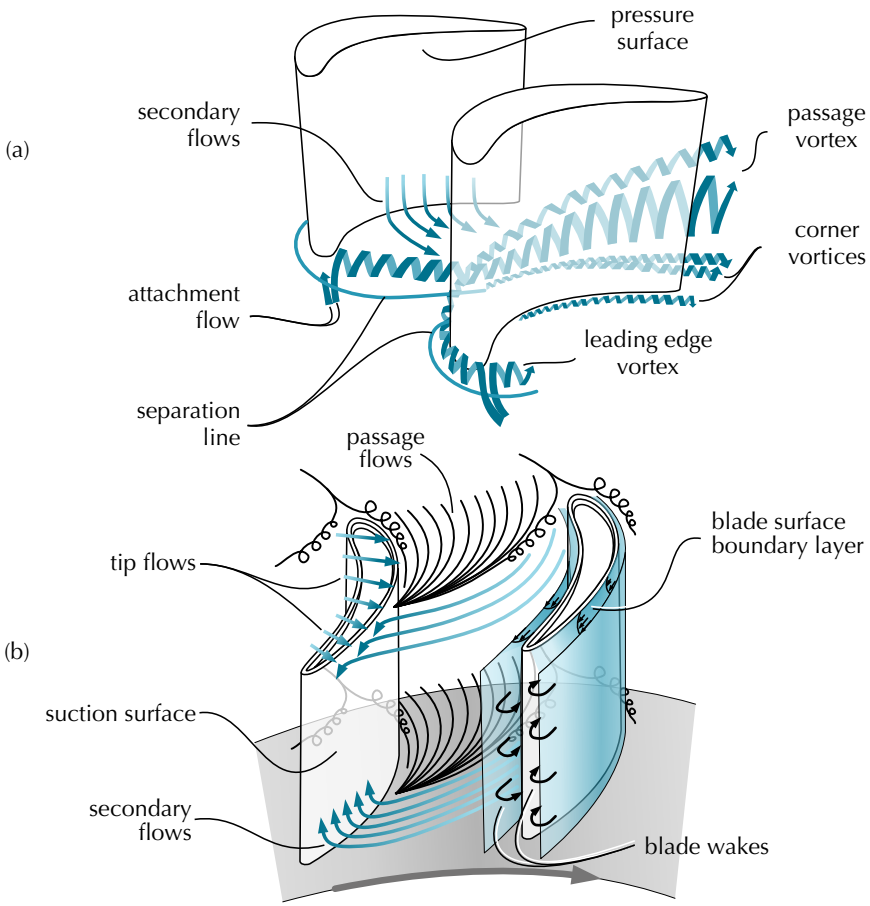

Figure 2.4. Three-dimensional flow field near the tips and roots of a turbine airfoils. (a) Based on Goldstein and Spores (1988) and (b) Based on Gladden et al. (1988).

2.2. Requirement for cooling

The cooling of gas turbine airfoils is not just a recommendation but instead it is a requirement. If this requirement is not met, significant failure of the airfoils can result. An example of such a failure is shown in Figure 2.5 for rotor airfoils near the rotor tip due to tip flows shown in Figure 2.4(b), and at the trailing-edge.

Cooling techniques are grouped into the categories of "external" cooling and "internal" cooling. External cooling utilizes film cooling and transpiration cooling techniques while internal cooling utilizes combinations of convection and impingement techniques. Both internal and external cooling require the injection of coolant into the internal structure of the airfoil. The coolant is then passed through a series of passages and internal structures, employing internal cooling techniques, before being ejected onto the outer surface of the airfoil where cooling is achieved through external cooling techniques. External cooling technologies are affected by the previously discussed characteristics of the mainstream flow surrounding the airfoil and by the coolant stream characteristics before ejection to the outer surface. Internal cooling technologies, however, are considered to be affected by the movement and orientation of the airfoil and the coolant stream characteristics as it moves through internal airfoil

structures. The extent of thermodynamic and fluid dynamic coupling between the internal and external cooling varies depending on individual airfoil designs.



Figure 2.5. Overheated turbine rotors (Rolls Royce, 1996).

The trailing-edge is especially susceptible to overheating due to a design requirement for a thin trailing-edge (as seen in the example profiles of Figure 2.3). This requirement limits the space available for internal cooling techniques. Further, as shown in Figure 2.2, while the thermal loads at the trailing-edges are not as high as other areas, they are also non-zero and cannot just be considered negligible (as evident by Figure 2.5). The cooling of the trailing-edge region around the mid-span (away from root and tip effects), will be considered here on. Some technologies to be discussed may be applicable to other regions but these applications will not be discussed further. The focus of this research work will be on internal cooling of the trailing-edge. A brief overview of external cooling techniques, however, is useful in understanding any possible effects or repercussions to those internal cooling techniques at the trailing-edge.

2.3. External cooling at the trailing-edge

External cooling aims to “minimize” heat transfer from hot exhaust gas streams to the components of a gas turbine airfoil, including airfoil surfaces, shrouds, tips, and hub/casing-side end-walls. This may sound counter intuitive. It needs to be reminded that a larger operating temperature difference between mainstream flow and airfoil enables a higher turbine inlet temperature (TIT), thus increasing the engine efficiency, and a simultaneous lower component temperature which increases the life of the component and prevents failure.

External cooling is implemented to protect the airfoil surface “externally” by creating a gaseous thermal barrier (or a film layer), which is consisted of a coolant stream between the airfoil surface and hot exhaust gases from the combustor. In this way, the heat flux that enters airfoil surfaces from the hot gaseous stream is based on temperature difference between the surface (T_w) and the film layer (T_f), instead of between the surface and the hot gases (T_g). The film layer temperature (T_f) is defined as a mixture of the hot gas (T_g) and the coolant (T_c). These parameters can be used to measure the cooling

effectiveness by way of a "film effectiveness" given by $\eta_{fc} = (T_g - T_f)/(T_g - T_c)$. This performance measure, however, does not consider the coolant consumption required for a given heat transfer and, therefore, do not give a complete indication as to the performance of external cooling in the context of gas turbine engine efficiency where the amount of heat transfer obtained is measured against the amount of coolant required to achieve it. Coolant consumption is separately considered by the blowing ratio (often denoted by either *M* or *G*), which is the coolant-to-mainstream mass flux ratio. Blowing ratios typically vary from 0.5 to 2.0 (Han, 2018).

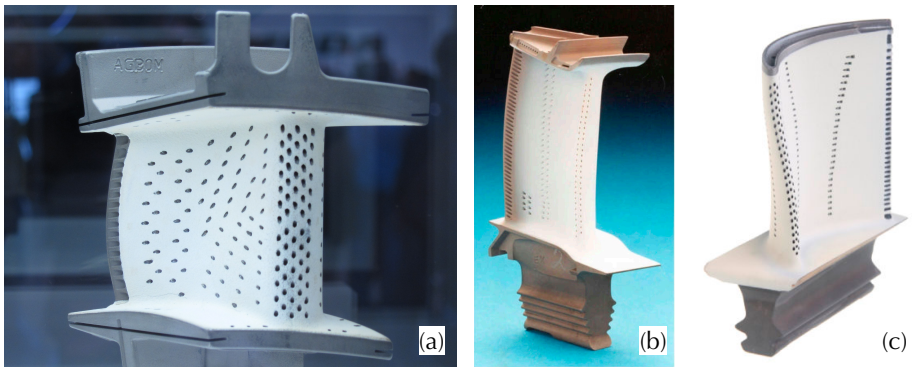

Figure 2.6. Example of turbine airfoils with external cooling schemes. (a) Stator vane showing pressure surface and trailing-edge (Cleynen, 2013), (b) A rotor blade showing leading-edge, trailing-edge, and suction surface (Parsons et al., 2011), and (c) A first stage rotor blade showing leading-edge, trialing-edge and pressure surface (Sulzer, 2019).

This cooling technique is traditionally referred to as film cooling but the term is not used for external cooling of the trailing-edge. Film cooling traditionally ejects the coolant out onto the exterior surface of the airfoil through discrete holes. Example of holes in airfoils are shown in Fig. 2.6. Of note is the limited number of holes near the trailing-edge. One of the major difficulties associated with this flow ejection is that aerodynamic design constraints require a thin trailing-edge for the airfoil. As a result, the thickness of the airfoil structure is not sufficient to allow enough coolant to pass through without large losses. While trailing-edge cooling ejects coolant to form a barrier between airfoil structure and mainstream flow, this is conventionally not done from discrete holes.

The most well-established cooling scheme to cool the trailing-edge requires a portion of the pressure side trailing-edge surface to be removed or cutback, thereby opening a slot through which the coolant stream can pass. This can be seen in Figure 2.6(a, c) and is schematically shown in Figure 2.7(a). In this way, the coolant stream not only acts as an insulating layer on the pressure side of the airfoil, but also as a convective heat sink for the suction side surface. The variation of film effectiveness for trailing-edge cooling is shown in Figure 2.7(b) and has similarities to film cooling from a discrete hole. Horbach *et al.* (2011) noted that, for low blowing ratios ($M = 0.2$), the flow field at the trailing-edge is very similar to that of a backward facing step flow, with the pressure side surface flow attaching

to the internal surface of the suction side of the airfoil, resulting in a sudden increase in heat transfer. As the blowing ratio is increased to a value similar to that in operating gas turbines (i.e. $M > 0.5$), this effect diminishes. Further, as the coolant is ejected from the trailing-edge at a very low streamwise inclination, almost tangential to trailing-edge surfaces, the coolant stream is expected to be less likely to separate from the surface. A separation (as occurs at $x/H_t \approx 4$) is seen as a notable decrease in film effectiveness for $M = 0.2$ in Figure 2.7(b). For all blowing ratios investigated, the film effectiveness monotonically decreases with increasing distance from ejection point.

A drawback of the cutback is the reduction in structural rigidity. To counteract this, land extensions and/or pin-fins are implemented (Figure 2.7(a)). In turn, these structures, have some effect on the external trailing-edge cooling performance. This appears to be largely based on the blockage of the ejection slot. The greater the blockage, the lower the mass flux through the trailing-edge and the lower the film effectiveness (η_{fc}) as per Figure 2.7(b) (Horbach et al., 2011). In this way, the external trailing-edge cooling of a turbine airfoil has a strong dependence on the internal cooling technologies.

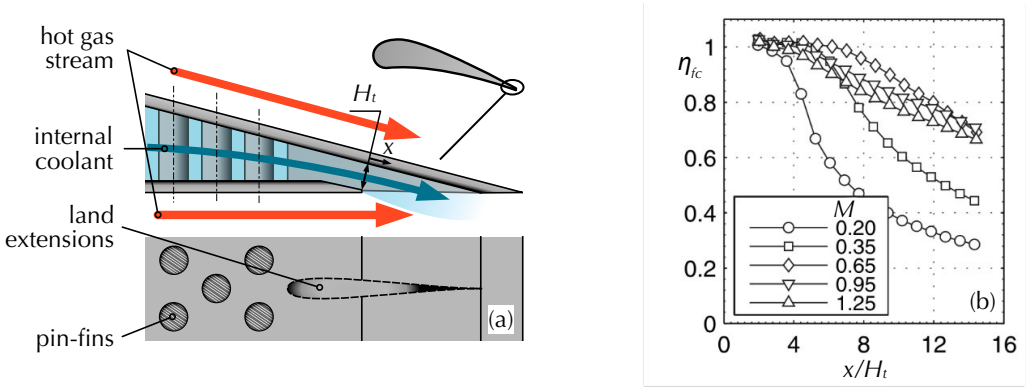

Figure 2.7. Trailing-edge cooling averaged in spanwise direction: (a) Schematic of trailing-edge cutback and (b) Variation of film effectiveness with blowing ratio M (Horbach et al., 2011).

2.4. Internal cooling at the trailing-edge

2.4.1. Background

The coolant enters the airfoils from the root and/or tip of the airfoil depending on the turbine stage and airfoil type. Rotors have coolant injection from the root due to the disconnect between the airfoil tip and outer casing of the turbine to account for rotation. The coolant then passes through the internal structure before being ejected, possibly as part of an external cooling scheme. There is little consensus on the appropriate Reynolds number range that is applicable for internal cooling for the trailing-edge. A lower end range that is commonly identified is $Re_{Dh} > 10{,}000$ (Han, 2013, 2018; Han et al., 2012; Han & Wright, 2006; Moon & Lau, 2003; Wright & Han, 2013). But, studies have considered lower values. It is generally accepted, however, that such flows are turbulent in nature.

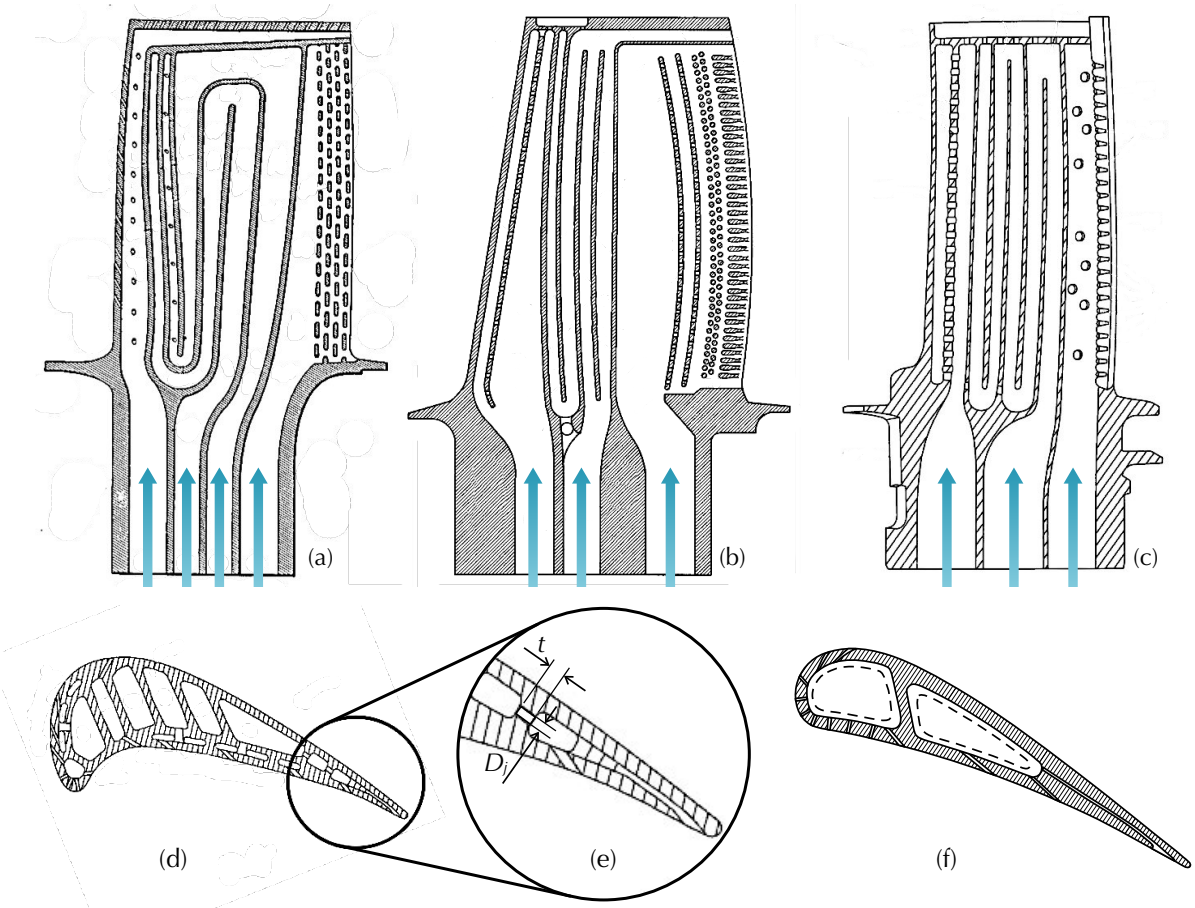

Figure 2.8. Examples of internal structure layouts of turbine airfoils for internal cooling purposes: (a) Vertical cross section from US patent 4,753,575, (b) Vertical cross section from European patent 1,420,142B1, (c) Vertical cross section from US patent 7,377,746, (d) Profile cross section from European patent 1,420,142B1, (e) Annotated close up of trailing edge from European patent 1,420,142B1, and (f) Profile cross section from Stage 1 vane of E^3 engine (Halila et al., 1982).

The internal cooling of turbine airfoils is predominantly governed by forms of convection cooling. Due to the temperature difference between the airfoil structure and coolant, heat is transferred from airfoil structure to coolant, thus cooling the airfoil. Most external cooling schemes share similar properties such as layout and geometries. Internal cooling schemes, on the other hand, can vary considerably between different designs. Typical internal geometries are shown in Figure 2.8, illustrating possible variations. It can be seen, in Figure 2.8, that the coolant stream is not simply passed through the internal structure from root to tip or out the trailing-edge. Instead, serpentine type paths, perforations in the structure and obstacles are introduced to further enhance the cooling performance or direct the coolant stream to areas that require more cooling. Near the trailing-edge a converging section may be expected, as the profile tends towards a “sharp” trailing-edge of the airfoil. Cross-section schematics vary between representing the internal channel at the trailing-edge as converging (as shown in Figure 2.8(d)) and with a constant height (as shown in Figure 2.8(f)). The majority of studies on trailing-edge

cooling technologies, as will be discussed below tends to implement a channel with constant height, isolating the effects of convergence as may be possible in certain airfoil designs.

Internal cooling of turbine airfoil trailing-edges is considered especially difficult. This is due to the compromise between the aerodynamic design constraints that require a thin trailing-edge for the airfoil and the increase in available space to allow enough coolant to pass through without large losses. Three approaches to trailing edge cooling will be considered here as:

(1) A conventional pin-fin array is shown in Figure 2.9(b) where short aspect ratio cylinders are exposed to a uniform-like flow field.

(2) Perforated blockages are shown in Figure 2.9(c) where perforations are made in the turbine blade internal structures (or "blockages") through which the coolant stream is forced to pass through.

(3) A combination of these two schemes is given in Figure 2.9(d).

These schemes will be discussed further below.

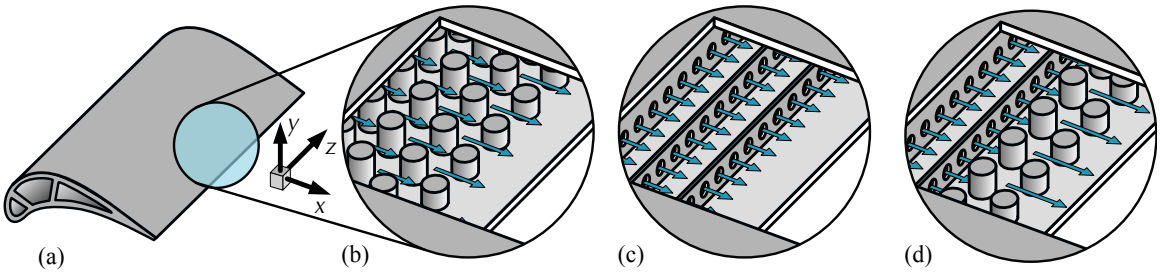

Figure 2.9. Schematic of internal cooling schemes used in the trailing edge of a turbine airfoil: (a) Gas turbine airfoil design, (b) A scheme employing a pin-fin array subjected uniform-like coolant stream, (c) A scheme employing perforated blockages plates, and (d) A combination of schemes into a blockage pin-fin configuration.

For the sake of consistency and clarity the terminology to be adopted for this research is shown in Figure 2.10. The origin of the axis in the vertical (*x*-*y*) plane will be placed against the lower end-wall. In the horizontal (*x*-*z*) plane the axis will be placed at the centre of the tunnel with the positive z-axis being towards the left side wall (relative to the oncoming flow direction). The origin of the axis along the x-axis may vary as necessary and will be clarified for each case. Directions (such as upstream, downstream, inner and outer) will be used for relative referencing of particular surfaces. Notably, an *inner* surface will be a surface facing towards the centre of the channel while an *outer* surface will be one facing towards the channel sidewalls. An *upstream* surface will be one facing in the negative *x* direction while a *downstream* surface will be one facing towards the positive *x* direction. The *x*-direction will also be referred to as the *streamwise* direction and the *z*-direction will be referred to as the *spanwise* direction. The terminology for the blockage pin-fin configuration will adopt those for the respective structures of the perforated blockage and pin-fins.

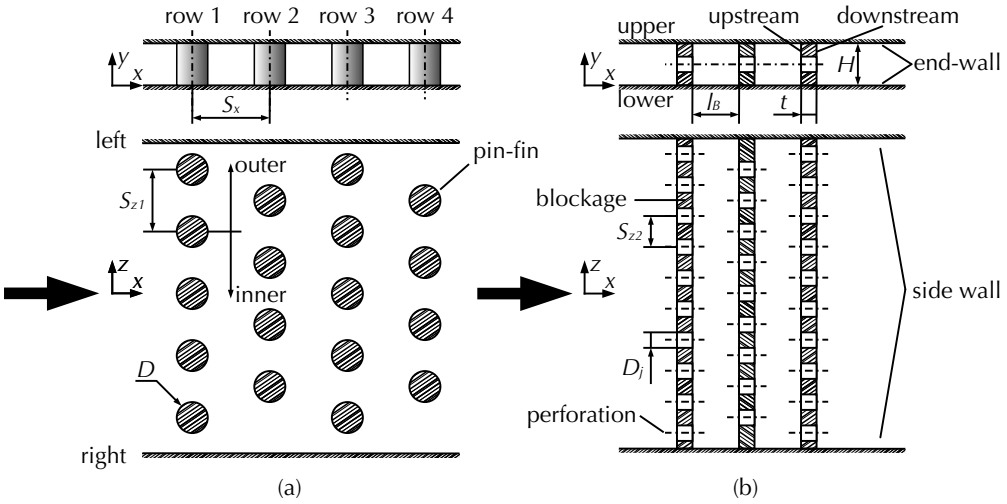

Figure 2.10. Trailing-edge cooling scheme terminology. (a) For a pin-fin array, and (b) For a perforated blockage configuration.

In comparison with external cooling technologies, which aim to "minimize" heat transfer from hot exhaust gases to airfoil surfaces, internal cooling technologies are required to "maximize" heat transfer between the inner airfoil surfaces and the coolant stream. The effectiveness by which an internal cooling scheme keeps the airfoils cool is most frequently measured by its thermal performance, defined as:

$$\eta_{TP} = \frac{\overline{\overline{Nu_{test}}}/Nu_o}{(f_{test}/f_o)^{1/3}} \tag{1}$$

The thermal performance provides a measure of the heat transfer per unit pumping power of a given cooling scheme in comparison to that of a smooth empty channel. A higher heat transfer allows for higher combustion temperatures and, therefore, higher engine efficiencies. Conversely, a higher pumping power is analogous to a requirement for more coolant to be bled from the compressor and thus lower engine efficiencies. A thermal performance below unity ($\eta_{TP} < 1$) indicates that for a given pumping power, the heat transfer from the cooling scheme is less than that of an empty smooth channel (without any internal structures or modifications). Alternatively, in seeking a target heat transfer a thermal performance less than unity implies that an empty channel requires less pumping power.

A limitation of this performance measure is that it does not directly consider the coolant consumption (or flow rate) which could be argued as being more applicable for gas turbine cooling. The pressure drop does not directly correlate to the coolant consumption. Regardless, thermal performance (η_{TP}) has been frequently used in previous literature to characterize various internal cooling techniques for turbine airfoils (Han, 2013; Han & Wright, 2006; Lawson et al., 2011; Moon & Lau, 2003; Shin & Kwak, 2008; Wright et al., 2004). Its use in this work thus allows for comparisons to those prior studies.

2.4.2. Pin-fin cooling at the trailing-edge

The most widely adopted scheme for trailing-edge cooling is the pin-fin array. This is due to the superior thermal performance being as high as $\eta_{TP} \approx 3.5$ (Lawson et al., 2011; Lyall et al., 2011). The increase in thermal performance is due to two primary factors. Firstly, the pin-fins increase the surface area on which the coolant stream acts. Secondly, the boundary layer separates from the end-walls ahead of each pin-fin due to an adverse pressure gradient. As a result, horseshoe vortex-type secondary flows (or simply called "horseshoe vortices") are formed around each pin-fin (Baker, 1979).

(a) Flow topology around pin-fins subjected to a uniform-like flow field

The expected horseshoe vortex flow topology and corresponding heat transfer distribution in the plane of symmetry are schematically illustrated in Figure 2.11. The schematics are combined from three separate studies (Baker, 1979, 1980; Praisner & Smith, 2006) and are representative of a laminar horseshoe vortex system. Such a system is characterized by a series of primary vortices (V) and smaller secondary vortices (V'). Primary vortices rotate in a clockwise direction, for mainstream flows from left to right. The secondary vortices rotate in the opposite direction. These vortices form in pairs to preserve the stream-line topology. The minimum number of vortices that can form is two (i.e., a single pair). A single vortex pair (V_1 and V_0') reported by Visbal (1991) was observed at $Re_D = 500$. As the Reynolds number increases ($Re_D \approx 1500$), two vortex pairs form followed by the formation of an additional pair (three vortex pairs) at $Re_D \approx 2500$. The existence of more than 3 vortex pairs is unlikely due to the limited space between the point of boundary layer separation and the pin-fin leading-edge.

The presence of the primary and secondary vortices results in a series of separation (S_n) and attachment (A_n) points to form on the end-wall. The most upstream separation point occurs where the boundary layer separates from the end-wall. The separation point, S_1, forms beneath the primary vortex, V_1. In this way a separation line S_n can then be used to indicate the position of V_n based on end-wall flow measurements (Baker, 1991). The vortices are convected downstream around the pin-fin by the mainstream. This downstream path travelled by the vortices mimics the shape of a "horseshoe" and hence the name given to the flow structures. As the vortices are convected downstream, so then are the attachment and separation points; forming stream-lines as shown in Figure 2.11.

The vortices cause a large level of flow entrainment, of the mainstream, near the end-wall. The convection of the vortices downstream prevents the entrained flow becoming trapped and consequently there is an increase in heat transfer along the end-wall compared to a setup without the pin-fin present. The local peaks in the heat transfer distribution correlate to the attachment points (A) where there will be the highest level of fresh flow at the end-wall. Conversely there will be a minimum heat transfer coefficient where the boundary layer flow separates from the end-wall, at S as shown by Schekman and Kim (2017). At where the vortex (V_0'), termed the "corner vortex", forms, there exists very low levels of flow entrainment. This results in a sharp decrease in the end-wall heat transfer in this region (Praisner & Smith, 2006).

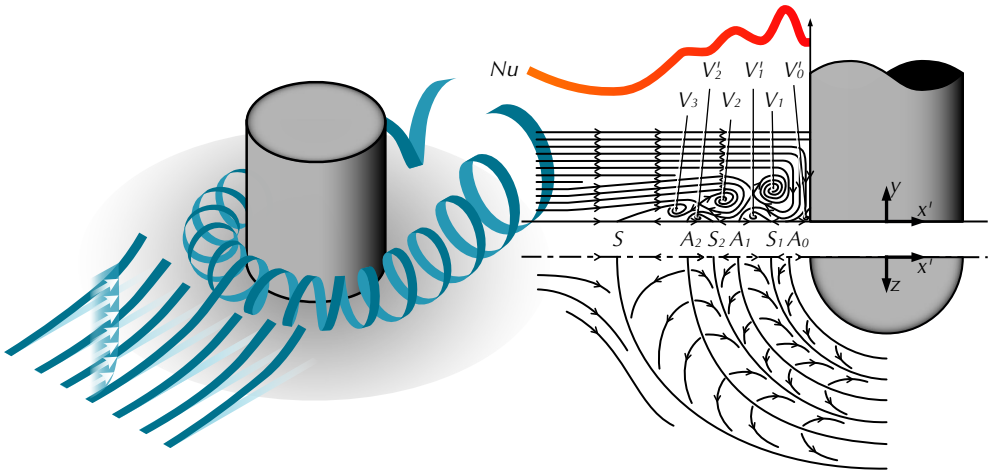

Figure 2.11. Flow topology of a laminar horseshoe vortex system around a circular short aspect ratio pin-fin (not drawn to scale, certain features are exaggerated for illustrative purposes).

The topology and kinematics discussed so far refer to stable horseshoe vortices whereby the vortices do not move or oscillate. Once the Reynolds number increases above a certain value, typically $Re_D \approx 5000$, the vortices begin to oscillate (Baker, 1979). A splitting and shedding of the vortices downstream of the pin-fin is also reported to occur during these oscillations. There are conflicting reasons given for why the vortices begin to oscillate. It is most likely, however, that the unsteady process is produced by a natural instability of the horseshoe vortex system and not by Karman-vortex shedding in the wake of the pin-fin (Agui & Andreopoulos, 1992; Baker, 1979; Fu & Rockwell, 2005; Thomas, 1987).

Higher Reynolds numbers of the approaching flow result in the approaching boundary layer becoming turbulent ($Re_D > 4000$ (Sahin et al., 2008)). When the horseshoe vortex system becomes turbulent, the flow structure becomes irregular. Time-averaged flow visualization on the plane of symmetry has been stated to either indicate no vorticity occurring (Eckerle & Awad, 1991) or form only a single vortex pair. Praisner and Smith (2006) visualized two vortex pairs with a time-averaged measurement. Baker (1980) only observed the separation lines S and S_1 (in Figure 2.11(b)) on the end-wall surface for the turbulent horseshoe vortex system. The absence of the separation line S_2, which is necessary for a 3-vortex pair system, was understood to indicate that only a two-vortex pair system was present. Praisner and Smith (2006) also performed instantaneous measurements of the streamlines in the plane of symmetry. Only the primary vortex, V_1 and secondary vortex, V_1' were identified. Additional vortices, V_2 and V_3, are possibly present as well at certain points in time. No satisfactory explanation is given as to the reason why the vortex system suddenly shifts to having only two-vortex pairs. It is then possible, and more likely, that three-vortex pairs still exist but vortices V_2 and V_3 become more time dependent; being absorbed into one another, ejected and dissipating in the flow regime. These behaviours of vortices are observable even in the laminar regime at high Reynolds numbers, typically just before the flow becomes turbulent (Praisner & Smith, 2006; Sahin et al., 2008; Simpson, 2001).

The vortices V_2 and V_3 are then present in a turbulent horseshoe vortex system but not all at a given instant in time - multiple instantaneous flow visualizations being required to ascertain their positions. As it is already a very weak vortex, V_3 would then likely disappear when taking time-averaged measurements, explaining its complete absence in previous publications.

With a turbulent horseshoe vortex system, the irregular movement and existence of the vortices, results in the local minima and maxima (seen in Figure 2.11) merging. Instead the end-wall heat transfer appears to monotonically decrease from the pin-fin surface (Baker, 1980; Praisner & Smith, 2006).

While the upstream flow pattern for a horseshoe vortex system is well-documented, the downstream flow pattern is scarcely investigated. The main effects of horseshoe vortices, namely an increase in drag and shear stresses on the end-wall around the pin-fin, are largely dependent on the upstream flow around it. The oscillation of the vortices is also due to the upstream flow rather than instabilities in the pin-fin wake. An example of the flow field at y/D = 0.05 (immediately above the end-wall) for Re_D = 6150 is shown in Figure 2.12. At this Reynolds number, the approaching boundary layer was turbulent (Sahin et al., 2008). The predominant feature of the downstream flow field is the vortex denoted as V_D. The horseshoe vortices that form upstream of the pin-fin move downstream and become entrained in the vortex V_D. This stimulates circulatory motion in the pin-fin wake resulting in the formation of two distinct flow regions, wake region I and II (as labelled in Figure 2.12). Wake region I is subjected to a limited amount of fluid being entrained from the mainstream, resulting in a decreased heat transfer. Wake region II receives a larger amount of fluid entrainment due to V_D and subsequently a higher local heat transfer is present.

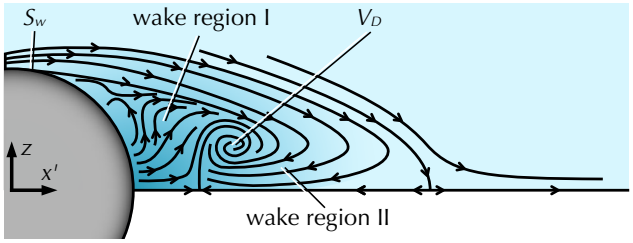

Figure 2.12. Near end-wall streamline patterns in pin-fin near wakes at y/H = 0.05, based on Laser-Doppler Velocimetry by Sahin et al. (2008) at Re_D = 6,150.

In the presence of neighbouring pin-fins, the overall structure of a horseshoe vortex system for a single pin-fin (shown in Figure 2.11 and Figure 2.12) remains largely unaltered. An example of the resulting end-wall flow topology is shown in Figure 2.13 compiled from prior studies such as Chyu et al., 1998; Goldstein and Chen, 1998; Kan et al., 2014; Metzger and Haley, 1982. Considering typical spacings employed in studies using pin-fin arrays ($S_{z1} \approx 2.5$) the horseshoe vortex streamlines from neighbouring pin-fins do not present end-wall flows with opposing or intersecting vectors – instead being somewhat conformal. It is possible to then, if necessary, extrapolate the flow patterns about a single pin-fin in an array to any other. This also applies to the heat transfer - in a given row of pin-fins,

the end-wall heat transfer contours at each pin-fin is, likewise, seen to be similar (Lawson et al., 2011; Otto et al., 2021; Park et al., 2016).

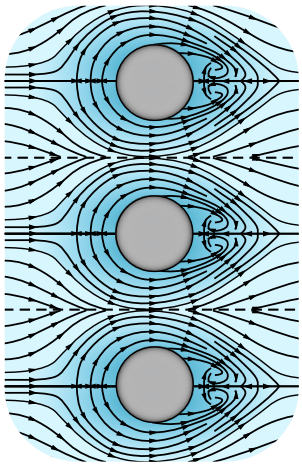

Figure 2.13. Schematic illustrating interaction between end-wall surface horseshoe vortex flows for multiple pin-fins exposed to a uniform flow field.

(b) Factors affecting the thermal performance of a pin-fin array

The thermal performance of a pin-fin cooling scheme needs to consider both heat transfer occurring at end-walls and on the pin-fin surface. The former is due to the presence of secondary flows at the base of the pin-fins and the latter from the coolant stream flowing over and around the conductive pin-fin surfaces. The overall heat transfer, including contributions from end-wall and pin-fin surfaces, are dependent upon the aspect ratio of pin-fins (H/D), the relative spacing of pin-fins in stream-wise direction (S_x/D) and spanwise direction (S_z/D), the pin-fin shape, and the Reynolds number of flows through the trailing-edge.

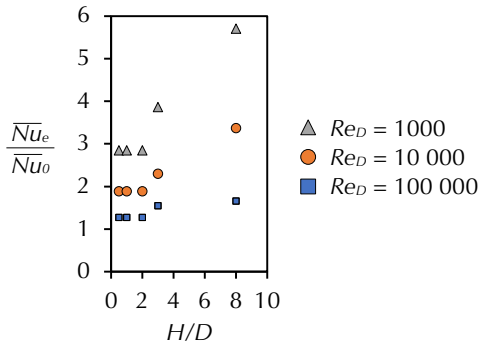

Figure 2.14. Variation of end-wall heat transfer around pin-fins with increasing pin-fin aspect ratio (H/D) reproduced from (Brigham & VanFossen, 1984).

The pin-fins at the trailing-edge of a turbine blade are commonly noted as having an aspect ratio of $0.5 \leq H/D \leq 4.0$ (Han et al., 2012; Lyall, 2006). However, the exact reference source of this range is

unknown. Considering its continued use, it is understood to hold some weight and despite the original source being unknown, it will be taken as correct. The effect of aspect ratio on heat transfer in the trailing-edge is presented in Figure 2.14. In summary, for an aspect ratio of $0.5 \leq H/D \leq 2.0$, the aspect ratio does not affect the heat transfer contribution but for $H/D > 2$, there is a larger heat transfer from the pin-fin array. This is due to the secondary flows at the base of the pin-fins decreasing the overall heat transfer - the secondary flows at the end-walls extend to a height of approximately $y/D = 0.1$ up the surface of the pin-fins (Baker, 1979) independent of the pin-fin height. The surface area of the pin-fin over which the mainstream coolant stream acts is then reduced – a portion of the surface area being taken up by the secondary flows. Increasing the pin-fin height for a given diameter (increasing the aspect ratio) would increase the relative portion over which the mainstream flow acts such that the heat transfer is enhanced.

The heat transfer from the surface of the pin-fins contributes more to the overall heat transfer compared to the end-wall surfaces. The specific difference in contribution, however, varies across literature. Chyu et al. (1999) measured that the pin-fins contribute approximately 10% more to the overall heat transfer (considering the end-wall and pin-fin surfaces). Goldstein & Chen (1998) measured that the heat transfer on the surface of the pin-fins was 20% higher than the end-wall surface over a range of Reynolds numbers from $4000 < Re_D < 20000$. Lawson et al. (2011) measured the heat transfer on the surface of the pin-fins was 35-40% for a Reynolds number (Re_D) above 20,000 which correlates against the estimated value of 35% by VanFossen (1982). At lower Reynolds numbers of ~5000, however, the pin-fin surface heat transfer was 63% higher (Lawson et al., 2011). Lyall et al. (2011) considered only a single row of pin-fins and measured a pin-fin heat transfer that was 156% higher than the end-wall surface at $Re_D = 5000$. There is no clear correlation between prior studies that explain the differences in pin-fin and end-wall heat transfer. This is compounded by the differences across the studies. Such differences including pin-fin spacing in the streamwise or spanwise direction, number of pin-fin rows, and pin-fin aspect ratios. It may be due to how the relative contribution to the overall heat transfer is calculated or how much of the end-wall surface is considered in its heat transfer contribution. In general, it is agreed that heat transfer at the pin-fin surface contributes more to overall heat transfer than secondary flows at the end-walls. This does, however, highlight that comparisons between various studies should be undertaken carefully.

The range of pin-fins spacings (referenced against the pin-fin diameter as S_x/D and S_{z1}/D as per Figure 2.10*)* that may be expected in practice are not as conveniently reported, but studies have been conducted for the range of $1.25 \leq S_{x/z1}/D \leq 4.0$ (Chyu et al., 1998; Goldstein & Chen, 1998; Lawson et al., 2011; Lyall, 2006; Lyall et al., 2011; Metzger et al., 1984) with the most common values averaging at 2.5. In general, smaller values of both stream-wise and span-wise spacings lead to enhanced heat transfer, although there is a greater dependence on stream-wise spacing (S_x). The pressure drop across the pin-fin array, in contrast, has a greater dependence on span-wise spacing (S_{z1}) due to flow blockage that occurs for low values of span-wise spacing. Despite the increase in pressure drop, a higher thermal

performance, measured by Lawson *et al.* (2011), occurred for the smaller stream-wise and span-wise spacing, as shown in Figure 2.15(a).

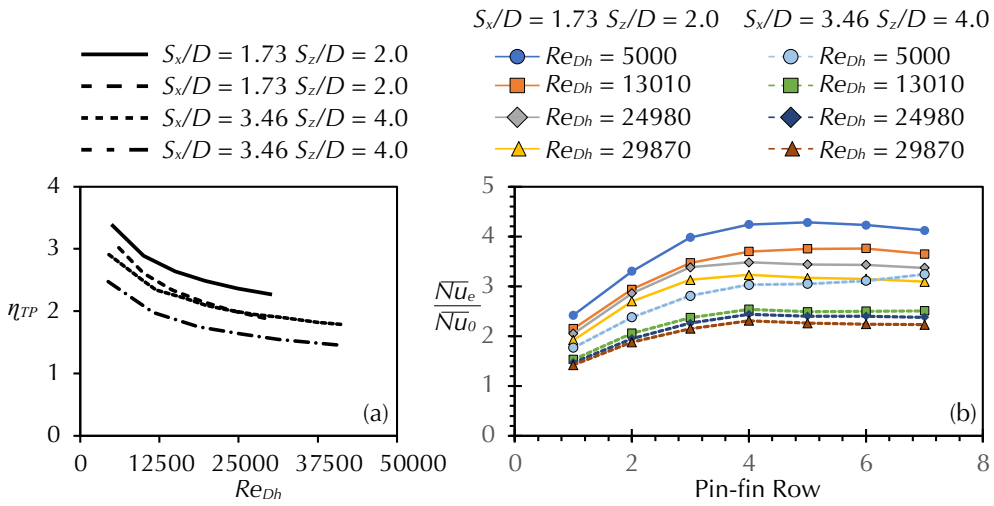

Figure 2.15. Cooling performance of pin-fin array with various spacings, reproduced from Lawson et al. (2011). (a) Thermal performance variation with Reynolds number and (b) End-wall heat transfer variation along length of pin-fin array.

A notable trend along the streamwise length of the array is that the local end-wall heat transfer increases with subsequent rows of pin-fins as shown in Figure 2.15(b) and other prior studies (Chyu et al., 1999; Goldstein & Chen, 1998; Lawson et al., 2011). An extension of this is that for a given flow rate and array spacings (S_x and S_z), there is a certain number of rows of pin-fins for which the heat transfer rate ($\dot{Q}$) will be maximized. This minimum number of rows increases for higher Reynolds numbers. Goldstein and Chen (1998) showed that to achieve a heat transfer rate that was 50% of the maximum, at a Reynolds number of Re_D = 18,000 would require more than 18 rows of pin-fins. A heat transfer rate that was 30% of the maximum would require more than 9 rows of pin-fins.

The heat transfer is affected by the spacings in both the streamwise (S_x) and spanwise (S_{z1}) directions although to differing degrees as per Lawson et al. (2011) and Chyu (1990). A larger streamwise spacing (S_x) will increase the heat transfer of downstream pin-fins due to the wake from upstream pin-fin rows being weaker before interacting with a successive pin-fin row – the wake flow weakening the end-wall heat transfer around the pin-fin (Chyu, 1990). By extension of this, it should be clear that the use of a staggered pin-fin array (Figure 2.16(a)) is superior over an inline array (Figure 2.16(b)). staggered array allows for a larger stream-wise spacing between inline pin-fins, by featuring a row of staggered pin-fins between each inline row. The inline array does result in a lower pressure drop, but the decrease in heat transfer is more significant.

The larger streamwise distance then results in the pin-fin rows downstream having a higher heat transfer. A larger spanwise (S_{z1}) spacing results in a lower heat transfer overall as there is less flow

acceleration between the pin-fins. The larger spanwise spacing does, however, result in lower pressure drop but in comparison to the heat transfer decrease, the thermal performance is lower as per Figure 2.15(a). A smaller spanwise spacing can increase the heat transfer around the first few pin-fin rows (from the second onward) due to the flow acceleration. Overall, there are then two design considerations that should be observed for the spacings in pin-fin array as concluded by Lawson et al. (2011) and observed in Figure 2.15(a). Firstly, the streamwise spacing should be larger than the spanwise spacing. Secondly, smaller spacings result in overall higher thermal performance.

These performance values are reported for circular, non-inclined pin-fins (Figure 2.16 (c, g)). Changes to the pin-fin profile results in this performance being altered. Possible pin-fin profile shapes are shown in Figure 2.16 (c-f). The most common pin-fin shape is perhaps the circular pin-fin (18 (c)), although oblong (Figure 2.16(d)), elliptical (Figure 2.16(e)), cubic (Figure 2.16(f)) shapes have also been investigated. The pin-fin shape not only affects the amount of flow separation that is induced but also generates turbulence in the surrounding flow, which in turn affects the amount of heat transfer that occurs. Less aerodynamic pin-fins, such as those having span-wise oblong (Figure 2.16(d)) or cubic (Figure 2.16(f)) shapes, cause more flow separation and generate more turbulence, thus increasing the heat transfer. The flow separation, however, also leads to increase in pressure drop across the pin-fin array. Cubic shapes appear to cause the highest increase in heat transfer, 30% to 80% more than that of a circular pin-fin, with a similar increase in pressure drop (Chyu et al., 1998). Conversely, a more aerodynamic shape, such as stream-wise oblong and elliptical pin-fins, leads to a decrease in both heat transfer and pressure drop.

Modifications to pin-fins are not just restricted to the profile shape. Modifications along their height (in the *x*-*y* plane) have also been considered. This includes partial length pin-fins (Figure 2.16(h)), stepped or varying cross section pin-fins (Figure 2.16(i)), end-wall fillets (Figure 2.16 (j)) and inclined pin-fins (Figure 2.16(k)). For partial pin-fins decreasing in height from the full channel height to half the channel height, the heat transfer could be interpolated between that of a full height pin-fin (Figure 2.16(g)) and a smooth channel (Arora, 1990). As the gap between the two-partial pin-fins increased then both the heat transfer and friction factor decreased linearly. Stepped pin-fins (Figure 2.16(i) can result a superior thermal performance and additionally allow for a smaller pin-fin array (in terms of the number of pin-fin rows) compared to constant diameter pin-fins (Figure 2.16(g)) (Goldstein & Chen, 1998). A large contributor to the increase in heat transfer was contribution by additional secondary flows arising from step in the cross section. These additional flows also served to reduce some turbulence intensity in the wake of the pin-fins. End-wall fillets (Figure 2.16 (j)) and inclined pin-fins (Figure 2.16(k)) reduce the adverse pressure gradient that end-wall flow experiences when interacting with the pin-fins, which in turn weakens secondary flow structures at the end-walls, thus decreasing the end-wall heat transfer. A sufficiently large fillet radius can decrease the overall heat transfer by 8% to 25%, depending on the Reynolds number, as a lower Reynolds number would lead to larger heat transfer decrease (Chyu et al., 1999). The fillets also increase pressure drop across the pin-

fins if $Re_D < 1.6 \times 10^4$ (Chyu et al., 1999). Although the effect on thermal performance is negative, limitations in the manufacturing of pin-fins within a turbine airfoil may produce fillets and the effect thereof cannot be ignored. The inclination of pin-fins (Figure 2.16(k)) causes different flow conditions at either end-wall of a pin-fin. At the leading end-wall (bottom end in Figure 2.16(k)) the inclination decreases the adverse pressure gradient in a similar manner to end-wall fillets, causing a decrease in local heat transfer. The inclination nonetheless forces the horseshoe vortices to merge, downstream of the pin-fin, more quickly, leading to a unique end-wall flow pattern that is responsible for increased average heat transfer (Choi et al., 2007).

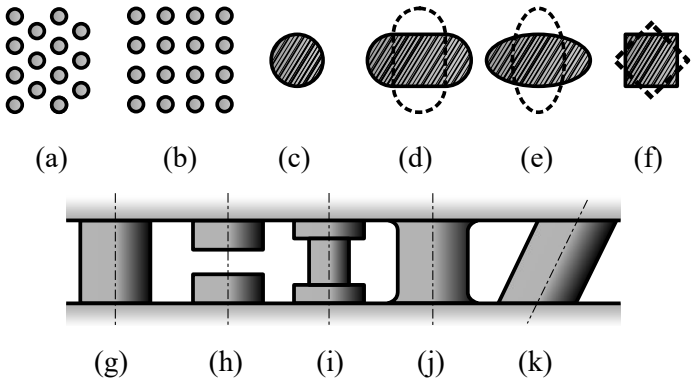

Figure 2.16. Sample of pin-fin profiles, configurations and orientations in the *x*-*z* and *x*-*y* planes where the flow direction is from left to right. (a) Circular profile, (b) Oblong profile, (c) Elliptical profile, (d) Cubic or diamond profile, (e) Staggered layout, (f) Inline layout, (g) Vertical straight, (i) vertical with stepped cross section, (j) Vertical with end fillets, and (k) Inclined.

2.4.3. Perforated blockages at the trailing-edge

An alternative to using a pin-fin array for cooling is the use of perforated blockage plates in the trailing-edge (Figure 2.9(c)). A series of perforated blockages are implemented in a confined channel and the coolant is forced to flow through the perforations as jet flows. With this scheme, the end-wall heat transfer is increased by 5.0 to 8.0 times, compared to that of an empty trailing-edge channel (Moon & Lau, 2003). The increase is attributed to circulation of the coolant in the confined region between sequential blockages.

(a) Flow topology between sequential perforated blockages

The coolant flow through such a scheme generates a set of jets impinging on a flat non-perforated target surface. The schematic in Figure 2.17(a) is based on prior studies (Gauntner et al., 1970; Geers, 2004; Geers et al., 2004; Jambunathan et al., 1992; Kumar & Prasad, 2008; Yeranee et al., 2020). Coolant interacts with the perforated blockage and is forced to flow through the perforations. The flow exits as a constrained jet flow and impinges on the target, stagnating. From stagnation, the flow is forced to flow outwards as a wall-jet along the target surface. In the presence of neighboring jet flows, wall-

jets will intersect and be forced upwards and away from the target surface, forming a "fountain-jet" flow. The counteracting flow from the fountain jet and core jet flow incites a vortical flow to form.

For a perforated blockage configuration in the trailing-edge there are distinct physical differences to consider in comparison to the case in Figure 2.17(a)). Firstly, the target plate will be a second perforated blockage. The perforations in the second blockage are conventionally staggered such that jet flows from one perforated blockage do not just flow directly through the perforation of the following blockage. In the perpendicular (*x*-*y*) plane, the flows are also constrained in the *y*-axis by the end-walls (being the suction and pressure surfaces of the airfoil). As a result, there exist different flow fields depending on whether the *x*-*y* plane (Figure 2.17(b)) or *x*-*z* plane (Figure 2.17(c)) are being considered.

In the *x*-*y* plane (Figure 2.17(b)) the flow field is of a single jet in Figure 2.17(a). Due to the staggered perforations of the second perforated blockage the jet will impinge on the downstream blockage and be directed towards the end-walls as wall-jets. As an equivalent to the intersection of wall-jets in Figure 2.17(a), the wall-jets in Figure 2.17(b) will intersect with the end-walls and be directed away from the second perforated blockage. This "back flow" is equivalent to the fountain jet flow in Figure 2.17(a) and gives rise to the circulating region that is attributed to the large increase in heat transfer. A further consequence of the circulating region is the restriction of the jet diffusion. Provided there exists a backflow the jet will never contact the end-wall upstream of the second perforation. A backflow may be prevented if the perforation is placed at the end-wall such that the jet flow is immediately contacting the end-wall at exit. Although in this latter case, the end-wall flow undergoes a separation near the second perforated blockage and vortical flows will form, like those for horseshoe vortices in Figure 2.11(b) (Chung et al., 2014)

Click or tap here to enter text.Prior studies focus the flow visualization on the flow in the *x*-*y* plane (Figure 2.17(b)) and so the flow patterns in the *x*-*z* plane (Figure 2.17(c)) should be seen as merely hypothetical. A key difference, due to the target surface being perforated, is that the intersection of wall jets does not require their redirection upstream away from the blockage surface and instead the flow is redirected through the second blockage. There is thus no fountain jet flow and no mechanism for the formation of the circulating regions. If the perforations are staggered not only in the z-axis (as represented in Figure 2.17(b,c)) but also in the *y*-axis then fountain jets may then exist. Their presence may be detected in the end-wall heat transfer contours by Chung et al. (2014) when this stagger pattern is employed.

(b) Correlation between flow patterns and end-wall heat transfer

Unlike those flows for pin-fins arrays, there are notably very few measurements or observations of the flow in the *x*-*z* plane for a perforated blockage configuration in the trailing-edge. The flow behaviour shown in Figure 2.17(c) is often assumed with no direct measurements referenced to corroborate these (Ahn et al., 2007; Lau et al., 2003, 2008; Moon & Lau, 2003; Park et al., 2016; Shin & Kwak, 2008). Heat transfer measurements are used to interpret the flow field, but these are limited

to the flows at the end-wall and extrapolations towards flows away from the end-wall should be viewed cautiously.

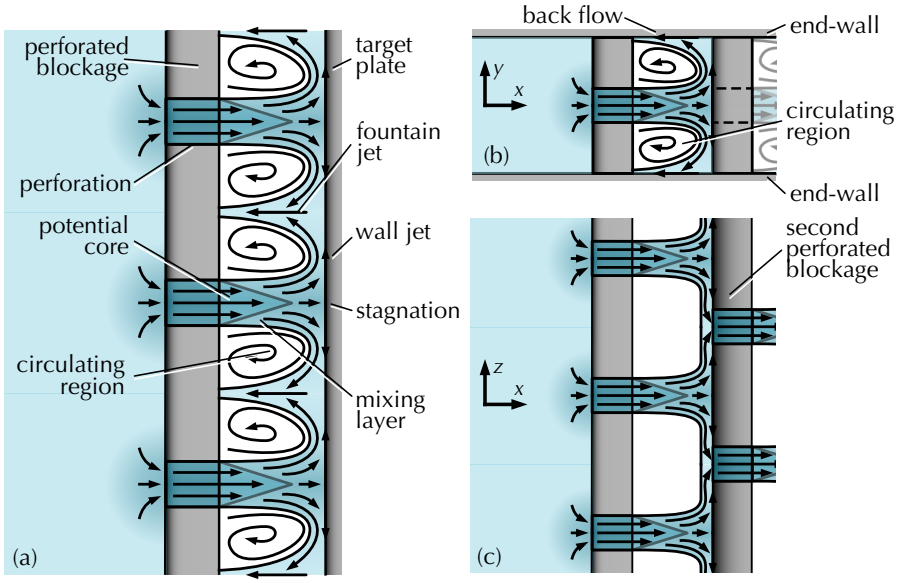

Figure 2.17. Flow patterns considering perforated blockages based on prior publications. (a) For jet impingement on a flat solid surface, (b) For jet impingement on a second perforated surface in the *x*-*y* plane, and (c) For jet impingement on a second perforated surface in the *x*-*z* plane.

The flow patterns shown in Figure 2.17 do not, however, completely explain the differences in end-wall heat transfer shown in Figure 2.18 from Moon and Lau (2003). With perforations positioned at the mid-height of the channel (Figure 2.18(a)), there is an almost uniform heat transfer distribution at the end-wall, away from the sidewalls. It implies the end-wall back flows from each of the mid-height plane jets have sufficiently merged or diffused such that their individual profiles or effects on the end-wall become indistinguishable. With the exit perforations (at the second blockage) staggered in the *y*-axis (Figure 2.18(a)) there are then no inline or co-planar perforations for which the jets can pass directly through. The jets are forced to stagnate in their entirety on the blockage surface and be redirected. This is apparently sufficient to result in the individual jet flows to become distinguishable in the end-wall heat transfer. It is possible that fountain jet like upstream flows, away from the end-wall may also exist although there are no measurements to confirm this. There are distinct bands of higher heat transfer in Figure 2.18(b) that correlate with the location of the jet centerlines as indicated. This is more evident for the end-wall closest to the first staggered perforation. At the opposite end-wall (Figure 2.18(c)), periodic regions of higher heat transfer exist although these do not correlate with the position of the jets at exit as neatly. If, however, the perforations in the second blockage are both co-planar and near the end-wall (Figure 2.18(d, e)). A wholly different set of heat transfer contours are noted on the nearest end-wall (Figure 2.18(d)) compared to either of Figure 2.18(a-c). On the opposite end-wall (Figure 2.18(e)) the contours are similar to those in Figure 2.18(a) implying that the distinct changes in Figure

2.18(d) are due to the close proximity of the jets to the end-wall. It is thus concluded that those fluid dynamics and kinematics responsible for the variations in the heat transfer contours of Figure 2.18(d) thus are not fully described in literature.

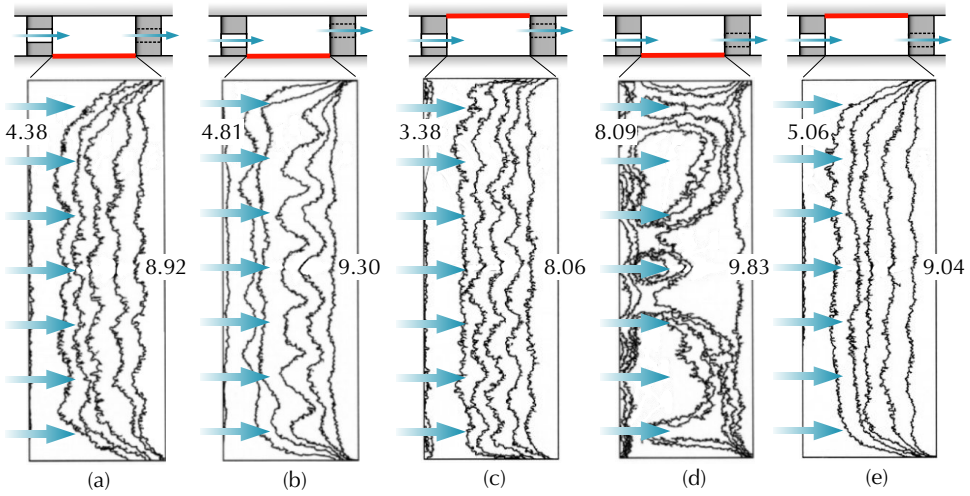

Figure 2.18. End-wall heat transfer contours between perforated blockages with spot Nu/Nu_0 values at Re_{Dh} = 10,000 adapted from (Moon & Lau, 2003).

(c) Thermal performance of a perforated blockage configuration

Alongside the increase in heat transfer, there is a significant increase in pressure drop across the blockages, as the coolant stream is constrained to flow through the perforations. An increase in the number of perforated blockages installed in the trailing-edge will increase both overall heat transfer and pressure drop. The latter is measured by friction factor and is significant enough that the thermal performance of a typical perforation blockage configuration is less than that of a smooth channel, with values of approximately $0.6 < \eta_{TP} < 0.95$ that decreases for higher Reynolds numbers. For a pin-fin array the friction factor is of the order of approximately f/f_0 = 1 - 5 (Lawson et al., 2011; Lyall et al., 2011). For a perforated blockage however, the friction factor is of the order of approximately $f/f_0 \approx 1300$ (Moon and Lau, 2003). As a result, the use of perforated blockages in the trailing edge is often avoided or viewed negatively.

In attempts to improve this poor thermal performance, numerous variations have been previously investigated as sampled in Figure 2.19. A "conventional" type perforated blockage setup, shown in Figure 2.19(a), has the perforations in the mid-height of the channel, symmetric about the channel width. Variations therein include different span-wise spacings between the perforations (S_{z2}) and different perforation diameters (D_j). Larger perforations decrease the end-wall heat transfer but significantly reduces the pressure drop and this results in a net increase in thermal performance of approximately 20% (Ahn et al., 2007). This performance is still, however, below unity. This should be expected as there would theoretically exist a case where the perforation diameter would increase such

that the entire channel was a single "perforation" – there being no blockage and instead an empty channel (against which the thermal performance is being measured).

A decrease in the spacing S_{z2} is typically associated with an increase in the number of perforations as more space becomes available between the outer perforations and channel sidewalls. This in turn increases the blockage ratio (A_b/A_j – the ratio between blockage area and total perforation area). An increase in the blockage ratio does result in an increase in thermal performance, albeit still below unity.

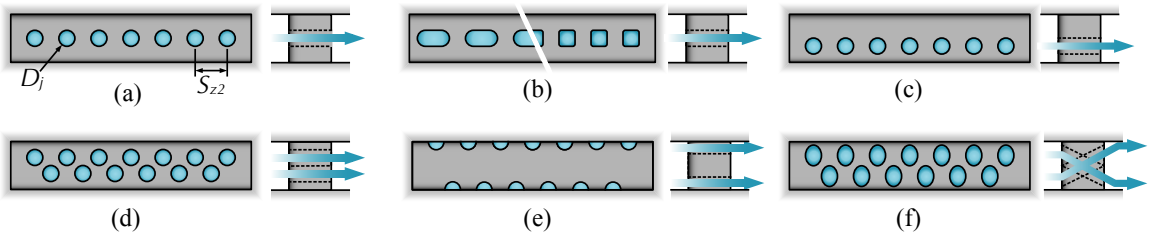

Figure 2.19. Variations in trailing edge blockage perforations configurations. (a) With circular perforations, (b) With slotted or square perforations, (c) With perforations not aligned with the channel mid-height, (d) With multiple rows of perforations, (e) With perforations at end-wall, and (f) With inclined perforations.

A further variation is the changing of the shape of the perforation (as shown in Figure 2.19(b)). Square, elliptical or slot type holes have been investigated and result in an increased thermal performance with slot perforations achieving a 16% increase compared circular holes (Ahn et al., 2007). This is likely due to the increase in the blockage ratio and associated decrease in pressure drop. As with changes to perforation spacing and diameter, a thermal performance below unity was obtained. An exception was that Lau et al. (2011) did record a thermal performance of η_{TP} = 1.05 and 1.1 at Re_{Dh} = 7500 between the second and third and third and fourth blockages respectively. A thermal performance below unity was obtained for the between the first and second blockages however and for higher Reynolds numbers, in the range purported to be applicable for turbine airfoil cooling (10 000 ≤ Re_{Dh} ≤ 30 000), the thermal performance of the entire configuration was consistently below unity. There are also additional manufacturing complexities associated with the requirement for square holes that should be considered.

Shifting of the perforations towards the end-wall (Figure 2.19(c)) was noted as increasing the thermal performance compared to the baseline case by Moon and Lau (2003). The resulting heat transfer contours are shown in Figure 2.18(b, c). Chung et al. (2014), however, noted a decrease in thermal performance. Both studies identified a lower pressure drop but the different heat transfer variations. The reason for the difference is unclear and there is insufficient flow visualization to elucidate further.

A variation of the configuration in Figure 2.19(c) is the use of two rows of perforations as shown in Figure 2.19(d). At a given spanwise (z-axis) location, such a configuration could be seen as equivalent

to that in Figure 2.19(c), and by extension Figure 2.18(b), due to perforation staggering. In the study conducted by Chung et al. (2014), the blockage ratio (A_b/A_j) between the configurations equivalent to that in Figure 2.19(a, d) was kept constant, resulting in different spanwise spacings and perforation diameters. This makes the effect of a double perforation rows unclear. Notably, despite the constant area reduction ratio, the double row configuration had a lower pressure drop. The heat transfer was also lower, and an overall lower thermal performance was noted compared to a conventional setup. If the perforations are moved such that their centers are on the end-wall (Figure 2.19(e)) a small increase in thermal performance (~5%) over a conventional setup was achieved (Chung et al., 2014). This setup is not easily comparable as the perforation position results in an end-wall flow between the blockages and no backflow.

A superior modification to that in Figure 2.19(d) is achieved by inclining each perforation as shown in Figure 2.19(f). This results in a significant increase in heat transfer due to the jet flow being targeted at the end-wall as a form of inclined impinging jet. Further, the pressure drop (f/f_0) is equivalent to a conventional setup. Overall, there is a thermal performance of approximately η_{TP} = 1.1. Notably, this performance is still well below that possible with a pin-fin cooling configuration.

(d) Elucidation of jet flow structures

The majority of studies involving jet type flows in confined channels, such as (Abraham & Vedula, 2019; Aillaud et al., 2017; Fenot et al., 2008; Gauntner et al., 1970; Lau et al., 2008; Lim et al., 2007; Long & New, 2019; Moon & Lau, 2003; N. Wang et al., 2018; Zhang et al., 2019) will often refer to turbine cooling as a possible application of the studies' findings. The jet flows in such an application are blockage jets, formed when the coolant is forced through perforations in the internal structure (or blockages). They will hereon be referred to as "blockage jets." Jet types can vary depending on whether they are formed through a nozzle or tube or from an orifice but this distinction is not always noted as is worth elucidating.

As the flow Reynolds number in a turbine blade is expected to be $Re_{Dh} > 10000$, any jet flow will be fully turbulent (Gauntner et al., 1970; McNaughton & Sinclair, 1966). Fully turbulent jets will, upon exit begin to immediately entrain the surrounding fluid. The entrainment forms a mixing layer between the surrounding fluid and the central core of the jet. This core region is referred to as the potential core. Flow within the potential core region will have an almost constant centerline velocity ($v_c/v_e \approx 1.0$) within 2-5%. The mixing layer is characterized by a large increase of turbulence as heat and mass exchanges occur. This mixing layer grows in width further from exit, decreasing the size of the potential core until the core has dissipated. The distance from the exit where the potential core has dissipated is termed the potential core length (l_p). Following this, the jet is considered developed (Bradbury, 1963, Gauntner 1970) and the jet centerline velocity undergoes a notable decay of a ratio inversely proportional to the distance from exit.

The downstream position where the centerline velocity drops below 95 - 98% that of the centerline velocity at exit is a common measure for where the potential core ends (i.e. the downstream position where v/ve < 0.98). Alternative measures have also been used but will not be considered here.

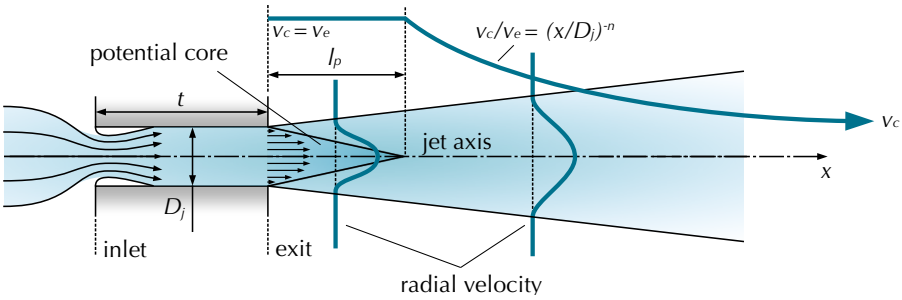

Figure 2.20. Schematic of characteristic turbulent jet and select flow properties.

Based on thickness of the airfoil internal structure (or blockage) and perforation diameter there will exist a particular thickness to diameter ratio (t/D_j) for the jet. The actual values utilised in practice are not available in open literature, being considered propriety, but previous studies of perforated blockages typically employ a thickness ratio of $t/D_j \approx 1.0$ (Chung et al., 2014; Moon & Lau, 2003; Park et al., 2016; Shin & Kwak, 2008). Material properties, manufacturing processes, tolerances and thermal loads would ultimately dictate how small a ratio that could be possible. It is assumed that a similar thickness ratio would be used in other areas of the turbine airfoil. Schematics, such as that in Figure 2.8, tend to have higher thickness ratios ($t/D_j \approx 2.0$ as labelled) but these diagrams may not reflect actual practices.

Despite this, numerous studies (Abraham and Vedula, 2019; Aillaud et al., 2017; Fenot et al., 2008; Lim et al., 2007; Long and New, 2019), use fully developed jets despite referencing turbine cooling applications. Here, the term, “fully developed” refers to a jet whose velocity profile within the “tube” has been fully established before exit. It should not be confused with the developed region of the jet as shown in Figure 2.20. It is here that the necessity for elucidation in jet types exists. A thickness ratio of $t/D_j \approx 10.0$ will guarantee a fully developed turbulent jet (Incropera and DeWitt, 2007; Çengel and Cimbala, 2014). On the other hand, at a thickness ratio of $0.1 \leq t/D_j \leq 0.5$ the jet will be considered similar to that from a blunt edge orifice jet (Hassan and Meslem, 2010; Lee and Lee, 2000; Quinn, 2006; Shakouchi and Kito, 2012). Between these two thickness ratios ($0.5 < t/D_j < 10$), where turbine airfoil cooling applications appear to fall, there is therefore a transition from an orifice type jet to that of a fully developed turbulent jet. This has not been directly noted in applicable studies referenced previously. The use of a thickness ratio of $t/D_j \geq 10.0$ is unlikely to be feasible and so it can be safely said that fully developed turbulent (tube) jets are not applicable to turbine cooling applications. It is unclear if the example application of turbine cooling was incorrectly referenced or if the investigations did not distinguish between the jet flows and assumed similar behaviours between the jet types regardless of the thickness ratio. For clarity, the distinction in jet types should be considered.

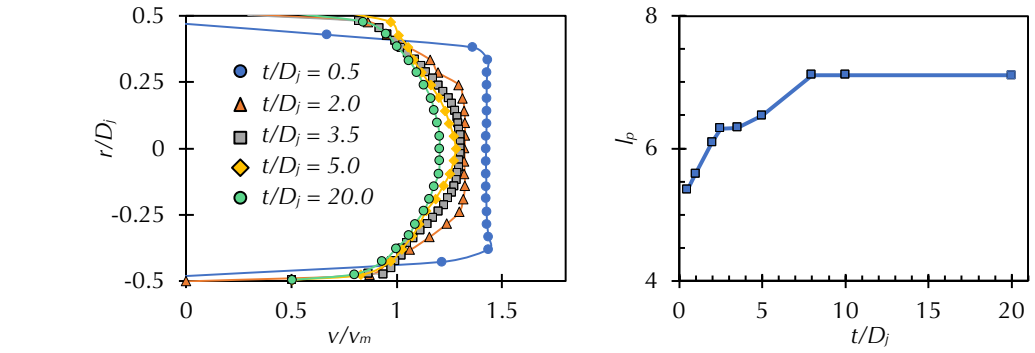

(a)

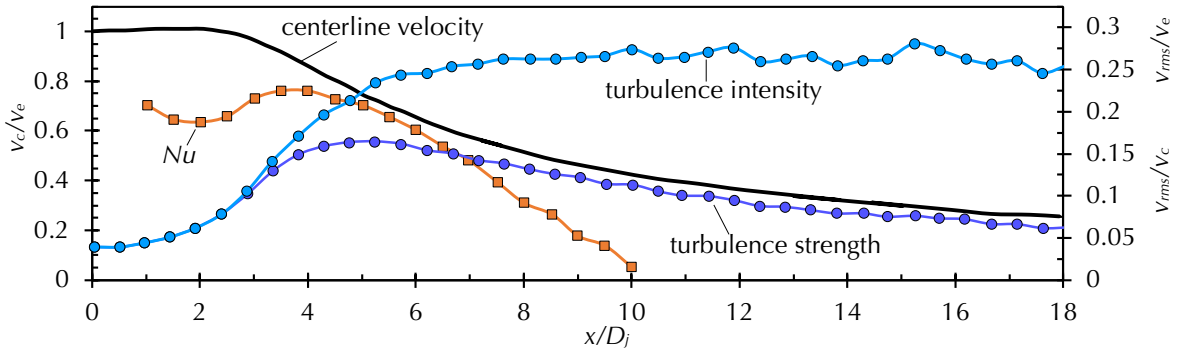

(b)

Figure 2.21. Blockage jet characteristics based on results from Liu et al. (2022): (a) Variation of potential core length (l_p) with t/D_j with shaded region indicating a more practical range of t/D_j for internal cooling at leading edge of gas turbine blades and (b) Radial profile at jet exit.

Such a distinction was investigated as part of a study in which the author contributed, investigating the effect of varying the thickness ratio directly (Liu et al., 2022). It was seen that within a thickness ratio range of $0.5 < t/D_j < 8.0$, a blockage jet behaves neither exactly as an orifice jet nor a tube jet. The blockage jet does, however, exhibit similar features to either jet, being either orifice-like or tube-like. These two types (either orifice-like or tube-like) are differentiated based on the velocity distribution in the radial direction at jet exit. This variation is shown in Figure 2.21(a). An orifice-like blockage jet will feature a uniform-like radial velocity distribution. As the thickness ratio increases, the size of the uniform-like velocity distribution decreases. In the absence of uniform-like distribution at jet exit, the blockage jet is then considered tube-like. This transition appeared to occur at approximately $t/D_j \approx 3.5$. The majority of blockage jet flows in a turbine airfoil should thus be considered orifice-like.

An increase in the thickness ratio (from orifice-like to tube-like) also sees an increase in the potential core length of the blockage jet. Upon exit a turbulent jet will begin to immediately entrain the surrounding fluid. As this occurs a mixing layer forms that gradually increases in size towards the jet centreline. The core jet flow (the potential core), where in the flow velocity remains constant, then decreases in size. The length of the potential core then is conventionally measured as the distance from

exit that the jet centreline velocity remains constant (within v_c/v_e = 0.95 or 0.98). This measurement method was found to be not appropriate for consideration of varying jet types (orifice, tube and transitioning between both). A definition collected by Gaunter et al. (Gauntner et al., 1970)] summarized a different definition of the potential core length, which was normalized by average jet velocity (v_m) at jet exit rather than the jet's centreline velocity at jet exit (w_e). The variation in potential core length, using this definition, is shown in Figure 2.21(b).

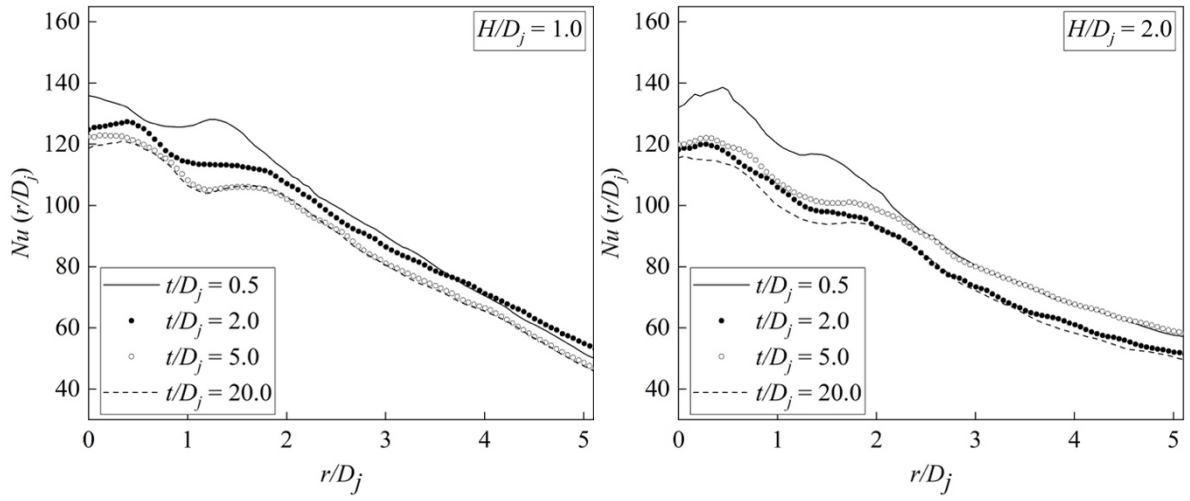

(a) (b)

Figure 2.22. Radial heat transfer distributions on target plate at Re_j = 20,000 for both blockage jets (t/D_j = 2.0 and 5.0), with H/D_j =: (a) 1.0, and (b) 2.0. (Liu et al., 2022).

Consideration of the potential core length is important as jet impingement heat transfer is consistently higher when the target surface is within the potential core length (Hrycak, 1983; Liu et al., 2022). Further, an orifice jet consistently results in a higher impingement heat transfer compared to a tube jet for a given target distance. During the transition between orifice and tube jet, however, the impingement heat transfer would be increase with an increase in thickness ratio, depending on the target distance (Figure 2.22). The target area in a turbine airfoil for impingement cooling however is not likely to be very large, there simply being additional jets added as necessary to account for the drop off in heat transfer away from stagnation (at r/D_j = 0.0). Thus, it can be seen that a general guide for designing perforated blockage configuration would be utilise a small thickness ratio.

2.4.4. Pin-fins cooled by blockage jet

The combination of both perforated blockages and a pin-fin array (Figure 2.9(d)) seeks to use the perforated blockage to focus the jet flows exiting the perforated blockages onto the pin-fins. This cooling scheme can be seen as a further variation to a perforated blockage configuration, over and above those in the previous chapter. Here, the jets are not targeted at the downstream blockage or towards the end-wall but instead targeted at a pin-fin array. To avoid confusion between pin-fin arrays without

perforated blockages and a pin-fin array in a "blockage pin-fin configuration" (here on referred to as such), the former will here on be referred to as a "conventional pin-fin array." To the best of the author's knowledge, only two studies have considered such a scheme (Kan et al., 2014; Kim et al., 2019). To clarify, this cooling scheme requires the perforation axis to be aligned perpendicular with the pin-fin axis as per Figure 2.23(a). This should not be confused with a configuration where the perforation axis was parallel to the pin-fin axis (Figure 2.23(b)). This latter case is applicable to cooling of the mid-chord of the turbine. It would not be applicable for turbine trailing-edge cooling due to space constraints.

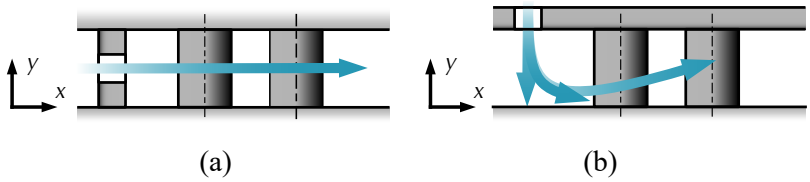

Figure 2.23. Distinction for a combination of perforated blockages and pin-fins. (a) With jets perpendicular to pin-fin axis and (b) With jets parallel pin-fin with parallel and perpendicular jets.

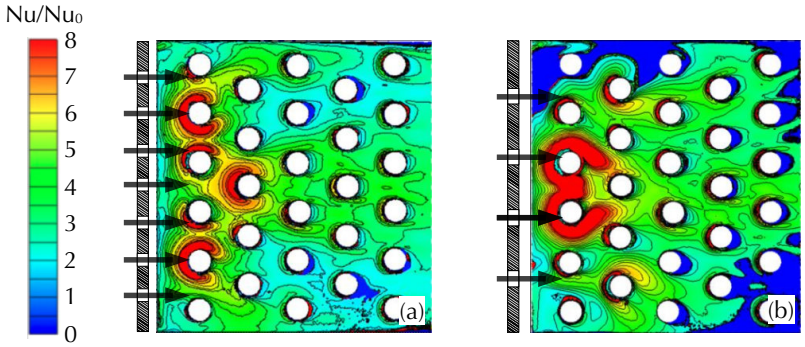

Figure 2.24. Sample of end-wall heat transfer contours adapted from Kan et al. (2014). (a) with 7 perforations and a blockage ratio of 11.45% and (b) With 4 perforations and a blockage ratio of 11.06%.

A sample of the results and observations by Kan et al. (2014) are shown in Figure 2.24. Five variations were considered that varied the perforation spanwise spacing (S_{z2}), diameter (D_j) and shape (circular and slots) while maintaining the same pin-fin array. The end-wall heat transfer for a case with seven round perforation is shown in Figure 2.24(a) while a case with four round perforations is shown in Figure 2.24(b). Both cases had a similar blockage ratio (Ap/Ab ≈ 0.11). For the case with seven perforations an end-wall heat transfer of Nu/Nu_0 = 3.77 and with four perforation the end-wall heat transfer was Nu/Nu_0 = 3.85. Both cases had a higher end-wall heat transfer than a conventional pin-fin array (Nu/Nu_0 = 2.64). There was however a significantly higher pressure drop for the blockage pin-fin configurations of f/f_0 = 315 and 364 for seven and four perforations respectively. This was notably higher than the pressure drop of f/f_0 = 22 for the conventional pin-fin array. Due to this, both Kan et al. (2014) and Kim et al. (2019) both noted thermal performance values below unity (i.e. a heat transfer per unit pumping power lower than an empty channel). It is suspected that this cooling scheme has seen

no further investigation or consideration considering these results.

These two studies may, however, be misrepresenting the blockage pin-fin configuration. This is noted by way of geometric misalignment of the blockage perforations and downstream pin-fins. Previous studies (Chung et al., 2014; Lau et al., 2008; Moon & Lau, 2003; Park et al., 2016; Shin & Kwak, 2008) have considered perforation spanwise spacings of $1.33 \leq S_{z2}/D_j \leq 3.33$ for circular holes with a common or base case spacing seen to be $S_{z2}/D_j = 2.0$. Seemingly in keeping within this common range, Kan et al (2014) used $S_{z2}/D_j = 3.0$ (Figure 2.24(a)) and Kim et al. (2019) used a value of $S_{z2}/D_j \approx 2.0$. Kan et al also used a larger spacing of $S_{z2}/D_j = 3.85$ (Figure 2.24(b)). None of the perforation spacings used by either Kan et al. (2014) or Kim et al. (2019) matched those of the spanwise pin-fin spacings (S_{z1}/D_j). This can be clearly seen in Figure 2.24. A consequence of this is that blockage jets were not geometrically aligned with the downstream pin-fins. In the case of Kan et al.'s (2014) end-wall heat transfer in Figure 2.24 there can clearly be seen superior heat transfer around those pin-fins for which the jets are aligned. Were all jets aligned then it could be argued that a superior heat transfer would be obtained. The pressure drop is also noted to not vary significantly (being more dependent on the blockage ratio than perforation spacing) and thus a higher thermal performance may have been possible).

Those results by Kan et al (2014) as shown in Figure 2.24 do highlight either issues in the measurement accuracy or at least in the flow distributions. For Figure 2.24(b) there are large regions of the end-wall that have an end-wall heat transfer $Nu/Nu_0 = 0.0$. The contours may be explained as more of a qualitative comparison but at the very least with four perforations (Figure 2.24(b)), there is a distinctly non-uniform or very irregular end-wall heat transfer.

In light of the above and in consideration of the blockage pin-fin configuration there are a series of factors that require elucidation. These are elaborated on below.

2.4.5. Knowledge areas requiring elucidation

(a) The distinction of flows at the base of pin-fins subjected to impinging jets

When a single pin-fin is exposed to a uniform like flow field, a horseshoe vortex pattern (Figure 2.11) results at the base of the pin-fins. This pattern largely remains when that pin-fin is in an array exposed to a uniform flow field. Kan et al. (2014) also observed this in the numerical simulation results shown in Figure 2.25(a). The characteristic horseshoe or tear drop type shape is largely similar at the base of all pin-fins in the array.

With the introduction of perforated blockages, forming a blockage pin-fin configuration, the end-wall flow patterns became very irregular in the results for Kan et al. (2014) as seen in Figure 2.25(b). This irregularity resulted in a very irregular end-wall heat transfer with regions of negligible heat transfer as seen in Figure 2.24. In discussing these results Kan et al. (2014) stated that "typical horse-shoe vortices for pin fin arrays are not significant" and later "Impingement changes the horseshoe vortex structure near the end-wall." It can almost be inferred from the discussion of results that horseshoe

vortices are understood to exist but that in a blockage pin-fin configuration they diminish or are varied. Inspection of the flow patterns near the end-wall show streamlines pointing radially from the pin-fin surface (as shown in the close up of Figure 2.25(b)). The radial end-wall flow could be interpreted as the upstream flow beneath the separated boundary layer of a horseshoe vortex system – between an attachment point (A) and separation point (P) in Figure 2.11. It is here proposed, however, that this interpretation is incorrect and that horseshoe vortices do not exist in any form.

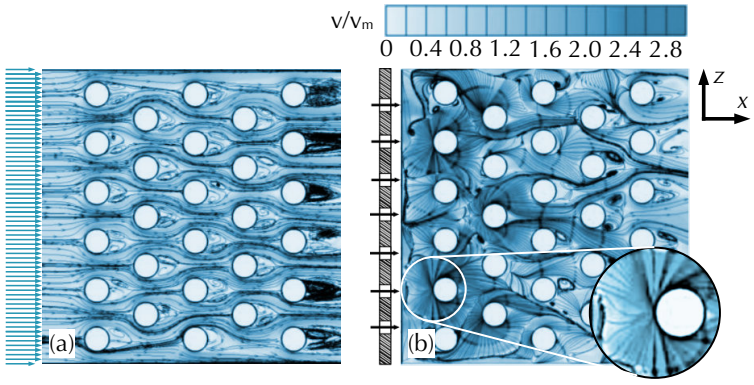

Figure 2.25. Velocity contours from numerical simulations for a pin-fin array near the end-wall (y/D = 2.5×10^{-4}) by Kan et al. (2014). (a) With a uniform-like upstream flow field and (b) With an upstream perforated blockage and close up (inset).

The basis for this proposition is simple: in a blockage pin-fin configuration there is no approaching end-wall boundary layer flow towards the pin-fin. This boundary layer flow is prevented by the upstream perforated blockage which constrains the entirety of the coolant flow in the mid-height of the channel ($y/H = 0.5$), away from the end-walls, as jet flows. Without a boundary layer stagnating on the pin-fin and separating from the end-walls, the mechanism for the formation of horseshoe vortices is completely absent. This was not acknowledged by Kan et al. (2014). Instead, a wholly different and as yet poorly realised end-wall flow structure is present.

Consider a single blockage jet impinging on a single pin-fin. In the plane of symmetry (x-y plane) this may be expected to be very similar to the flow structure shown in Figure 2.17(b) for the flow between perforated blockages – the adapted schematic shown in Figure 2.26(a). The jet will impinge on the pin-fin, stagnating. From this stagnation point the flow will be redirected along the pin-fin surface as wall-jet type flows. A portion of the redirected flow will be towards the end-walls. Using laser induced fluorescence (LIF) flow images Jiao (2016) studied these wall-jet flows. The pin-fin aspect ratios, however, were sufficiently high ($H/D > 5$) such that the subsequent stagnation of the wall-jets at the base of the pins (the end-walls) were not considered. For sufficiently low aspect ratio pin-fins, such as may be expected in the trailing edge of a turbine blade ($0.5 \leq H/D \leq 4.0$), these end-wall flows cannot be ignored. There, the wall-jet flows will stagnate on the end-wall and be redirected outwards. Some of which will be equivalent to the back flow between perforated blockages. There, the “back flow” may

extend out radially from the leading edge, corresponding with certain patterns noted in Figure 2.25(b).

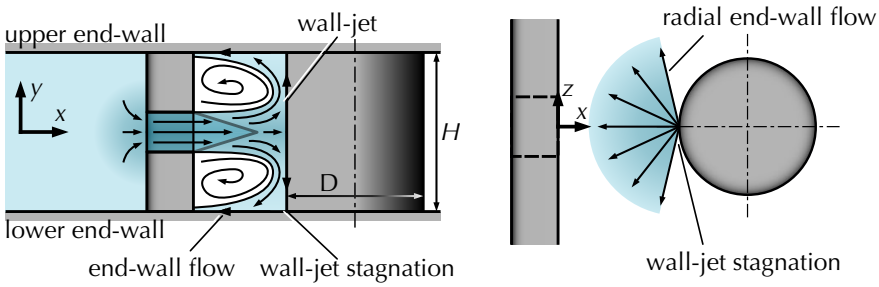

Figure 2.26. Envisaged flow patterns considering perforated blockages. (a) In the plane of symmetry (*x*-*y* plane) and (b) On the end-wall (*x*-*z* plane).

Note that the flow schematics shown in Figure 2.26 are merely conjectured. In the plane of symmetry (*x*-*y* plane) the schematic is not based on any measurements. The end-wall flow schematic (Figure 2.26(b)) is identifiable in the measurements by Kan et al. (2014). Other flow structures (vortical flows and non-radial type flows) in Figure 2.25(b) are not explained by the basic flow schematic conjectured.

To seek and produce a blockage pin-fin configuration with an optimal cooling performance, an understanding of the fluid dynamics and kinematics within is critical. Design parameters such as pin-fin spacing in the streamwise (S_x) and spanwise (S_z) directions will be dependent on the flow structure around the pin-fins and how these flow structures interact. Further, there is likely a correlation between the spacing and alignment of the perforations with the pin-fins to ensure that jet flows are concentrated onto the pin-fins for a more effective cooling. For conventional pin-fin arrays and perforated blockages such design parameters have been thoroughly studied. These values are not necessarily applicable to a blockage pin-fin configuration given the differences in fluid dynamics and kinematics. The end-wall flow interactions between a pin-fin and an impinging jet thus requires further elucidation.

(b) Distinction of flows in mid-height of channel

An extension to the above, is the consideration of flows in the mid-height of the channel (y/H = 0.5). The end-wall flow patterns in a blockage pin-fin configuration are directly attributable to these flows. If no flow interacts with the pin-fin in the mid-height of the channel, then no end-wall flows around the pin-fins can be expected. Such an occurrence may explain the regions of negligible heat transfer in Figure 2.24(b) – there being no end-wall flows in the vicinity to cool the end-wall.

In a conventional pin-fin array the mid-height flows are, like the end-wall flows, expected to be regular – flow patterns around a single pin-fins being a near mirror image of those around another. This is demonstrated in the flow field based on numerical simulations in Figure 2.27(a) by Kan et al. (2014). There the oncoming flow, upstream of the pin-fin array, was in the x-direction. If that oncoming flow

is turned 90º (the z-direction) then there continues to exist a degree to regularity based on the numerical results in Figure 2.27(c) by Kim et al. (2019). There, as the flow is required to exit in the *x*-direction, the mid-height flow is required to turn before exit. This resulted in the flow through the pin-fin array being curved.

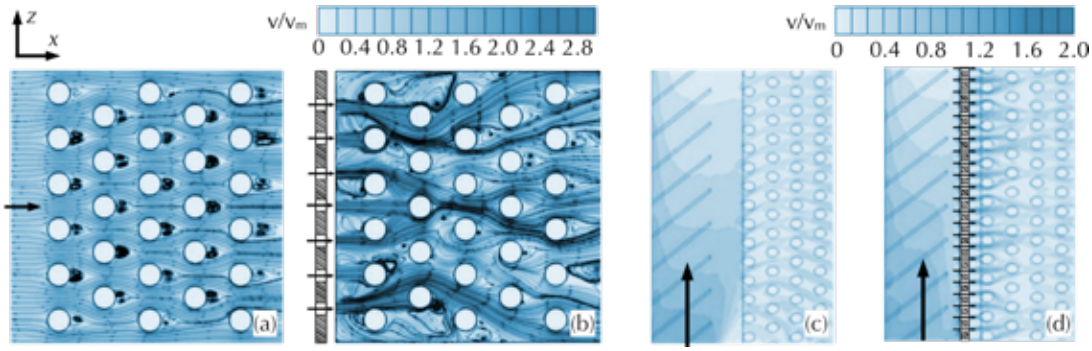

Figure 2.27. Velocity contours in the mid-height plane through a pin-fin array from previous studies. (a) With uniform-like upstream flow field and upstream flow in the x-direction (Kan et al., 2014), (b) With upstream perforated blockage and upstream flow in the x-direction (Kan et al., 2014) (c) With uniform-like upstream flow field and upstream flow in the y-direction (Kim et al., 2019) and (d) With upstream perforated blockage and upstream flow in the y-direction (Kim et al., 2019)

With perforated blockages, the flow through the array is very irregular for both setups (Figure 2.27(b, d)). Each successive row is exposed to different flows. Unlike a conventional pin-fin array, the flow structure around or past a single row of pin-fins cannot be reasonably extrapolated for multiple rows. There is a strong dependency on the flow conditions through a row of pin-fins on the flow through the previous row. Of particular interest of the flow patterns in Figure 2.27, is the notable curvature of jet flows through the pin-fin array. This flow curvature appears to be responsible for a large portion of the irregular flow field through the pin-fin arrays in Figure 2.27(b, d). Curvature here refers to the deviation of the jets core flow from its original axis (illustrated in Figure 2.28(a)).

It is not referring to the curvature noted in Figure 2.27(c). There, the curvature is of a distributed mainstream flow (rather than concentrated jet flow) and is due to the flow being required to change direction before exiting the channel. The curvature is different to the jet curvature noted in Figure 2.27(d) with the upstream perforated blockage. Notably, with the perforated blockages (Figure 2.27 (d)), the jet flows immediately downstream of the blockage appear to be aligned with the perforation axis – the perforated blockage appearing to realign the flow and prevent the noted without the blockage present (Figure 2.27(c)). This realignment of the flow by the perforated blockage can be seen in the uniform end-wall heat distributions observed by Lau et al. (2008) and affirms this property of the blockages. This should be considered as a potential advantage for the use of a perforated blockage as part of a turbine trailing edge cooling scheme.

The curvature of a jet flow (seen in Figure 2.27(b, d)) may be expected based on prior studies (Ghahremanian et al., 2014; Laban et al., 2019; Svensson et al., 2016; Tanaka, 1969, 1974; Walker & Kors, 2973; Yimer et al., 1996). The curvature is due to the asymmetric presence of neighbouring jets. Conventionally, a fully turbulent jet (Re_j > 3000), upon exit, immediately begins to entrain the surrounding fluid toward it, forming the mixing layer in Figure 2.20 (Gauntner et al., 1970; Hrycak et al., 1970). The surrounding fluid is both the stationary fluid immediately surrounding the jet but also is nearby jet flows – the jet entraining its neighbouring jets towards itself and vice versa (Ghahremanian et al., 2014; Gordon & Gerber, 1990; Laban et al., 2019; Svensson et al., 2016; Tanaka, 1969, 1974). This can cause the jets to curve towards each other (Figure 2.28(b)). If there is some sort of restoring action (such as the jet being entrained symmetrically in both directions), a jet's curvature may be prevented altogether (Figure 2.28(c)). Besides blockage pin-fin setups, studies of perforated blockages (without downstream pin-fins) (Ahn et al., 2007; Lau et al., 2003; Moon & Lau, 2003; Park et al., 2016; Shin & Kwak, 2008) do demonstrate a very small amount of asymmetric end-wall heat transfer which may indicate that there exists a small flow curvature – although the actual flow curvature was not directly observed in any of those studies. In those latter cases, the flow curvature would be very small and far less than noted in the results of (Kan et al., 2014; Kim et al., 2019), as seen in Figure 2.27(b, d).

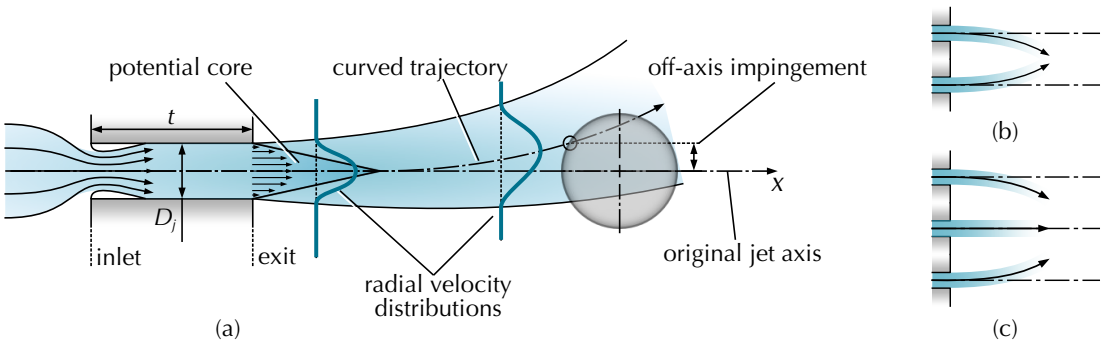

Figure 2.28. Flow schematics regarding blockage jet curvature. (a) For a blockage jet exhibiting curvature and off-axis impingement on a pin-fin, (b) Mutual entrainment and symmetrical flow curvature, and (c) Symmetrical entrainment preventing curvature.

The possibility of flow curvature is therefore not in question. Instead, its role and prevalence in a blockage pin-fin configuration is not clear. Note in both setups of Kan et al. (2014) and Kim et al. (2019) there is a lack of geometric alignment between the perforation axis's and the pin-fins Figure 2.27(b, d). Preceding the impingement of the jets on the pin-fins there does not appear to be significant curvature of the jets. It may then be argued that the observed jet curvature occurs due to this geometric misalignment – the off-axis impingement causing the jets to curve and follow the profile of the pin-fins due to the Coanda effect. The pin-fins may incite a unstable behaviour in the wake of the pin-fins – the flow between the pin-fins becoming biased towards one pin-fin (Bearman and Wadcock, 1973; Sumner

et al., 1999; Wang and Zhou, 2005). It may be a combination of these effects. Regardless, the curvature of a blockage jet can result in an off-axis impingement of the jet flow on the pin-fin (Figure 2.28(a)). It is clear from the end-wall heat transfer contours in Figure 2.24 that the curvature is detrimental and to be mitigated. The means of achieving this is however unclear in the context of a blockage pin-fin configuration.

(c) The complete heat transfer in a blockage pin-fin configuration

The thermal performance (η) of a cooling scheme considers both the heat transfer (Nu/Nu_0) and pressure drop (f/f_0) through the cooling scheme (as per equation (1)). There, however, exists an issue with its use in prior studies. Specifically, for perforated blockage or blockage pin-fin configurations. The pressure drop values naturally consider the contribution of all surfaces in the cooling scheme from pin-fins, channel walls and the perforated blockages themselves. In the case of perforated blockage and blockage pin-fin configurations, the largest contributor to the pressure drop comes from forcing the flow through the perforated blockage. It is this high pressure drop that results in the thermal performance being below unity. In the applicable studies (Ahn et al., 2007; Chung et al., 2014; Lau et al., 2008; Moon & Lau, 2003; Park et al., 2016; Shin & Kwak, 2008; Ye et al., 2019; Zhang et al., 2019), however, the heat transfer measurements exclude the heat transfer occurring on the perforated blockage surfaces themselves. In this way, the measured pressure drop is based on the entire setup. The heat transfer, on the other hand, is only partially considered. Perforated blockage studies (previously referenced) and the study by Kim et al (2019) only considered the end-wall heat transfer. Kan et al (2014) measured the end-wall and as well as the pin-fin surface heat transfer. No studies, however, have considered the contribution of the heat transfer on the perforated blockages themselves.

Studies of conventional pin-fin arrays can and have considered just the end-wall heat transfer. This is because the contribution of the pin-fin and end-wall surfaces, to the overall heat transfer is established (as previously discussed in chapter 2.4.2b). In comparisons between just perforated blockage setups or just pin-fin arrays separately, it may be warranted to ignore common surfaces (such as the perforated blockages plates or pin-fins). Consider a situation where there exists a difference in the types of flow structures being employed (i.e. a conventional pin-fin array and a blockage pin-fin configuration). The different structures will have a distinct effect on the thermal performance. Unless the heat transfer and pressure drop consider the contribution of all surfaces similarly, there will thus be an inconsistency or bias in how the thermal performance is measured.

In a blockage pin-fin configuration, the cooling airflow is interacting with the surface of the perforated blockage plate (in Figure 2.17 and Figure 2.26(a)). As such, there will be a transfer of heat between the blockage surface and the airflow. If a second perforated blockage exists (Figure 2.17(b, c)) then there will be jet impingement cooling on the upstream surface of this second blockage. Further if that radial end-wall flow shown in Figure 2.26(b) interacts with the downstream surface of the perforated blockage then the blockage may experience additional cooling as well. It is unlikely that this

heat transfer is negligible such that it can be discounted. Lau (2008) did acknowledge that such surfaces will contribute to the heat transfer but did not perform a measurement on the surface. It is thus hypothesized that, with the heat transfer contribution of all surfaces, in a blockage pin-fin configuration, that the thermal performance may be higher than that previously reported. It may even be above unity.

2.5. Research questions and objectives

2.5.1. Research questions

The primary research question to be addressed within this dissertation is as follows: Can the previously purported thermal performance of a blockage pin-fin internal cooling scheme be improved upon? Furthermore, is there merit in any further consideration of this configuration for cooling applications? To answer this question there are further questions that require elucidation:

- What is the nature of end-wall flows around a pin-fin array subjected to impinging jets?
- What sizing specifications are required to ensure a more optimal performance?
- What is the heat transfer contribution of the perforated blockage structures themselves?

2.5.2. Objectives

In order to address these questions, the following objectives will be sought.

- Identify the flow features around a pin-fin, subjected to an impinging jet.
- Determine what factors need to be considered for a blockage pin-fin configuration to have a more optimal performance than previously purported.
- Determine the heat transfer contribution of all applicable surfaces or structures in a blockage pin-fin configuration to the overall heat transfer and thermal performance.

3. EXPERIMENTAL APPROACH AND METHODOLOGY

3.1. Experimental approach

This research work will be broken down into three parts. Each part will utilize distinct setups aimed at isolating or focusing on factors or behaviours that are present. Schematics of these setups are shown in Figure 3.1. The rationale is to build up the understanding of the fluid dynamics, fluid kinematics and thermodynamic behaviours present in a blockage pin-fin configuration. The findings of the first and second parts will be used in developing or optimising the parameters for the second and third parts respectively. The specifics of each setup will thus be presented at the start of each setup. A summary of each part is made below.

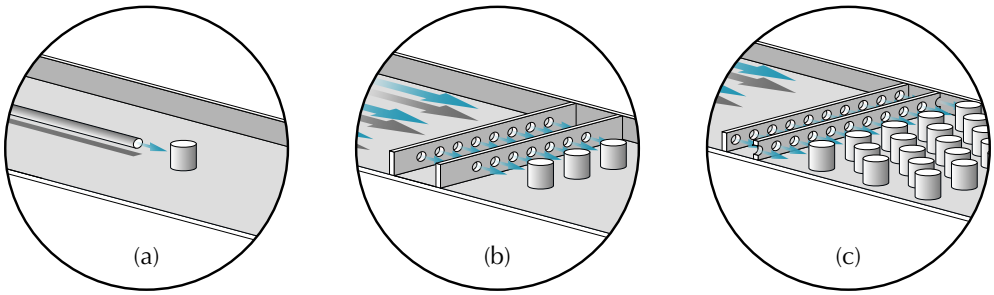

Figure 3.1. Summary of setups to be assessed. (a) With a single tube jet impinging on a single pin-fin, (b) Considering the effects of perforated blockages and multiple pin-fins, and (c) With a full blockage pin-fin configuration.

3.1.1. A singular pin-fin subjected to a singular impinging jet

The case with a single tube jet impinging on a single pin-fin aims to clarify the end-wall flow topology and consequential heat transfer characteristics around a single short circular pin-fin subjected a single jet impingement (Figure 3.1(a)). The specific focus will be on experimentally demonstrating end-wall flow patterns and their effect on heat transfer characteristics around the pin-fin. An emphasis will be on their dissimilar features, if present, to those of horseshoe vortices. A tube jet rather than orifice jet (formed through a perforated blockage) will be considered. This is intended to ensure the only structure contacting the end-wall surface is the pin-fin. The end-wall flow will thus be unhindered, similar to that for a horseshoe vortex system.

3.1.2. The effect of perforated blockages

The case with perforated blockages aims to elucidate on a series of points. The first of which will be the variation in those results noted from Chapter 4 by considering a single pin-fin being subjected to an impinging blockage jet instead of an impinging tube jet. Interactions between the end-wall flow and the perforated blockage can also be considered.

Thereon multiple blockage jets with multiple pin-fins will be investigated. This will consider those interactions and additional flow behaviours arising from the additional jets and pin-fins. Further, the presence and effect of jet curvature in a blockage pin-fin configuration can be better discerned. In this way a full understanding of how jets interacting with pin-fins can be made. From this, it is envisaged that a more optimal design for a blockage pin-fin configuration can be developed for testing.

3.1.3. The thermal performance of a full blockage pin-fin configuration

Based on the findings from those foregoing cases, a setup representing a more optimal blockage pin-fin configuration will be developed – being more optimal than those considered in prior studies. The case with a full blockage pin-fin configuration focuses on determining its thermal performance.

3.2. Experimental measurements to be considered

A purely experimental approach will be followed in this research. Numerical studies would require validation against previous data. As already presented, there are key features that require elucidation and for which validation would not be feasible. Numerical studies may then follow in future studies, using the findings of this research. The following core parameters are to be considered during testing:

- Flow visualization of the end-wall surface flows
- Flow visualization of the through channel flows, away from the end-wall
- Flow velocity and pressure measurements
- Surface temperature measurements

Time-averaged measurements will be considered for the flow visualization, flow velocity and pressure parameters. Surface temperature measurements will be captured under steady state conditions. Thus, no unsteady or time-resolved measurements will be considered. The techniques used in measuring these parameters will be detailed in the following chapters.

3.3. End-wall surface flow visualization using an oil-dye mixture technique

The visualization of the end-wall flow patterns would be necessary in both elucidating the patterns around a pin-fin subjected to an impinging jet and understanding the heat transfer characteristics of a blockage pin-fin configuration. For the purpose of end-wall surface flow visualization, an oil-dye mixture technique was used. This approach was seen as simpler and cheaper than alternatives such as shear-sensitive liquid crystal mixtures. Further it allows for the direct end-wall patterns to be visualized compared to those visualization or measurement techniques such as particle image velocimetry (PIV), where the measurement can be close to the end-wall but not directly on the surface itself. The measurement technique has been previously used in published studies requiring end-wall flow visualization by Choi et al. (2006), as well as the author (Schekman and Kim, 2017).

Using this technique, florescent powder is mixed with light diesel oil and the mixture is applied to the end-wall surface. The airflow was then allowed to interact with the test section. The shear stresses between the airflow and the end-wall surface then cause the oil-dye mixture to be repositioned. As this is done, some dye is deposited on the end-wall surface resulting in dye patterns that reveal the end-wall flow patterns.

Once the test is complete an ultraviolet light was positioned to cause the deposited florescent powder to be highlighted. Images were then taken with a digital camera. To aid in the contrast between the deposited powder and the end-wall surface the end-wall was painted matte black. Imaging of the dye patterns required the removal of the lid due to oil-dye mixture often being splattered onto the lid surface during testing due to the presence of three-dimensional flows (as shown in Figure 3.2). The lid also acted to reflect some of the ultraviolet light and cause artefacts to be introduced into the image – confusing or misleading the interpretation of the image. These factors also prevented imaging during the test.

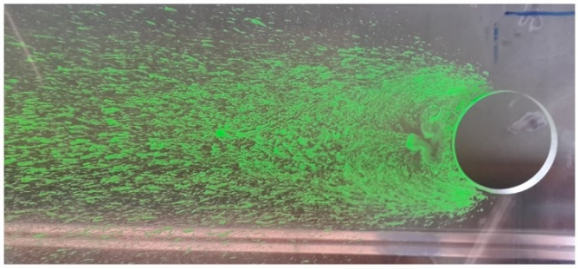

Figure 3.2. Example of residual oil-dye splatter on lid of test section following a test.

The mixture ratio depended on the Reynolds number and was obtained by trial and error depending on the test setup. Too much dye would result in the mixture having too little movement on the end-wall when subjected to shear stresses from the airflow. Too little dye would result in the mixture being repositioned by the surface shear flows too quickly. There would then be insufficient dye particles deposited in regions of the end-wall surface – an absence of flow visualization. Too much mixture, on the other hand, would inevitably result in dye pooling. Regions of trapped or circulating flow would pool the mixture and require unreasonable test times to wait for the diesel to evaporate.

It is found that a paint roller was the most effective way of applying the mixture to the end-wall surface. This allows for a more consistent, even distribution on the end-wall surface. Uneven distributions can result in the end-wall flows be manipulated or cause misleading end-wall flow patterns to remain. Further, in the event of a region of the end-wall not being subject to any end-wall flows (such as may be present in the wake flow of a pin-fin), then patterns created during the application of the mixture would remain undisturbed. A clear distinction between undisturbed and disturbed dye pattens is critical.

3.3.1. Processing of images

Green fluorescent powder was used for all tests. These colours were often dull in images as seen in an example raw image from a pin-fin exposed to a uniform flow field (Figure 3.3(a)). For interpretation of the image it was found useful to enhance the images. Images were enhanced using the software package Affinity Photo, a raster graphics editor developed by Serif Ltd. The enhanced version of the example image is shown in Figure 3.3(b). Enhancement was undertaken through photo editing software. The software's built-in functions for colour balancing, adjustment of the brightness and contrast of the image and adjustment of the relative shadows and highlights in the image were used. There was no warping or skewing of the image or manipulation of the pixels through, for example, sharpening functions. Those areas not representing the end-wall flow (i.e. beneath the pin-fin) were masked as necessary. This processing approach was self-derived and would be varied depending on the ambient lighting conditions present in each set of tests. As the images were being used for qualitative measurements only, the image processing was purely to amplify the features in the image for interpretation purposes. It was not necessary to exactly match ambient lighting conditions or the processing elements.

The processing typically resulted in a predominantly green image but this was not necessarily the case (depending on ambient light conditions). Regardless, the final image does not have to be green and colour filters could be applied to the image if desired (as done for Figure 3.3(b)).

It is taken that the final processed images presented, here-on, continue to represent those actual flow patterns obtained during testing. Any and all adjustments are purely for the purposes of more easily interpreting the images. No flow patterns are adjusted or manipulated.

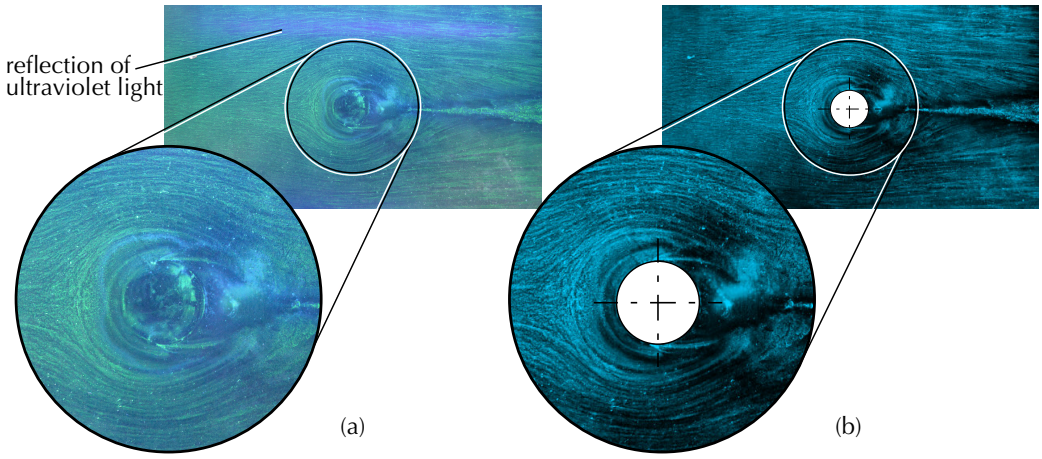

Figure 3.3. Processing transition of oil dye flow visualization technique including closeup for a pin-fin exposed to a uniform flow field at Re_D = 35,000. (a) Original raw image and (b) Processed final image.

3.3.2. Interpretation of the image

Interpretation is made by way of comparing darker regions (with less or no dye particles) and the

highlighted regions where dye was deposited. A pin-fin subjected to a uniform flow field, resulting in the formation of horseshoe vortices, is well established and can therefore be used to as a reference case for the interpretation of oil dye. The resulting dye pattern has already been shown in Figure 3.3(b) that used the setup for Chapter 4 (for a single pin-fin subjected to a single impinging jet). An annotated version of this image with matching flow schematic is shown in Figure 3.4(a). Another example of the same test is shown in Figure 3.4(b), obtained using an oil-dye mixture with a larger proportion of dye. The thicker mixture results in apparently more clearly defined or exaggerated flow patterns.

The overall end-wall surface flow patterns, in both images of Figure 3.4, show similar topological features previously reported (Baker, 1979, 1980; Choi et al., 2007; Sahin et al., 2008; Schekman & Kim, 2017). As per the flow topology shown in Figure 3.4 (b), there will exist separation and attachment lines, on the end-wall, that will wrap around the pin-fin. Separation lines (S_n), where the end-wall flow is separates from the end-wall surface, will result in an accumulation of dye particles. The attachment lines (A_n), where flow is attaching to the end-wall, will disperse the dye particles in the vicinity. There can be seen narrow bands of dark or black annotated in Figure 3.4. As the horseshoe vortex system is turbulent the attachment and separation lines are continuously shifting (Baker, 1979) and so they lack a degree of definition. For example, the separation lines become separation "bands". The characteristic horseshoe shape can also be seen formed by the path of the vortices and corresponding separation lines around the pin-fins. The most upstream of the identified separation bands in the plane of symmetry is located at approximately $(-)1.2 < x'/D < (-)1.1$ (noted as position S in Figure 3.4). This location is consistent with the value that could be estimated by the equations by Ballio et al. (1998), having the boundary layer separating from the end-wall at a position of $x'/D = (-)1.2$.

Regions of accumulated and disperse dye do not necessarily indicate only separation and attachment points respectively. This is demonstrated in the end-wall flow patterns away from the pin-fin surface. There the streamlines are curved, conforming to the flow patterns around the pin-fin but these do not feature any separation or attachment regions. Instead the resulting streamlines are simply due to the natural deposition of the dye as the oil-dye is convected downstream by the end-wall boundary layer. Even in the absence of separation and attachment points, streamlines can still be seen. For an oil-dye mixture featuring a higher ratio of dye (as used in Figure 3.4(b)) there can result large or thick bands of dispersed dye. This could be easily misinterpreted as separation points in other situations (such as the surrounding end-wall around a pin-fin subjected to an impinging jet). As such mixtures with a lower dye ratio are preferred.

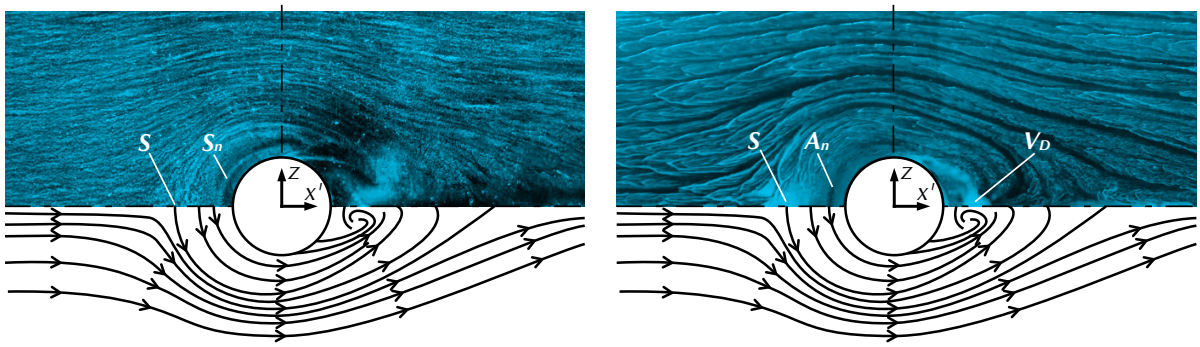

(a) (b)

Figure 3.4. Oil-dye flow visualization for a uniform-like flow around a short circular pin-fin at $Re_D = 3.5\times10^4$, showing an end-wall flow topology image (upper part) and corresponding interpreted schematic (lower part). (a) With the typical mixture ratio of oil and dye and (b) With a larger ratio of dye in the mixture.

In the wake of the pin-fins there exists the vortical structure V_D (first shown in Figure 2.12). Such a flow structure will result in a large level of dye accumulation and pooling. This is not clearly noted in Figure 3.4(a) although it is very evident in Figure 3.4(b). Pooling can present a problem whereby the moment the airflow is stopped, those shear stresses forcing the dye to remain pooled disappear. The pooled dye then disperses and in doing so an surrounding flow patterns are redistributed, no longer representing the flow patterns while the airflow is active. To counter this the airflow needs to remain active until the majority of the diesel has then evaporated. Careful application of the oil-dye mixture can also minimize the pooling by anticipating the sources of the pooled dye and applying less mixture in advance.

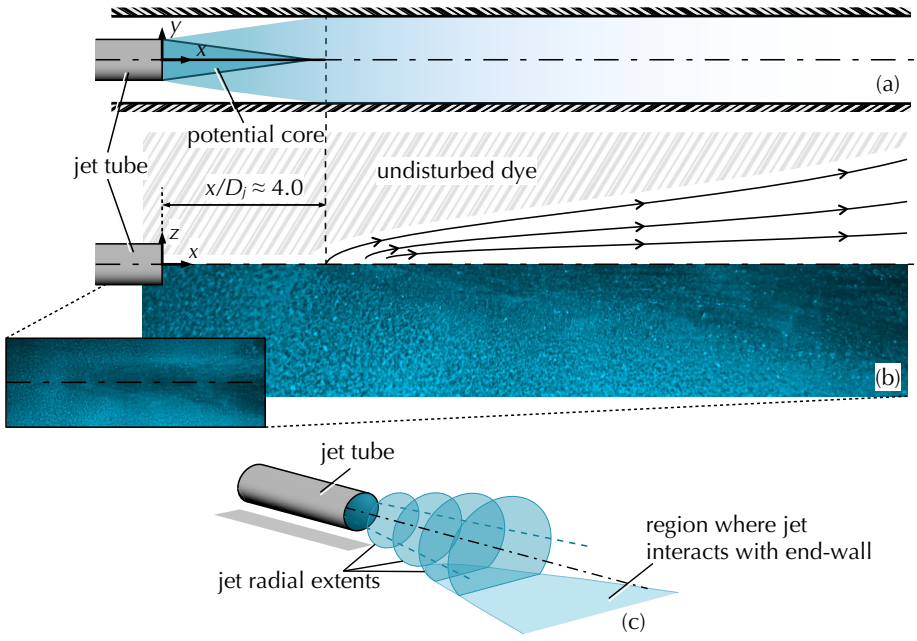

Figure 3.5. Oil-dye end-wall flow visualization for a tube jet exiting into an empty narrow channel (Re_j = 17,500). (a) Jet schematic in the *x*-*y* plane, (b) At the end-wall (*x*-*z* plane) with flow schematic (top), processed oil-dye image (bottom) and full oil-dye image (inset), and (c) Schematic explaining shape of end-wall patterns.

In the presence of weak end-wall flows, the flow features are often unclear or obscure. Using the test setup for Study 1 with just a tube jet exiting into an empty channel (Figure 3.1(b)), the resulting end-wall flow visualization is shown in Figure 3.5. As the jet diffuses in the *x*-*y* plane it will eventually contact the end-wall at a specific downstream location (marked by the dotted line in Figure 3.5(a)). This in turn results in the oil-dye mixture being disturbed as seen in Figure 3.5(b). The size of the region where the jet interacts with the end-wall will increase downstream as the jet diffuses further as shown in Figure 3.5(c). Near the centreline (z/D_j = 0) there is a clear disruption of the dye patterns seen in Figure 3.5(b) but near the periphery of the region the distinction is less clear. This is compounded by the jet velocity decreasing from exit (as per refs) and the jet flow interacting with the end-wall will likewise be weaker further from exit. While there is a clear region where the jet interacts with the end-wall in Figure 3.5(b), there are no clear streamlines as seen in Figure 3.4. Inferring these streamlines as done in the schematic of Figure 3.5(b) as an example is to be avoided without further data to corroborate their interpretation.

3.4. Mainstream flow measurement techniques

Velocity measurements were primarily obtained through Particle Image Velocimetry (PIV) measurements. This technique is further detailed in chapter 3.5. Independent velocity measurements were made using a pitot tube for both establishing the settings for PIV and as a part of the validation of the PIV results. For the fully turbulent round jet impingement on the short circular pin-fin, a Pitot tube is positioned at the jet exit, at the centre. For monitoring velocity decay or distributions, pitot position was progressively increased through a modified traversal rig with digital vernier. The position of the pitot tube could then be adjusted to an accuracy of ±0.01 mm.

Static pressure measurements were measured through pressure taps in the sidewall of the channel. The position of the static ports is reported for the respective sections of each study, below. Static ports were machined into the sidewalls using a CNC with a purported accuracy of ±0.03mm. Hypodermic needles were then inserted into the ports and sealed. The static pressure tapping's, and Pitot tube were connected to the differential pressure transducer (DSA^{TM}, Scanivalve Inc.), which sends data via a TCP/IP protocol to a data acquisition personal computer. This has an accuracy of ±0.05%. Alternatively, pressure measurements were obtained with a DPM TT 550CV micromanometer with an accuracy of ±0.05 Pa.

The flow rate through the channel was obtained, where necessary, using an Airflow LCA501 turbine flow meter with an accuracy of ±1.0% of the reading. A housing was developed to allow the

flow meter to be fitted to the inlet of the wind tunnel.

Air temperature at the inlet to the test channels (T_{in}) was measured by way of a Moving Air Type-K temperature probe. Alternatively, for tests involving the tube jet, a pre-calibrated bead T-type thermocouple was used. The thermocouples were attached to a Fluke 51 II digital thermocouple with accuracy of ±0.05%.

3.4.1. Data reduction parameters

Velocity measurements using the pitot from the pitot tube was calculated as:

$$v_{pitot} = \sqrt{(2q/\rho)} \tag{2}$$

where q is the dynamic pressure measured by the pitot tube in Pa and ρ is the air density in kg/m^3 found to be approximately 0.995 kg/m^3 during testing. The flow Reynolds number was calculated as:

$$Re = \frac{\rho v_{ref} D_{ef}}{\mu} \tag{3}$$

where v_{ref} is the reference air velocity in m/s and D_{ref} is the characteristic reference length in m and μ is the dynamic viscosity of air in kg/ms. As applicable v_{ref} would be the jet flow velocity at exit (v_e) or the average velocity through the channel v_{avg} based on the measured flow rate. As applicable the characteristic length was either the pin-fin diameter (D), the blockage perforation, tube or jet diameter (D_j) and the hydraulic diameter of the test channel (D_h). Hydraulic diameter for a rectangular channel was calculated as $D_h = 2(W*H)/(W+H)$. Reference length dimensions were measured to an accuracy of ±0.25%. The values for ρ and μ were based on standard atmosphere tables using the ambient air temperature and interpolating. The assessment of the thermal performance (equation 1) considers the ratio f/f_0. The Moody friction factor (f) was calculated as:

$$f = -\frac{\left(\frac{dp}{dx}\right) D_h}{\frac{1}{2}\rho v_{avg}^2} \tag{4}$$

where dp/dx is the measured change in pressure between two static pressure ports separated by a distance x. The baseline friction factor (f_0) for fully developed turbulent flow in a smooth channel was given by Kakac et al. (1987), as used by Lawson et al. (2011), as:

$$f_0 = 0.507 Re_{Dh}^{-0.3} \tag{5}$$

3.4.2. Measurement uncertainties

Measurement uncertainties were estimated using a method as follows. If $y = f(x_1, x_2, \ldots, x_n)$, then the uncertainty propagated by x_i in the variable y is given by (Coleman & Steele, 2018):

$$\Delta y = \sqrt{\left(\frac{\delta y}{\delta x_1}\Delta x_1\right)^2 + \left(\frac{\delta y}{\delta x_2}\Delta x_2\right)^2 + \cdots + \left(\frac{\delta y}{\delta x_n}\Delta x_n\right)^2} \tag{6}$$

Using this method, the uncertainties associated with the general flow measurements were

calculated as shown in Table 3.1.

Table 3.1. Uncertainties in flow measurements

Parameter	Uncertainty
v_{pitot}	±1.3%
Re	±1.5%
f	±3.0%

3.5. Flow field mapping using particle image velocimetry (PIV)

The primary means of measuring and visualizing the flow through the channel was by means of particle image velocimetry (PIV). The setup was configured in 3 primary configurations, shown in Figure 3.6. These variations depending on whether measurements were being made in the *x-z* plane (Figure 3.6(a)) or the *x-y* plane (Figure 3.6(b-c)). In the latter case two different configurations were assessed depending on the orientation and implementation of the laser light.

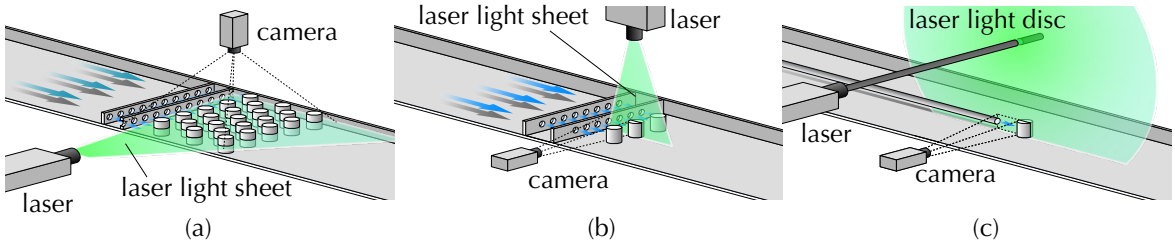

Figure 3.6. Test configurations for a particle image velocimetry (PIV). (a) With light sheet aligned with the *x-z* plane, (b) With the light sheet aligned with the *x-y* plane, and (c) Setup employing an isotropic planar illumination of the *x-y* plane.

In all configurations the flow field was illuminated by a pulsed laser light, generated from a frequency doubled, dual cavity Nd:YAG laser (New Wave Research™), with a light wavelength of 532 nm. For the configurations in Figure 3.6(a, b) the laser light was emitted as a flat sheet emanating from the laser source. The laser and sheet were aligned by a physical reference grid plate that was fitted into the test channel at the required position. Alignment was taken as achieved when the laser light would illuminate the entire alignment grid plate. For measurement in the *x-z* plane (Figure 3.6(a)) the laser was aligned with the mid-height of the channel (y/H = 0.5) and at a quarter height (y/H = 0.25). Measurements nearer the end-wall surface were also obtained by lowering the laser sheet down to a minimum height of y/H = 0.08. For measurement in the *x-y* plane (Figure 3.6(b)) it was found easier to rotate the channel rather than fix the laser into a vertical position. It is shown otherwise in Figure 3.6(b) for convenience. An alternate configuration Figure 3.6(c) was to use light disc forming options that employed a 90º cone mirror that created a light disc with 360º illumination. This latter configuration and optics were the same as employed by Atkins and Kim (2015).

In all cases, the CCD camera was positioned approximately 500 mm - 600 mm away from and perpendicular to the measurement plane, where the laser light sheet crossed. At this distance the image magnification factor, between object plane (coplanar with the laser light sheet) and image plane of the camera, was of the order of $M_0 \approx 0.1$.

The recorded flow field is represented by the random pattern of particle images in the object plane that are mapped onto the image plane of the (CCD) camera sensor. The camera was positioned so the optical axis was perpendicular to the laser light sheet and focused at the on a plane coinciding with the light sheet. Alignment and focusing of the camera were achieved through the same physical reference grid plate that was used for the laser alignment. The images are recorded on the sensor frame that had a 2048×2048 pixel resolution and a pixel pitch of 7.4 μm. The field of view would be adjusted by increasing or decreasing the distance between the light sheet and the camera lens. The size of the flow field was set based on both how much of the flow field needed to be observed and also the resolution in the flow field necessary. The flow fields measured for the various configurations studied are shown in Figure 3.7, represented by the green regions.

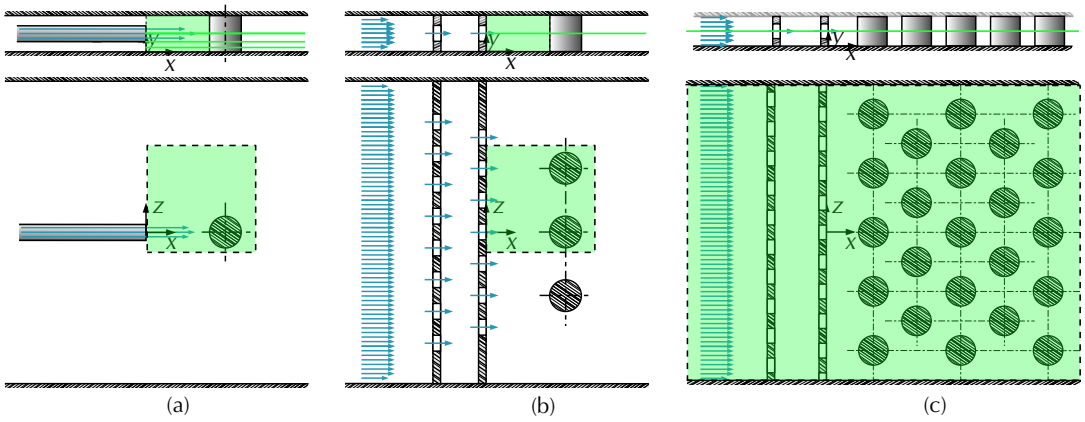

Figure 3.7. Particle image velocimetry (PIV) measurement windows in the *x*-*y* and *x*-*z* planes for various setups. (a) With a single tube jet impinging on a single pin-fin, (b) For considering the effect of perforated blockages on a single row of pin-fins, and (c) With a full blockage pin-fin configuration.

The PIV images were divided into sub-regions referred to as interrogation areas that were 16 × 16 pixels in size and overlapped by 50%, hence each velocity map contains 255 × 255 vectors and the resulting vector spacing was 0.4 mm. The evaluation of the image field between two successive frames yielded an instantaneous vector map which was achieved with a Dantec Dynamic Studio V1.45 software. The ensemble-averaged velocity field for a specific location in the flow field was then evaluated over an ensemble of 124 instantaneous vector maps sampled at a frequency of 5 Hz. The measurement techniques and setup were based on the work established by (Atkins & Kim, 2015).

The flow field was seeded with an atomized mineral oil (Shell Ondina 901L0996) that was introduced into the test section through the jet nozzle. Seeders have a mean particle diameter of

approximately 1μm. This results in a Stokes number less than 0.01 for all likely frequencies of the fluid that may be present. It was thus assumed that the trajectory of the seeding particles was the same as the actual flow field and that the particles did not interact with one another.

The flow field in the plane of symmetry of the pin-fin (*x*-*y* plane) was illuminated by a pulsed laser light, generated from a frequency doubled, dual cavity Nd:YAG laser (New Wave Research™), with a light wavelength of 532 nm. Light disc forming optics that employs a 90° cone mirror was used to create a light disc with 360 illumination as shown in Figure 3.6(c) as this configuration enabled a simplified experimental setup. This illumination method and apparatus was developed for the work by Atkins and Kim (2015). The measurement period is defined by two sequential pulses of the laser light sheet that are separated by a finite time interval (20 μs).

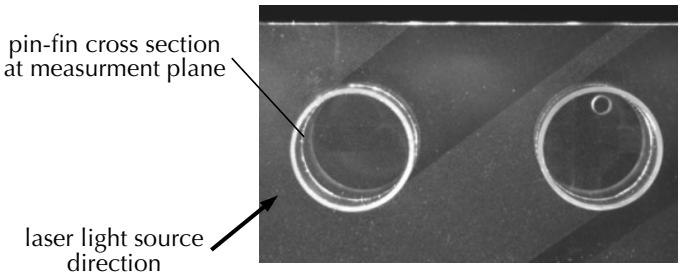

Figure 3.8. Instantaneous image from PIV demonstrating perspective along height of the pin-fins.

Due to the presence of pin-fins and perforated blockage plates, there existed an element of occlusion of the flow field by the structures due to perspective. This can be seen in Figure 3.8. This could not be prevented but it could be managed by positioning the camera such that any structures would not obscure those flow fields of interest. In the case of Figure 3.8, the wake flow of the pin-fins would be partially obscured. Those obscured regions were masked off which is why some PIV measurements give the appearance that pin-fins are elliptical or oblong in nature.

The measurement period is defined by two sequential pulses of the laser light sheet that are separated by a finite time interval - approximately 15-25 μs to ensure a particle displacement ¼ of the interrogation region (16 × 16 pixels). The anticipated displacement of the particle was based on the expected flow velocities which were obtained from preliminary tests using a Pitot tube in situ. The velocities were verified against the velocities measured by the PIV test.

The uncertainty of the instantaneous PIV velocity was estimated based the contributions of the mean bias and random errors present during PIV interrogations. Westerweel (2000) showed that the random measurement errors are directly proportional to the particle image diameter and are a function of the number of particle images within the interrogation area, and sub-pixel displacements. In addition, background noise contributes to the random error. Taking these factors into consideration the random error is estimated to be 0.17 pixels, based on an average particle image diameter of 2.8 pixels. The particle image diameter was measured using the autocorrelation of the PIV recordings, where the

resulting self-correlation peak width is $2^{1/2}$ times the particle image diameter. This method to determine the particle image diameter was preferred to the analytical diffraction-limited spot size estimation, that tends to underestimate the value due to non-ideal performance of the lens and imaging arrangement. The ideal number of particle image pairs (10) for the displacement-correlation was assumed according to (Adrian & Westerweel, 2011), based on the high valid vector detection percentage (i.e., ~98 %), with ~1000 vectors being rejected out of ~55000 valid vectors detected with 8300 masked vectors. The bias error was shown by (Westerweel, 2008) to be a function of the displacement correlation peak width. The present bias error was estimated to be 0.06 pixels. Therefore, the total measurement uncertainty was determined to be 3.4 % based on the valid full-scale displacements of 6.4 pixels, where the total bias and random errors are combined by using the root-sum-square of these terms.

3.6. Surface temperature measurements

Surface temperature measurements were measured with two techniques: infrared thermography and using thermochromic liquid crystals (TLC). All temperature measurements were made at a steady state, using a film heater to heat the base surface and the airflow, at ambient air temperature, for cooling. The two techniques, data reduction and uncertainties associated are detailed below.

3.6.1. End-wall surface heating

The end-wall surfaces were heated using film heaters. The film heaters were sized such that they would be cover an area in excess of this measurement area to avoid any issues with cooling near the perimeter of the heater. The heaters were then connected to a Variac variable AC power supply. The outputs from the power supply, during test conditions were measured by multi-meter.

Depending on the test setup the film heater would either be mounted on top of the end-wall surface and a thin foil applied over to distribute the heat from the coils of the heater. Alternatively, the heater was fitted between an aluminium plate (forming the end-wall surface) and a Teflon board for insulation.

3.6.2. End-wall surface temperature mapping using infrared thermography

Initially tests were conducted, mapping the local temperature distribution using an infrared (IR) thermal camera (FLIR T640) with a purported accuracy of ±2 % at 25 ºC. Early tests used a polymer based upper substrate as a viewing window manufactured by Edmund Optics™. The viewing window proved to be insufficient in size and offered too small an area on the end-wall surface. Instead tests were conducted by allowing the test setup to reach steady state and then shutting down the tunnel and removing the Perspex lid. The IR camera then captured images - a sample of which is shown in Figure 3.9. The process was optimised to take less than 10 seconds and repeated to ensure that repeated measurements offered the same result within 3 %. This procedure was deemed acceptable for Chapter 4 of the research but an alternative (thermochromic liquid crystals) was sought for Chapter 6.

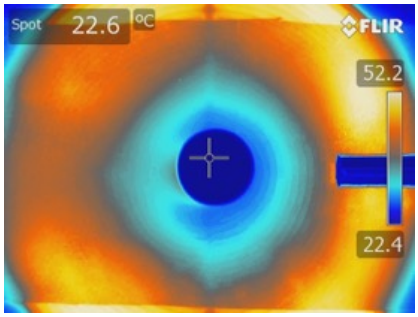

Figure 3.9. Sample image taken by infrared thermal camera for a tube jet impinging on a circular pin-fin.

3.6.3. Surface heat transfer mapping using thermochromic liquid crystal (TLC)

The surface temperature of the end-wall, perforated blockage and pin-fin surfaces, in Chapter 6 of this research work, were measured through the use of thermochromic liquid crystals (TLC's). The TLC's were obtained from LCR Hallcrest Ltd. The specific details of the setup, applicable to TLC measurements, are shown in Figure 3.10.

All applicable surfaces were coated, including: the pin-fins, the end-wall surface and the perforated blockages. The channel lid and sidewalls were kept as transparent so that images of the TLC paint could be captured. The entire end-wall between the perforated blockages was coated. Around the pin-fin array, the end-wall was coated to a downstream position of $x/D_j = 19$ ($x/D = 9.5$). The end-wall upstream of the first blockage was coated to a position $x/D_j = -10$ (not shown in Figure 6.1). A matte black backing was first applied to the surfaces before the application of TLC's. A clear over coat was also applied.

The surfaces coated with TLC were imaged by a 12 MP digital camera that was suspended above the test section. No digital zoom or additional image enhancements over and above those automatically applied by the camera software were utilised. No colour adjustments or sharpening functions were made to the any of the images captured in post processing either. These same settings were used across all images, including calibration and thus were considered sufficiently consistent. Image captures of the end-wall surface were obtained with the camera positioned horizontal and perpendicular to the end-wall surface. For the vertical surfaces (the pin-fins and perforated blockages) the camera was aligned $\alpha = 30^{o}$ from the horizontal. This inclination prevented occlusion of portions of surfaces by neighbouring surfaces while also allowing a better view of the actual surface. Images while directly behind or ahead of the vertical surfaces was not possible for obvious reasons. The devices' built in inclinometer was used to ensure the correct alignment was maintained.

For illumination it was found that the built-in, single-point, flash of the camera provided the best results with the most uniform lighting least refraction from the transparent walls and lid of the channel. The refraction was a significant problem for the inclined images. Shadows also provided an issue with

the pin-fins in place whereby a light position that was not aligned or positioned near to the camera would result in the pin-fins casting shadows onto the observable end-wall. The onboard flash thus allowed for an illumination source that was as close as possible to the camera lens without either the camera body obscuring the light or light source obscuring the camera viewpoint.

The TLC's were to be used in steady state measurements. Both the film heater and wind tunnel would be turned on and sufficient time allowed for steady state to be reached. Steady state was considered reached when TLC colours changed with the hue colour of the specific point did not vary by more than 2 to 4 units. This consistently appeared to occur within 5 minutes from a change in input conditions but 15 minutes would be allowed for. The TLC's had a temperature range (from when the colours activated until when the colours disappeared) of approximately ΔT = 25 ºC. This range was based on anticipated temperature differences. As previously discussed there is a lack of data on heat transfer values for the surface of the perforated blockages. During testing, a large heat transfer range was noted with the perforated blockages and pin-fin surfaces having higher heat transfer compared to the overall end-wall surface. To account for this, the input power Q_{in} was adjusted depending on whether the vertical surfaces or end-wall were being imaged. This was preferred over the use of TLC with a larger temperature band to ensure greater temperature sensitivity over a given surface. The wind tunnel flow rate was maintained for consistency.

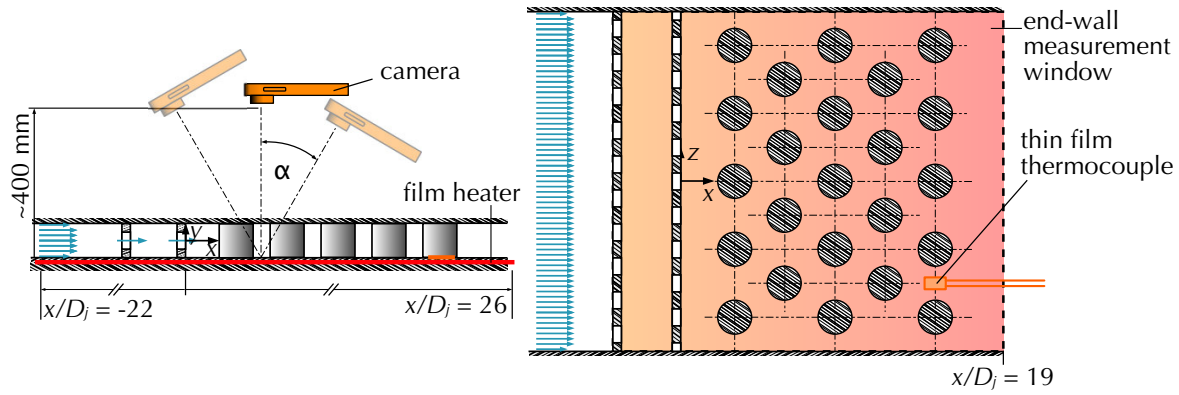

Figure 3.10. Specifications for setup utilising thermochromic liquid crystals in a full blockage pin-fin configuration.

(a) Calibration of thermochromic liquid crystals

Calibration of the TLCs was achieved by mounting a thin film thermocouple to the aluminium end-wall surface in the position marked in Figure 3.10. The thermocouple was an Omega CO2-K type with a 2 to 5 millisecond response time. It was plugged into a Fluke 51 II digital thermocouple with accuracy of ±0.05%.

Power was supplied to the film heater such that the temperature would then increase gradually (approximately 0.5ºC - 1ºC per minute). Images were taken from when the TLC's were transparent (a

black surface visible). During this time the camera was fixed into positioned and remotely triggered.

For the overhead images, the camera was positioned directly overhead the thermocouple. For the inclined images, the camera was positioned at 60º to the horizontal (accounting for the 90º difference in vertical and horizontal surfaces). The hue values at the thermocouple, extracted from the images, were then matched with those from the temperature measurement by the thermocouple as shown in Figure 3.11. Regression fits were made to the data plots to obtain calibration equations. From this an uncertainty of ±0.65% was determined. The calibration was repeated, including before and after testing to account for any potential aging effects of the TLC's. No discernible aging was noted.

The hue values were calculated by using the R, G and B values (red, green and blue) from the digital image. These were normalised to a value between 0 and 1 as (R_n=R/255, G_n = G/255 and B_n = B/255). The maximum (max) and minimum (min) of the normalised colour values are identified. The hue value is then calculated based on the following conditions:

- If max = 0, Hue = 0 (the colour is black)
- If R_n is max, Hue = 60((G_n-B_n) Mod 6) / (max – min)
- If G_n is max, Hue = 60(2.0 + (B_n-R_n)) / (max – min)
- If B_n is max, Hue = 60(4.0+ (R_n-G_n)) / (max – min)

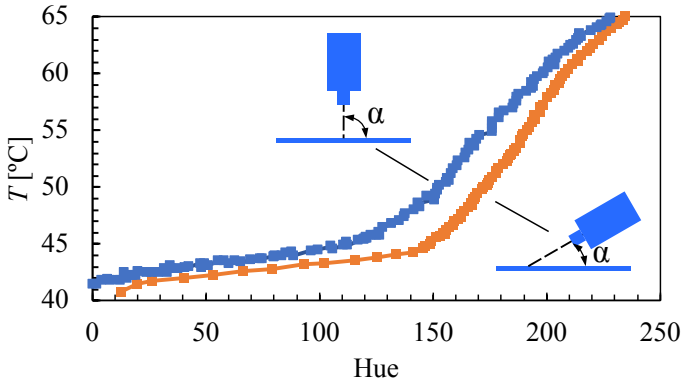

Figure 3.11. Calibration curves for the present thermochromic liquid crystal (TLC) for $\alpha = 90°$ and $\alpha = 30°$ inclined viewpoints.

As seen in Figure 3.11, different calibration curves were captured depending on the inclination of the camera. This is an expected result as the TLC hue varies with change in inclination. For an image of the end-wall, those areas further from the centre of the image would have an increased inclination and this change would need to be considered. With a camera centred above the channel at a height of approximately 400 mm (as per Figure 3.10), the end-wall at the sidewalls would have an inclination of approximately 14º to the camera lens. Placing the camera higher was avoided at risk of insufficient resolution of the images. The effect of 14º inclination is noted in Figure 3.12 showing the end-wall surface upstream of the first perforated blockage. There, a constant heat input was used with no flow being active through the channel. It would be expected that an approximately uniform temperature

would result on the surface. The temperature contours based on the processed raw image in Figure 3.12(a) is shown in Figure 3.12(b). As per Figure 3.12(b), however, the there is a temperature difference of approximately 2.5 ºC near the sidewall on the upper side compared to the centre of the channel. To accommodate this, images would only be considered over a smaller region (as indicated in Figure 3.12(b)) such that the temperature variation was less than 1 ºC. This increased the uncertainty in the temperature measurements to ±1.54 %. In this way the effects of temperature bias were assumed to be suitably considered. It was also assumed that this similar approach would apply to the perforated blockage surfaces.

This approach of using smaller capture regions ultimately proved necessary to allow for the end-wall surface around the pin-fin array to be fully captured, as discussed below.

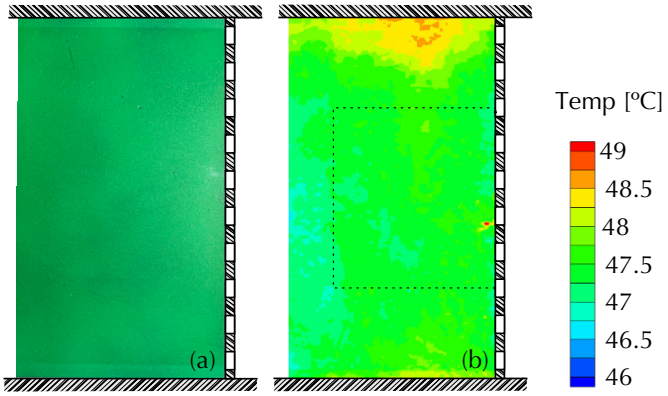

Figure 3.12. End-wall of empty channel upstream of first perforated blockage coated with TLC's with no flow through the channel and a constant heat input. (a) Raw image showing TLC colours and (b) the calibrated temperature contours.

(b) Preliminary processing of TLC images

Due to the height of the pin-fins there existed a perspective issue. Depending on where the camera was positioned there would be a region of the end-wall masked by the pin-fins. The raw images are shown in Figure 3.13(a). Both were captured with the camera positioned centrally in the section both from two different downstream positions. The top image being further downstream than the bottom image. The areas masked by the pin-fins are encircled. By combining the images, only those masked regions that were common to both regions would remain and the overall masked area on the end-wall could be reduced. The combined schematic is shown in Figure 3.13(b) and the adapted image is then shown in as shown in masked regions can be reduced in size using image data from corresponding schematics showing the masked regions are shown in Figure 3.13(c).

The combination was achieved by importing all images into a photo editing software. The images were then overlayed and aligned relative to the end-wall using the pin-fin end-wall edges as reference. The pin-fins were then selected and erased from the image. The combination did result in some visible

differences from the overlap, for example in the trailing region behind the last row of pin-fins. This was due to small changes in the lighting and the hue was found to be unaffected. To sufficiently reduce all masked regions a patchwork approach, as shown Figure 3.13(d) needed was then followed. A similar approach was then used for the end-wall surface between the perforated blockages although less masking existed due to the lack of pin-fins and instead patchwork was merely undertaken to prevent those regions near sidewalls from giving incorrect values to the angular offset (as shown in Figure 3.12(b)).

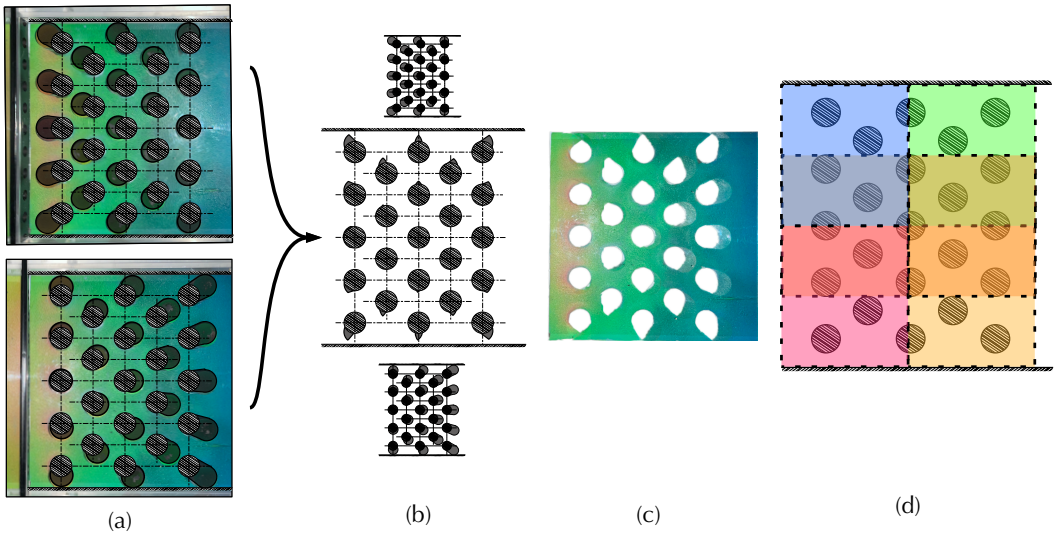

Figure 3.13. Preliminary TLC image processing approach using patchwork splicing of images for complete capture of end-wall. (a) Raw images taken from two perspectives with overlay of pin-fins, (b) Schematic showing regions masked by pin-fins (top and bottom) and spliced schematic (centre), (c) Resulting end-wall compilation image, and (d) Image capture regions used.

For the perforated blockages, these surfaces were captured at an inclination. An example image is shown in Figure 3.14(a). First the surface perforated blockage was isolated as shown in Figure 3.14(b). It can be seen in the source image (Figure 3.14(a)) the internal surfaces of the perforations themselves had been coated with TLC's. Given the constantly changing inclination to the camera these surfaces were excluded. Heat transfer measurements would then focus purely on the vertical surfaces, excluding the perforation internal surfaces. The isolated image could then be straightened as shown in Figure 3.14(c) for processing. To do so, a template was applied with the correct ratios and relative sizes of the circular perforations to the blockage frontal area. The image was then straightened to line up with template.

The entirety of the end-wall surface (e.g. Figure 3.13(c)) or the perforated blockage surface (e.g. Figure 3.14(c)) was then processed extracting the hue values. Due to the curvature of the pin-fins, a mapping of the entire surface was deemed impractical. An approach similar to that Figure 3.13 would have had to be adopted. The heat transfer on the surface of a pin-fin subjected to an impinging jet,

including off-axis impingement has been previously studied (X. L. Wang et al., 2014). It was thus seen as unnecessary to completely map the pin-fins for a blockage pin-fin configuration. Of interest was the average heat transfer of the whole pin-fin. For this each pin-fin was captured from an upstream location, downstream location and from overhead. Multiple points on each surface were then averaged and the hue value extracted. This was repeated for every pin-fin. The surface temperature varied by 1-3 % across a given pin-fin. To account for this, the uncertainty for the pin-fin surface temperature was thus considered higher than the flat end-wall or perforated blockage plates at ±3.0 %. This uncertainty was also considered to account for any possible temperature bias along the pin-fin surface.

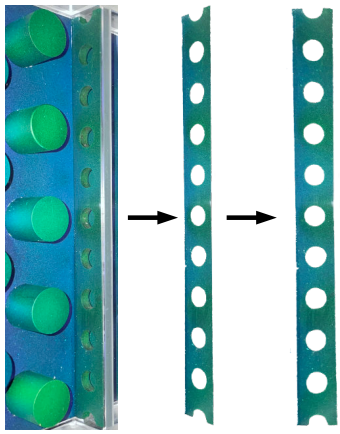

Figure 3.14. Preliminary TLC image processing approach for straightening the surfaces of the perforated blockages. (a) The raw image, (b) The isolated blockage surface, and (c) The final straightened image.

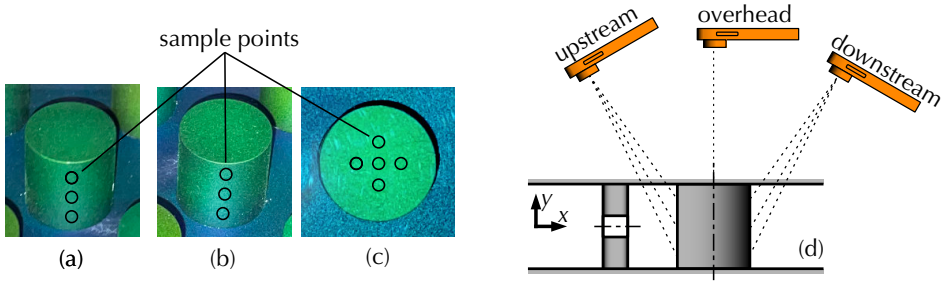

Figure 3.15. Points on TLC images of pin-fins where measurements were taken. (a) Of the upstream surface, (b) Of the downstream surface, (c) Of the top of the pin-fin from overhead, and (d) Schematic of camera positions.

3.6.4. Data reduction parameters and uncertainties for surface temperature measurements

For all surface temperature measurements, a constant heat flux was generated by a film heater. The dimensions and position of the heater is shown in the respective test setup for each study. The heat flux (q'') is estimated as:

$q''=Q_{net} / A_h$ (7)

where Q_{net} is the net heat removed by the convective flow in the channel in W, and A_h is the heating area in m^2. Q_{net} was obtained as:

$Q_{net} = Q_{input} - Q_{loss}$ (8)

where Q_{input} is the heat input in W and Q_{loss} is the heat loss in W. Q_{input} calculated from the measured input current and voltage supplied the film heater. Q_{loss} along the end-wall was calculated to be approximately 2.5% of the Q_{input} based on q''_{loss} as:

$$q''_{loss} = \frac{T_s - T_{amb}}{\frac{t_{ins}}{k_{ins}} + \frac{t_s}{k_s} + \frac{1}{h_{amb}}} \quad (9)$$

where T_s is the heated surface temperature, T_{amb} is the ambient air temperature, t_{ins} and k_{ins} is the thickness and thermal condtivity of the Teflon insulating board beneath the heater, t_s and k_s is the thickness and thermal conductivity of the end-wall surface being heated, h_{amb} is the ambient free convection heat transfer coefficient, assumed to be 5 W/m^2K. In accounting for the various other surfaces such as pin-fins and perforated blockages, the overall losses were conservatively estimated to be 5% of the Q_{input}. The resulting heat transfer between the heated surface and cooling flow was:

$$h = \frac{q''}{(T_s - T_{bulk})} \quad (10)$$

where T_{bulk} is the air temperature at a given position, calculated as:

$$T_{bulk} = T_{in} + \frac{Q_{net}}{\dot{m}C_p}\left(\frac{x_h}{L}\right) \quad (11)$$

where $\dot{m}$ is the mass flow rate through the channel in kg/s, C_p is the specific heat of the air, x_h/L is the relative distance along the length of the heater in the streamwise (x) direction. T_{bulk} was approximately 10 K higher than T_{in} by the end of the heated portion of the channel. The resultant Nusselt number based on the hydraulic diameter is calculated as:

$$Nu = \frac{hD_h}{k_{amb}} \quad (12)$$

where k_{amb} is the thermal conductivity of air in W/m/K.

The assessment of the thermal performance (equation 1) considers the ratio Nu/Nu_0. The baseline heat transfer for an empty smooth channel (Nu_0) was calculated as (Kays et al., 2005):

$$Nu_0 = 0.022Pr^{0.5}{Re_{Dh}}^{0.8} \quad (13)$$

where Pr is the Prandtl number at 0.705 at the operating conditions. This was the same equation was used by Lawson et al. (2011). As that data (as seen in Figure 2.15) would be used as a comparison case, it was deemed prudent to use the same base measure.

Using equation (6), the uncertainties associated with the surface temperature measurements were calculated as shown in Table 3.2. Note that a different heat transfer uncertainty was determined for those flat end-wall surfaces (the end-wall and perforated blockages) compared to the pin-fin surfaces.

Table 3.2. Uncertainties in surface temperature measurements.

Parameter	Uncertainty
q''	±0.37%
T_{bulk}	±0.36%
$Nu_{flat\ surface}$	±2.01%
$Nu_{pin\text{-}fin}$	*±3.83%*

4. A PIN-FIN SUBJECTED TO AN IMPINGING TUBE JET

4.1. Objective

This chapter aims to identify the flow features around a short circular pin-fin, subjected to an impinging tube jet that ejects fully developed turbulent jet flow at Re_j = 17,500 based on the circular jet diameter. The flow structures present are considered insufficiently realized or understood in prior studies. Such flow structures are prevalent in a blockage pin-fin configuration, and it is therefore considered necessary to investigate these in an isolated case.

4.2. Test setup

The test setup is shown in Figure 4.1, consisting of a straight rectangular channel with constant height (H) and width (W) along its length. The lid and side-walls of the channel were constructed from transparent Perspex. A single circular pin-fin, machined from PVC, was positioned in the centre of the channel (z/D = 0.0) with a height equal to that of the channel. A long tube (t/D_j > 10) is positioned at the mid-height (y/H = 0.5) and mid-span of the channel. Supports for the tube were positioned sufficiently far upstream of the jet exit such that they would not interfere with any end-wall flows. Air is fed through the tube by a centrifugal fan. Honeycomb was fitted inside the tube approximately half way down its length to improve the flow quality at exit.

The Reynolds number was fixed at Re_j = 17,500 (Re_D = 35,000), which falls within the range of 5000 < Re_D < 50,000, accepted to cover most of turbine applications as reported by Metzger et al. (1984).

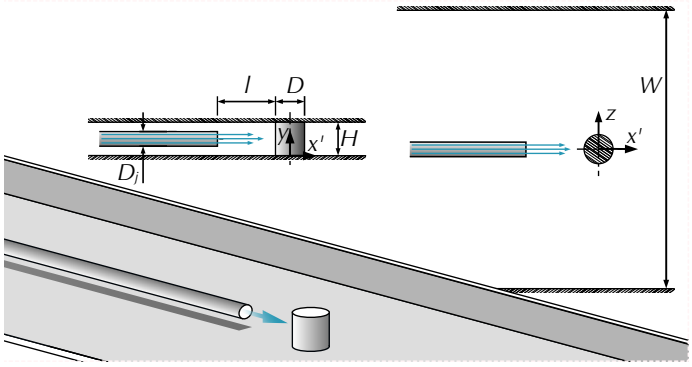

Figure 4.1. Test section schematic for consideration of a single tube jet impinging on a single pin-fin.

The rectangular test section has a width W = 0.4 m and a height H = 45 mm. The pin-fin had a diameter of D = 42 mm. This results in a pin-fin aspect ratio of H/D = 1.08. The tube internal diameter was sized to achieve a pin-to-jet diameter ratio of D/D_j = 2.0. The distance l, between the jet exit and pin-fin leading-edge, could be adjusted as necessary. The values of l used were determined based on jet characteristics to be determined later. The blockage plates, perforations, pin-fins and relative positions were machined to an accuracy of ±0.03 mm or 0.3 % of the jet diameter (D_j).

The axis *x'-y-z* was placed at the centre of the pin-fin's base. The term *x'* is used here to avoid confusion where *x* is being reserved for reference from the jet exit.

For end-wall heat transfer measurements, a film heater (A_h = 0.33 m × 0.33 m) was attached to the perspex end-wall surface with a thin foil applied. The foil ensured the ridges from the heater coils were less pronounced and that the heat was better distributed across the end-wall surface. A teflon board was fitted beneath the end-wall plate to minimize heat loss. The PVC pin-fin was replaced by a copper pin-fin of the same dimensions. This arrangement ensures that the pin-fin would conduct heat from the end-wall surface.

4.2.1. Rationale for specifications

(a) Pin-fin and jet diameter sizing

The setup used resulted in the specific ratios that warrant substantiation. A pin-fin aspect ratio was set as H/D = 1.07 where H is the channel height and D is the pin-fin diameter. This was a result of modifying an existing test rig for applications to this study. The aspect ratio, nevertheless, falls into the range purported to be applicable for trailing-edge cooling schemes ($0.5 \leq H/D \leq 4.0$ (Han et al., 2012; Lyall, 2006)). The heat transfer around of a pin-fin will be made up of heat transfer both on pin-fin surface and end-wall surface around the pin-fin. From data of Kan et al. (2014), the pin-fin surface and end-wall surface heat transfer was consistently higher than that of a conventional pin-fin array. As a starting point a similar pin-fin aspect ratio was deemed a suitable value. This same logic was applied to the ratio between pin-fin to jet diameter (D/D_j = 2.0).

Circular pin-fins (Figure 2.16(a)), instead of square or elliptical pin-fins, are here considered as a baseline shape and will be the basis of this research work. Further, these will be pin-fins with a vertical inclination and a square base (Figure 2.16(g)). Modifications such as end-wall fillets (Figure 2.16(h)) or inclined pin-fins (Figure 2.16(j)) will not be considered. The circular pin-fin is used in the majority of previous studies on conventional pin-fin arrays. Further, circular perforations in the mid-height of the blockages (Figure 2.19(a)), instead of slots or square holes, will be used for similar reasons. The use of circular pin-fins and perforations allows for a larger scope of existing literature to be referred to for validation and comparison purposes.

(b) Channel Shape

The inlet and exits of the test sections are to be inline (a straight through channel) such that the flow through the channel will not be required to undertake any turns before exiting the channel. One of the behaviours to be investigated is the curvature of the jet flows. A right-angled channel would naturally result in flow curvature as seen in the results of Kim et al. (2019) plotted in Figure 2.27(c). To isolate this curvature from any other flow curvature, it is necessary to use a straight through channel instead. This was maintained throughout the research work (in all three parts). Further, the channel height will be constant along its length – the channel will not feature a converging height towards the

exit. Channels that feature converging test sections result in very non-uniform flow fields through the pin-fin array (Effendy et al., 2019; Hwang & Lu, 2001; Hwang & Lui, 1999; Tarchi et al., 2008). Such added variation, brought on by the convergence, then further obscures the interactions and flow behaviours that require elucidation.

A right-angled channel with converging exit may be seen to better represent flow through the trailing-edge of a turbine blade as shown by the schematics in Figure 2.8. Prior studies of trailing-edge cooling schemes, however, predominantly use straight through, non-converging, channels. Their use here in this research is thus be seen as both reasonable and warranted.

4.2.2. Consideration of the distances between jet exit and pin-fin leading-edge

The centreline velocity variation for the tube jet is shown in Figure 4.2. The centreline velocity of the blockage jet begins to decay, dropping below 98% of the exit velocity (v_c/v_e < 0.98) at approximately x/D_j = 2.0. The downstream distance where v_c/v_e < 0.98 is taken as the jet potential core length of the tube jet being l_p/D_j = 4.0. Further, following the dissipation of the potential core, the centreline velocity exhibits a decay that was inversely proportional to the distance from jet exit (x/D_j). A large factor affecting jet impingement heat transfer is the distance between the target surface and jet exit or the distance relative to the length of the potential core of the jet - the distance between the jet exit and the leading edge of the pin-fin (l/D_j). There are thus three pin-fin positions that will be considered as:

(a) With the pin-fin inside the jet's potential core. This is taken as l/D_j = 2.0 and will referred to as case l_2.

(b) With the pin-fin at the tip of the potential core. This was taken as l/D_j = 4.0 and will be referred to as case l_4.

(c) With the pin-fin outside the potential core. This was taken as l/D_j = 8.0 and will be referred to as case l_8.

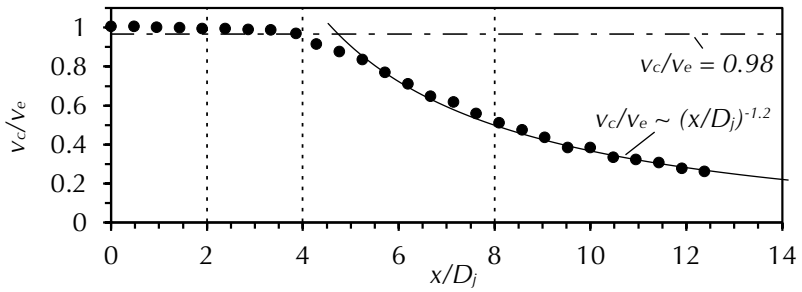

Figure 4.2. Jet centreline velocity variation with increasing distance from the exit for tube jet with Re_j = 17,500.

The large distance for the l_8 case, instead of l/D_j = 6.0, was partly selected due to the possibility of the jet having sufficiently diffused contact the end-wall upstream of the pin-fin. Figure 3.5 shows the

oil-dye patterns on the end-wall surface, without a pin-fin in place. It is seen that the end-wall surface is disrupted from approximately $x/D_j \approx 4.0$. A backflow on the end-wall (in Figure 2.26(a)) may or may not prevent this end-wall interaction. Alternatively, there then may exist an end-wall boundary layer interacting with the pin-fin, similarly to the pin-fin immersed in the uniform mainstream for in these final test cases. Given the different flow regimes impinging on the pin-fin and end-wall flows approaching the pin-fin, in each case, these three test cases should present a large enough spectrum to best consider the end-wall flow topologies for a pin-fin subjected to an impinging jet. The case of the pin-fin within the potential core (l_2) will be considered first.

4.3. Flows around pin-fin subjected to an impinging tube jet

4.3.1. Flows at the end-wall surface

The end-wall flow pattern from oil-dye visualization for $l/D_j = 2.0$ (l_2) is shown in Figure 4.3(a). At a brief glance such a pattern bears a resemblance to that of a horseshoe vortex pattern shown in Figure 2.11 and Figure 3.4. Specifically, the profile has a teardrop like shape with a brighter line of dye (annotated as the "dye line") that arcs around the pin-fin. The dye line could be mistaken as the separation point S from Figure 3.4 as it even originates from the x-axis at $x'/D = -1.25$ where S is predicted to occur for a horseshoe vortex system (Ballio et al., 1998). In Figure 3.5, however, the jet should not have diffused sufficiently to contact the end-wall upstream of the pin-fin and therefore no end-wall boundary layer flow exists. This is also noted in the end-wall surface away from the teardrop pattern featuring undisturbed dye. The mechanism required for the formation of horseshoe vortices is absent and the flow profile shown in Figure 4.3(a) cannot be attributed to horseshoe vortices.

Instead, streamlines radiate outwards from the pin-fin surface, towards the dye line. Around the leading-edge these streamlines appear to be radial, eminating from the leadinge edge as predicted as part of Figure 2.26(b). Such streamlines fan outwards until becoming tangential to the leading-edge of the pin-fin surface. Thereafter, streamlines appear to remain tangential to the pin-fin surface. Such streamlines are not overtly clear in the oil-dye pattern – especially when compared against those for a horseshoe vortex system as shown in Figure 3.4. To confirm their interpretation a PIV measurement was made at a height $y/H = 0.08$. This measurement is shown in Figure 4.3(b), compared to the oil-dye pattern. The two end-wall streamline types (radial and tangetial), as interpreted in the oil-dye patterns, are clearly seen in the PIV measurement.

The PIV data provides additional observations that could not be immediately interpreted from the oil-dye patterns. The dye line does not represent a termination in the end-wall flows or some form of separation point/line. A separation point (S) would present as streamlines of opposing vectors shown in Figure 2.11 for horseshoe vortices. A dye line in Figure 4.3 cannot then be interpreted as an indication of the extent of the end-wall flows. Instead, the oil-dye is disturbed beyond the dye line. The "flow extent," as marked in Figure 4.3(a), refers the extent, away from the surface of the pin-fin that the oil-dye is disturbed. This position correlates to a similar radial extent of the end-wall streamlines from the

PIV measurement – originating at x'/D = -1.4 at z/D = 0.0. The dye line then merely represents an accumulation of dye particles that have been redistributed from near the pin-fin surface. It does, however, serve as an approximate indication of the end-wall flow profile.

Fluid from the surrounding region, where the dye remains undisturbed, is entrained towards the end-wall streamlines. This flow entrainment is of a very low velocity flow which is why the oil-dye remains undisturbed. Upon interacting with the end-wall streamlines, the streamlines are made to curve slightly near their extents. There then forms a flow along the flow extent (a "periphery flow"), conformal to the pin-fin shape. This flow is predominantly in the downstream (positive x) direction, directing the periphery of the end-wall streamlines downstream. There is, however, a region along the leading-edge periphery where the flow is directed upstream and towards the centre of the channel. It is unclear why this occurs and its existence is only apparent in the oil-dye by the extra region of disturbed dye (marked as position A in Figure 4.3(a)). Besides the streamline curvature near the flow extent, both the radial and tangential end-wall streamlines are predominantly straight, exhibiting very little curvature with the notable exception being the tangential streamlines directly behind the pin-fin.

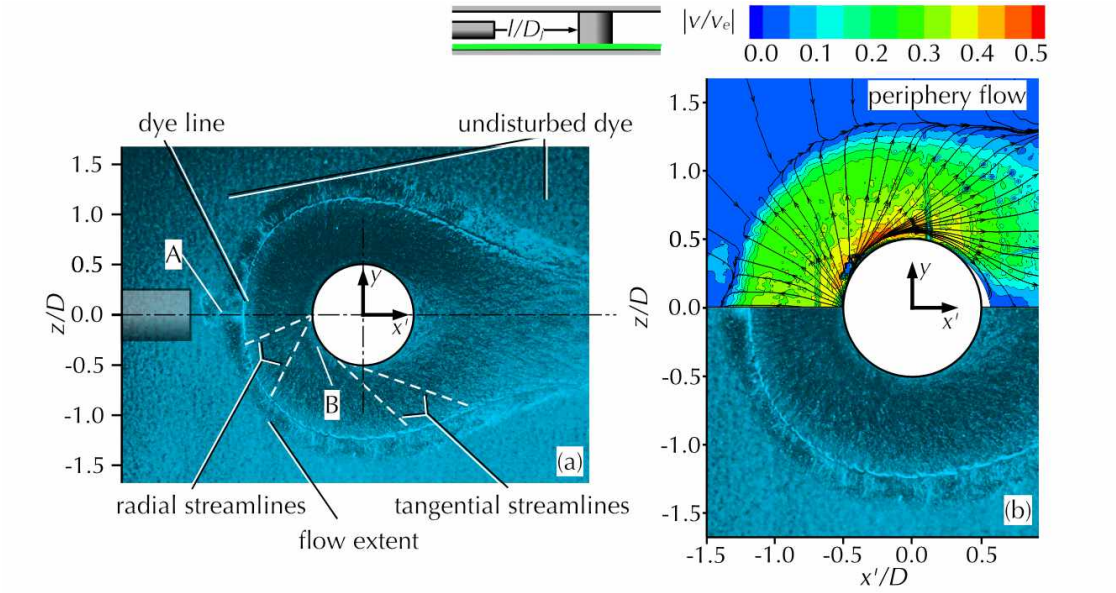

Figure 4.3. End-wall flows around a short circular pin-fin subjected to an impinging jet for Re_j = 17,500 (Re_D = 35,000). (a) Oil-dye flow visualization and (b) Combination of PIV velocity contours (top) and corresponding oil-dye flow visualization (bottom).

Further observations and explanation for the noted flow patterns require consideration of the flow fields away from the end-wall surface. First, the flows in the vertical (x-y) plane will be considered next.

4.3.2. Flows in the vertical plane

The velocity contours in the x-y plane, from PIV measurements upstream of the pin-fin, are shown in Figure 4.4. A clear correlation of the measured streamlines in Figure 4.4(a) to those predicted

from Figure 2.26(a) can be made. Specifically, the jet flow stagnates on the pin-fin surface and then is redirected towards the end-wall surfaces. After which, it stagnates and is redirected upstream as a backflow. The counteracting flow directions of the backflow, on the end-wall surface, and the core jet flow incite a region of circulating flow in the vertical plane – similar to that in Figure 2.17. This will hereon be referred to as a circulating region as per the convention established earlier in Figure 2.17(b). This was chosen so as to avoid confusion between this circulating, vortical flow and those of a horseshoe vortex system.

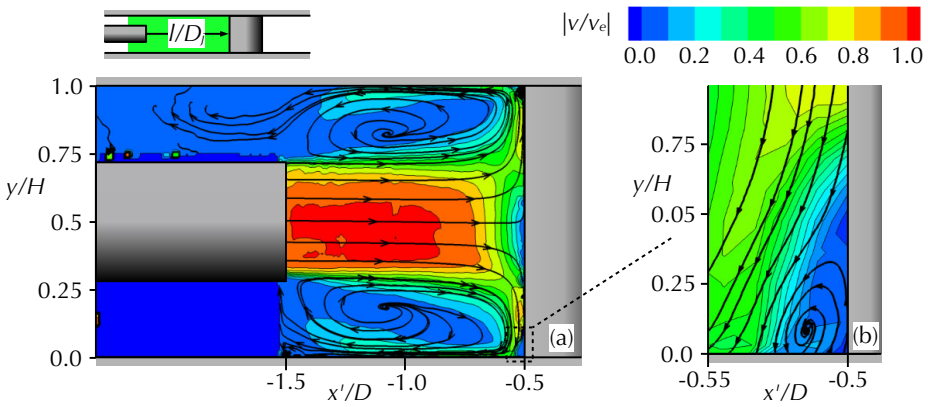

Figure 4.4. Flow fields in the *x-y* plane at z/D_j = 0.0 for Re_j = 17,500 (Re_D = 35,000). (a) Velocity contours from PIV and (b) Closeup of the velocity contours from PIV at the corner between the lower end-wall and pin-fin base.

Another vortical flow occurs at the junction between the pin-fin base and the end-wall surface. This vortical flow, a corner vortex, was measured in Figure 4.4(b). The flow is analogous to the corner vortex V_0' in Figure 2.11. It arises from the flow on the pin-fin surface, encountering an adverse pressure gradient from the end-wall surface. This causes the surface flow to separate just before the end-wall and form a vortical flow. The flow is considered "trapped" in that it does not entrain in fresh flow. Given that the surface flow is not just constrained to the vertical plane (at z/D = 0.0), it should be expected that the corner vortex may wrap around the pin-fin surface. This may explain the band of brighter dye on the end-wall around the pin-fin surface, marked as B in Figure 4.3(a). As the flow is trapped in this region, the dye particles are not dispersed outwards, away from the pin-fin. There then remains a larger accumulation of dye and the region appears brighter. In the PIV velocity contours of Figure 4.3(b), the tangetial streamlines are seen to be clearly separated from the outer side of the pin-fin surface (near x'/D = 0.0). Along the leading edge of the pin-fin such a separation is not visible in Figure 4.3(b) with the streamlines radiating directly from the pin-fin surface. This makes sense considering the PIV velocity contours in Figure 4.3(b) are taken at a height of y/H = 0.08, above point where separation from the pin-fin occurred in Figure 4.4(b). The appearance of the separation away from the leading edge in Figure 4.3(b) does imply that the height of the corner vortex is not constant.

The two end-wall streamline types, radial and tangential, as observed in Figure 4.3 can now be explained using Figure 4.5. Following the stagnation of the jet flow on the pin-fin surface, a surface flow forms on pin-fin surface. A portion of the surface flow then moves towards the end-wall. As it approaches the end-wall it will experience an adverse pressure gradient and separate from the pin-fin surface before attaching to the end-wall. The surface flows can be broken into two types: those surface flows directly towards the end-wall and without a flow component tangential to the pin-fin surface and those surface flows with a tangential component. These are represented in Figure 4.5(a) and (b) respectively. The direct surface flow (Figure 4.5(a)) is responsible for the radial streamlines. As it stagnates on the end-wall it forms a nodal point of attachment from which end-wall flows radiating outwards in multiple directions. The tangential surface flows (Figure 4.5(a)) are responsible for the tangential streamlines. Following stagnation, the tangential flow vector is maintained and the end-wall flow continues to be tangential to the pin-fin surface.

An extension of this is that if there exists no surface flow on the pin-fin then there can be no end-wall flow in that region. From the near end-wall PIV velocity contours (Figure 4.3(b: top)) the streamlines appear to stop radiating from the pin-fin surface at approximately $x'/D = 0.25$. There is still a measure of flow in the wake, however, as noted by the oil-dye patterns being disturbed in this region. But, this is due to a large amount of streamline curvature in this region, the tangential streamlines not being straight as previously noted. It would thus appear that that there are no surface flows for $x'/D > 0.25$. A more complete consideration of the flow, interacting with the pin-fin, away from the end-wall is thus necessary.

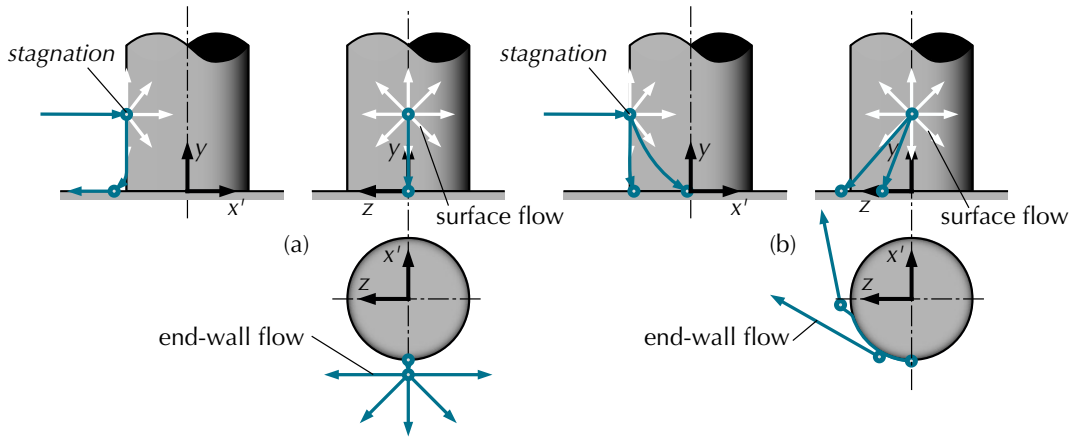

Figure 4.5. Flow field schematics for the development of the end-wall jet stream-lines: (a) For radial end-wall jets and (b) For tangential end-wall jets.

4.3.3. Flows away from the end-wall

The velocity contours from PIV in the *x*-*z* plane are shown in Figure 4.6 at (a) $y/H = 0.5$ and (b) $y/H = 0.25$. Especially at $y/H = 0.25$, there is no disernable flow for $x'/D < -1.5$ as the jet is insufficiently diffused by that position – this can also be seen in Figure 4.4(a). Along the surface of pin-fin, a higher

flow velocity around the outer leading-edge exists at both $y/H = 0.25$ and $y/H = 0.5$. This arises as the flow accelerates along the pin-fin surface, following stagnation. The acceleration appears lessened at $y/H = 0.25$ but the flow has significant component in the y-axis (out of plane of the measurement). A higher flow velocity is correspondingly noted for $y/H = 0.08$ (Figure 4.3(b: top)). Due to the higher end-wall velocity in this region, those tangential streamlines extend further from the pin-fin surface than the radial streamlines. The extent of the end-wall streamlines is thus dependant on the velocity magnitude of the surface flow. Further, the surface flow separates from the pin-fin at a similar position (marked as S_w) at $y/H = 0.25$ and 0.5. The end-wall streamlines stop radiating from the pin-fin surface at a similar position on the end-wall (Figure 4.3(b: top)). There is then a direct correlation between the behaviour of the end-wall streamlines and the flow at the mid-height of the channel (where the jet core interacts with the pin-fin).

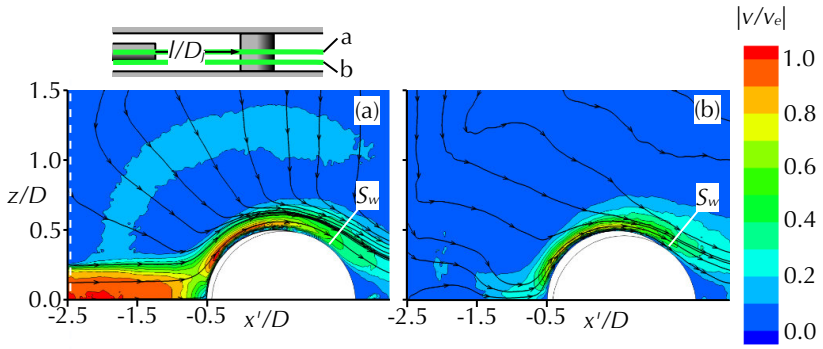

Figure 4.6. Flow features from PIV in the *x-z* plane for $Re_j = 17{,}500$ ($Re_D = 35{,}000$). (a) PIV at the mid-height of the channel ($y/H = 0.5$), (b) PIV at the quarter height of the channel ($y/H = 0.25$).

There also exists a band of relatively higher flow velocity arcing around the pin-fin, at the mid height, originating from $x'/D < -1.75$ in Figure 4.6(a). No such band occurs at the quarter height of the channel (Figure 4.6(b)). The increased velocity is attributed to a circulating region, observed in the vertical plane (Figure 4.4(a)). In the vertical plane the circulating is formed by the counteracting flows of the backflow and jet mainstream. Away of the vertical plane there continues to exist the counteracting flow. Specifically from the end-wall streamlines and the flow being entrained towards pin-fin surface (as visible in Figure 4.6(a)). The vortical flow is not evident at the quarter height (Figure 4.6(b)) as the circulating flow, at that height, is predominently vertical (Figure 4.4). It is thus out of plane for the PIV measurements in Figure 4.6(b). The band of higher velocity thus indicates the circulating region is not constrained to the central axis of the pin-fin and, like a horseshoe vortex system, wraps around the pin-fin in a horseshoe shape. Unlike a horseshoe vortex system, however, the circulating region extends to the mid-height of the pin-fin.

The flow topology around a pin-fin subjected to an impinging jet flow can thus be seen to be wholly distinct from that of a pin-fin subjected to a uniform-like flow (featuring horseshoe vortex

flows). By extension, the end-wall heat transfer behaviour of such flows (from an impinging jet) may differ from those of horseshoe vortices. It is thus necessary to now consider the cooling behaviour of such flows.

4.3.4. Heat transfer on the end-wall surface

The end-wall heat transfer (*Nu*) contours from infrared thermography are shown in Figure 4.7(a: top). The corresponding flow schematic in Figure 4.7(a: bottom) was derived from Figure 4.3. The heat transfer contours are similar to that measured by Kan et al. (2014), shown in Figure 2.24(a). But the contours also bear a strong resemblance to those for a pin-fin subjected to a uniform-like flow (featuring horseshoe vortices at the end-wall) based on measurements by Chyu and Natarajan (1996). The variation of the heat transfer along the radial length (*r*) from the pin-fin surface is shown for multiple inclinations (Figure 4.7(b)). These inclinations consider the variation in heat transfer for various radial and tangential end-wall streamlines. The variations in heat transfer are also very similar to that for a turbulent horseshoe vortex system (Lyall et al., 2011; Schekman & Kim, 2017). Consideration of end-wall heat transfer alone could easily lead to the flow being misattributed to that of horseshoe vortex flows. It has, however, already been established that horseshoe vortices are not present.

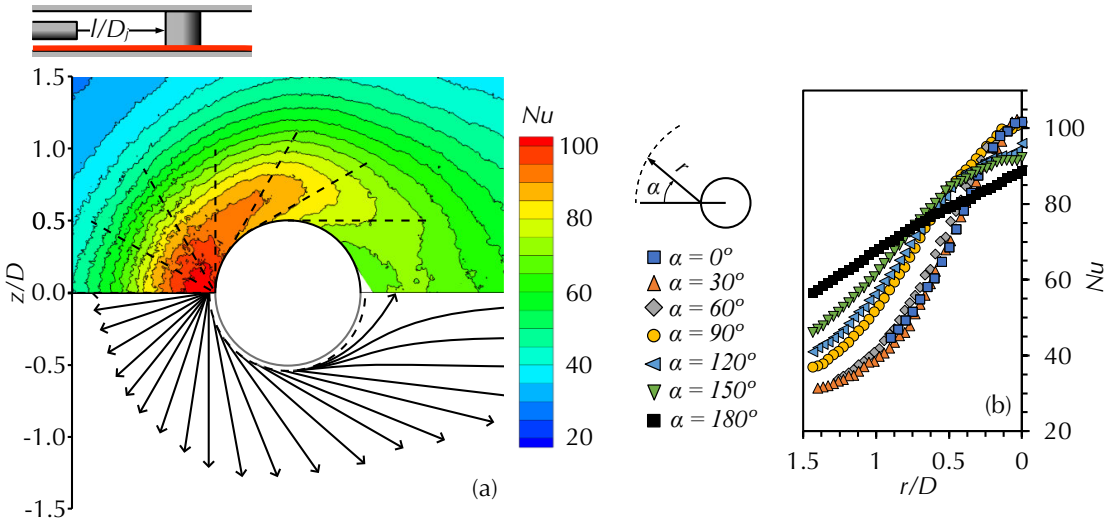

Figure 4.7. End-wall heat transfer for for a short pin-fin subjected to a jet impingement at $l/D_j = 2.0$ from the pin-fin leading edge for $Re_D = 3.5\times10^4$. (a) Temperature contour from infrared thermography on the end-wall surface (top) with corresponding end-wall flow pattern and (b) Nusselt number distribution in the plane of symmetry.

The variation in heat transfer along the *r* vector is largely the same for all radial streamlines ($0^o \leq \alpha < 90^o$). There is also a very slight region of constant heat transfer near the leading-edge of the pin-fin for radial type streamlines. Thereafter, the heat transfer decreases monotonically. Considering the

radial streamlines are sourced from the same nodal point of attachment (Figure 4.5(a)), the similarity in heat transfer variation is expected. There is then a transition from the 90º vector onwards. The 90º inclination marks the approximate transition from radial to tangential streamlines. For α = 90º the heat transfer starts off at a similar value, being sourced from the same attachment point but its monotonic decrease is to a lesser degree and by $r/D > 0.5$, the end-wall heat transfer is higher. For subsequent (tangential) streamlines (α = 120º and 150º), the heat transfer at the surface of the pin-fin is lower but from approximately $r/D > 0.3$, the end-wall heat transfer is consistently higher than the radial streamlines. This corresponds to those tangential end-wall streamlines having a higher flow velocity as per the PIV velocity contours in Figure 4.3(b). For α = 180º, the heat transfer near the pin-fin surface is lower still but the rate of decrease in end-wall heat transfer is likewise lower along the r vector. Interestingly the average end-wall heat transfer along each vector (radial and tangential) is approximately the same at Nu ≈ 79 ±6% for $r/D \leq 1.0$. This implies that the average end-wall heat transfer around the pin-fin is approximately constant.

So far only the l_2 case has been considered. A further understanding of the thermofluidic behaviour for a pin-fin subjected to an impinging jet can be obtained by considering the effect of increasing the distance l/D_j for cases l_4 and l_8.

4.4. Effect of the jet exit-to-pin-fin leading-edge distance

The end-wall flows around a pin-fin subjected to an impinging jet can be directly correlated to the flows away from the end-wall. This section considers the effect of the jet exit-to-pin-fin leading-edge distance, l/D_j, on flows in the mid-height and symmetry planes. Following from this, the effect of l/D_j on both the end-wall flow and heat transfer distributions will be considered.

4.4.1.Flows away from the end-wall

The velocity contours in the mid-height of the channel are shown in Figure 4.8(a-c) for the three distances l/D_j = 2.0, 4.0, and 8.0 (denoted as l_2, l_4 and l_8 respectively). The velocity contours at the quarter-height are shown in Figure 4.9(a-c) for the same three distances. For l_4, the velocity contours are largely similar compared to l_2 at both heights. Similarities include the band of higher velocity arcing around the pin-fin, the surface flow acceleration around the outer leading-edge of the pin-fin and a similar position where the flow separates from the pin-fin (S_w). For l_4, however, the band of higher flow velocity also appears in the quarter-height plane for a short distance.

With the pin-fin placed well outside of the potential core (l_8), however, there is a marked difference in the flow field interacting with the pin-fin. The jet flow has diffused substantially before impinging on the pin-fin surface and the separation point (S_w) occurs much earlier compared to the l_2 and l_4 cases. Notably, however there is a still a flow acceleration on the pin-fin surface at l_8, albeit to a lesser degree. The relative similarities and differences for the mid- and quarter-heights flows are more

clearly seen by considering the distribution of the flow velocity magnitudes and flow directions at x'/D = 0.75 – just preceding jet impingement. These are shown in Figure 4.10.

Comparing l_2 and l_4, the velocity magnitude distribution at the mid-height is very similar (Figure 4.10(a)). The jet has diffused slightly more in the spanwise (z) direction for l_4, considering where the velocity magnitude reaches approximately zero. For l_2 the flow width is $z/D_j \approx \pm 0.35$ while it is $z/D_j \approx \pm 0.45$ for l_4. Considering the larger distance between the jet exit and pin-fin leading edge, this increased diffusion is expected. The diffusion is further evident by the higher velocity magnitude at the quarter height (Figure 4.10(b)) for l_4 – as well as in comparisons of Figure 4.9(a-b) with there being a non-zero velocity magnitude for $z/D_j < 1.5$. At the quarter height, the velocity magnitude is significantly lower than at the mid-height (y/H = 0.5) for both l_2 and l_4. This is in part due to the flow having a large component in the y-direction (being out of plane of the PIV measurement).

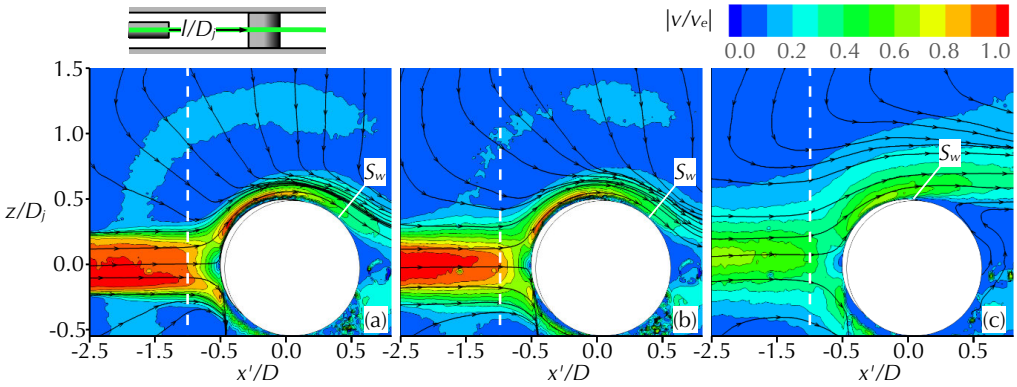

Figure 4.8. Velocity contours from PIV in the x-z plane at the mid-height of the channel (y/H = 0.5) for Re_j = 17,500 (ReD = 35,000). (a) For l/D_j = 2.0, (b) For l/D_j = 4.0, and (c) For l/D_j = 8.0.

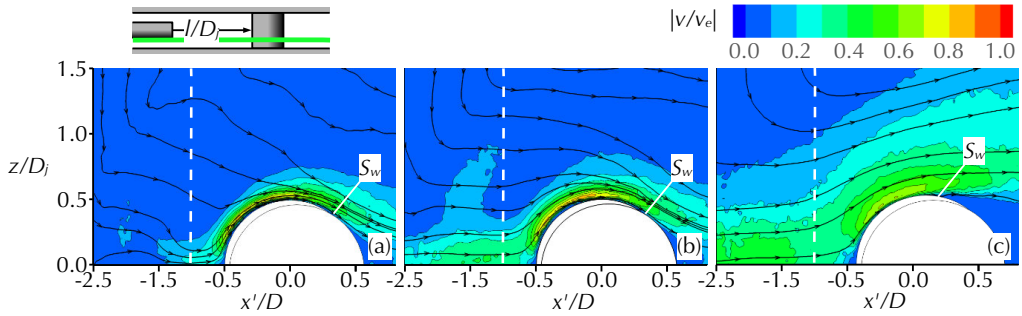

Figure 4.9. Velocity contours from PIV in the x-z plane at y/H = 0.25) for Re_j = 17,500 (ReD = 35,000). (a) For l/D_j = 2.0, (b) For l/D_j = 4.0, and (c) For l/D_j = 8.0.

For both cases in the mid-height, the flow direction (Figure 4.10(c)) is near zero (±4º) over the width of the jets (z/D ≈ ±0.35 for l_2 and z/D ≈ ±0.45 for l_4). Outside of those widths, there is a rapid increase in flow direction. The large flow directions are from the flows being entrained towards the jet and pin-fin surface flow. At the quarter height (Figure 4.10(d)) there is a larger difference between the

l_2 and l_4 cases for flow direction. Of interest is the near constant flow direction, along the spanwise direction for the l_4 case. As also seen in Figure 4.9(b), the majority of the streamlines appear to have a vector aligned with the positive x direction. While there is some flow entrainment towards the jet seen in periphery of Figure 4.9(b), the flow is otherwise seemingly flowing downstream. This is also the case of l_2 (Figure 4.9(a)), but to a lesser degree.

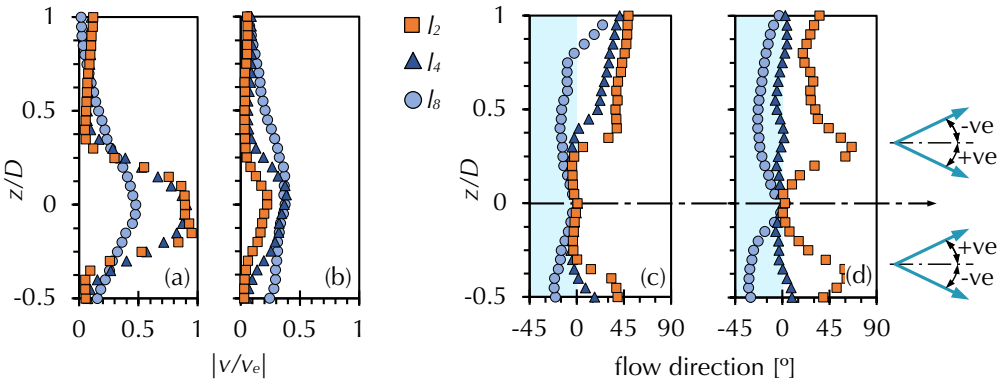

Figure 4.10. Flow distributions along the z-axis at x'/D = -0.75 for the l_2, l_4 and l_8 cases for Re_j = 17,500 (ReD = 35,000). (a) Velocity magnitude at y/H = 0.5, (b) Velocity magnitude at y/H = 0.25, (c) flow directions at y/H = 0.5, and (d) Flow directions at y/H = 0.25.

For l_8 (l/D_j = 8.0) the velocity magnitude and flow direction distributions vary significantly compared to those for l_2 and l_4 (Figure 4.10). In the mid-height of the channel the velocity magnitude is almost half that of l_2 and l_4 and the jet has diffused beyond z/D = ±0.5 – the jet width is wider than the pin-fin diameter preceding impingement. Only a portion of the jet flow will therefore be interacting with the pin-fin. The velocity magnitude does not significantly decrease by the quarter height, unlike l_2 and l_4. This indicates a more even distribution of flow along the height (H) of the channel in the y-axis. The flow direction distribution is also distinctly negative over the full diameter of the pin-fin (z/D = ±0.5) at both the mid-height and quarter heights of the channel – the flow direction is away from the jet axis (z/D = 0.0). The lower velocity magnitudes for l_8 coupled with the flow directions way predominantly away from the pin-fin are likely to result in lower end-wall heat transfer values.

4.4.2. Flows in the vertical plane

The velocity contours in the vertical plane are shown in Figure 4.11 for cases l_2(a), l_4(b) and l_8(c). Again, there are similarities between velocity contours of l_2 and l_4. Both feature a circulating region, centred at approximately x'/D = -1.5. The circulating region is smaller for l_4, however, being between $0 < y/H < 0.25$. This is also noted in the velocity contours in the mid-height plane (Figure 4.8) and quarter-height plane (Figure 4.9). For l_2, the circulating region arced around the pin-fin and was only noted in the mid-height of the channel by the band of higher velocity. At the quarter height (y/H = 0.25), the velocity vectors were near vertical and thus not noted in the velocity contours (Figure 4.9(a)). For

l_4, however, the circulating region is constrained $y/H < 0.25$ and its presence is thus seen in Figure 4.9(b) by the short arc of relatively higher velocity. At the mid-height the presence of the circulating region appears diminished at least initially. By $x'/D = 0.0$, however, the band of higher velocity is similar between l_2 and l_4 in the mid-height of the channel (Figure 4.8(a-b)). This implies that the circulating region increases in height as it arcs around the pin-fin for l_4. The similarities between the l_2 and l_4 cases are further noted in the velocity magnitude distributions at $x'/D = -1.0$ (Figure 4.12(a)). The flow direction distributions are almost complete opposites but this is attributed to the differences in circulating region. Otherwise the flow direction is of similar magnitudes for both l_2 and l_4 at corresponding y/H positions.

The l_8 case is distinct from the other two. Notably the jet has sufficiently diffused to contact the end-wall before interacting with the pin-fin. For the l_2 and l_4 cases the U component velocity (aligned with the x-axis) is negative near the end-wall (Figure 4.12(a)), implying a backflow. For l_8, however, the U component velocity is consistently positive, implying that there is almost no discernible backflow and instead there is a potential end-wall boundary layer approaching the pin-fin. To clarify, there has to be a very small backflow beneath the vortical flow centred at $x'/D = -0.65$. Without this backflow the vortical flow would not be able to form. But this backflow is not visible in the velocity distribution of Figure 4.12(a) and it is considered distinct from that noted in l_2 and l_4. Notably it does not prevent the jet from contacting the end-wall. As per Figure 3.5, the jet is expected to contact the end-wall at x/Dj = 4.0. For $l/D_j = 4.0$ (l_4) this would theoretically mean the jet flow would contact the end-wall at the base of the pin-fin. It does not do so, however, as is clearly seen in Figure 4.11(b). This is due to the backflow and resulting circulating region. For l_8 the contact point of x/Dj = 4.0 is at $x'/D = -2.5$ or half the distance between jet exit and pin-fin leading edge. The backflow would need to extend at least that far upstream in order for it to have prevented the jet contacting the end-wall. Alternatively, the pin-fin aspect ratio (H/D) would need to be larger such that the jet would have to diffuse further to contact the end-wall. Regardless, considering the lower flow velocities interacting with the pin-fin at l_8, however, it is likely that the thermal performance of such a large distance would be unsuitable.

Due to the jet contacting the end-wall in l_8, there is much smaller variation in the velocity distribution along the y-axis compared to l_2 and l_4, as per Figure 4.12(a). Further, the flow direction distribution (Figure 4.12(b)) is almost constant for l_8 across the height of the channel, implying predominantly parallel flow along the height of the channel (as is also noted in Figure 4.11(c)). The mechanism for the formation of horseshoe vortices is thus understood to be present for l_8. The vortical flow at $x'/D = -0.65$ in Figure 4.11(c) is therefore not a circulating region, as is present in Figure 4.11(a-b) but instead it is likely a small horseshoe vortex. Considering the low flow velocity in the region it would be equivalent to a low Reynolds number horseshoe vortex system and only a single vortex pair is expected to exist – specifically, V_1 and a small corner vortex. A corner vortex was not as clearly visible for l_4 or l_8 as it was for l_2 (Figure 4.4(b)) but flow towards the pin-fin can be noted in Figure 4.11(d-e). Such a flow direction would incite some form of vortical flow in the corner even if the vortex

was not noted directly in the streamlines.

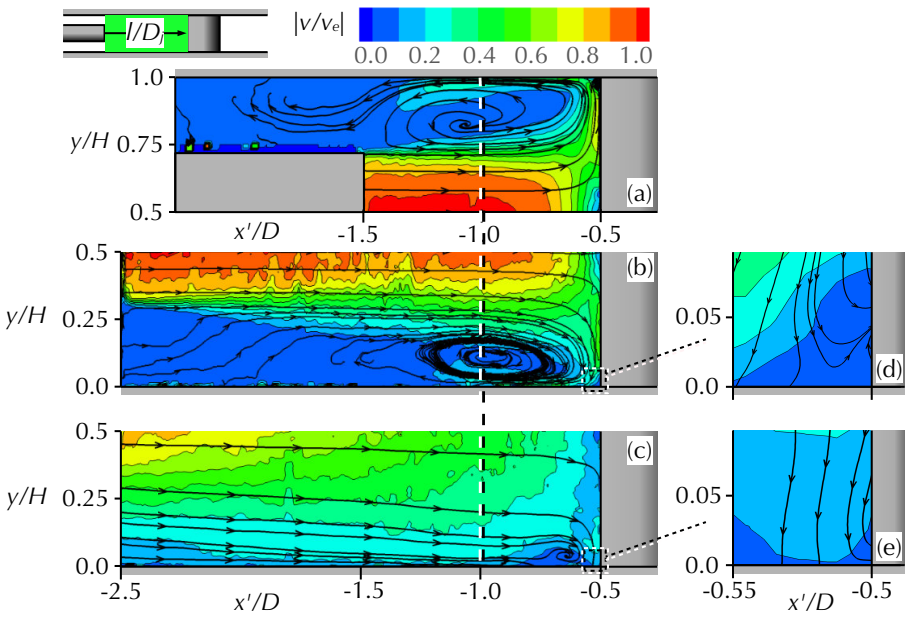

Figure 4.11. Velocity contours from PIV in the vertical (*x-y)* plane at z/D_j = 0.0 for Re_j = 17,500 (Re_D = 35,000). (a) For l/D_j = 2.0, (b) For l/D_j = 4.0, (c) For l/D_j = 8.0, (d) closeup of pin-fin and end-wall interface for l/D_j = 4.0, and (e) Closeup of pin-fin and end-wall interface for l/D_j = 8.0.

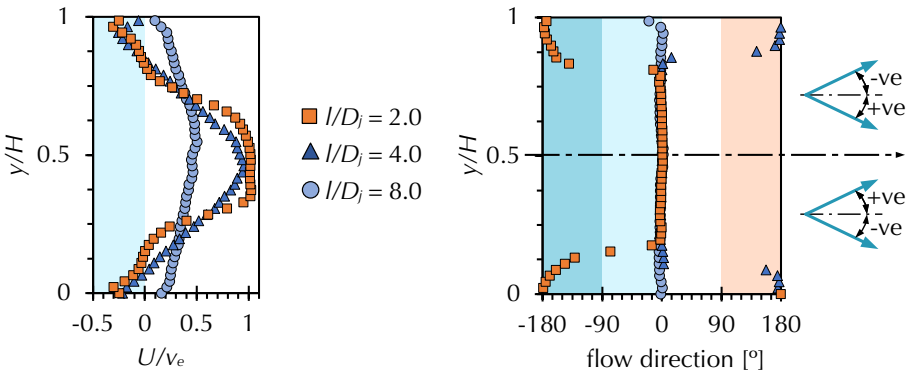

Figure 4.12. Flow distributions along the *y*-axis at *x'/D* = -1.0 for the l_2, l_4 and l_8 cases for Re_j = 17,500 (Re_D = 35,000). (a) Velocity magnitude distributions and (b) Flow direction distributions.

4.4.3. Flows at the end-wall surface

The velocity contours from PIV and end-wall flow patterns from oil-dye visualization are shown in Figure 4.13 for l_2(a), l_4(b) and l_8(c). The previously discussed similarities in the flow fields at the mid-height, quarter-height and vertical plane for l_2 and l_4 result in the end-wall flow patterns also being similar, as should be expected. Notable similarities include the presence of radial and tangential streamlines, a dye line, periphery flow and a separation between the pin-fin surface and the tangential

streamlines. The profile created by the dye line is subtly different due to the radial streamlines being shorter for l_4. At z/D = 0.0, the flow extent is to x'/D = -1.1 for l_4 and x'/D = -1.4 for l_2. This was also noted in the flows in the vertical plane (Figure 4.11(a-b) with the backflow extending a shorter distance from the pin-fin leading edge for l_4 compared to l_2. The tangential streamlines, however, are of a similar length for l_2 and l_4. Further, the point where the end-wall flows stop radiating from the pin-fin surface is similar across Figure 4.13(a,b). This should be expected considering the separation points (S_w) in the mid-and quarter-height planes were also similar for l_2 and l_4. This further emphasizes that the end-wall flows can be directly correlated with those from the mid-height plane.

The end-wall flows for l_8 (Figure 4.13(c)) are distinctly different to l_2 and l_4. Specifically, there is a clear separation line (S) in the streamlines originating at x'/D = 0.7. Such a line is associated with horseshoe vortex flow topologies (Figure 2.11). This confirms that there exists a horseshoe vortex system for l_8 and the vortex noted in Figure 4.11(c) is the V_1 vortex (as per Figure 2.11).

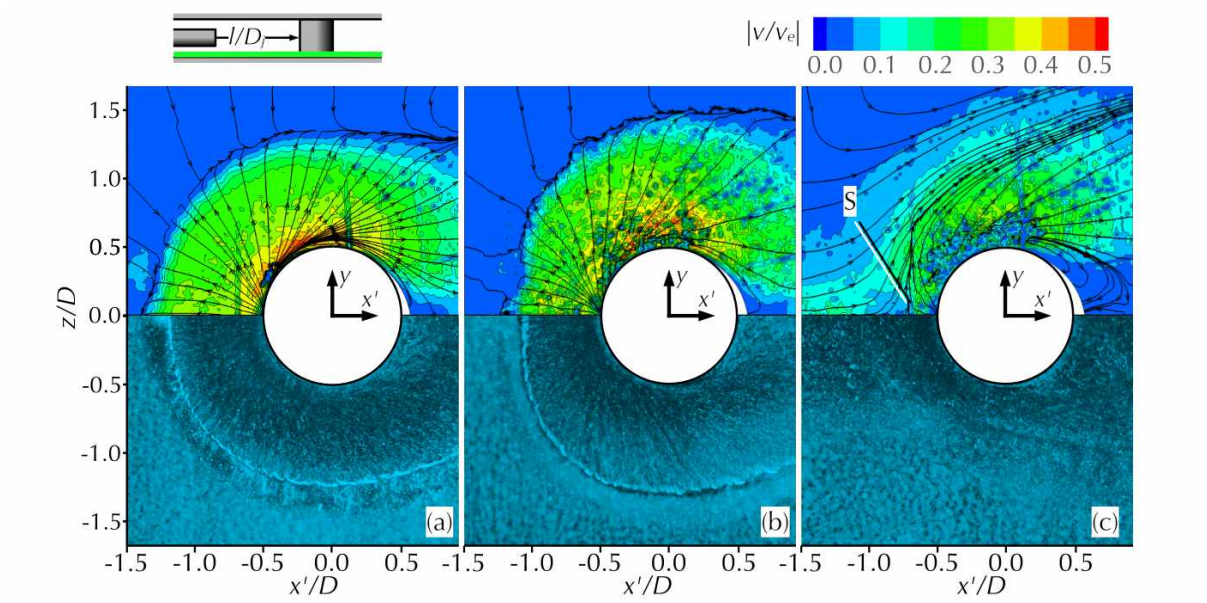

Figure 4.13. End-wall flow field with velocity contours from PIV (top) and flow visualization from oil-dye (bottom) for Re_j = 17,500 (Re_D = 35,000). (a) For l/D_j = 2.0, (b) For l/D_j = 4.0, and (c) For l/D_j = 8.0.

4.4.4. Heat transfer on the end-wall surface

The corresponding end-wall heat transfer contours and matching flow topologies (derived from those in Figure 4.13) are shown in Figure 4.14. The heat transfer contours for (a) l_2 and (b) l_4 share similarities. This is expected considering that the end-wall surface, in both cases, is exposed to a similar flow field (featuring radial and tangential streamlines). However, a notably lower end-wall heat transfer near leading-edge of the pin-fin for l_4 is noted. The heat transfer contours for l_8 are understood to more closely resemble those for a low Reynolds number equivalent horseshoe vortex system rather than the

contours of l_2 and l_4. Unlike the contours for a horseshoe vortex system, on the other hand, the contours in l_8 are more triangular. With a conventional horseshoe vortex system, the entirety of the end-wall surface experiences an end-wall boundary layer flow. As seen in Figure 4.13(c), however, a region of the end-wall that does not have any surface flow exists. While the l_8 case thus exhibits horseshoe vortex like features, they are not exactly the same.

Overall the l_2 case experiences the highest end-wall heat transfer. Considering a region from the pin-fin surface 1D (the full extent of the measurement window shown in Figure 4.14), the end-wall heat transfer is $Nu \approx 79 \pm 6\%$. For l_4 this decreases to $Nu \approx 69 \pm 7\%$. For l_8 the end-wall heat transfer is further decreased to $Nu \approx 61 \pm 8\%$. It should then be considered that shorter l/D_j distances are preferable. Further, allowing the jet flow to contact the end-wall upstream of the pin-fin (as for l_8), does not result in beneficial end-wall heat transfer and should be avoided in practice.

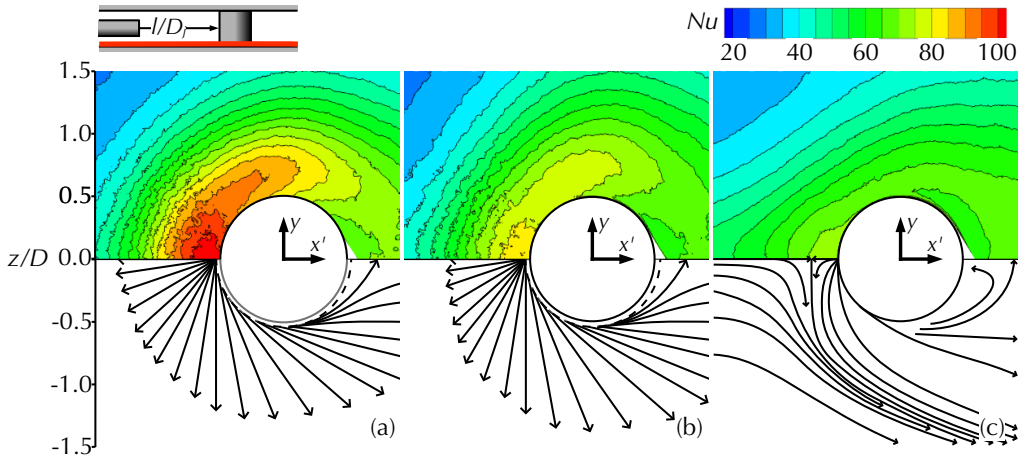

Figure 4.14. End-wall heat transfer for for a short pin-fin subjected to a jet impingement at l/D_j=2.0 from the pin-fin leading edge for Re_j = 17,500 (Re_D = 35,000). (a) For l/D_j = 2.0, (b) For l/D_j = 4.0, and (c) For l/D_j = 8.0.

4.5. Summary

When a pin-fin is subjected to an impinging jet, flow features and heat transfer variations are wholly new and not identified prior to this work. These flow features are summarised in Figure 4.15 and will here on be referred to as "jet-pin" flows. While some of these features can be mistaken to represent a horseshoe vortex system, they are, however, distinct.

On the end-wall, two distinct streamline types: radial and tangential exist. Radial streamlines originate from a nodal point of attachment just upstream of the pin-fin leading-edge and radiate outwards at inclinations up to approximately 90º from the x-axis. Away from the pin-fin leading-edge, the streamlines radiate from the pin-fin surface tangential to its surface. The end-wall flows are initially sourced from the jet flows interacting with the pin-fin. Flows in the mid-height of the pin-fin, in the x-z plane, directly correlate to those flows on the end-wall. There exist higher flow velocities on the pin-

fin surface as the flow accelerates following stagnation and thus there is a corresponding higher end-wall flow velocity. Further, where the flow separates from the pin-fin surface at the mid-height, streamlines cease radiating from the pin-fin surface at similar position at the end-wall.

The radial and tangential streamlines do not directly radiate from the pin-fin surface, being slightly away from it. This is due to a corner vortex that forms due to the pin-fin surface flow separating preceding impingement on the end-wall surface. Also, there exists a low velocity flow at the periphery of the end-wall streamlines that have flow perpendicular to the streamlines. This periphery flow is formed from the interaction between the end-wall streamlines and the surrounding end-wall fluid being entrained towards the pin-fin. It appears to predominantly have a downstream flow component.

Radial streamlines exhibit a similar heat transfer along their length, due to being sourced from the same attachment point. There can be a variation in heat transfer between tangential streamlines. All streamlines exhibit a similar trend in heat transfer variation, decreasing monotonically from the pin-fin surface. Radial streamlines typically have a higher heat transfer initially but by r/D = 0.5 from the surface, the tangential streamlines have a higher heat transfer. The radial streamlines extended from the pin-fin approximately r/D = 1.0 from the leading-edge. Tangential streamlines extend further due to a local higher velocity on the pin-fin surface in the vicinity. This higher velocity arises from the pin-fin surface flows accelerating from the stagnation point on the pin-fin surface. Over a radial distance of r/D = 1.0 from the pin-fin surface, the average end-wall heat transfer around a pin-fin with jet-pin flows is relatively constant within 6-7%.

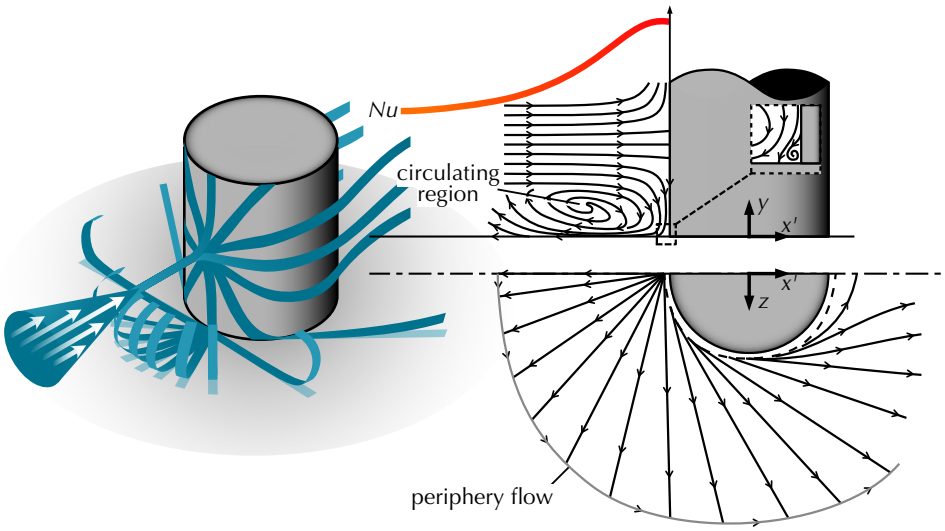

Figure 4.15. Schematics of flow topologies in the vertical (x'-y) plane and on the end-wall surface, and corresponding end-wall heat transfer distribution for a pin-fin subjected to an impinging jet.

There exists counteracting action between the flows at the end-wall and mid-height plane. At the end-wall, flows radiate outwards from the pin-fin surface but at the mid-height flow is entrained towards the pin-fin surface from the surrounding stationary air. The counteracting flows incite a circulating

region that wraps around the pin-fin, similar to (but distinct from) a horseshoe vortex. This circulating region can cause the end-wall streamlines to dissipate more rapidly, leading to lower overall heat transfer at the end-wall.

If a sufficient distance between the jet exit and pin-fin leading-edge is ensured, the jet may diffuse and contact the end-wall upstream of the pin-fin. Flow features similar to that of a low Reynolds number horseshoe vortex system would be achieved. Common features include separation line and vortices. The end-wall heat transfer is consistently lower there, compared to an end-wall where the jet has not contacted the end-wall before interacting with the pin-fin.

Two further parameters require consideration before investigating a full blockage pin-fin configuration. First is the consideration of perforated blockages. In this part, the jet was formed by way of a tube jet, so as to isolate any effects of end-wall flows interacting with the blockage surface upstream. The perforated blockage will also result in an orifice-like (blockage) jet. While this should not fundamentally alter the behaviour represented in Figure 4.15, the overall effect is unclear and warrants investigation. Secondly, an interaction of the end-wall flows with those from neighbouring pin-fins in a jet-pin system is expected. In a horseshoe vortex system, the end-wall flows are relatively conformal (as per Figure 2.13). With jet-pin flows, the end-wall streamlines radiate outwards and those from neighbouring pin-fins will have opposing vectors. There is likely to be a region of flow interaction between the pin-fins, more distinct than that between pin-fins exposed to a uniform-like flow.

5. EFFECTS OF PERFORATED BLOCKAGES AND NEIGHBOURING PIN-FINS

5.1. Objectives

This chapter aims to determine what effect the presence of the perforated blockages has on jet-pin flows and how such flow fields interact when multiple pin-fins are present. All this is aimed towards concluding on the primary objective of determining what factors need to be considered for a blockage pin-fin configuration to have a more optimal performance than purported in previous studies.

5.2. Test setup

5.2.1. General setups

The schematic representing the test setup used in this Chapter is shown in Figure 5.1. The majority of the setup was maintained from Chapter 4 for consistency purposes. An axial fan supplied ambient air by a downstream axial fan into a rectangular tunnel. Two perforated blockage plates were installed. The first blockage plate had 8 perforations and the second blockage plate had 7 perforations. The perforations in the second blockage were staggered from those in the first blockage by one diameter. All perforations had the same internal diameter of D_j = 21 mm (producing the same jet diameter). The blockage plate thickness (t) was half that of the jet diameter (i.e., t/D_j = 0.5), which assumes an orifice-type jet flow (Liu et al., 2022; Ward-Smith, 1971).

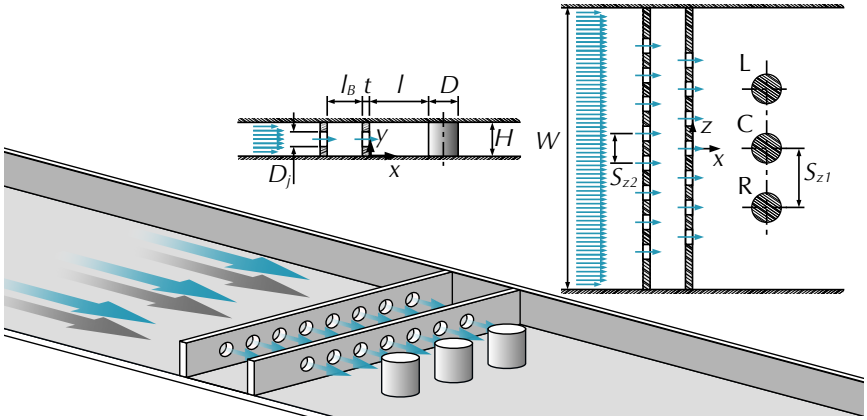

Figure 5.1. Test section schematic for consideration of perforated blockages with multiple pin-fins.

Three circular pin-fins were positioned downstream of the perforated blockage plates and had a diameter (D) twice that of the jet diameter (i.e., D/D_j = 2.0), and aligned with the perforations denoted as L, C, and R in Figure 5.1. The pin-fins had an aspect ratio of H/D = 1.07 and a center-to-center spacing of S_{z1}/D_j = 4.0 (S_{z1}/D = 2.0). The perforation spacing (S_{z2}/D_j) was fixed at 2.0. The distance between perforated blockage plates, relative to the height of the channel was kept constant at l_b/H = 2.0.

The values of l used were determined based on jet characteristics. The blockage plates, perforations, pin-fins and relative positions were machined to an accuracy of ±0.03mm or 0.3% of the jet diameter (D_j).

The Reynolds number was fixed at Re_j = 22,000, based on jet diameter (or Re_D = 44,000 based on pin-fin diameter). A fully turbulent jet would, thus, be expected (McNaughton & Sinclair, 1966).

5.2.2. Rationale for additional specifications

(a) Perforated blockage plates

Two perforated blockages were utilised in all studies to follow, which is distinct from the previous studies by Kan et al. (2014) and Kim et al. (2019). Moon and Lau (2003) observed that the friction factor (f/f_0) for perforated blockages varies very slightly (by approximately 4%). This difference results in a negligible variation in the thermal performance of the cooling scheme (with friction factor applied as $(f/f_0)^{-1/3}$ per equation 1). The end-wall surface enclosed by the additional perforated blockage will however experience much higher end-wall heat transfer. Between perforated blockages a end-wall heat transfer can be as high as Nu/Nu_0 = 7.0 ~ 8.0 (Moon and Lau, 2003, Shin, 2008, Chung, 2014). Around a pin-fin array, however the end-wall heat transfer is Nu/Nu_0 = 3.0 ~ 5.0 (Lawson, 2011, Lyall, 2011, Kan et al., 2014) for a conventional pin-fin array and Nu/Nu_0 = 4.0 ~ 5.0 (Kan et al, 2014) for a blockage pin-fin configuration. As such, with a negligible change in pressure drop, there is a higher end-wall heat transfer and, as per equation 1, the thermal performance is expected to be higher. If a blockage pin-fin configuration is to be presented in a more optimal state, the use of at least two blockages is seen as necessary.

The blockages had the same thickness ratio of t/D_j = 0.5. This assumes an orifice-type jet flow (Liu et al., 2022; Ward-Smith, 1971) and results in the highest impingement heat transfer as shown in Figure 2.22 (Liu et al, 2022) at least for near exit-to-target distances (l/D_j) as expected in a blockage pin-fin configuration. This thickness ratio is lower than those employed by previous studies for perforated blockages ($t/D_j \approx 1.0$ (Chung et al., 2014; Moon & Lau, 2003; Park et al., 2016; Shin & Kwak, 2008). Again, the rationale is to present a blockage pin-fin configuration in a more optimal state than previously considered. Thus so the smaller thickness ratio of t/D_j = 0.5 was used.

(b) Pin-fins and the spanwise spacings

The use of multiple pin-fins will be necessary to determine how the flows from neighbouring pin-fins interact. The use of a single row of pin-fins isolates any effects from downstream pin-fins on the variations to focus more on transverse interactions between pin-fins in a given row. Further, it was seen as only necessary to have three pin-fins. The central pin-fin would have pin-fins on either side and a mirrored interaction could be considered. The two outer pin-fins would then see asymmetric conditions as there is only a single pin-fin neighbouring each. The spanwise spacing of the pin-fins (S_{z1}/D) was selected to be 2.0. The end-wall flow extent in the spanwise (z) direction was approximately

z/D = 1.3. It was desired to force an interaction between the end-wall streamlines from neighbouring pin-fins. By using S_{z1}/D = 2.0 (S_{z1}/D_j = 4.0) it ensured such an interaction. This spacing is lower than that typically employed for horseshoe vortex systems ($S_{z1}/D \approx 2.5$).

The pin-fin spacing then drives the perforation spacing to ensure geometric alignment of the jets with the pin-fins. Two jet configurations were considered as shown in Figure 5.2. To have jets that would impinge on the pin-fins directly, only three perforations would be required with a spanwise spacing of S_{z2}/D_j = 4.0. This would be referred to a "3-jet configuration". In a blockage pin-fin configuration, however, there will be a second row of pin-fins and the use of additional jets to impinge on that second row would then be employed. Considering a staggered second row of pin-fins, as employed in conventional pin-fin arrays, then an additional 4 jets would be active (Figure 5.2(b)). The spacing of this "7-jet configuration" would be thus be S_{z2}/D_j = 2.0. For consistency, the implementation of a single jet would be referred to as "1-jet configuration." For easier reference the various jets were assigned terms as given in Figure 5.2. The centre jet exited at z/D_j = 0.0. Outer jets exited at z/D_j = ±4.0. Inner flanking jets exited at z/D_j = ±2.0 and outer flanking jets exited at z/D_j = ±6.0.

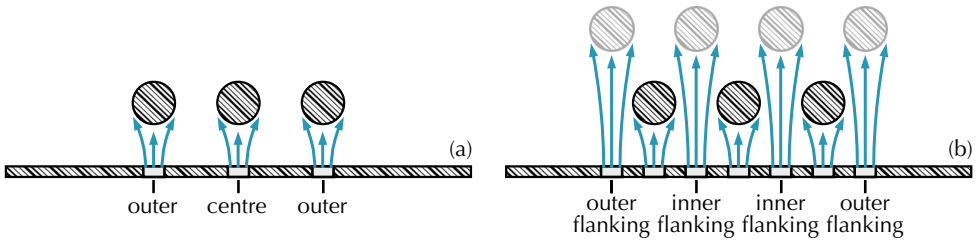

Figure 5.2. Terminology applied to jet configurations used in Chapter 5. (a) With only direct impingement on the pin-fins and (b) With flanking jets.

The perforations in the first blockage have the same spacing of S_{z2}/D_j = 2.0. The perforations would be staggered such that flow could not flow directly from one perforation and directly through the second. Instead the flow would be required to stagnate first. This is essential for optimal end-wall heat transfer between perforated blockages. It was decided to use 8 perforations in the first blockage rather than the same 7 for the second blockage. Seven perforations would have resulted into an asymmetric flow into the channel between blockages which in turn would have either incited further flow curvature or at least resulted in asymmetric jet flows. The use of different blockage ratios (A_b/A_j) for each blockage is likely not ideal for pressure drop performance. As that was not being considered in this chapter, the effect was considered satisfactory.

The test channel employed in Chapter 4 was used here. With the spanwise spacing of pin-fins and jets there resulted a large space between the L and R pin-fins and their nearest sidewalls. This was deemed acceptable as it isolates the effect of the sidewall from any flow interactions or jet curvature effects.

5.3. The effect of perforated blockages for a singular pin-fin

5.3.1. Consideration of the distances between perforation exit and pin-fin leading-edge

The variation in centreline velocity for the tube jet (from Chapter 4) and the blockage jet (t/D_j = 0.5) is shown in Figure 5.3. The blockage jet centreline velocity begins to decay ($v_c/v_e < 0.98$) at x/D_j = 2.0. The blockage jet potential core length is thus taken at l_p/D_j = 2.0, half that of the tube jet. This value agrees with that by Nguepnang et al. (2016). For a thickness ratio of t/D_j = 0.5, the blockage jet here does not behave like the orifice jet of the same thickness ratio tested by Liu et al. (2022). Notably, here the velocity variation does not exhibit a vena contracta (or increase in the centreline velocity downstream of exit) and the jet has a shorter potential core length. This is attributed to a narrow test section upstream of the blockage and closer proximity of a perforated blockage upstream.

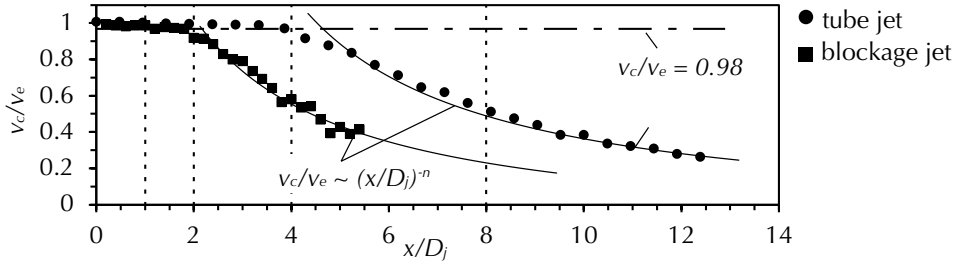

Figure 5.3. Jet centreline velocity variation with increasing distance from the exit for a tube jet at Re_j = 17,500 and a blockage jet (t/D_j = 0.5) at Re_j = 22,000.

Similar to the test cases in Chapter 4, three l/D_j distances are considered here, using the potential core length as reference:

(a) Half the length of the jet's potential core: l/D_j = 1.0 or case l_1.

(b) The length of the potential core: l/D_j = 2.0 or case l_2.

(c) Twice the length of the potential core: l/D_j = 4.0 or case l_4.

Too large l/D_j distance results in the unfavourable formation of low Reynolds number equivalent horseshoe vortex system type flows. There was not seen to be any merit in the further investigation of such a system here. For this reason, the third test case was set at l/D_j = 4.0 instead of 6.0 or 8.0. Further, the consistency of the l_2 and l_4 case here allows for comparisons between the l_2 and l_4 cases from Chapter 4.

5.3.2. Flows at the end-wall surface

The end-wall patterns for a singular pin-fin subjected to a singular impinging blockage jet are realized by an oil-dye technique and shown in Figure 5.4. The jet-pin flow patterns, established in Chapter 4, are identifiable for l_1 and l_2. For l_1 (Figure 5.4(a)), however, the leading-edge profile (marked by the dotted line) is deformed, being conformal to the downstream surface of the blockage. This is in contrast to those profiles noted in Chapter 4 (Figure 4.13(a, b)) where the profile appeared more

conformal to the pin-fin surface. In Chapter 4, with the tube jet and no obstruction on the end-wall surface, the radial streamlines were able to radiate upstream until dissipating or being entrained into the circulating region. The end-wall flow extent was approximately 0.6D and 0.9D upstream of the pin-fin leading edge for l_2 and l_4 respectively. For l_1, with a blockage jet (Figure 5.4(a)), there is an obstruction in the form of the blockage plate at the distance of 0.5D (1.0D_j) upstream of the pin-fin leading-edge. The radial streamlines are therefore not expected to reach their full extent before interacting with the blockage surface. The flow pattern from the radial streamlines thus becomes conformal to the blockage plate instead of the pin-fin. For l_2, the distance between the pin-fin leading-edge and the blockage plate is 1.0D (2.0D_j) and so the end-wall radial streamlines are expected to reach their extent before interacting with the downstream surface of the blockage plate. This is confirmed in Figure 5.4(b) as the leading-edge profile of the dye pattern does not deform and has a very similar shape to l_2 in Figure 4.3. The radial streamlines are, however, notably shorter – having a flow extent 0.4D (0.8D_j) upstream of the pin-fin leading-edge. It is not immediately clear why this occurs and may just be due to a slightly different oil-dye mixture.

Both radial and tangential streamlines can be discerned in the flow patterns for l_1 and l_2 (Figure 5.4(a, b)). The presence of the corner vortex can also be noted in the closeup of l_1 (Figure 5.4(c)) by way of a region of brighter dye near the pin-fin surface. The corner vortex presented in the same manner with a tube jet in Chapter 4 (Figure 4.3). The jet-pin flow structure is thus preserved when using a perforated blockage instead of tube jet. But there are some differences. This includes the interaction with the blockage plate for l_1 and shorter streamlines for l_1 and l_2. Further to this, the streamlines appear more curved as annotated and seen in the close up for l_1 in Figure 5.4(c). With the tube jet, the end-wall streamlines did curve slightly at their periphery (as in Figure 4.13(a-b)). This was due to their interaction with the stationary fluid, away from the pin-fin, being entrained towards it. The larger degree of curvature noted in Figure 5.4(a-c) implies that the fluid away from the pin-fin is behaving differently. This difference is attributed to the perforated blockage - due to its close proximity, for l_1, there is going to be a notable amount of flow along the blockage surface in the spanwise (z) direction as schematically represented in Figure 5.4(d). The periphery flow (identified in Figure 4.3 from Chapter 4) is thus augmented and the streamlines curve more.

For l_4 (Figure 5.4(e)), with the pin-fin outside of the potential core of the blockage jet, the flow patterns still match those of the characteristic jet-pin flows (Figure 4.13(a, b) or Figure 5.4(a, b)). There are no apparent horseshoe vortex flows as was seen for l_8 in Figure 4.13(c). There are faint radial and tangential streamlines that can be discerned based on the interpretations made in Chapter 4. The weak profiles in the oil-dye do indicate that the end-wall flows are of a lower velocity compared to l_1 and l_2, as should be expected due to the deceleration of the jet outside of the potential core (Figure 5.3).

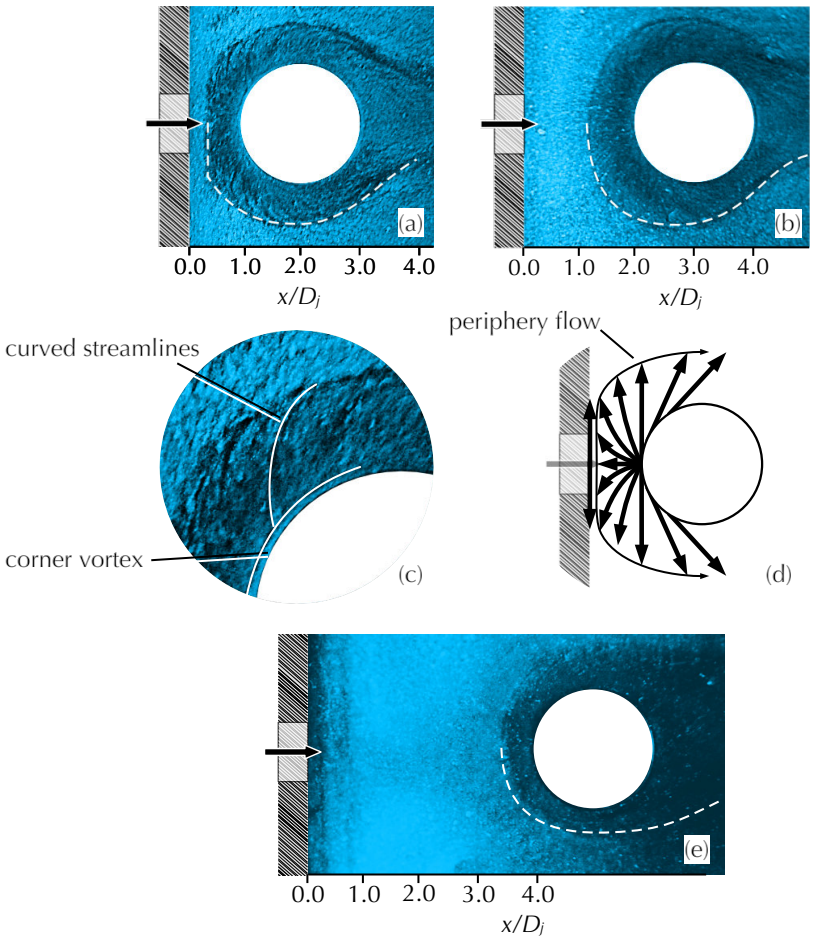

Figure 5.4. End-wall flows from oil-dye visualization around a single pin-fin subjected to an impinging blockage jet at Re_j = 22,000. (a) For l/D_j = 1.0, (b) For l/D_j =2.0, (c) A closeup of the outer leading edge of the pin-fin for l/D_j = 1.0, (d) Flow schematic for flow interaction between radial streamlines and blockage plate, and (e) For l/D_j = 4.0.

5.3.3. Flows in the vertical plane

The velocity contours in the vertical plane, from PIV, are shown in Figure 5.5 for both tube jet (a, b) and corresponding blockage jet flows (c-e). In all cases l_1, l_2 and l_4 with blockage jets, the circulating region continues to exist. The interaction between the radial end-wall streamlines and the perforated blockage for l_1 and l_2 (Figure 5.5(c, d)) are clear. The end-wall flow stagnates on the downstream surface of the blockage and is redirected upwards and along the blockage surface (in the y-direction) towards the jet core flow. This is the case for both l_1 and l_2. While the interaction of the radial streamlines with the perforated blockage was evident in the oil-dye patterns of l_1 (Figure 5.4(a)), there is still a non-zero flow along the downstream side of the blockage plate surface based on the PIV measurements in Figure 5.5(d) – this is despite the lack of profile deformation for l_2 (Figure 5.4(a)). The flow along the blockage surface is expected to be beneficial to the heat transfer on the perforated blockage itself as it increases the amount of cooling flow acting on the blockage plate surface.

For l_4, there is no clear flow on the blockage surface (at x'/Dj = -4.5) based on Figure 5.5(e). This

may be expected considering the larger l/D_j distance and weak end-wall flows already noted in Figure 5.4(e). The flow near the end-wall does, however, extend upstream further than is apparent in the oil-dye image (Figure 5.4(e)). Based on Figure 5.5(e) there exists a backflow beyond x'/D_j = -3.5 despite it appearing to only extend to x'/D_j = -1.5 in the oil-dye image (Figure 5.4(e)). Further, the circulating region is of a similar height (in the y-direction) to that in l_1 and l_2. This is contrary to the tube jet case where the circulating region for l_4 (Figure 5.5(b)) is smaller along the y-axis than for l_2 (Figure 5.5(a)). This indicates a difference in the interactions between the end-wall and mid-height flows for blockage and tube jets. The difference in the jet structures, including the shorter potential core for the blockage jet are attributed as the cause.

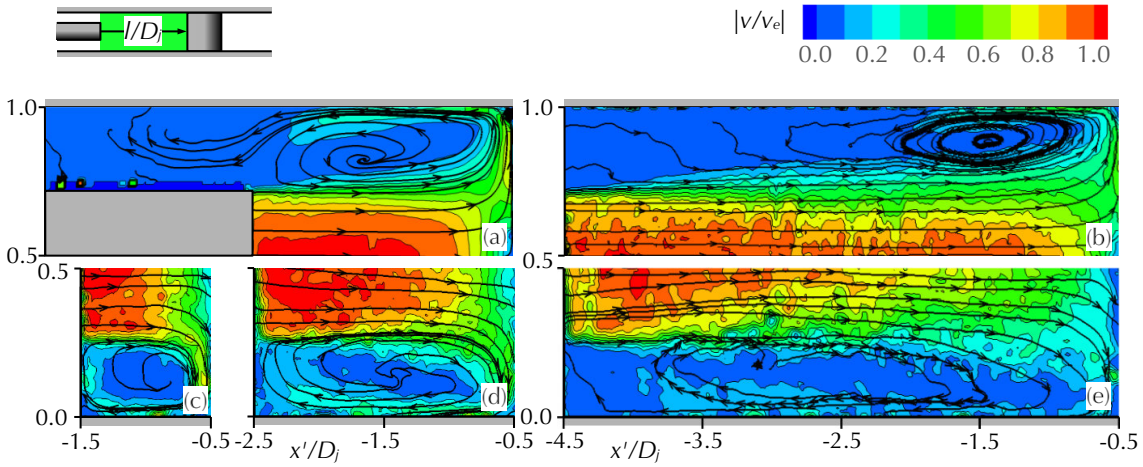

Figure 5.5. Flow field in the vertical (x-y) plane of a single pin-fin subjected to an impinging jet. (a) For l/D_j = 2.0 for a tube jet at Re_j = 17,500, (b) For l/D_j =4.0 for a tube jet at Re_j = 17,500, (c) For l/D_j = 1.0 with a blockage jet at Re_j = 22,000, (d) For l/D_j = 2.0 with a blockage jet at Re_j = 22,000, and (e) For l/D_j = 4.0 with a blockage jet at Re_j = 22,000.

The shorter potential core of the blockage jet can also be in noted in the velocity magnitude distributions at x'/D_j = -1.5 (Figure 5.6(a)) between the tube (a) and blockage jets (b). The velocity for l_4 is consistently lower for the blockage jet. The overall lower velocity for the blockage jet is the likely explanation for the circulating region being less constrained for l_4 with the blockage jet. For l_2, however, the two jet types have a similar velocity magnitude distribution at x'/D_j = -1.5. This also includes the diffusion of the jet (where its velocity becomes 0) being similar for l_2 between the tube and blockage jets. The diffusion appears different for the l_4 case, with the blockage jet diffusing slightly more. No significance could be drawn from the flow direction distributions (Figure 5.6) between the tube (c) and blockage jets (d). Those differences near the end-wall are due to differences in the circulating regions.

For sufficiently short l/D_j distances, the radial streamlines interact with the downstream surface of the perforated blockage, resulting in redirected flows along the blockage surface in both the y- and z- directions. This is expected to be beneficial for cooling performance. The redirected flow along the

z-axis can augment the periphery flow at the flow extent of the radial streamlines. This results in an increased curvature of the streamlines and a possible deformation of the flow pattern along its leading-edge. Given the preservation of flow features noted in Chapter 4, those heat transfer characteristics observed for the tube jet are expected to be maintained for the case of a pin-fin subjected to a blockage jet. How the jet-pin flows interact with those from neighbouring pin-fins still remains to be determined.

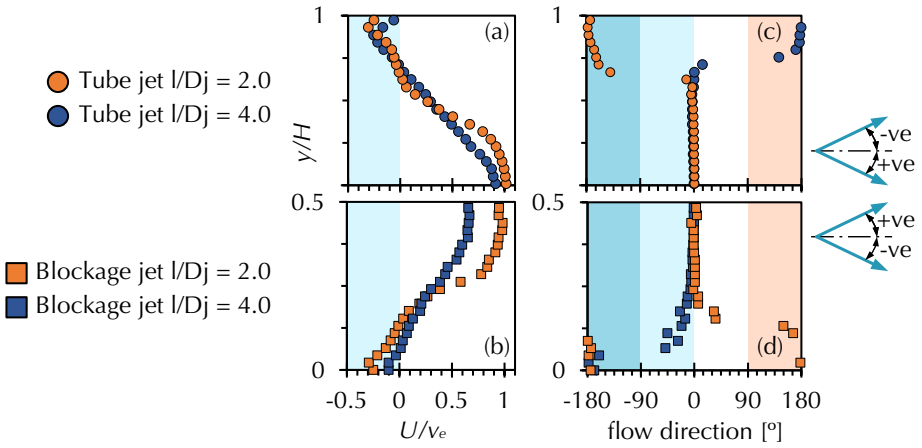

Figure 5.6. Extracted distributions in the mid-height plane (y/H = 0.5) along the y-axis at x'/D_j = -1.25 for a tube jet flows at Re_j = 17,500 and blockage jet flows at Re_j = 22,000. (a) Velocity distribution for tube jet flows, (b) Velocity distribution for blockage jet flows, (c) Flow direction distribution for tube jet flows, and (d) Flow direction distribution for blockage jet flows.

5.4. The effect of multiple jets interacting with multiple pin-fins

Before investigating the interaction of multiple blockage jets with multiple pin-fins, it is necessary to consider the possible curvature of the blockage jets and their behaviour without the influence of downstream pin-fins. Here, "curvature" is defined as the deviation of the jets core flow from its original axis as schematically shown in Figure 2.28.

5.4.1. Flows in the mid-height of an empty channel

The velocity contours from PIV measurements in the mid-height plane (y/H = 0.5) without downstream pin-fins are shown in Figure 5.7 for 1-jet (a), 3-jet (b) and 7-jet (c) configurations. The intended positions of the pin-fins (for l_1, l_2 and l_4) are marked by the dotted circles for reference.

For a 1-jet configuration (Figure 5.7(a)), no significant curvature of the jet is observed. This is the same configuration as applied in Chapter 5.3. As the end-wall flow patterns around the pin-fins were seen to be symmetrical (Figure 5.4), the lack of curvature in the mid-height plane is expected. With the introduction of additional jets (Figure 5.7(b, c)), the centre jet (exiting at z/D_j = 0.0) remains relatively straight. There is, however, a very slight curvature in the positive z-direction. The outer jet (exiting at z/D_j = -4.0) as well as the flanking jets (exiting at z/D_j = -2.0 and -6.0) exhibit notable

curvature for the 3- and 7-jet configurations. Note that the outer flanking jet (z/D_j = -6.0) of the 7-jet configuration exits outside of the measurement window. It can, however, be observed as it curves into the measurement window at approximately $x/D_j \approx 2.0$. With the 3-jet configuration, the outer jet exhibits a greater degree of jet curvature compared to the 7-jet configuration. The curvature, for both cases is sufficient that L and R pin-fins are likely to be exposed to no symmetric flows about their centres.

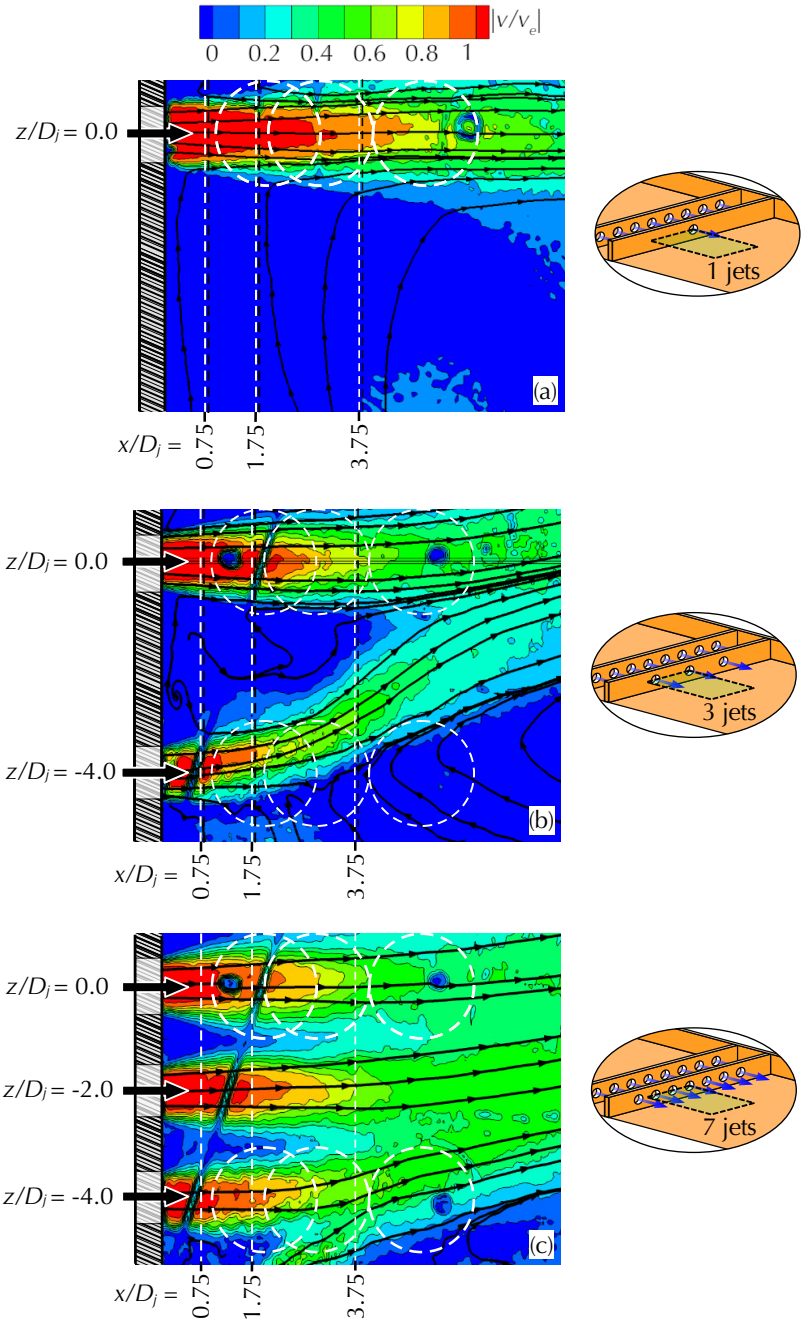

Figure 5.7. Velocity contours from PIV for jets exiting into an empty channel in the mid-height plane (y/H = 0.5) comparing three configurations of blockage jets at Re_j = 22,000. (a) For a 1-jet configuration (b) For a 3-jet configuration, and (c) For a 7-jet configuration.

With the neighbouring jets, for 3- and 7-jet configurations, the potential core length of the centre jet is reduced as seen in Figure 5.8. For the 1-jet configuration, the potential core length was $l_p/D_j = 2.0$. With neighbouring jets, however, the potential core length reduced to $l_p/D_j = 0.75$ for the 3-jet and $l_p/D_j = 0.5$ for the 7-jet configuration. The shorter potential core is attributed to the flow entrainment by neighbouring jets. For the 7-jet configuration the nearest neighbouring jet is exiting closer to the centre jet ($z/D_j = \pm 2$ compared to $z/D_j = \pm 4.0$ for the 3-jet configuration). It thus has a stronger influence on the centre jet, causing its potential core to be shorter. This means that with neighbouring jets the l/D_j distances of 1, 2 and 4 (l_1, l_2 and l_4) do not necessarily reflect the initial conditions that they were selected for (i.e., half of, equal to and double the potential core length). At all cases, l_1, l_2 and l_4, with multiple blockage jets, the pin-fins will be positioned outside the potential core of the jet. It was decided to continue with the l_1, l_2 and l_4 cases regardless.

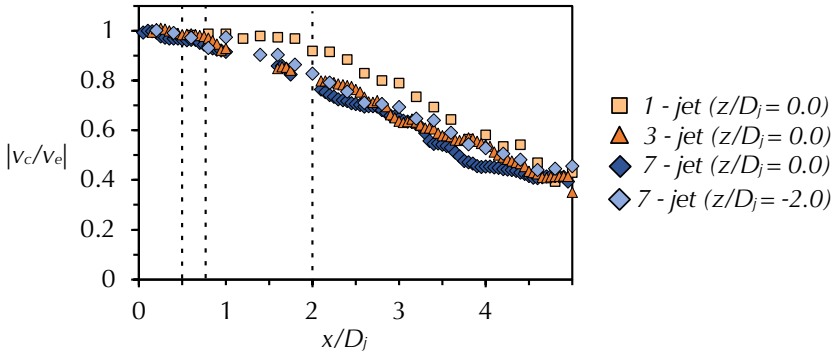

Figure 5.8. Extracted jet centreline velocity distribution along the x-axis for 1-jet, 3-jet, and 7-jet configurations at $Re_j = 22{,}000$.

The velocity magnitude and flow direction distributions were extracted from the PIV measurements of Figure 5.7. Three downstream locations were selected: $x/D_j = 0.75$, 1.75 and 3.75 as shown by the dotted lines in Figure 5.7. These locations correspond with the position $x'/D_j = -1.25$ for the intended pin-fins positions of l_1, l_2 and l_4, (i.e. $0.25D_j$ upstream of the pin-fin leading edge, preceding impingement). Consideration of both the velocity magnitude and flow direction distributions (plotted in Figure 5.9) should allow for the extent of the jet curvature to better interpreted. In this way, a baseline consideration of the jet flows can be established without the pin-fins in place.

The curvature of the outer jets for 3- and 7-jet configurations are clearly visible in both the velocity distributions (Figure 5.9(c-e)) and flow direction distributions (Figure 5.10(c-e)). The distributions are distinct between the 3- and 7-jet configurations for all three positions. Further, there are large flow directions at the periphery of the outer jet in the 3-jet configuration for all three positions. Again, however, considering that there is a low flow velocity in this same region (Figure 5.9(d)), the differences are considered less consequential. At $x/D_j = 0.75$, the peak velocity occurs at $z/D_j = -4.0$, indicating that there is minimal or no flow curvature by this position. By $x/D_j = 1.75$, however, the

position of the peak velocity of the outer jet, for the 3-jet configuration, has shifted to z/D_j = -3.6 (Figure 5.9(e)) - the distribution being asymmetric. At x/D_j = 1.75 for the 3-jet configuration the flow direction is approximately -13º at the position of peak velocity magnitude (Figure 5.10(e)) - the position of peak flow has a notable vector component towards the centre of the channel. By x/D_j = 3.75, there is no significant flow for $z/D_j \leq$ -4.0 with the 3-jet configuration and the peak velocity skewed to z/D_j = -3.0 (Figure 5.9(f)). At the position of peak velocity, the flow direction is -30º (Figure 5.10(f)) - the flow is predominantly towards the centre of the channel. A pin-fin in x/D_j = 3.75 may then have no flow impinging on its outer side with a 3-jet configuration.

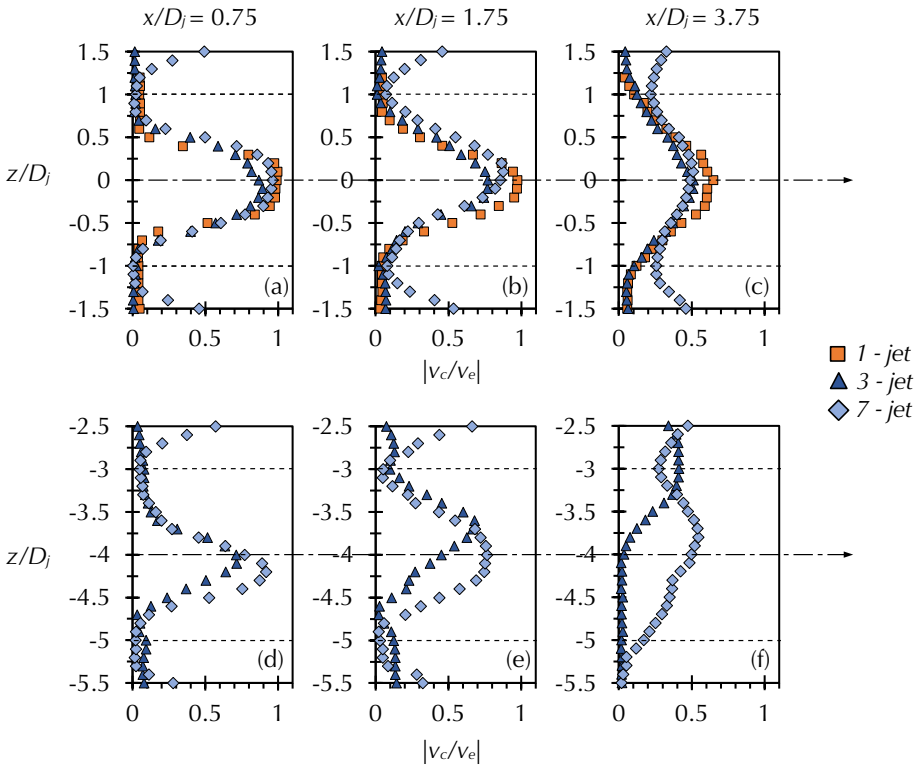

Figure 5.9. Distribution of flow velocity magnitude along the jet axis for the centre jet (at z/D_j = 0.0) and outer jet (at z/D_j = -4.0) for x/D_j = 0.75, 1.75 and 3.75 for blockage jets exiting into empty channel at Re_j = 22,000.

The additional (flanking) jets and smaller transverse spacing of the 7-jet configuration reduce the curvature of the outer jet as is seen in Figure 5.7(c). At both x/D_j = 0.75 and 1.75, the peak velocity of the outer jet occurs at approximately z/D_j = -4.0 (Figure 5.9(e)) and the velocity distribution is largely symmetrical. Further, the flow direction is less than ±1º at the position of peak velocity (Figure 5.10(e)). The jet could be considered to be exhibiting negligible flow curvature for a pin-fin at l/D_j = 2.0. By x/D_j = 3.75, however, the peak velocity has shifted to z/D_j = -3.8. The velocity magnitude and flow direction distributions have become asymmetrical, with a larger proportion of flow at -2.5 $\leq z/D_j \leq$ -4.0 compared to -4.0 $\leq z/D_j \leq$ -5.5. The flow direction, at the position of peak velocity for x/D_j = 3.75, is approximately

-19º and the majority of flow has a component inclined towards the channel centre (Figure 5.10(f)). Note that, as shown in Figure 5.7(c), the flanking jet (exiting at z/D_j = -6.0) has already merged with the outer jet (exiting at z/D_j = -4.0) by x/D_j = 3.75. Very little flow exists at the outer periphery ($z/D_j \leq$ -4.5) of the outer jet of a 7-jet configuration at x/D_j = 3.75 (Figure 5.9(f)). The velocity magnitude in that region is, however, still higher for the 7-jet compared to the 3-jet configuration.

The jets clearly exhibit flow curvature. It is possible that pin-fins for the l_1 case may be sufficiently close that the flow curvature is negligible. For cases l_2 and l_4, however, the curvature is sufficient such that the outer pin-fins (L and R) are expected to be exposed to asymmetric flows in a 3 jet configuration. The curvature may only be noticed for l_4 with the 7-jet configuration. Variations from the flow behaviour noted in Figure 5.7, Figure 5.9, Figure 5.10, if any, can then be said to be due to the presence of the downstream pin-fins.

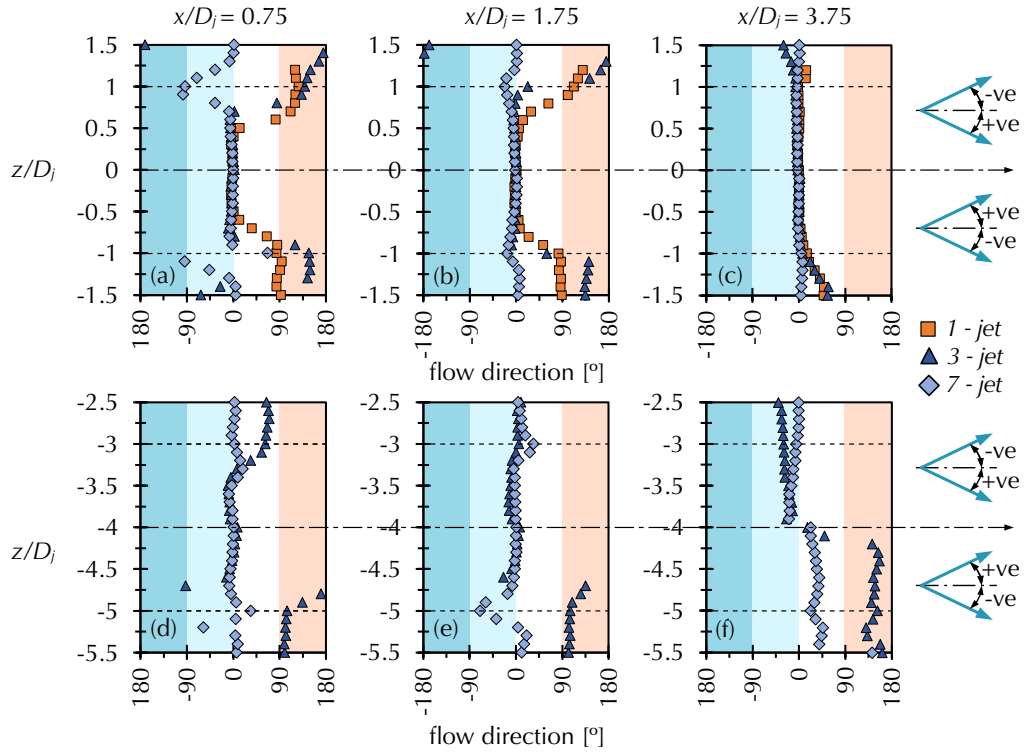

Figure 5.10. Distribution of flow direction along the jet axis for the centre jet (at z/D_j = 0.0) and outer jet (at z/D_j = -4.0) for x/D_j = 0.75, 1.75, and 3.75 for blockage jets exiting into empty channel at Re_j = 22,000.

5.4.2. Flows in the channel mid-height with downstream pin-fins

The velocity contours, from PIV, in the mid-height plane for blockage jets interacting with the pin-fins at three downstream positions are shown Figure 5.11. For l_1 (Figure 5.11(a, b)) the flow around both the C and L pin-fin appear to be symmetrical about the pin-fin axis for both the 3- and 7-jet configurations.

There is a band of relatively higher velocity upstream of C and L pin-fins at l_1 with the 3-jet

configuration (Figure 5.11(a)). In Chapter 4 such velocity bands were attributed to circulating regions arcing around the pin-fin leading edge. These circulating regions require counteracting flows between the mid-height and end-wall planes. The flow patterns around the C pin-fin in Figure 5.11(a) are, however, distinct from those of a singular jet impinging on a singular pin-fin as in Figure 4.8. Specifically, the surrounding flow away from the jet core in in Figure 5.11(a) appears more aligned with the x-direction instead of towards the pin-fin surface. The mechanism required for the circulating regions to extend and wrap around the pin-fins then does not exist. Further, besides l_1 for the 3-jet configuration, no notable velocity bands are noted in the other configurations (Figure 5.11(b-f)). It is possible that the region of higher velocity in Figure 5.11(a) is due to the closer proximity of the perforated blockage resulting in a local acceleration of the surrounding flow. While the circulating region will still exist, it is limited to near the pin-fin centreline (z/D_j = 0.0 and 4.0) where there are counteracting flow between the core jet flow and the radial streamlines. The introduction of neighbouring jets and pin-fins, however, prevent the circulating region from existing away from the pin-fin centrelines.

Further considerations of the velocity contours in Figure 5.11 are with regards to the flow curvature. For l_2 (Figure 5.11(c, d)), the outer jet, exiting at z/D_j = 4.0 continues to curve with the pin-fins in place. The curvature appears similar for both the 3- and 7-jet configurations. This is despite the apparent lack of curvature for the 7-jet configuration without the pin-fins at l_2 (Figure 5.9(e) and Figure 5.10(e)). The curvature of the outer jet (for l_2) results in a notably asymmetric flow around the surface of the L pin-fin. An additional feature in the flow field, compared with the pin-fins at l_1 (Figure 5.11(a-b)), is a vortical flow at the outer leading edge of the L pin-fin for l_2. The size of the vortical flow differs between the 3- and 7- jet configurations – being smaller for the 7-jet configuration. Such a vortical structure can be observed in the numerical results of (Kan et al., 2014) as shown in Figure 2.28(b). Like the circulating region in the vertical plane (Figure 5.5), this vortical flow appears to form due to counteracting flows. The flow on the outer leading edge of the L pin-fin in the 3-jet configuration (Figure 5.11(c)) appears to separate early. The flow leaves the pin-fin surface with a flow component in the positive z direction. This is counteracted by flow, in the negative z direction, being entrained towards the jet core and pin-fin surface flow. The vortical flow does not form for the l_1 case due to the surface flow on the L pin-fin not separating from the pin-fin. While it is not completely apparent in Figure 5.11(d), the formation of the vortex for l_2 with the 7-jet configuration implies that the pin-fin surface flow is also separating from the L pin-fin early. However, the proximity of the flanking jet (exiting at z/D_j = 6.0) constrains the separated flow and, in turn, the size of the vortical flow.

For l_4 (Figure 5.11(e, f)) the outer jet curves less for the 7-jet configuration. This was expected based on the velocity contours without pin-fins in Figure 5.7(c). In contrast to Figure 5.7(c), however, the outer flanking jet appears to curve less in Figure 5.11(f) – it does not merge with the outer jet preceding the interaction with the pin-fin. Further, the vortical flow by the outer leading edge of the L pin-fin only forms for the 3-jet configuration. For the 7-jet configuration, the flanking jet (exiting at

z/D_j = 6.0) appears to prevent the flow from separating from the pin-fin surface instead of just constraining the flow once separated. The mechanism for the formation of the vortical flow then doesn't exist for the 7-jet configuration at l_4.

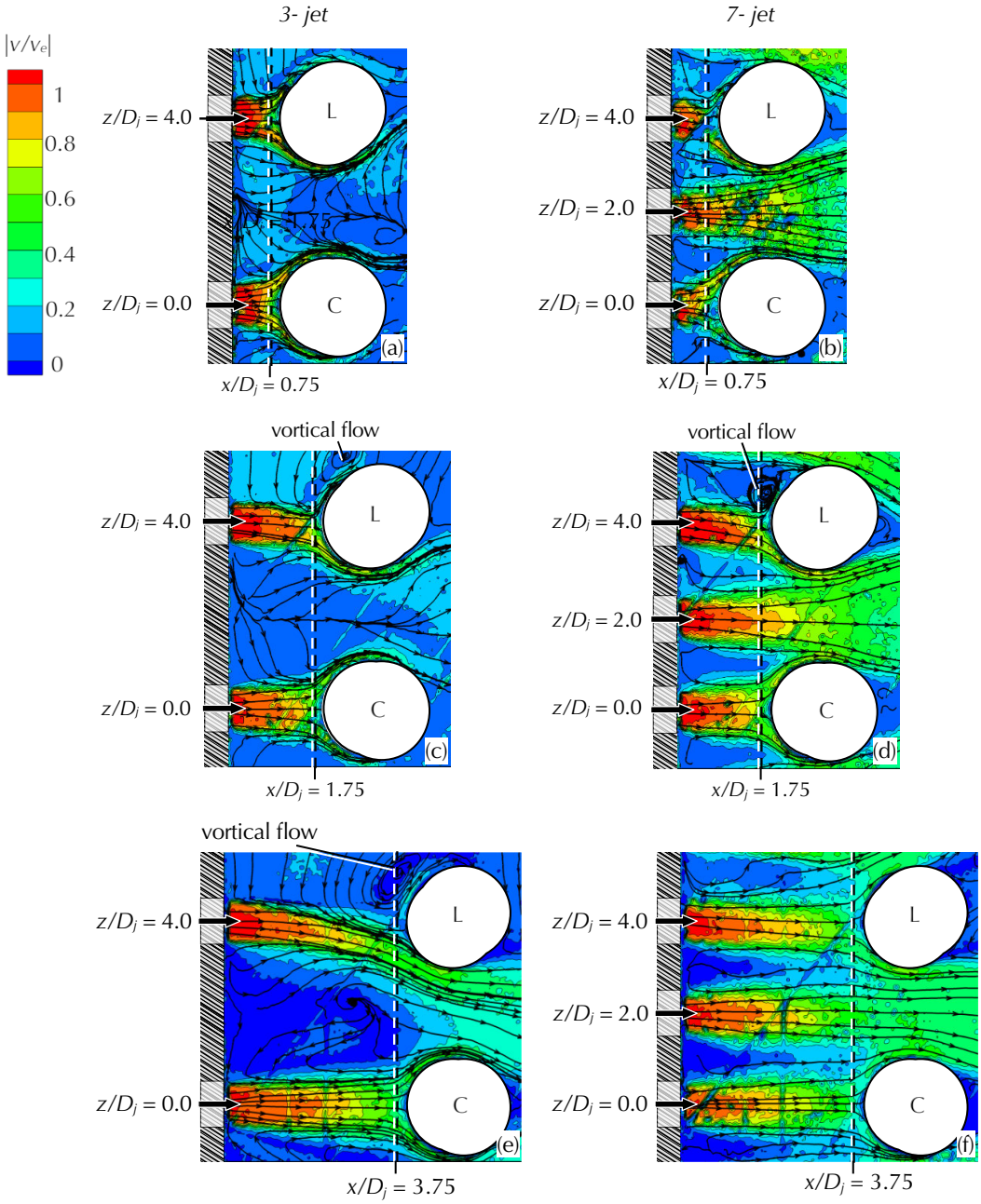

Figure 5.11. Velocity contours in the mid-height plane (y/H = 0.5) from PIV at Re_j = 22,000. (a) For a 3-jet configuration at l/D_j = 1.0, (b) For a 7-jet configuration at l/D_j = 1.0, (c) For a 3-jet configuration at l/D_j = 2.0, (d) For a 7-jet configuration at l/D_j = 2.0, (e) For a 3-jet configuration at l/D_j = 4.0, and (f) For a 7-jet configuration at l/D_j = 4.0.

When off-axis impingement occurs, most of the jet flow is asymmetrically distributed on the surface of the pin-fin. Severe off-axis impingement as seen on the L pin-fin Figure 5.11(e) will be detrimental

to the pin-fin surface heat transfer. It is also expected to have a notable effect on the end-wall flow patterns. While the effect of curvature on the end-wall flows remains to be seen, it is likely that significant flow curvature is to be avoided for a blockage pin-fin configuration.

The velocity magnitude and flow direction distributions, extracted from the PIV measurements in Figure 5.11, are plotted in Figure 5.12, Figure 5.13 and Figure 5.14 respectively. For l_1, there is insufficient distance for the jets to notably curve before impingement as seen in the velocity contours of Figure 5.11(a, b). This is reflected in the negligible changes in velocity magnitude and flow direction distributions at x'/D_j = -1.25 with and without pin-fins for either the 3- or 7-jet configurations (Figure 5.12). For the centre jet (exiting at z/D_j = 0.0), the velocity magnitude and flow direction distributions are largely unchanged when the pin-fins are introduced. The peak velocity near the core of the jet is lower with pin-fins due to the jet decelerating as it stagnates on the pin-fin. There are also some larger flow inclinations at the periphery of the jet but these are seen as inconsequential due to the relatively low velocities in the region. This same behaviour is noted for the centre jet with the pin-fins at l_2 and l_4 as per Figure 5.13(a-d) and Figure 5.14(a-d). More significant differences are, however, observed for the outer jet (exiting at z/D_j = 4.0) with the pin-fins at l_2 and l_4 as shown in Figure 5.13(e-h) and Figure 5.14(e-h).

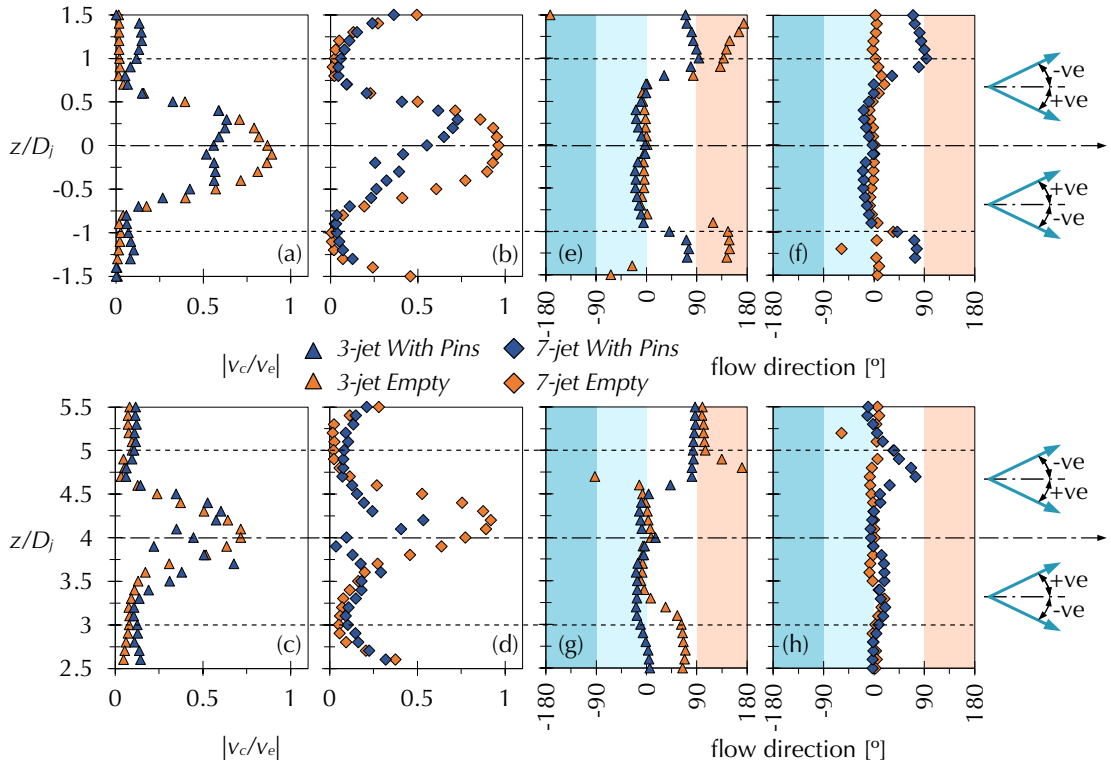

Figure 5.12. Extracted distributions in the mid-height plane (y/H = 0.5) along the z-axis at x'/D_j = -1.25 without downstream pin-fins (empty) and with the pin-fins at l/D_j = 1.0 for 3-jet and 7-jet configurations at Re_j = 22,000.

For the 3-jet configuration, the flow distributions (velocity magnitude and direction) of the outer jet remain unchanged with pin-fins at l_2 (Figure 5.13(e) and Figure 5.14(e)). For l_4, the peak velocity with a 3-jet configuration remains skewed towards the centre of the channel (Figure 5.13(f)). But there is a sharper peak in the velocity distribution with the pin-fin in place. The velocity distribution towards the outer side of the channel ($z/D_j > 4.0$) remains the same. At the outer side, however, the flow direction distribution become reversed with the pin-fins in place (Figure 5.14(f)). Specifically, the flow in this region changes from being consistently towards the centre of the channel to predominantly away from the channel centre. The flow direction is approximately 45º, although an inclination as much as 65º is noted near the centre of the pin-fin at $z/D_j = 4.0$ (Figure 5.14(f)). The large inclinations are due to the circumferential flow around the surface of the L pin-fin (seen in Figure 5.11(e)) redirecting the flow outwards away from the channel centre. This is the same flow that is attributed to cause the vortical flow off the outer leading edge of the L pin-fin. While the inclusion of pin-fins does result in the vortical flow, they have a negligible effect on the jet curvature for the 3-jet configuration. Consequently, there exists an asymmetrical flow field interacting with the L pin-fin at l_2 and l_4 in a 3-jet configuration.

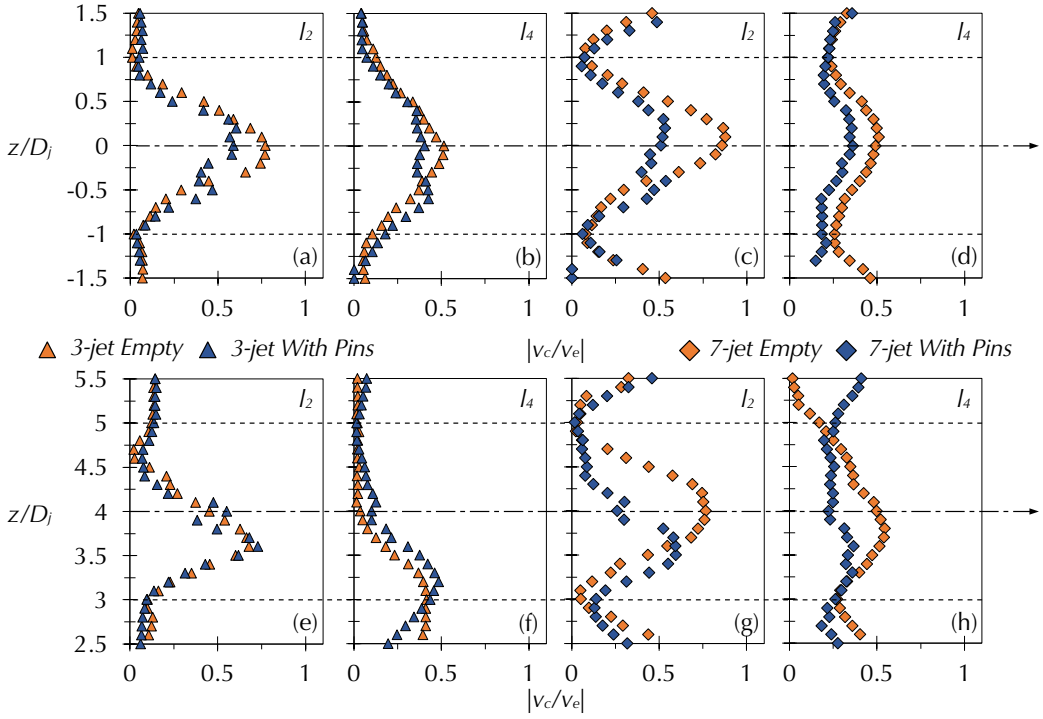

Figure 5.13. Extracted velocity distributions at $l/D_j = 2.0$ and 4.0 in the mid-height plane ($y/H = 0.5$) along the z-axis at $x'/D_j = -1.25$ upstream of the pin-fin at $Re_j = 22{,}000$ for 3-jet and 7-jet configurations.

Without the pin-fins, the outer jet curves less for a 7-jet compared to a 3-jet configuration as seen in Figure 5.7(c). This is attributed to a combination to the entraining action by the outer flanking jet and the inner flanking jet (exiting at $z/D_j = 6.0$ and 2.0 respectively) that acts to prevent the outer jet from curving more. With pin-fins and a 7-jet configuration the peak velocity magnitude for the outer jet is

further skewed towards the centre of the channel for both l_2 and l_4 (Figure 5.13(g, h)). For l_2 (Figure 5.13(g)) the position of the peak velocity in the z-direction approximately matches that of the 3-jet configuration – being $z/D_j = 3.6$ (in Figure 5.13(e)). The flow direction (Figure 5.14(g)) also becomes more similar to the 3-jet configuration with pin-fins in place. This same behaviour is less obvious for l_4 with the 7-jet configuration (Figure 5.13(h)). There, the position of the peak velocity of the outer jet (shifted to $z/D_j = 3.5$) approximately matches that for l_4 with the 3-jet configuration (Figure 5.13(f)). There is also the same reversal of flow direction for the 7-jet configuration (Figure 5.14(h)) as noted in the 3-jet configuration (Figure 5.14(f)). It may be concluded that the pin-fins appear to inhibit the corrective action of the flanking jet such that the outer jet behaves as though there is no flanking jet and curves more. This is clearly seen in for l_2 in the velocity contours of Figure 5.11(c-d). It is less clear, however, in the velocity contours for l_4 (Figure 5.11(e-f)). To further investigate, consider the outer flanking jet (exiting at $z/D_j = 6.0$) for l_4.

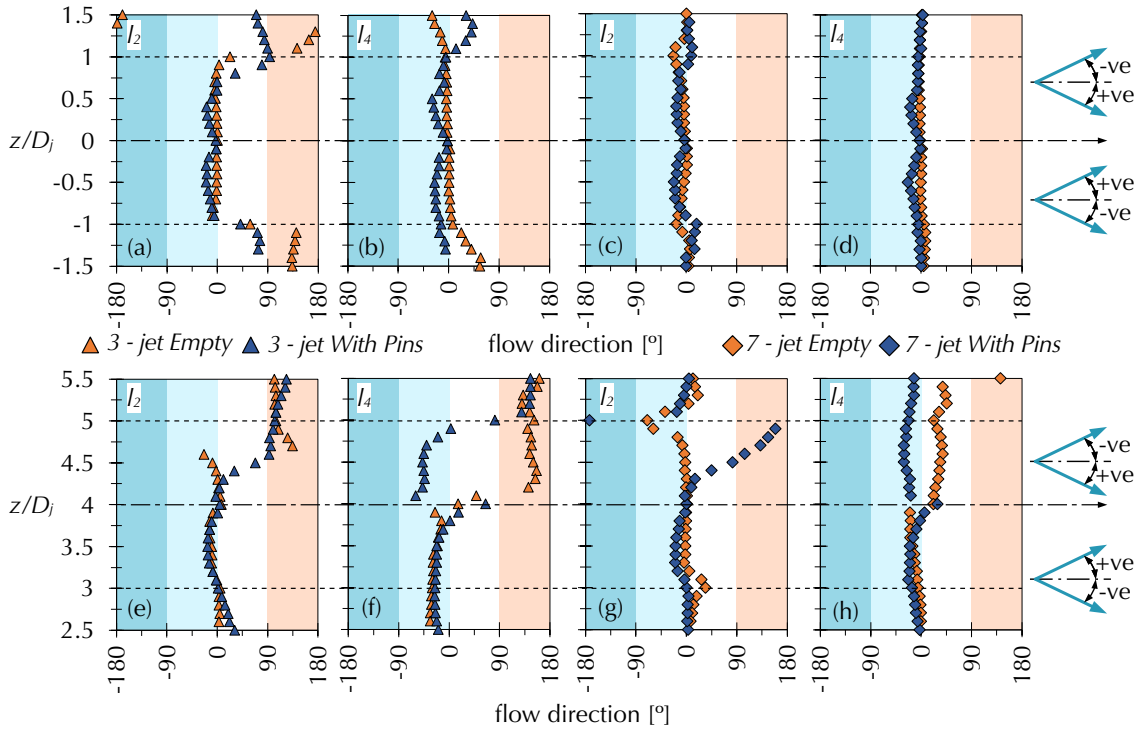

Figure 5.14. Extracted flow direction distributions at $l/D_j = 2.0$ and 4.0 in the mid-height plane ($y/H = 0.5$) along the z-axis at $x'/D_j = -1.25$ upstream of the pin-fin at $Re_j = 22{,}000$ for 3-jet and 7-jet configurations.

In Figure 5.13(h), there is an increased velocity magnitude at the outer jet periphery ($5.5 \geq z/D_j \geq 5.0$) due to the presence of outer flanking jet. For $z/D_j < 3.0$, however, the velocity magnitude is lower with pin-fins implying that the inner flanking jet has curved further towards the centre of the channel by l_4. This also occurs for l_2 (Figure 5.13(g)). Without the pin-fins, the outer flanking jet curves and merges with the flow of the outer jet before $x/D_j = 3.75$ (as in Figure 5.7(c)). With the pin-fins in place,

the outer flanking jet has not merged by the point where the flow interacts with the pin-fin. The pin-fin is thus acting to inhibit the curvature of the flanking jet. It may seem conflicting that the pin-fins allow the outer jet and inner flanking jet to curve more but cause the flanking jet to curve less. Instead, the pin-fin can be seen to inhibit the entrainment between the jets. With less entrainment the outer flanking jet will curve less as there is no entraining flow from the sidewall side of the channel. The inner flanking jet will curve more as it is seeing less entrainment from the outer jet. The outer jet then also curves more due to the limited entrainment from the outer flanking jet.

Despite this and considering both the velocity magnitude and flow direction distributions (Figure 5.13 and Figure 5.14), the L pin-fin is exposed to more flow for a 7-jet configuration compared to the 3-jet configuration. In a 3-jet configuration (S_{z2}/D_j = 4.0), the pin-fins have a largely negligible effect on the curvature of the blockage jets leading up to impingement. For the 7-jet configuration (S_{z2}/D_j = 2.0) the pin-fins appear to inhibit the flow entrainment between jet flows. The jets then exhibit curvature that is equivalent to a 3-jet configuration.

Finally, the presence of neighbouring jets, without downstream pin-fins causes a decrease in the length of the potential core for the centre and outer jets as in Figure 5.8. The presence of the pin-fins is seen to also manipulate the flanking jets. Consider the centreline velocity decay of the flanking jet exiting at z/D_j = 2.0 (Figure 5.15). The introduction of pin-fins (for l_2 or l_4) do not notably alter the length of the potential core but they do cause the centreline velocity decay to increase slightly. Specifically, the centreline velocity begins to decrease more once it passes between the pin-fins. This is contrary to what is be expected in a pin-fin array exposed to a uniform flow field. There, the flow accelerates as it passes between the pin-fins. This therefore presents another unique feature of a blockage pin-fin configuration in comparison to a conventional pin-fin array. It also implies that a second row of pin-fins should be placed nearer the first row so that the flow velocity those pin-fins are exposed to is not too low. This also applies for a conventional pin-fin array as in Figure 2.15. There the typical streamwise spacing is S_x/D = 2.5 which is expected to be too high – it would add an additional $5D_j$ between the first-row pin-fin and the second. But even a streamwise pin-fin spacing of S_x/D = 1.73, as used by Lawson et al. (2011), or S_x/D = 2.0 as used by Kan et al. (2014), may also be too high. The use of pin-fin spanwise and streamwise spacings, as appropriate for a conventional pin-fin array, should not be blindly used for a blockage pin-fin configuration.

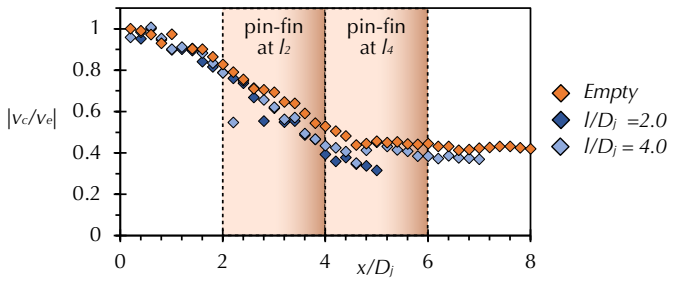

Figure 5.15. Centreline velocity decay of the flanking jet exiting at z/D_j = ±2.0 without pin-fins (empty)

and with pin-fins at l/D_j = 2.0 and 4.0.

5.4.3. Flows at the end-wall surface with multiple pin-fins

It is worth considering the end-wall flows around three pin-fins subjected to a uniform-like flow first, as shown Figure 5.16. This was achieved by removing the upstream blockages from the setup specified in Figure 5.1. Despite possible interactions with the flows around neighbouring pin-fins, the characteristic features of a horseshoe vortex system appear preserved. This includes the separation line (S) and wake vortex V_D as annotated. The horseshoe vortex patterns at each pin-fin are similar to one another, being of equal size and shape. Between the pin-fins, streamlines are focused into a narrow band and directed downstream. Overall, the distinct horseshoe vortex patterns around each pin-fin maintain their characteristic features when neighbouring pin-fins are present, similar to the that shown in Figure 2.13 based on prior studies.

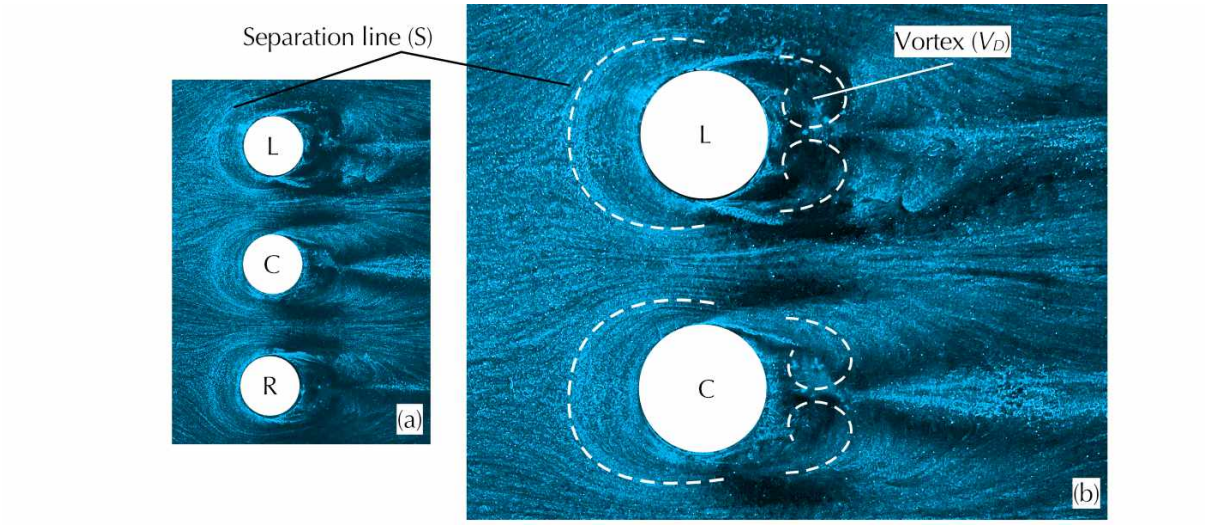

Figure 5.16. End-wall flow fields from oil-dye with 3 pin-fins subjected to a uniform like flow field for Re_D = 44,000. (a) Overview of all three pin-fins and (b) Closeup of end-wall around C and L pin-fins.

With blockage jets instead of a uniform-like flow field, however, the characteristic jet-pin flows noted in Chapter 4 appear altered as seen in Figure 5.17, Figure 5.19 and Figure 5.20. The end-wall patterns for l_1 (Figure 5.17) will be considered first. At this pin-fin position there is minimal jet curvature noted in the mid-height plane and the flows around the L and C pin-fins are relatively symmetrical (Figure 5.11(a-b)). There is then expected to be negligible effects of flow curvature present, and the end-wall flow patterns can be taken as representing the base end-wall flow interactions.

For both the L and C pin-fins, there can be seen the typical jet-pin radial and tangential streamlines in Figure 5.17. The profile around the leading edge of the C pin-fin is very similar to the case with just a single pin-fin at l_1 (Figure 5.4(a)) – including the leading-edge profile being conformal to the blockage plate surface. The flow pattern around the L pin-fin, however, appears to be asymmetric about the pin-fin centre. This may be misleading as the main dashed line does not represent the flow

extent which is marked separately – the dashed line instead represents something more equivalent to the "dye-line" noted in Chapter 4 (Figure 4.3(a)). Despite this, there does appear to be a dissimilarity in the amount of dye disruption between the inner and outer sides of the L pin-fin – the dye on the inner side being distinctly more disrupted. There is therefore some degree of asymmetry present about the L pin-fin. There also exists a lack of flow convergence behind the pin-fins.

The lack of convergence and asymmetry about the L pin-fin is attributed to the flow interactions between the pin-fins. Unlike for a horseshoe vortex system, with jet-pin flows the streamlines from neighbouring pin-fins will have opposing vectors. The interactions from those opposing flows result in a band of disrupted dye with no clear streamlines – this band is here on termed the "interaction band" (as in Figure 5.17(a)). This is contrary to the band of focused but clear streamlines between the pin-fins that are exposed to a uniform like flow field as per Figure 5.16.

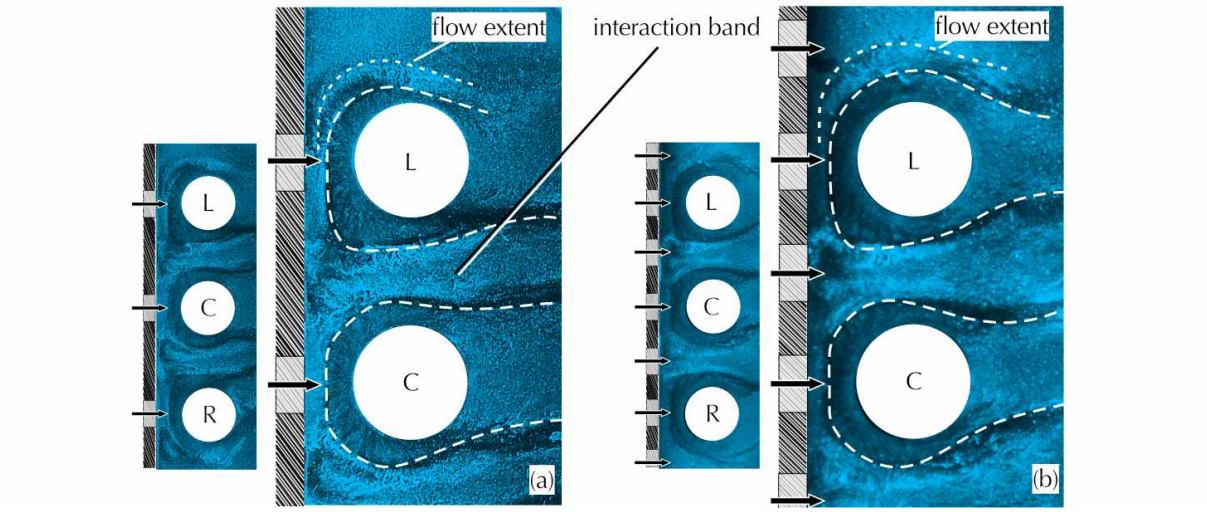

Figure 5.17. End-wall flow fields from oil-dye with 3 pin-fins for Re_j = 22,000 (Re_D = 44,000) with overviews for l/D_j = 1.0. (a) For a 3-jet configuration and (b) For a 7-jet configuration.

The interaction band extends both downstream and upstream to the blockage plate surface. Near the surface of the blockage plate, the interaction band will be augmented by those flows along the blockage plate surface (as per Figure 5.4(d)). Downstream, the interaction band appears to entrain the wake flows from the pin-fins, thereby preventing their convergence. Due to the lack of an interaction band on the outer side of the L and R pin-fins, the wake flows on the outer side of those pin-fins are not similarly entrained. Those wake flows are seen to converge inwards towards the channel centre. This asymmetry about the L and R pin-fins, with an interaction band only to one side, is attributed as the primary cause for the asymmetry of the flow patterns about the L and R pin-fins noted in Figure 5.17(a).

It is notable that the wake is seen to converge in the mid-height plane for l_1 Figure 5.11(a-b). This may seem to be in contradiction to the findings of Chapter 4- the end-wall flows do not appear to directly correlate to the mid-height plane flows, at least downstream of the pin-fins. To clarify, however, the

correlation between the end-wall flows and mid-height flows is, however, understood to still exist. The region where the flows cease radiating from the downstream side of the pin-fin surface still correlate between the two planes. The entrainment of the wake by the interaction band, however, obscures this. The correlation between the mid-height and end-wall flows only pertains to flows on the surface of the pin-fin. Away from the pin-fin surface, no correlation or inferred behaviour can necessarily be made between the flows. For example, converging wake flows in the downstream of the pin-fin in the mid-height plane do not imply that there will exist converging wake flows, downstream of the pin-fin on the end-wall surface.

With a 7-jet configuration (Figure 5.17(b)) the end-wall flow patterns are almost indistinguishable from those of a 3-jet configuration (Figure 5.17(a)). The flow profile around both the C and L pin-fin are very similar. The wake flows do appear to converge slightly more with the 7-jet configuration. Considering that the primary difference is the inclusion of the flanking jets in the mid-height plane it is clear why there is little difference between Figure 5.17(a) and (b). As per the velocity and flow direction distributions in the mid-height plane for l_1 (Figure 5.12), significant differences between the 3- and 7-jet configurations were not expected. Further, the jets would not have contacted the end-wall in the vicinity of the pin-fins for l_1 and so their direct interaction with the end-wall surface is unlikely. The flanking jets do result in an increased amount of flow on the downstream side of the pin-fin, despite the interaction band entraining the wake flow. The interactions observed from Figure 5.17 are schematically represented in Figure 5.18.

The interaction band is likely to be beneficial for cooling purposes due to the large level of interaction, noted by the oil-dye disruption, in the region (Figure 5.17). In turn the formation of the interaction band will be dependent on the spanwise spacing (S_{z1}/D) of the pin-fins. Too large a spacing will result in a weaker interaction band. If there is too small a spacing then the flanking jet centreline velocity, in mid-height plane of a 7-jet configuration, will likely decay even further when passing between the pin-fins. The current spacing of S_{z1}/D =2.0 is seen as appropriate.

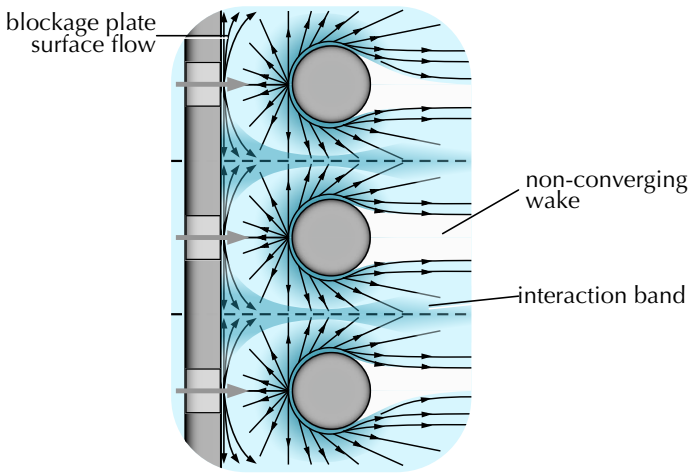

Figure 5.18. Schematic illustrating interaction between end-wall surface jet pin flows for multiple pin-

fins exposed to multiple impinging blockage jets.

Further, it was initially envisaged that the flanking jets would impinge on a second row of pin-fins (as in Figure 5.2). It is now seen that a second row of pin-fins would have both an end-wall flow (from the interaction band) and a mid-height flow (from the flanking jets) interacting with them. This should be beneficial for cooling purposes due to the increased amount of flow interacting with the pin-fin. This does imply that a staggered pin-fin array is necessary. The alternative would be an inline array with the second row of pin-fins being directly behind those of the first row (Figure 2.16(b)). There, however, the first row of pin-fins would block the jet flows from interacting with the second-row pin-fins in mid-height plane. The interaction bands would entrain the wake flows around the pin-fins and prevent an end-wall flow from interacting with the second-row pin-fins as well. A staggered array and flanking jets are therefore concluded as necessary for a more optimal performance of a blockage pin-fin configuration. This coincidentally aligns with the approach for conventional pin-fin arrays – with staggered pin-fin arrays having superior performance to inline pin-fin arrays. Further, the streamwise spacing between the first and second row of pin-fins (S_x/D) must not be so large such that the interaction band has dissipated before interacting with the second-row pin-fins. A spacing of $S_x/D = 1.5$ is proposed.

With the pin-fins positioned at l_2 there are distinct differences the end-wall flows of the 3- and 7-jet configurations (Figure 5.19). These differences between the 3- and 7-jet configurations are attributed to the presence of the flanking jets in the 7-jet configuration. With the 3-jet configuration the flow patterns are asymmetrical about the L pin-fin (Figure 5.19(a)). Unlike for l_1 with the 3-jet configuration (Figure 5.17(a)) the asymmetry for l_2 presents differently. Specifically, there is very little oil-dye disruption on the outer downstream side of the L pin-fin and a vortical structure has formed off the outer leading-edge. With the 3-jet configuration, the pin-fin surface flow on the outer side separated early at the mid-height of the channel (as seen Figure 5.11(c)). This was due to the curvature and off-axis impingement of the outer jet on the pin-fin. End-wall flows therefore do not radiate from the outer surface of the L pin-fin and there exists a large region of undisturbed dye (Figure 5.19(b)). Further, those outer end-wall flows appear to incite the formation of a vortical flow. For the 7-jet configuration, the outer flanking jet forces the separated flow to remain attached to the outer surface of the L pin-fin (Figure 5.11(d)). End-wall flows therefore continue to radiate from the outer surface of the L pin-fin – as seen by the disruption of oil-dye in the region. The increased flow on the pin-fin surface by the outer flanking jet, results in more flow radiating from the downstream side of the L pin-fin. In turn this results in the noted disturbance of the dye in the wake. While the interaction band appears to continue entraining the wake flow of the pin-fins, there exists more flow in the wake of the pin-fin for the 7-jet configuration. Despite the differences in Figure 5.19 for 3- and 7-jet configurations, those flow features represented in the schematic of Figure 5.18, appear to still exist for l_2.

Additionally, it is concluded that any off-axis impingement of a jet on a pin-fin is undesirable. Such a curvature results in a large portion of the end-wall that is not exposed to cooling flows Figure 5.19(a). This has negative consequences for end-wall cooling as per the end-wall heat transfer results

by Kan et al. (2014) in Figure 2.24. It should thus be seen as necessary for any jet curvature to be controlled such that jet flows directly impinge on the pin-fins in a blockage pin-fin configuration.

For l_4 there is a lower velocity magnitude interacting with the pin-fins due to the larger distance between the pin-fin and blockage plate. This results in weaker end-wall flows that are less distinguishable in Figure 5.20. As per flows in the vertical plane (Figure 5.5(e)), the jets are not expected to contact the end-wall upstream of the pin-fins for l_4. There continues to exist the circulating region and backflow along the end-wall surface. Those oil-dye patterns on the end-wall surface, at least upstream of the pin-fins, must be from jet-pin flows.

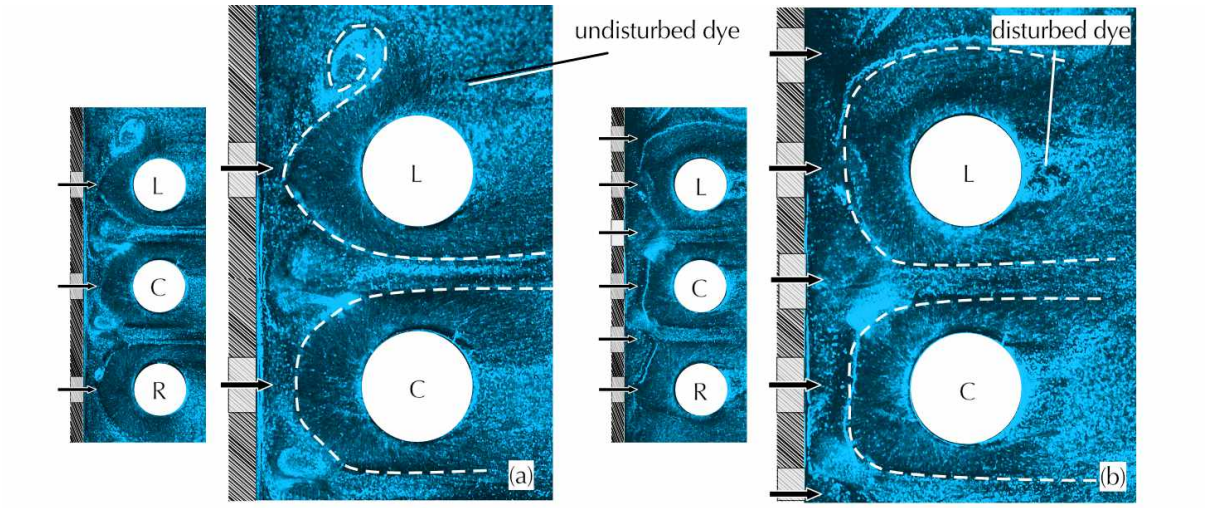

Figure 5.19. End-wall flow fields from oil-dye with 3 pin-fins for Re_j = 22,000 (Re_D = 44,000) with overviews for l/D_j = 2.0. (a) For a 3-jet configuration and (b) For a 7-jet configuration.

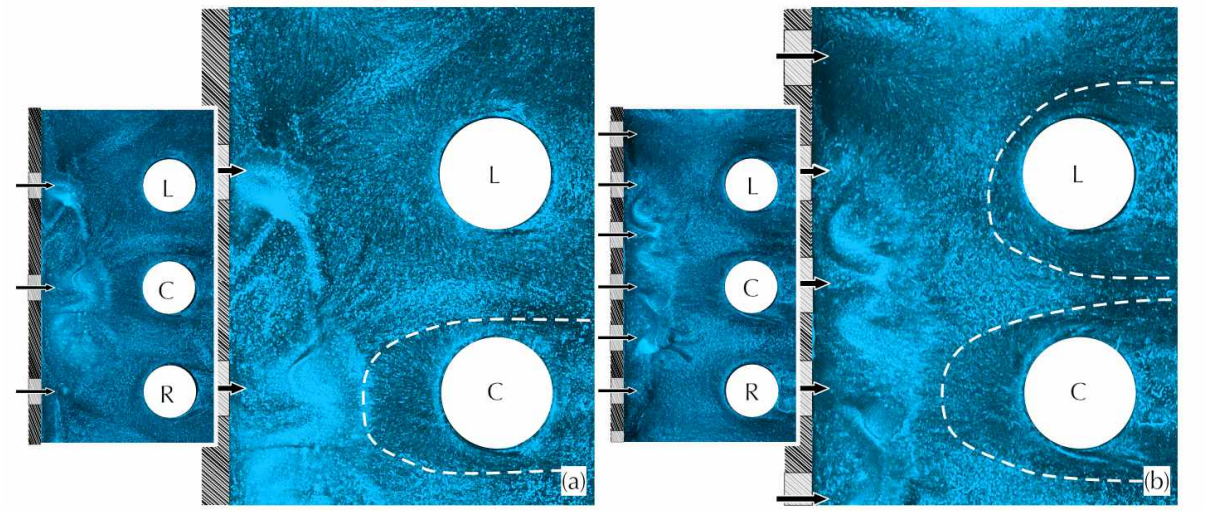

Figure 5.20. End-wall flow fields from oil-dye with 3 pin-fins for Re_j = 22,000 (Re_D = 44,000) with overviews for l/D_j = 4.0. (a) For a 3-jet configuration and (b) For a 7-jet configuration.

The patterns are clearer about the L pin-fin for the 7-jet configuration (Figure 5.20(b)) compared

to the 3-jet configuration (Figure 5.20(a)). This should be expected considering there is more flow acting on the L pin-fin in the mid-height plane (Figure 5.13(g, h) with the 7-jet configuration. This further confirms that flanking jets serve to increase the end-wall flow around the first row of pin-fins. Further discussion of the end-wall flows is, however, seen as unnecessary. The weak end-wall flows for l_4 are likely to result in too low an end-wall heat transfer. Flows around a second row of pin-fins (on which the flanking jets will impinge) be even lower due to the centreline velocity decay noted in Figure 5.3. There is also less flow interacting with the downstream surface of the perforated blockage which, in turn, is expected to result in a poorer heat transfer on that structure. An optimal setup is thus understood to require the first row of pin-fins to be positioned at approximately $l/D_j \approx 2.0$ at most.

5.5. Summary

Following on from the findings of Chapter 4, Chapter 5 introduced the perforated blockage plates. The blockages plates had a significantly shorter thickness to diameter ratio (t/D_j) compared to the tube in Chapter 4. This means that instead of tube jet flows, the perforated blockage formed orifice-like jet flows. Such jet flows featured a potential core length half that of the tube jet in Chapter 4.

Despite the difference in jet type, for a single jet impinging on a single pin-fin, the blockage plates did not fundamentally alter the jet-pin flow structures. There still remains radial and tangential streamlines and a circulating region forms between the counteracting end-wall and channel mid-height flows. Flows predominantly behave similarly for similar l/D_j distances for tube and blockage jet cases. Up to an including a blockage plate to pin-fin spacing of $l/D_j = 4.0$ the blockage jets did not contact the end-wall upstream of the pin-fins. Jet-pin flows existed for all three test cases (l_1, l_2 and l_4). The low velocity of the jet flow interacting with the pin-fin for l_4, due to the shorter potential core, resulted in very weak end-wall flows. It was ultimately concluded that the first row of pin-fins should be placed within $l/D_j \leq 2.0$ for a more optimal blockage pin-fin configuration.

In contrast to the tube jet setup of Chapter 4, with blockage jets, the radial streamlines interacted with the blockage plate at the end-wall. This resulted in flows along the blockage surface in the both y and z directions. Such blockage plate surface flows augmented the periphery flow of the jet-pin flow structure which appeared to further curve the end-wall streamlines. The interaction is expected to be beneficial for cooling performance.

When a row of blockage jets are active, the potential core of the jet is further reduced. This arises due to flow entrainment between the pin-fins. The smaller the spanwise spacing of the jets (S_{z2}/D_j), the shorter the potential core. Flow entrainment also means that the jet flows may be expected to converge downstream. In doing so, each jet except a centrally positioned jet exhibits curvature with those jets further from the channel centre having a higher curvature. The curvature presents as both a shift in the peak velocity magnitude towards the centre of the channel (in the direction of curvature) and an inclination of the flow vectors towards the centre of the channel. The curvature can be sufficient such that the position of peak velocity magnitude skews in the spanwise direction by as much as half the

diameter of the pin-fin. Further the flow can be inclined as much as 45º - 60º from its original trajectory before impinging on the pin-fins. With flanking jets, resulting in a closer transverse spacing of the jets, the jet curvature can be inhibited.

The presence of pin-fins downstream of the perforated blockages does not significantly affect the affect the curvature of the jets for a 3-jet configuration (without flanking jets). In a 7-jet configuration (with flanking jets) the pin-fins appear to inhibit the flow entrainment between jet flows. Jets exhibit a flow curvature similar to that for a 3-jet configuration. Depending on the severity of curvature the flow interacting with the pin-fins is asymmetric about the pin-fin centre. Such asymmetry results in larger amounts of the end-wall not being exposed to end-wall flows. This outcome is viewed negatively for cooling purposes. The jets must be made to impinge on the pin-fins directly whether by controlling the jet curvature or altering the pin-fin spacing to place the pin-fins in the path of the curving jets. The pin-fins also serve to cause the centreline velocity of the flanking jets, passing between the pin-fins, to decay more rapidly than the case without pin-fins. This is in contrast to a conventional pin-fin array where the flow instead accelerates between the pin-fins. The velocity decay between pin-fins necessitates that the spacing between the first and second row of pin-fins (S_x/D) be sufficiently low such that they not exposed to too weak an impinging jet.

When multiple pin-fins are subjected to impinging blockage jets, the end-wall flows can vary from the jet-pin flow structure, as established in Chapter 4, around a single pin-fin. This is in contrast to multiple pin-fins subjected to a uniform flow where the end-wall flows remain largely unchanged. In a blockage pin-fin setup, the end-wall flows between pin-fins have opposing and intersecting vectors. There results a band of interacting flow, referred to as the “interaction band” that extends both upstream to the blockage plate surface and downstream. At the blockage surface, surface flows on the blockage plate augment the flows in the interaction band. Downstream, the interaction band entrains the downstream wake flows from the pin-fins preventing their convergence. The minimal flows in the wake of the pin-fins both in the mid-height plane and on the end-wall require that a staggered pin-fin array is used to ensure a more optimal cooling performance from the blockage pin-fin configuration.

A blockage pin-fin cooling setup should therefore utilise the following: a) Flanking jets, aligned to pass between the first row of pin-fins, b) a blockage to pin-fin spacing of at most $l/D_j = 2.0$ and c) a staggered pin-fin array, with pin-fin array spacings of $S_{z1}/D = 2.0$ and $S_x/D = 1.5$. A configuration using such specifications will be studied in the following chapter.

6. THERMAL PERFORMANCE OF A BLOCKAGE PIN-FIN CONFIGURATION

6.1. Objective

This chapter aims to determine the individual heat transfer contribution of all applicable surfaces or structures in a blockage pin-fin configuration to the overall heat transfer. This will allow for the primary research question regarding the thermal performance to be addressed. Further, this chapter implements the understanding obtained from the previous chapters to propose a new blockage pin-fin configuration. This blockage pin-fin configuration is intended to represent a more optimal thermal performance of this cooling scheme.

6.2. Test setup

6.2.1. General setups

The schematic representing the present test setup is illustrated in Figure 6.1. An axial fan supplies ambient air into a rectangular channel with cross sectional dimensions of W = 200 mm and H = 20 mm. Two perforated blockage plates were staggered and installed in the channel. All perforations had the same diameter of D_j = 10 mm. The blockage plate thickness (t) was half that of the perforation diameter (t/D_j = 0.5) which assumes an orifice-type jet flow (Liu et al., 2022; Ward-Smith, 1971).

Five rows of staggered circular pin-fins were positioned downstream of the two perforated blockage plates and had a diameter (D) twice that of the perforation diameter (D/D_j = 2.0). The pin-fin spacings were S_{z1}/D = 2.0 and S_x/D = 1.5. The pin-fins had an aspect ratio H/D = 1.0. This was based on previous studies using pin-fin arrays (Lawson et al., 2011; Lyall et al., 2011; Metzger et al., 1984). To ensure the alignment of the second blockage plate perforations with the pin-fins, the perforation spacing was set at S_{z2}/D_j = 2.0 (S_{z2}/D = 1.0). Both blockages had 10 perforations. For the second blockage, the first and tenth perforations were split into two half circles at the channel edge.

The first pin-fin row was positioned x/D = 1.0 downstream from the exit of the second blockage (l/D_j = 2.0). The distance between the perforated blockage plates, relative to the height of the channel was $l_b/H = l_b/D$ = 1.5. The pin-fins, perforated blockages, and bottom end-wall were machined from aluminium for heat transfer measurements. The channel sidewalls and lid (top end-wall) were machined from transparent Perspex to allow for an optical access using thermal and velocity field mapping techniques (to be discussed later). A sidewall was machined for static pressure taps, which were positioned along the channel at selected locations as indicated in Figure 6.1. The furthest downstream location was positioned x/D = 10 from the second perforation blockage. Heating and heat transfer specifications were covered previously in Chapter 3.6.3.

The Reynolds number was fixed at Re_D = 26,000, based on the pin-fin diameter (Re_j = 13,000 based on the perforation diameter or Re_{Dh} = 10,000 based on the hydraulic diameter of the test

rectangular channel). Fully turbulent flow would thus be expected for the blockage jets (McNaughton & Sinclair, 1966). This Reynolds number falls in the range that is accepted to cover most turbine applications of $3.0 \times 10^3 < Re_D < 5.0 \times 10^4$ (Metzger et al., 1984).

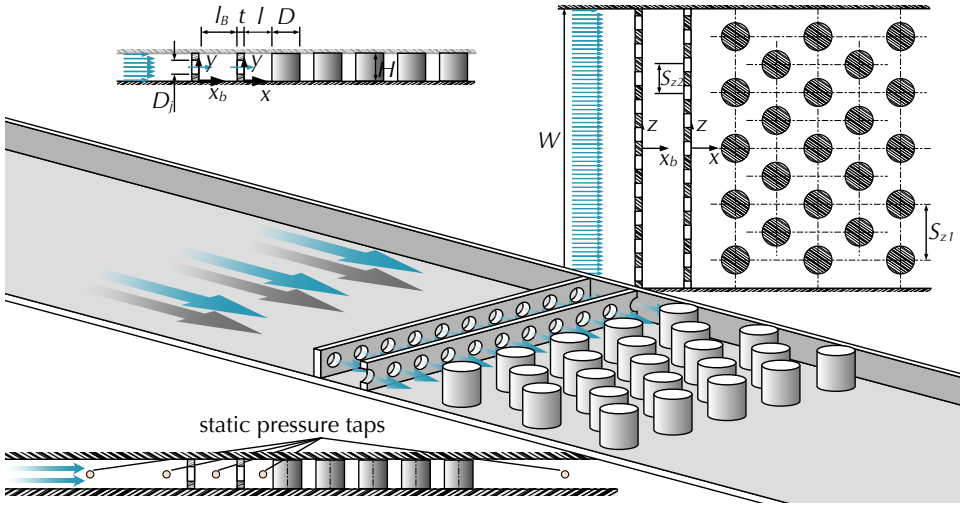

Figure 6.1. Test section schematic for consideration of a complete blockage pin-fin configuration.

The naming convention of centre, outer and flanking jets used in Chapter 5 is not appropriate here. Instead the blockage jets can be broken down into three groups: "1st row jets" (via $z/D_j = 0.0, \pm4.0$ and ±8.0), "2nd row jets" (via $z/D_j = \pm2.0$ and ±6.0) and "sidewall jets" (via $z/D_j = \pm10.0$). 1st row jets are those that are geometrically aligned with the first row of pin-fins. Likewise, the 2nd row jets are geometrically aligned with the second row of pin-fins. Sidewall jets are those exiting along the sidewalls.

As the convention established previously, the origin would be situated on the end-wall surface. Measurements around the pin-fin array would use the downstream surface of the second perforated blockage as the origin. Measurements between blockages would use an alternate x_b axis.

6.2.2. Rationale for specifications

A whole new setup was developed to accommodate those findings from Chapters 4 and 5. The final design was developed based on the following design requirements:

- The channel width (W) was reduced by half to 0.2m. The channel width from Chapters 4 and 5 was 0.4 m. This was too large for the PIV system to capture the full flow field. A reduction of half was necessary. The final width of 0.2m was also governed by the spacings associated with the pin-fin array and perforated blockages.
- A pin-fin spanwise spacing of $S_{z1}/D = 2.0$ ($S_{z2}/D_j = 4.0$) would be maintained from Chapter 5. This spacing was sought to encourage interactions between the end-wall flows from neighbouring pin-fins. This interaction resulted in the interaction band that is anticipated to have favourable heat

transfer behaviours.

- Blockage perforations would therefore also have a spanwise spacing of S_{z2}/D_j = 2.0. As per the findings of Chapter 5, flanking jets were strictly necessary.
- A constant blockage ratio must exist for the first and second blockage. This was set at A_b/A_j = 0.196 (19.6%). This ratio is similar to that used by Kan et al. (2014) at 22.5% and Moon and Lau (2003) at 16.3%.
    - To maintain the same blockage ratio, the same number of perforations in both blockages is required. These perforations need to be staggered to ensure a more optimal heat transfer on the end-wall between the blockages. As such, one perforation was split at either end of the second blockage (as seen in Figure 6.1).
    - The use of a split perforation at the sidewalls was chosen for the second perforated blockage as the main means of preventing jet curvature through the pin-fin array. The jet curvature occurred in Chapter 5 due to an asymmetric entrainment of the jets. The outer flanking jets were only entrained towards the center of the channel with no corrective action to prevent this. An interaction with the sidewall can cause a jet to be entrained towards it. This was achieved by placing the jet directly on the sidewall (by way of half perforations on the surface).
    - The pin-fins would span the full width of the channel with a spacing of 1.0D between the centre of the outer pin-fin and channel side-wall.
- A staggered pin-fin array would be employed for the findings of Chapter 5.
- Five pin-fins rows would be used as this aligns with what was used by Kan et al. (2014) for better comparisons.
- A pin-fin aspect ratio was set at H/D = 1.0. As the test channel was being completely redesigned, it was not necessary to work to the restrictions offered by the existing setup. The more ideal aspect ratio of 1.0 could thus be used.

6.3. Flows in the channel mid-height

6.3.1. Without pin-fins

In establishing a base case, without the influence of pin-fins, a perforated blockage (PB) configuration is considered first. Velocity contours from PIV in the mid-height of the channel (y/H = 0.5) and no downstream pin-fins are shown in Figure 6.2. Upstream of the first blockage (Figure 6.2(a: i)), the fluid is largely uniform across the full width of the channel. Near the upstream surface of the first blockage plate, regions of higher velocity flow exist. These correlate to the z-axis position of the perforations of the first blockage surface (z/D_j = 0.0, ±2.0, ±4.0, ±6.0 and ±8.0) – the flow accelerating through the perforations. Elsewhere, flow on the upstream surface is stagnated – there low velocity flows exist.

From the first blockage, a row of blockage jets is observed in Figure 6.2(a: ii). These travel downstream and stagnate on the upstream surface of the second perforated blockage. There are no fountain jet flows present. This is due to the staggered spacing of perforations between the first and second blockage plate. Those wall-jet flows on the upstream surface of the second blockage are redirected through the perforations of the second blockage instead of back upstream as a fountain jet. This was predicted as shown in Figure 2.17(c), which was based on prior studies. Those prior studies, however, either inferred such flows or observed them through numerical simulations. To the best of the authors' knowledge, this is the first experimental flow visualization of the flows between and downstream of perforated blockages.

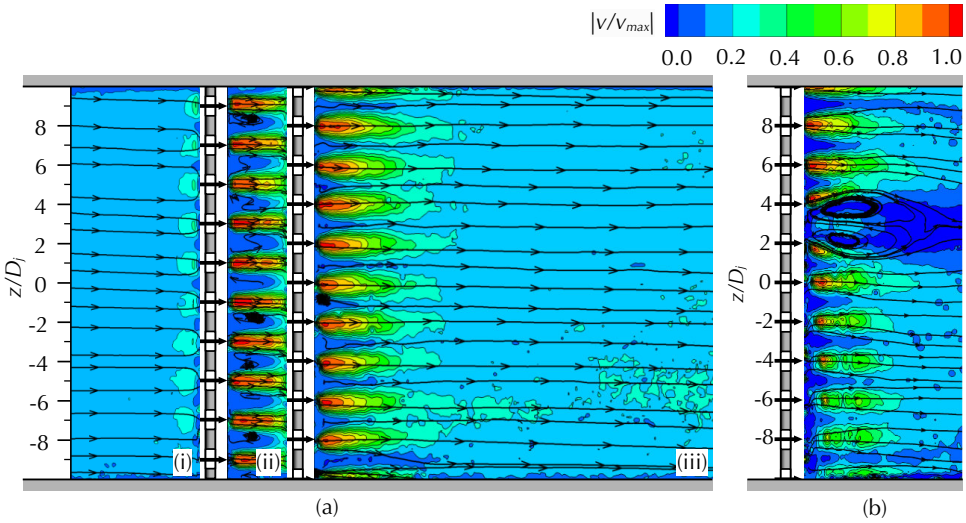

Figure 6.2. Velocity contours from PIV at the channel mid-height ($y/H = 0.5$) for a perforated blockage configuration, without downstream pin-fins at Re_j = 13,000 (Re_{Dh} = 10,000). (a) A standard result and (b) An anomalous result.

Downstream of the second perforated blockage there is no evident jet curvature (Figure 6.2(a: iii)). Unlike the setup used in Chapter 5, the blockage jets in the second perforated blockage are spread across the full width of the test channel with two half perforations at either end, $z/D_j = \pm 10.0$. During a repeated measurement, however, the velocity contours shown in Figure 6.2(b) were captured where the jets exiting at z/D_j = 2.0 and 4.0 are seen to clearly curve and merge with the jets exiting at z/D_j = 0.0 and 6.0, respectively. It is unclear why this occurred and was not noted in other measurements. The velocity contours in Figure 6.2(b) are seen to represent an anomaly but do serve to demonstrate that jet curvature can occur even when the jets are distributed across the full width of the channel. Here on it is, assumed that the velocity contours in Figure 6.2(a: iii) represent the actual flow conditions through the test section.

The centreline velocity decay for various blockage jets considered in this study, from Chapter 5 and extracted from the PIV measurements in Figure 6.2 are presented in Figure 6.3. Between blockages,

the blockage jets appear to follow a decay somewhere between that of a 1-jet and 7-jet configuration from Chapter 5 (Figure 6.3). There is a steep drop-off in centreline velocity preceding the jets stagnation on the upstream surface of the second blockage. Prior to the deceleration, there is a local minimum in the centreline velocity at $x_b/D_j = 0.65$. It is unclear if this is an artefact from the PIV measurements or an actual flow behaviour. It does make the identification of the potential length difficult. The local minima in the centreline velocity distribution is, however, seen as being generally inconsequential and is not considered further.

It was also seen in Chapter 5 that the presence of neighbouring jets resulted in the potential core of the jet being shorter. With the current 10-jet configuration setup, the centreline velocity of centre jet (exiting $z/D_j = 0.0$ of the second blockage) has an even shorter potential core as shown in Figure 6.3. For the 1-jet configuration, the potential core length was $l_p/D_j = 2.0$. With the 3-jet configuration ($S_{z2}/D_j = 4.0$) the potential core was $l_p/D_j = 0.75$. The potential core was $l_p/D_j = 0.5$ for the 7-jet configuration ($S_{z2}/D_j = 2.0$). In the current setup ($S_{z2}/D_j = 2.0$), the potential core is just $l_p/D_j = 0.4$. This slightly shorter potential core length is attributed to the small differences in some parameters used between Chapter 5 and the current setup (for example different H/D_j ratios). The lower Reynolds number used in the current study should not result in a shorter potential core as the jets are turbulent in both cases ($Re_j > 3000$). According to Gauntner et al. (1970), the potential core length is independent of the nozzle Reynolds number for a turbulent jet. It thus appears that the spanwise spacing (S_{z2}/D_j) of the blockage jets is the governing factor in determining a decrease in potential core length.

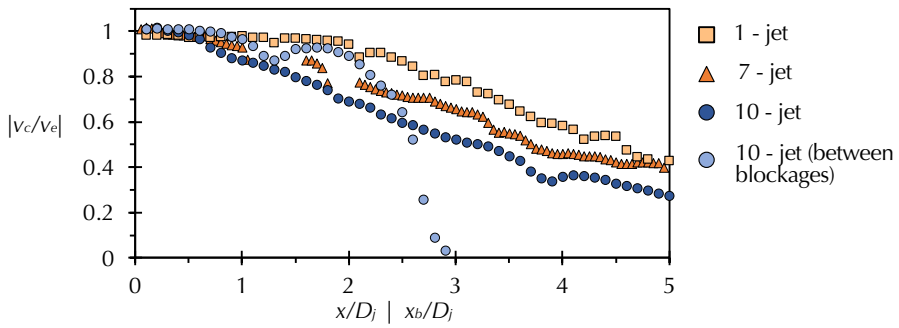

Figure 6.3. Centreline velocity decay for blockage jets ($t/D_j = 0.5$) in various configurations at Re_j = 22,000 for 1- and 7-jet configurations and Re_j = 13,000 for 10-jet configurations.

6.3.2. With pin-fins

Velocity contours from PIV in the mid-height of the channel for a blockage pin-fin (BPF) configuration is shown in Figure 6.4(a). The 1st row blockage jets (exiting at $z/D_j = 0.0, \pm 4.0$ and ± 8.0) stagnate on the first row of pin-fins, set at a distance $l/D_j = 2.0$. The resulting flow features around the first row of pin-fins resemble those from Chapter 4 (as in Figure 4.8) and Chapter 5 (as in Figure 5.11).

Notably, in contrast to the l_2 case in Chapter 5, none of the blockage jets exhibit any significant flow curvature. All blockage jets appear to be impinging directly and in line with the pin-fins. Curvature

of the blockage jets was previously noted for a blockage pin-fin configuration by Kan et al. (2014) and Kim et al. (2019). Based on those results, it was not clear whether the curvature was due to either the natural behaviour of the blockage jets, the pin-fins inciting the flow curvature and/or the misalignment of the blockage perforations with the pin-fin positions. From Chapter 5, it was seen that blockage jets can exhibit curvature. This curvature can, however, be controlled or manipulated as evidenced by the lack of curvature in Figure 6.2(a: iii). Chapter 5 further showed that the pin-fins can inhibit the entrainment between jets and allow for increased jet curvature. Based on Figure 6.4(a), it is then further confirmed that, in the event of jets not curving, the presence of pin-fins does not incite flow curvature. This appears to hold for the case of pin-fins being geometrically aligned with the perforations.

For comparison the velocity contours from PIV in the mid-height of the channel for a conventional pin-fin array (CPF) configuration is shown in Figure 6.4(b). There is a near uniform flow approaching the first row of pin-fins. That region of higher velocity flows between the pin-fins arises from the flow accelerating between the first row of pin-fins. The velocity distributions along the length of the BPF and CPF arrays have been extracted from Figure 6.2(a: iii) and Figure 6.4. These are plotted in Figure 6.5(a) for $z/D_j = 2.0$ and Figure 6.5(b) for $z/D_j = 0.0$

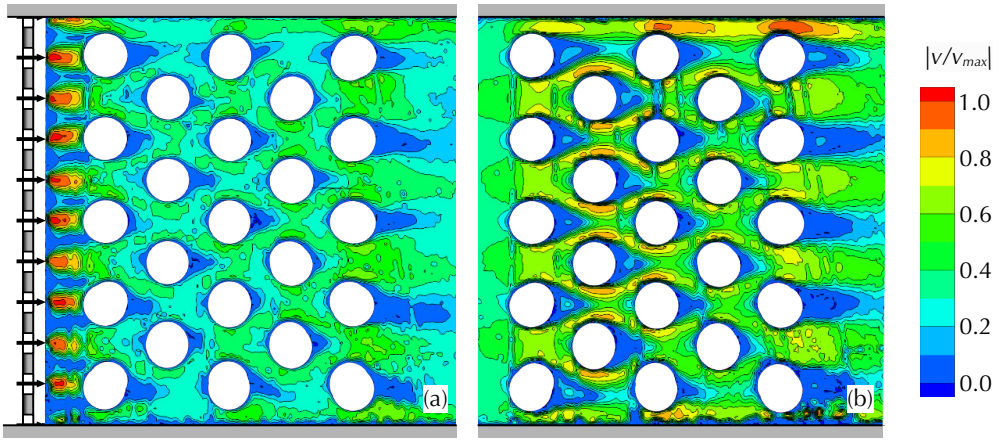

Figure 6.4. Mid-height velocity contours with pin-fins from PIV at Re_D = 26,000 (Re_{Dh} = 10,000). (a) With upstream perforated blockages as a blockage pin-fin configuration and (b) Without upstream perforated blockages as a conventional pin-fin array configuration.

The 2nd row blockage jets (exiting at $z/D_j = \pm 2.0$ and ± 6.0) behave similarly to the 1st row blockage jets (exiting at $z/D_j = 0.0, \pm 4.0, \pm 8.0$) up until the first row of pin-fins. From Figure 6.5(a) it is seen that the 2nd row blockage jets decay more rapidly when passing between the first row of pin-fins. This behaviour was also noted in Chapter 5 (as per Figure 5.15). After the first row of pin-fins, however, the flow does accelerate between the pin-fins as seen along $z/D_j = 0.0$ (Figure 6.5(b)) and $z/D_j = 2.0$ (Figure 6.5(a)). This is equivalent to how the flow in a conventional pin-fin array (Figure 6.4(b)) behaves, with the accelerations correlating between the two configuration types as seen in Figure 6.5.

This implies that downstream of the first row of pin-fins the flow through the array begins to behave like that of a uniform flow through a conventional pin-fin array. This is not unexpected. As shown in the findings of Chapter 4 when there was sufficient distance between the jet exit and pin-fin, horseshoe vortex like flows were noted. The jet flows will eventually diffuse such that they occupy the full span and height of the channel. If there is sufficient distance this flow will eventually be equiavalent to a uniform flow through a pin-fin array.

Despite this similarity, the velocity distribution along the span of the channel for the BPF configuration (Figure 6.4(a)) appears more uniform compared to the CPF configuration (Figure 6.4(b)). Consider the standard deviation of the velocity magnitude along the z-axis and at a given x position. For the BPF configuration, the standard deviation was approximately 0.13 while it was approximately 0.23 for the CPF configuration. While the flow through a BPF may then develop to behave like that of a CPF configuration, there remain differences even by the 5th row of pin-fins.

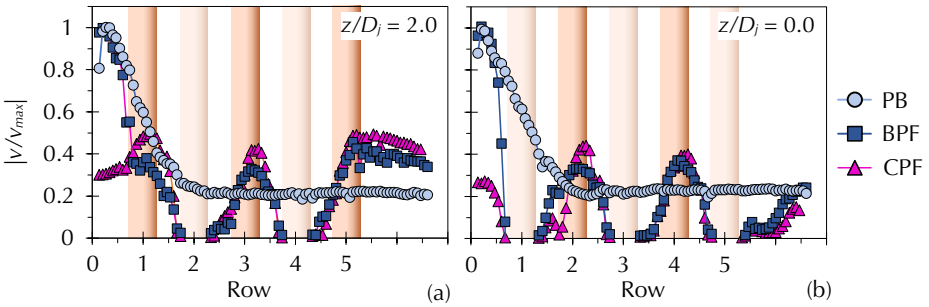

Figure 6.5. Velocity variations along the x-axis through perforated blockage (PB), blockage pin-fin (BPF) and pin-fin (PF) array configurations at Re_D = 26,000 (Re_j = 13,000, Re_{Dh} = 10,000). (a) From z/D_j = 0.0 and (b) From z/D_j = 1.0.

6.4. Flows at the end-wall surface

The end-wall surface flows were visualized using oil-dye mixtures in Figure 6.6 for the BPF configuration (a-b) and for a CPF configuration (c). No notable end-wall flow patterns were noted downstream of the second perforated blockage for the PB configuration and are thus not considered here.

Between the perforated blockages, the blockage jets impinge on the second perforated blockage in the mid-height plane (Figure 6.2(a: ii)). The jet flows are subsequently redirected away from the stagnation point, a portion of which is towards the upper and lower end-walls as wall-jet flows. The wall-jets stagnate on the end-wall surface and accelerate upstream as back flows. The backflow stagnates on the downstream surface of the first blockage. It is then redirected back downstream as a fountain jet (similar to Figure 2.17 in the mid-height plane). Such back flows and fountain jet flows can be discerned in the close up of end-wall flow patterns in Figure 6.6(a). The presence of these fountain jets on the end-wall surface is not discussed or acknowledged in prior studies involving perforated

blockages.

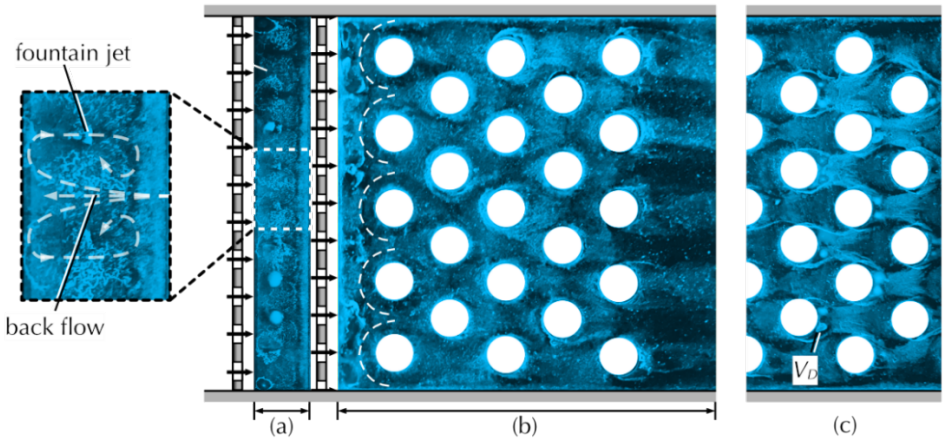

Figure 6.6. End-wall surface flow patterns by oil-dye flow visualization at Re_D = 26,000 (Re_{Dh} = 10,000). (a) Between perforated blockage plates in blockage pin-fin configuration with closeup on the left, (b) Around a pin-fin array in a blockage pin-fin configuration, and (c) Section of end-wall around a pin-fin array in a conventional pin-fin array.

Around the pin-fin array, the end-wall flow patterns in Figure 6.6(b) appear somewhat symmetrical along the span of the channel, including those pin-fins nearest the channel side wall. This corresponds with the flow in the mid-height the channel being symmetrical along the channel span (Figure 6.4). The front profile of jet-pin flows can be identified, as annotated, around all pin-fins in the first row (Figure 6.6(b)). As per the findings of Chapters 4 and 5, only jet-pin flows should exist around the first row of pin-fins. Despite the flow interaction band between the pin-fins, the wake flows appear to converge in downstream of the first row of pin-fins. In Chapter 5 it was seen that the interaction band (as in Figure 5.18) entrained the wake flows from the pin-fins, preventing their convergence. Second row blockage jets (there flanking jets) did increase some flow immediately downstream of the pin-fins but the wakes did not converge. The converging wakes is attributed to the nearby presence of the second row of pin-fins. The flows in the interaction band are forced to flow around those pin-fins which in turn causes a convergence of sorts.

At the second row of pin-fins, there are no clear flow patterns. This is partly due to the small size scale present in the setup. But it is also expected considering these pin-fins exposed to the 2nd row blockage jets from a distance l/D_j = 5.0. By l/D_j = 4.0, in Chapter 5, the end-wall flow patterns were already weak and showed little disruption of the oil-dye particles (Figure 5.20). By the third row of pin-fins, flow patterns analogous with horseshoe vortex flows begin to exit as seen around the C pin-fin in row 3. These are not exactly like those of horseshoe vortices based on a comparison to a convectional pin-fin array in Figure 6.6(c). There exist distinctly different end-wall flow patterns, including the wake vortex V_D behind many of the pin-fins. This further illustrates that despite the similarities in the velocity contours at the channel mid-height (Figure 6.4), the flows are not behaving the same for BPF and CPF

configurations over the full length of the channel.

6.5. End-wall heat transfer

The end-wall heat transfer contours for a blockage pin-fin configuration from TLC measurements are shown in Figure 6.7. A very high end-wall heat transfer is noted between the perforated blockages (Figure 6.7(a)). The heat transfer decreases in bands of similar heat transfer away from the upstream surface of the second blockage. There are no localised regions of higher heat transfer from the back flows. While the back flows can be identified in the end-wall flows (Figure 6.6(a)), they are seemingly absent in the end-wall heat transfer contours. This is attributed to the presence of the fountain jets on the end-wall. These result in the more uniform heat distribution amongst the back flows seen in Figure 6.7(a). Further, the heat transfer contours do correlate well with those from Moon and Lau (2003) (shown in Figure 2.18(a)) for a similar Reynolds number and configuration setup. It is only when the blockage perforations were staggered in the y-axis (as in shown in Figure 2.18(b)) that the presence of backflows is noted.

A larger variation of end-wall heat transfer occurs along the end-wall heat transfer surface around the pin-fin array (Figure 6.7(b)). At the first row of pin-fins, clear contour bands surrounding the leading-edge of the pin-fins in the first row are observed. These correlate with the jet-pin flows around the pin-fins in the first row and are very similar to the heat transfer contours noted in Chapter 4 (as in Figure 4.14). Downstream from the second row of pin-fins, there are no such contour bands and the end-wall heat transfer decreases consistently through each row of pin-fins. This corresponds with the end-wall flow patterns from oil dye visualization in Figure 6.6(b) where no clear jet-pin flows were observed.

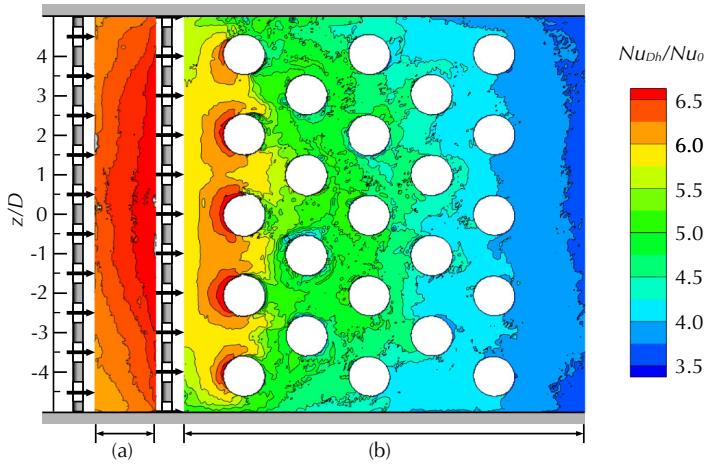

Figure 6.7. End-wall surface heat transfer contours measured by TLC for the BPF configuration at Re_D = 26,000 (Re_{Dh} = 10,000). Between perforated blockage plates and (b) Around a pin-fin array.

There is consistently lower end-wall heat transfer near the channel sidewalls. Further, there

appears to be asymmetric end-wall heat transfer contours around the outer pin-fins (for the first, third and fifth rows). Such asymmetry is not apparent in Figure 6.6(b). It is also not expected based on the findings of Chapter 5. There for $l/D_j = 2.0$ and with 2nd row blockage jets (there flanking jets) the end-wall flow patterns were largely symmetrical about the L pin-fin as shown in Figure 5.19(b). The asymmetry is then likely due to a combination of the closer proximity of the side-walls in comparison to the setup in Chapter 5 and the end-wall interaction bands between the pin-fins. For the outermost pin-fins there is no interaction band with the outer side of the pin-fins and the side-walls. There is a corresponding lower end-wall heat transfer. The interaction bands are thus seen to contribute significantly to the end-wall heat transfer as surmised in Chapter 5.

To highlight local end-wall features, the end-wall heat transfer was extracted from Figure 6.7 at two transverse locations ($z/D_j = 0.0$ and 2.0). These heat transfer variations are plotted in Figure 6.8. Along $z/D_j = 0.0$ (Figure 6.8(a)), the local end-wall heat transfer can be seen to increase leading up to the first row of pin-fins. This variation correlates with that from Chapter 4 (Figure 4.7(b) for $\alpha = 0.0$). Along $z/D_j = 2.0$ (Figure 6.8(b)) there is also an increase in end-wall heat transfer leading up to the first row of pin-fins. This increase is attributed to the end-wall interaction bands between the pin-fins. Downstream of the first pin-fin row, along $z/D_j = 0.0$, there is a slight increase in heat transfer leading up to the second row of pin-fins. This is also attributed to an interaction band type flow and indicates that jet-pin type flows may exist around the second row of pin-fins. There are increases following the 3rd pin-fin row along $z/D_j = 0.0$ in Figure 6.8(a) and 2nd and 4th pin-fin rows along $z/D_j = 0.0$ in Figure 6.8(a). These increases, however, stop short of the subsequent pin-fin row. Following these increases the end-wall heat transfer consistently decreases through the pin-fin rows. There is, however, a slight increase in heat transfer leading up to the next aligned pin-fin, specifically the 3rd pin-fin row along $z/D_j = 0.0$ and 4th pin-fin row along $z/D_j = 2.0$. The increase are likely due low Reynolds number equivalent horseshoe vortex flows based on Chapter 4.

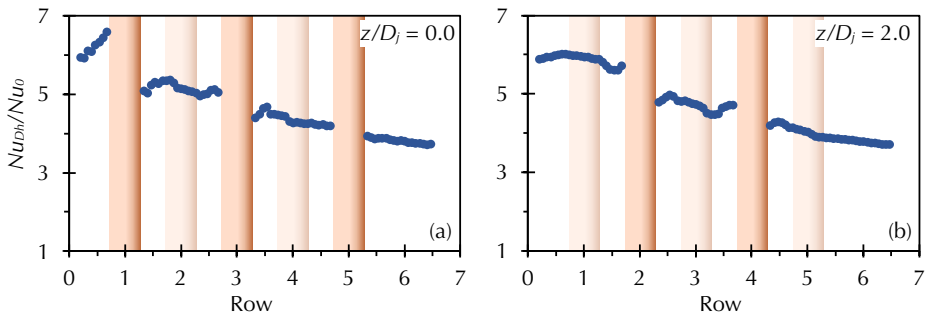

Figure 6.8. Local end-wall heat transfer variation along the length of a pin-fin array in a blockage pin-fin configuration for at $Re_D = 26{,}000$ ($Re_j = 13{,}000$, $Re_{Dh} = 10{,}000$). (a) At $z/D_j = 0.0$ and (b) At $z/D_j = 2.0$.

Figure 6.9 shows the end-wall heat transfer averaged in the spanwise (z) direction along the

streamwise (x) direction. Between the blockages (Figure 6.9(a)), the end-wall heat transfer is almost uniform with a variation of approximately $\Delta Nu/Nu_0$ = 0.5 across the end-wall surface and an average heat transfer of $\overline{Nu_{Dh}}/Nu_0$ = 6.37. The variation is much smaller compared to Moon & Lau (2003) as seen in Figure 6.9(a). This is attributed to the relatively short distance between the perforated blockages (l_b/H = 1.5 compared to 2.0 or higher in previous studies such as Moon & Lau (2003)) and a narrow spacing between perforations (S_{z2}/D_j = 2.0). The average heat transfer, however, correlates with that seen by Moon & Lau (2003), Ahn et al. (2007), and Park et al. (2016) for a conventional perforated blockage (PB) configuration (i.e., without downstream pin-fins).

Those local variations in the end-wall heat transfer shown in Figure 6.8(a-b) result in a predominantly monotonic decrease in end-wall heat transfer along the length of the pin-fin array (Figure 6.9(b)). Near 1st row of pin-fins, however, the setup by Kan et al (2014) resulted in a higher end-wall heat transfer compared to the current setup. Over the length of the pin-fin array, however, the current setup has a superior end-wall heat transfer performance. Specifically, the area-averaged end-wall heat transfer of the current study was $\overline{Nu_{Dh}}/Nu_0$= 4.65. Kan et al. (2014) obtained an area-averaged end-wall heat transfer of $\overline{Nu_{Dh}}/Nu_0$= 3.45. The end-wall heat transfer by Kan et al. (2014) plotted in Figure 6.9(b) correlates with the heat transfer contours of Figure 2.24(a). The higher heat transfer in the current setup is attributed to those optimisations made to the BPF. This includes the alignment between the pin-fins and blockage perforations and the streamwise spacings of the pin-fins. Note that Kan et al. (2014) used a streamwise spacing of S_x/D = 2.0, compared to S_x/D = 1.5 in the current study.

In comparison to a CPF configuration (by Lawson et al. (2011)), the blockage pin-fin configuration resulted in a consistently higher end-wall heat transfer. The area-averaged end-wall heat transfer for the conventional pin-fin array was $\overline{Nu_{Dh}}/Nu_0$= 2.72 (Lawson et al., 2011). The higher heat transfer for the current study is attributed to the unique end-wall flow features of the blockage pin-fin configuration (identified in Chapters 4 and 5) but also the optimisation of the BPF configuration in comparison to that used by Kan et al. (2014). One could argue against the superior performance of the blockage pin-fin configuration compared to the conventional pin-fin array. Specifically, that the space occupied by the perforated blockages limits the number of pin-fin rows that could be implemented downstream. The more perforated blockages used or a larger the space between the blockages would result in less space being available for pin-fins. Considering a pin-fin streamwise spacing of S_x/D = 1.5 in the present study, the perforated blockages occupied a space of two pin-fin rows. The averaged end-wall heat transfer for the blockage pin-fin configuration (from both between the blockages and around the pin-fin array) was $\overline{Nu_{Dh}}/Nu_0$ = 4.93. For the conventional pin-fin array of seven rows (accounting for the extra two pin-fin rows taken by the perforated blockages), the averaged end-wall heat transfer was $\overline{Nu_{Dh}}/Nu_0$ = 3.3 (Lawson et al., 2011). There is then a clear increase in the end-wall heat transfer offered by the inclusion of perforated blockages. This also confirms the design logic of using at least two perforated blockages instead of one.

In contrast to a CPF configuration, the end-wall heat transfer for a BPF configuration decreases monotonically downstream from the first pin-fin row. For a CPF configuration the end-wall heat transfer increases with successive pin-fin rows. As a result, a CPF configuration requires a minimum number of rows in order for an optimal heat transfer to be achieved as per the findings of Goldstein and Chen (1998). A blockage pin-fin configuration is the opposite, and appears better suited to fewer pin-fin rows – a more compact setup.

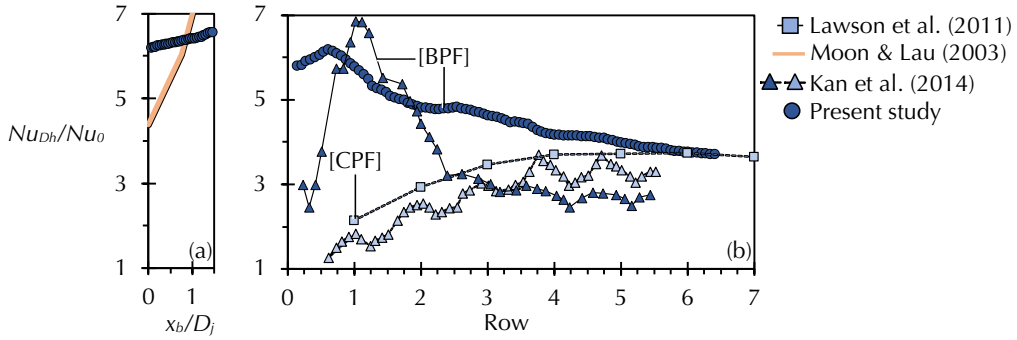

Figure 6.9. End-wall heat transfer averaged in the transverse (z) direction for the blockage pin-fin (BPF) and conventional pin-fin (CPF) configurations at $Re_{Dh} \approx 10{,}000$. (a) Between perforated blockages and (b) Around the pin-fin array.

The heat transfer at the end-wall, however, only represents a portion of the heat transfer for the overall blockage pin-fin configuration. The flow in the mid-height plane and the end-walls is acting on both the perforated blockages and the pin-fins directly. The heat transfer on these elements, therefore, needs to be considered as well.

6.6. Heat transfer on perforated blockage surfaces

The heat transfer on the perforated blockage surfaces is shown in Figure 6.10. For both first and second perforated blockages (Figure 6.10(a, b)), a clear variation across the mid-height line ($y/H = 0.5$) is observed with the upper half of the blockages ($y/H > 0.5$) having higher heat transfer. This is not due to an asymmetry in the flow across the bottom and top half of the channel. Instead, only one end-wall surface was heated. Therefore, the farther from the heat end-wall the lower the perforated blockage surface temperature and higher the calculated heat transfer. The heat transfer across the span of the blockage (in the z-axis), the heat transfer is largely symmetrical about $z/D_j = 0.0$. The higher heat transfer towards the centre of the blockages ($z/D_j = 0.0$) correlates to where there is higher end-wall heat transfer (Figure 6.7(b)).

On the second perforated blockage (Figure 6.7(b)) distinct vertical bands of high heat transfer on the downstream surface are formed. These vertical bands correlate with the position of the first row of pin-fins. From these pin-fins, there will exist radial flows in an upstream direction. The upstream

flowing end-wall flows from these pin-fins. Such flows were observed in Chapter 5 for Figure 5.5(c-e). The flow interaction with the blockage surface results in a localised region of higher heat transfer. Less heat transfer occurs at the outer pin-fins ($z/D = \pm 4.0$).

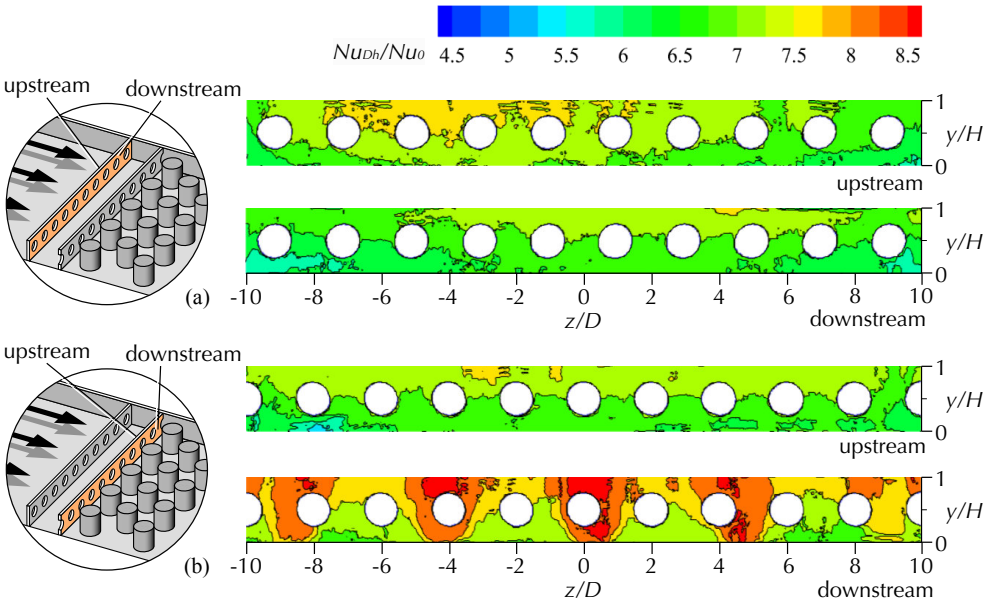

Figure 6.10. Heat transfer contours measured using TLC on the surface of the perforated blockages of a blockage pin-fin configuration at Re_{Dh} = 10,000: (a) The first blockage and (b) The second blockage.

The vertical bands were not evident on the upstream surface of the perforated blockage, despite the relatively thin blockage (t/H = 0.25, t/D_j = 0.5). The upstream surface, however, is exposed to a more distributed cooling flow of ten blockage jets impinging on its surface (as seen in Figure 6.2(b)). On the downstream surface, the cooling flow is coming from the five pin-fins in the first row with a spacing twice that of blockage jets ($S_{z2}/D_j = 0.5\ S_{z1}/D_j$). Despite the distinct variations in the heat transfer contours, the average heat transfer on the downstream surface of the second blockage is only $\Delta Nu_{Dh}/Nu_0$ = 0.86 higher than that of the upstream surface. On the first blockage the difference between the upstream and downstream surface is smaller at $\Delta Nu_{Dh}/Nu_0$ = 0.39. On the second blockage, however, the downstream surface has a higher heat transfer than the upstream surface while the upstream surface has a higher heat transfer than the downstream surface. The second blockage has an average heat transfer only $\Delta\overline{Nu_{Dh}}/Nu_0$ = 0.47 higher than that of the first blockage.

To the best of the authors' knowledge, the heat transfer on the surface of a perforated blockage, used for cooling applications has not been presented previously. It was commented by Lau (2008) that the heat transfer on the blockages would not be negligible. Based on the present measurement data, the average surface heat transfer for the two perforated blockages is $\overline{Nu_{Dh}}/Nu_0$ = 7.11. This high value should be expected considering the plates are being exposed to direct jet impingement.

The blockages make up 21% of the overall cooling surface area in the configuration. Even a

single perforated blockage, as used in the setup by Kan et al. (2014) and Kim et al. (2019), could be expected to contribute notably to the overall heat transfer performance. Their contribution to the overall heat transfer cannot therefore be considered negligible.

6.7. Pin-fin heat transfer

The heat transfer on the pin-fins, based on TLC measurements, is shown in Figure 6.11. The average surface heat transfer on each pin-fin is shown in Figure 6.11(a). There is a slight variation in the heat transfer across the pin-fins in each row of approximately 5%. This is unlikely to be due to asymmetrical flows, as per the flow in the mid-height of the channel (Figure 6.4(a)). Similar variations were noted by Chyu et al. (1998) and Chyu et al. (1999) for conventional pin-fin arrays where uniform flow across the span of the channel would be expected. The small variations in the flow field seen around each pin-fin in each row (Figure 6.4(a)) are attributed as the primary cause for the variations.

From these values, the row averaged heat transfer is calculated (Figure 6.11(b)). The measurements by Chyu (1989) used the naphthalene sublimation mass transfer analogy while Kan et al. (2014) used the direct heat transfer measurements using TLC. Lawson et al. (2011) did not present the row averaged heat transfer for the pin-fins. The pin-fin heat transfer for the BPF configuration by Kan et al. (2014) should be viewed sceptically as only the central pin-fins were measured. The pin-fins in each row were not necessarily subjected to the same flow conditions based on inconsistent heat transfer around the base of the pin-fins. Those values plotted in Figure 6.11(b) are from the same test condition as the end-wall heat transfer contours in Figure 2.24(a). This is why there appears to be a small difference between the first and second row pin-fins for the Kan et al. (2014) data – the centre pin-fins in the first row do not have direct flow impingement. Therefore, the pin-fin heat transfer values by Kan et al. (2014) does not necessarily represent the average heat transfer for a given row or the entire array of the blockage pin-fin configuration. They are included here for completeness.

With the current setup, the pin-fin heat transfer for the blockage pin-fin configuration is consistently higher than that of a CPF configuration (Figure 6.11(b)). The pin-fin heat transfer, however, decreases monotonically along the pin-fin array, similar to the end-wall heat transfer, while it remains relatively constant for a conventional pin-fin array. It is likely that the pin-fins for the blockage pin-fin configuration exhibit such high heat transfer, compared to a CPF array due to the concentration of the cooling flow in the mid-height plane. The decrease downstream then occurs due to the diffusion of the blockage jets in the *y*-direction, towards the end-wall surfaces.

The average heat transfer for the pin-fins across the full array was $\overline{Nu_{Dh}}/Nu_0 = 6.58$ for the blockage pin-fin configuration. This is more than double that of the CPF array. Further, the pin-fins had heat transfer that was 53% higher than the end-wall around the pin-fins (excluding the end-wall space between the perforated blockages). This difference is more than the 35% relative difference noted by VanFossen (1981) and Goldstein et al. (1998) for a full pin-fin array. This is attributed to the distinctly

different flow features as noted in Fig. 6, notably the concentration of the flow as aligned blockage jets in the mid-height plane. Overall, the pin-fin array makes up 34.7% of the cooling surfaces in the present study. It, therefore, contributes $\overline{Nu_{Dh}}/Nu_{0_{pin-fin}}$ = 2.28 to the overall heat transfer, 4.9% more than the end-wall surfaces ($\overline{Nu_{Dh}}/Nu_{0_{endwall}}$) = 2.18.

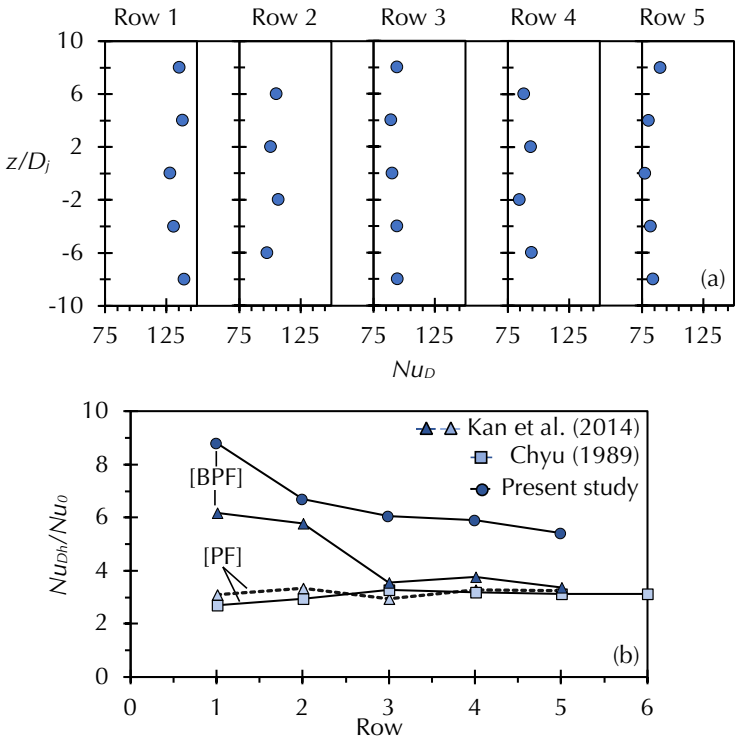

Figure 6.11. Pin-fin surface heat transfer measured using TLC at $Re_{Dh} \approx$ 10,000. (a) Individual pin-fin surface heat transfer for a blockage pin-fin configuration and (b) Spanwise-averaged pin-fin heat transfer for a blockage pin-fin (BPF) and conventional pin-fin (CPF) configurations.

6.8. Thermal performance

The heat transfer, pressure drop and thermal performance results are summarised in Figure 6.12. The combination of perforated blockages and a pin-fin array results in consistently higher heat transfer compared to a conventional pin-fin array. This is in all three primary regions: the end-wall ($\overline{Nu_{Dh}}/Nu_{0_{end-wall}}$ = 4.93), perforated blockages ($\overline{Nu_{Dh}}/Nu_{0_{blockages}}$ = 7.11) and pin-fins ($\overline{Nu_{Dh}}/Nu_{0_{pin-fins}}$= 6.58). The relative surface area of each region to the total surface area, on which the cooling flow acted, is then used to scale those relative heat transfer values. The resulting combined heat transfer for the BPF configuration is $\overline{Nu_{Dh}}/Nu_0$ = 5.96. Further, due to considered alignment of the perforations with the pin-fins, a greater heat transfer was attained, compared to previous ones (Figure 6.12(a)).

There is, however, a large increase in the pressure drop through the test channel due primarily to the perforated blockages. Across the perforated blockages, the friction factor ratio of f/f_0 = 773.9 was

measured. It was also seen that the pressure drop across the first blockage was very slightly higher than that across the second blockage. This results in a reduced pressure drop across two perforated blockage plates compared to a single blockage plate, per unit space occupied by the blockage. This agrees with the results by Moon and Lau (2003) and confirms that use of a double perforated blockage is warranted. Across the full blockage pin-fin configuration, this decreases to $f/f_0 = 165.6$ due to the minimal pressure drop from to the pin-fin array and increased streamwise distance. These values are shown in Figure 6.12(b) in comparison to other cooling schemes.

The thermal performance of the blockage pin-fin configuration at the Reynolds number of Re_{Dh} = 10,000 is therefore $\eta = 1.09$. In contradiction to previous studies, this implies a performance greater than that of a smooth channel (Figure 6.12(c)). This is attributed to two primary differences from the previous studies. First, the perforations (and therefore the blockage jets) were geometrically aligned with the pin-fins. With this change and considering only the end-wall and pin-fin surface heat transfer around the pin-fin array alone, the thermal performance is η_{TP} = 0.90. While below unity it is still higher than previous studies. Secondly, the consideration of the combined heat transfer on the blockage, pin-fin and end-wall surfaces meant a more complete measure of the heat transfer taking place. The thermal performance of a conventional pin-fin array configuration, however, is still significantly higher than a blockage pin-fin configuration as per Figure 6.12(c).

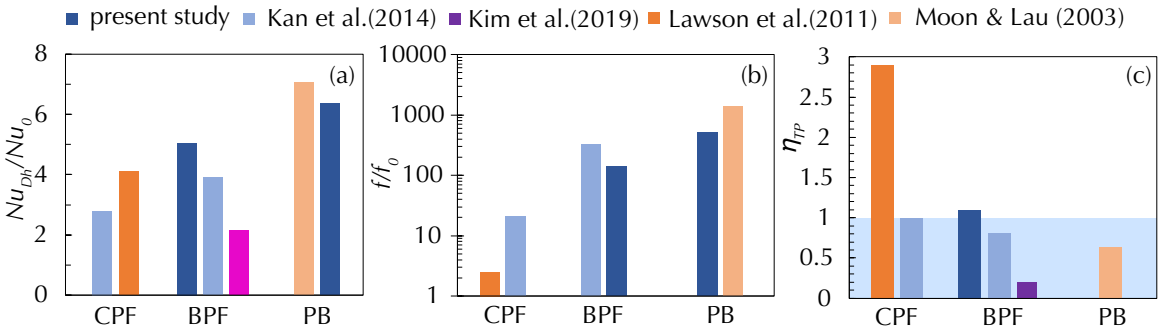

Figure 6.12. Comparisons of cooling performance with conventional pin-fin arrays (CPF), blockage pin-fin configurations (BPF) and perforated blockages (PB) at $Re_{Dh} \approx$ 10,000. (a) Heat transfer, (b) Friction factor, and (c) The thermal performance (η) with different cooling configurations.

6.9. Summary

The thermal performance of a blockage pin-fin configuration represents both the heat transfer potential of the cooling scheme and the pressure drop through it. In such a scheme, heat transfer comes from four distinct regions: 1) The surfaces of the perforated blockage plates, 2) the end-wall surface between perforated blockages, 3) the end-wall surface around the pin-fin array, and 4) the surfaces of the pin-fins.

Previous studies involving perforated blockages have only considered the end-wall heat transfer

and not the heat transfer on the blockage plate surfaces themselves. The highest heat transfer in the scheme was recorded on these surfaces: $\overline{Nu_{Dh}}/Nu_0$ = 7.11. By making up 21 % of the total surface area of the configuration tested, the perforated blockage plates make a notable contribution to the overall heat transfer.

The heat transfer on the end-wall surface between blockages was the second largest contributor to the overall heat transfer of the cooling scheme. This was anticipated based on previous studies involving such structures. The end-wall heat transfer around the pin-fin array was higher than previously reported for a blockage pin-fin configuration. This was primarily attributed optimisations of the physical test setup compared to setups used in prior studied. Such optimisations included geometric alignment between the jets and pin-fins and smaller spacings between the pin-fins in the array. The end-wall heat transfer around the pin-fin array was also higher than that of a conventional pin-fin array along the length of the array. This is due to the unique flows present in a blockage pin-fin configuration. Notably the interaction band of flows between pin-fins in the first row appeared to result in a large increase in end-wall heat transfer.

Unlike a conventional pin-fin array the end-wall and pin-fin heat transfer of a blockage pin-fin configuration decreases along the length of the pin-fin array. The averaged heat transfer for a blockage pin-fin configuration would be expected to be higher if there are fewer pin-fin rows while the opposite would occur for a conventional pin-fin array. On the other hand, fewer pin-fin rows would not significantly alter the relative pumping power given the small pressure drop through a pin-fin array. The thermal performance of the blockage pin-fin configuration would therefore increase with fewer pin-fins rows while the conventional pin-fin array would decrease for a given pumping power. There may then exist a design condition involving limited space, such as the turbine airfoil trailing-edge, where a blockage pin-fin configuration would produce a superior cooling performance to a conventional pin-fin array. This can be explored in future studies.

Overall with a configuration of two perforated blockage plates and five rows of pin-fins, a thermal performance above unity (e.g., η = 1.09) can be achieved. This performance is still notably lower than a conventional pin-fin array.

7. CONCLUSIONS

A blockage pin-fin configuration combines a pin-fin array with perforated blockage plates for application in trailing-edge cooling of a turbine blade. Such a cooling scheme has been investigated prior to this research work. The thermal performance of this scheme was, however, measured to be below unity ($\eta < 1.0$). This implies that for a given pumping power, the scheme produces less heat transfer than an empty channel. As a result, a blockage pin-fin configuration has been perceived as ineffective for cooling the trailing edge of a turbine airfoil. There were, however, some deficiencies identified in the prior studies. It was hypothesized that the results were unfairly represented. As a part of this, the understanding of fluid dynamics and kinematics present in such a scheme were seen as deficient.

The primary research question being considered is whether the previously purported thermal performance can be improved and, further, whether there is merit in the future consideration of a blockage pin-fin configuration. In building up to answering this question, those deficiencies in prior studies needed to be specifically investigated. Of specific interest was the consideration of flows around pin-fins subjected to impinging jets. In addressing these points, a series of investigations were conducted using flow measurement techniques (including particle image velocimetry and oil-dye mixtures) and temperature measurements with thermal cameras and thermochromic liquid crystals. Tests were conducted with turbulent flows ($Re_{Dh} \geq 10000$). The findings of this research work are as follows.

When a short circular pin-fin is exposed to an impinging jet flow the resulting end-wall flows can resemble those of a characteristics horseshoe vortex system. Similar features include a tear drop like flow pattern around the pin-fin and a heat transfer variation, from the leading-edge of the pin-fin, that mirrors that for a pin-fin array. But the end-wall flow topology is instead wholly different: termed here as a “jet-pin” flow system. This flow topology has previously not been specifically recognised or characterized. In a jet-pin flow system, there exists almost straight streamlines that radiate outwards from the pin-fin surface. These streamlines can be broken down into two types depending on where they originate on the pin-fin surface. Radial streamlines radiate from a nodal point of attachment at the pin-fin leading edge. Away from the leading-edge, streamlines radiate tangential from the pin-fin surface. These streamlines, in conjunction with flows at the mid-height of the pin, incite the formation of a circulating region upstream of the pin-fin. The circulating region, like horseshoe vortices, wraps around the leading-edge of the pin-fin. The end-wall flows can be directly correlated with the flows in the mid-height plane with similar regions of higher relative flow velocity and a similar separation point on the pin-fin surface. If there exists sufficient distance between the pin-fin and jet exit, however, then the jet flow can diffuse to contact the end-wall upstream of the pin-fin. Subsequently, there may result the formation of a flow system equivalent to a low Reynolds number horseshoe vortex system. This

latter system should be avoided if possible due to an associated lower end-wall heat transfer compared a typical jet-pin flow.

The understanding of jet-pin flow systems was expanded upon further in consideration of multiple pin-fins and the use of perforated blockages - representing a blockage pin-fin configuration. In a blockage pin-fin configuration, the jet flows are formed through a perforated blockage plate. This plate extends across the full height of the channel and there are resulting flow interactions from the end-wall radial streamlines that radiate from the pin-fins. These interactions can subtly alter the jet-pin flow topology. Further and more significant alterations occur when multiple jets and multiple pin-fins are present. This is unlike horseshoe vortex flows, where neighboring pin-fins still result in the characteristic horseshoe vortex flow patterns being present. With a jet-pin system, neighboring pin-fins interact with one another and form of a band of disrupted flow between the pin-fins – termed as the "interaction band." This local region entrains the wake flow of the pin-fin but also results in a local increase in heat transfer due to the large amount of flow interaction. These behaviors can be noted in the measurements of some previous studies but were either not recognized or mis-identified.

The blockage jets can, however, exhibit some flow curvature in the mid-height plane. Specifically, the jets entrain one another resulting in their convergence in the center of the channel. Jet entrainment and curvature has been studied previously but its presence in a configuration using perforated blockages in a channel of narrow height was seemingly overlooked or discounted. The curvature can be mitigated by adjusting the spanwise spacing between jets and increasing their distribution over the width the channel. While present, the jet curvature results in asymmetric flow interaction with the pin-fins and corresponding asymmetric end-wall flow topologies. Such asymmetric end-wall flows are seen as detrimental and to be avoided.

Due to the unique characteristics of jet-pin flows, the standard sizing parameters applied to either perforated blockage or conventional pin-fin arrays do not apply to a blockage pin-fin configuration. New sizing parameters were thus proposed. As a priority is that the spanwise (S_z) spacing of pin-fins and blockage perforations need to be matched. Specifically, there needs to be geometric alignment between the pin-fins and perforations. Pin-fin spacing and sizing is the guiding parameter to control or optimize the end-wall cooling flows with small spacings, compared to those typically applied in conventional pin-fin arrays, being preferable. Perforation spacing and sizing is subsequently governed based on those pin-fin specifications. Additionally, it was proposed that the use of two perforated blockages, instead of just one as applied in previous blockage pin-fin studies, would result in a superior cooling performance. This was confirmed to be accurate and a necessity for an optimal blockage pin-fin configuration.

Following these findings, the understanding of the fluid dynamics and kinematics that are potentially present in a blockage pin-fin configuration were better understood. This was such that a more optimal blockage pin-fin configuration, compared to those considered in prior studies, could be developed and tested. Such a configuration featured two perforated blockages and five rows of pin-fins.

The heat transfer performance exceeded that of the prior studies with blockage pin-fin configurations. This included a higher heat transfer on the pin-fin and end-wall surfaces. This increase was predominantly attributed optimisations of the setup. The pin-fin and end-wall heat transfer also demonstrated a heat transfer that was superior to that of a conventional pin-fin array. The heat transfer on the surfaces of the perforated blockages was also considered. Such heat transfer has not been previously considered, even for standard perforated blockage cooling configurations. It was seen that the perforated blockages make a distinct contribution to the overall thermal performance.

Using the setup that was developed based on the understanding of flows present, a thermal performance above unity (η = 1.09) was obtained. This confirms that the prior studies misrepresented the cooling scheme. The primary objective of the research work has thus been met. The value is however still significantly lower than a conventional pin-fin array due to high pressure drop through the perforated blockages. Blockage pin-fin configurations, in typical situations, are thus not appropriate. There may be situations or setups where a blockage pin-fin configuration is beneficial. As such, this research work has established that they may be merit in the continued investigation of such a cooling scheme with the goal of improving thermal performance in the trialing-edge of a turbine blade.

8. RECOMMENDATION FOR FUTURE WORK

8.1. Further development of a more optimal blockage pin-fin configuration

A thermal performance above unity can be achieved for a blockage pin-fin configuration. The thermal performance obtained is, nevertheless, very low. An application involving a long channel (such that there will be sufficient space for multiple rows of pin-fins) is better suited to a conventional pin-fin array. But with limited streamwise space (limiting the number of pin-fin rows possible), a blockage pin-fin configuration may be of benefit. A short setup considering both conventional pin-fin arrays and perforated blockages would need to be considered. Additionally, an alternative configuration could use slots or elongated perforations (as in Figure 2.19(b)) instead of circular perforations. This latter configuration would distribute the jet flow such that it is no longer focused on the pin-fins. This may reduce the pin-fin surface heat transfer and local end-wall heat transfer around the pin-fins. The slots would, however, result in a lower pressure drop as per Ahn (2007) and Shin (2008). The pressure drop has a significant impact in a blockage pin-fin configuration, as observed in this research work. The compromise of poorer heat transfer from jet impingement cooling against decreased pressure drop may be sufficient to have a net higher thermal performance. Such a configuration may, however, significantly alter the characteristic jet-pin flow structure. This would need to be considered in developing such a setup for study. Further work could consider further configurations of perforations such as that shown in Figure 2.19.

Additionally the perforated blockages may serve to realign or more evenly distribute the internal flow in the turbine airfoil. In Figure 2.8, the internal coolant enters at the root of the airfoil (in a relative vertical direction). The coolant leaves the trailing edge at relative horizontal direction, being required to turn before exiting. This can result in a non-uniform coolant distribution and therefore heat transfer in the trailing edge of the airfoil. It was seen that jet curvature could be controlled by adjusting the perforations in the blockage. This may be extended to have the blockages serve to better distribute the coolant through the airfoil.

8.2. Numerical studies

Flow features identified in this study, including the jet-pin flow structure, can be discerned in the numerical simulations undertaken by Kan et al. (2014). The features were, however, not clear and this may in part be due to the actual modelling of the flows. With the experimental results obtained from this study, a numerical model could be accurately validated. This may then allow for more rapid or varied testing and investigation of blockage pin-fin configurations compared to more time consuming and expensive experimental measurements. As it stands the applicability of numerical simulations in modelling blockage pin-fin flows is seen to be unclear.

8.3. Consideration of additional parameters

This study, following the convention used in prior studies, used a stationary test channel, of constant height, with an inline inlet and outlet. Such a setup may not be necessarily applicable to all turbine blade cooling layouts. Specifically, there are layouts where the inlet flow is perpendicular to the outlet flow and the trailing edge of the turbine blade converges. Rotation effects are strongly applicable to rotor airfoils. The effect of channel convergence and inclined oncoming flow has been studied for both conventional pin-fin arrays and perforated blockages (Effendy et al., 2019; Hwang & Lu, 2001; Hwang & Lui, 1999; Tarchi et al., 2008). The effect for a blockage pin-fin configuration is, however, not yet determined. Converging and angled channel configuration results in flow behaviours unique to those of both perforated blockage and pin-fin cooling configurations without such features. It is thus unclear what effect, whether detrimental or beneficial, converging end-walls and/or inclined flow may then have on the thermal performance. Additionally, the effects of turbine rotor rotation on the internal flows is also unclear. The presence of flow curvature, determined to be detrimental in Chapter 5 due to asymmetric flows around the pin-fins may be inevitable with rotating channels. In turn, this may require the non-geometric alignment of the pin-fins with the jets to ensure the jets, once curved, impinge directly on the pin-fins. This in turn would require the prediction of the jet curvature so that the pin-fins could be placed correctly. The effects of the pin-fins on the jet curvature, as considered in Chapter 5, would need to be expanded upon for a larger variety of cases.

Furthermore, as previously mentioned, the thermal performance index does not consider the coolant consumption. This parameter is likely of more relevance for turbine cooling technologies than the friction factor. Those previous studies of both conventional pin-fins and perforated blockage schemes, mentioned in this work, have not directly considered coolant consumption along with the heat transfer. The coolant consumption would thus necessitate a baseline consideration of both those schemes (CPF and PB), along with any future blockage pin-fin schemes.

9. REFERENCES

Abraham, S., & Vedula, R. P. (2019). Heat Transfer Distribution on a Cylindrical Convex Surface due to Obliquely Impinging Row of Circular Jets. *International Journal of Heat and Mass Transfer*, *137*. https://doi.org/10.1016/j.ijheatmasstransfer.2019.03.170

Abuaf, N., Bunker, R. S., & Lee, C. P. (1998). Effects of Surface Roughness on Heat Transfer and Aerodynamic Performance of Turbine Airfoils. *Journal of Turbomachinery*, *120*(3), 522–529. https://doi.org/10.1115/1.2841749

Adrian, R. J., & Westerweel, J. (2011). *Particle Image Velocimetry*. Cambridge University Press.

Agui, J. H., & Andreopoulos, J. (1992). Experimental Investigation of a Three-Dimensional Boundary Layer Flow in the Vicinity of an Upright Wall Mounted Cylinder (Data Bank Contribution). *Journal of Fluids Engineering*, *114*(4), 566–576. https://doi.org/10.1115/1.2910069

Ahn, H. S., Lee, S. W., Lau, S. C., & Banerjee, D. (2007). Mass (Heat) Transfer Downstream of Blockages With Round and Elongated Holes in a Rectangular Channel. *Journal of Heat Transfer*, *129*(12), 1676–1685. https://doi.org/10.1115/1.2767748

Aillaud, P., Gicquel, L. Y. M., & Duchaine, F. (2017). Investigation of the Concave Curvature Effect for an Impinging Jet Flow. *Physical Review Fluids*, *2*(11), 114608. https://doi.org/10.1103/PhysRevFluids.2.114608

Ames, F. E. (1997). The Influence of Large-Scale High-Intensity Turbulence on Vane Heat Transfer. *Journal of Turbomachinery*, *119*(1), 23–30. https://doi.org/10.1115/1.2841007

Ames, F. E., & Plesniak, M. W. (1997). The Influence of Large-Scale, High-Intensity Turbulence on Vane Aerodynamic Losses, Wake Growth, and the Exit Turbulence Parameters. *Journal of Turbomachinery*, *119*(2), 182–192. https://doi.org/10.1115/1.2841100

Ashworth, D. A., LaGraff, J. E., Schultz, D. L., & Grindrod, K. J. (1985). Unsteady Aerodynamic and Heat Transfer Processes in a Transonic Turbine Stage. *Journal of Engineering for Gas Turbines and Power*, *107*(4), 1022–1030. https://doi.org/10.1115/1.3239806

Atkins, M. D., & Kim, T. (2015). Isotropic-Planar Illumination for PIV Experiments. *Experiments in Fluids*, *56*(3), 63. https://doi.org/10.1007/s00348-015-1932-8

Azad, G. S., Han, J. C., Bunker, R. S., & Lee, C. P. (2002). Effect of Squealer Geometry Arrangement on a Gas Turbine Blade Tip Heat Transfer. *Journal of Heat Transfer*, *124*(3), 452–459. https://doi.org/10.1115/1.1471523

Baker, C. J. (1979). The Laminar Horseshoe Vortex. *Journal of Fluid Mechanics*, *95*(2), 347–367. https://doi.org/10.1017/S0022112079001506

Baker, C. J. (1980). The Turbulent Horseshoe Vortex. *Journal of Wind Engineering and Industrial Aerodynamics*, *6*(1–2), 9–23. https://doi.org/10.1016/0167-6105(80)90018-5

Baker, C. J. (1991). The Oscillation of Horseshoe Vortex Systems. *Journal of Fluids Engineering*, *113*(3), 489–495. https://doi.org/10.1115/1.2909523

Ballio, F., Bettoni, C., & Franzetti, S. (1998). A Survey of Time-Averaged Characteristics of Laminar and Turbulent Horseshoe Vortices. *Journal of Fluids Engineering*, *120*(2), 233–242. https://doi.org/10.1115/1.2820639

Bearman, P. W., & Wadcock, A. J. (1973). The Interaction Between a Pair of Circular Cylinders Normal to a Stream. *Journal of Fluid Mechanics*, *61*(3), 499–511. https://doi.org/10.1017/S0022112073000832

Blair, M. F., Dring, R. P., & Joslyn, H. D. (1989). The Effects of Turbulence and Stator/Rotor Interactions on Turbine Heat Transfer: Part II—Effects of Reynolds Number and Incidence. *Journal of Turbomachinery*, *111*(1), 97–103. https://doi.org/10.1115/1.3262243

Boyce, M. P. (2012). An Overview of Gas Turbines. In *Gas Turbine Engineering Handbook* (pp. 3–88). https://doi.org/10.1016/B978-0-12-383842-1.00001-9

Boyle, R. J., & Senyitko, R. G. (2005). Effects of Surface Roughness on Turbine Vane Heat Transfer. *Volume 3: Turbo Expo 2005, Parts A and B*, 931–942. https://doi.org/10.1115/GT2005-69133

Brigham, B. A., & VanFossen, G. J. (1984). Length to Diameter Ratio and Row Number Effects in Short Pin Fin Heat Transfer. *Journal of Engineering for Gas Turbines and Power*, *106*(1), 241–244. https://doi.org/10.1115/1.3239541

Bunker, R. S. (2008). *Innovative Gas Turbine Cooling Techniques* (pp. 199–229). https://doi.org/10.2495/978-1-84564-062-0/07

Camci, C., & Arts, T. (1990). An Experimental Convective Heat Transfer Investigation Around a Film-Cooled Gas Turbine Blade. *Journal of Turbomachinery*, *112*(3), 497–503. https://doi.org/10.1115/1.2927685

Carter, S., Li, J., Mitchell, A., Saposnik, M., Riedel, R., & Hyde, D. (2023, May). *Target True Zero: Infrastructure for Alternative Propulsion Flight*. McKinsey & Company. https://www.mckinsey.com/industries/aerospace-and-defense/our-insights/target-true-zero-infrastructure-for-novel-propulsion-flight#

Choi, I. K., Kim, T., Song, S. J., & Lu, T. J. (2007). Endwall Heat Transfer and Fluid Flow Around an Inclined Short Cylinder. *International Journal of Heat and Mass Transfer*, *50*(5–6), 919–930. https://doi.org/10.1016/j.ijheatmasstransfer.2006.08.012

Chung, H., Park, J. S., Sohn, H.-S., Rhee, D.-H., & Cho, H. H. (2014). Trailing Edge Cooling of a Gas Turbine Blade with Perforated Blockages with Inclined Holes. *International Journal of Heat and Mass Transfer*, *73*, 9–20. https://doi.org/10.1016/j.ijheatmasstransfer.2014.01.062

Chyu, M. K. (1990). Heat Transfer and Pressure Drop for Short Pin-Fin Arrays With Pin-Endwall Fillet. *Journal of Heat Transfer*, *112*(4), 926–932. https://doi.org/10.1115/1.2910502

Chyu, M. K., Hsing, Y. C., & Natarajan, V. (1998). Convective Heat Transfer of Cubic Fin Arrays in a Narrow Channel. *Journal of Turbomachinery*, *120*(2), 362–367. https://doi.org/10.1115/1.2841414

Chyu, M. K., Hsing, Y. C., Shih, T. I.-P., & Natarajan, V. (1999). Heat Transfer Contributions of Pins and Endwall in Pin-Fin Arrays: Effects of Thermal Boundary Condition Modeling. *Journal of Turbomachinery*, *121*(2), 257–263. https://doi.org/10.1115/1.2841309

Chyu, M. K., & Natarajan, V. (1996). Heat transfer on the Base Surface of Three-Dimensional Protruding Elements. *International Journal of Heat and Mass Transfer*, *39*(14), 2925–2935. https://doi.org/10.1016/0017-9310(95)00381-9

Cleynen, O. (2013). *Repair Process for a V2500 High-Pressure Turbine Guide Vane*. https://upload.wikimedia.org/wikipedia/commons/0/05/Repair_process_for_a_V2500_high-pressure_turbine_guide_vane_%2810%29.jpg

Coleman, H. W., & Steele, W. G. (2018). *Experimentation, Validation, and Uncertainty Analysis for Engineers.* John Wiley & Sons.

Doorly, D. J., & Oldfield, M. L. G. (1985). Simulation of the Effects of Shock Wave Passing on a Turbine Rotor Blade. *Journal of Engineering for Gas Turbines and Power*, *107*(4), 998–1006. https://doi.org/10.1115/1.3239847

Dullenkopf, K., Schulz, A., & Wittig, S. (1991). The Effect of Incident Wake Conditions on the Mean Heat Transfer of an Airfoil. *Journal of Turbomachinery*, *113*(3), 412–418. https://doi.org/10.1115/1.2927890

Dunn, M. G., George, W. K., Rae, W. J., Woodward, S. H., Moller, J. C., & Seymour, P. J. (1986). Heat-Flux Measurements for the Rotor of a Full-Stage Turbine: Part II—Description of Analysis Technique and Typical Time-Resolved Measurements. *Journal of Turbomachinery*, *108*(1), 98–107. https://doi.org/10.1115/1.3262030

Dunn, M. G., Martin, H. L., & Stanek, M. J. (1986). Heat-Flux and Pressure Measurements and Comparison With Prediction for a Low-Aspect-Ratio Turbine Stage. *Journal of Turbomachinery*, *108*(1), 108–115. https://doi.org/10.1115/1.3262008

Eckerle, W. A., & Awad, J. K. (1991). Effect of Freestream Velocity on the Three-Dimensional Separated Flow Region in Front of a Cylinder. *Journal of Fluids Engineering*, *113*(1), 37–44. https://doi.org/10.1115/1.2926493

Effendy, M., Yao, Y., Yao, J., & Marchant, D. R. (2019). *Pin-Fin Shape and Orientation Effects on Wall Heat Transfer Predictions of Gas Turbine Blade*. 020008. https://doi.org/10.1063/1.5112392

El Hassan, M., & Meslem, A. (2010). Time-Resolved Stereoscopic Particle Image Velocimetry Investigation of the Entrainment in the Near Field of Circular and Daisy-Shaped Orifice Jets. *Physics of Fluids*, *22*(3), 035107. https://doi.org/10.1063/1.3358465

Erickson, E. L., Ames, F. E., & Bons, J. P. (2012). Effects of a Realistically Rough Surface on Vane Heat Transfer Including the Influence of Turbulence Condition and Reynolds Number. *Journal of Turbomachinery*, *134*(2). https://doi.org/10.1115/1.4003026

F. Incropera, & D. DeWitt. (2007). *Fundamentals of Heat and Mass Transfer* (6th ed.). J. Wiley & Sons.

Fenot, M., Dorignac, E., & Vullierme, J. J. (2008). An Experimental Study on Hot Round Jets Impinging a Concave Surface. *International Journal of Heat and Fluid Flow*, *29*(4). https://doi.org/10.1016/j.ijheatfluidflow.2008.03.015

Fu, H., & Rockwell, D. (2005). Shallow Flow Past a Cylinder: Transition Phenomena at Low Reynolds Number. *Journal of Fluid Mechanics*, *540*(1), 75. https://doi.org/10.1017/S0022112005003381

Gauntner, J. W., Livingood, B., & Hrycak, P. (1970). Survey of Literature on Flow Characteristics of a Single Turbulent Jet Impinging on a Flat Plate. *NASA, TN D-5652 NTIS N79-18963*.

Geers, L. F. G. (2004). *Multiple Impinging Jet Arrays. An Experimental Study on Flow and Heat Transfer*. Technische Universiteit Delft.

Geers, L. F. G., Tummers, M. J., & Hanjalic, K. (2004). Experimental investigation of impinging jet arrays. *Experiments in Fluids*, *36*(6), 946–958. https://doi.org/10.1007/s00348-004-0778-2

Ghahremanian, S., Svensson, K., Tummers, M. J., & Moshfegh, B. (2014). Near-Field Mixing of Jets Issuing from an Array of Round Nozzles. *International Journal of Heat and Fluid Flow*, *47*, 84–100. https://doi.org/10.1016/j.ijheatfluidflow.2014.01.007

Goldstein, R. J., & Chen, S. B. (1998). Flow and Mass Transfer Performance in Short Pin-Fin Channels with Different Fin Shapes. *International Journal of Rotating Machinery*, *4*(2), 113–128. https://doi.org/10.1155/S1023621X98000104

Goldstein, R. J., & Spores, R. A. (1988). Turbulent Transport on the Endwall in the Region Between Adjacent Turbine Blades. *Journal of Heat Transfer*, *110*(4a), 862–869. https://doi.org/10.1115/1.3250586

Goldstein, R. J., Wang, H. P., & Jabbari, M. Y. (1994, June 13). The Influence of Secondary Flows Near the Endwall and Boundary Layer Disturbance on Convective Transport From a Turbine Blade. *Volume 4: Heat Transfer; Electric Power; Industrial and Cogeneration*. https://doi.org/10.1115/94-GT-165

Gordon, E. B., & Gerber, I. (1990). *The Entrainment Rate For a Row of Turbulent Jets*.

Graziani, R. A., Blair, M. F., Taylor, J. R., & Mayle, R. E. (1980). An Experimental Study of Endwall and Airfoil Surface Heat Transfer in a Large Scale Turbine Blade Cascade. *Journal of Engineering for Power*, *102*(2), 257–267. https://doi.org/10.1115/1.3230246

Guenette, G. R., Epstein, A. H., Giles, M. B., Haimes, R., & Norton, R. J. G. (1989). Fully Scaled Transonic Turbine Rotor Heat Transfer Measurements. *Journal of Turbomachinery*, *111*(1), 1–7. https://doi.org/10.1115/1.3262231

Halila, E. E., Lenahan, D. T., & Thomas, T. T. (1982). High Pressure Turbine Test Hardware Detailed Design Report. *National Aeronautics and Space Administration*.

Han, J. C. (2013). Fundamental Gas Turbine Heat Transfer. *Journal of Thermal Science and Engineering Applications*, *5*(2). https://doi.org/10.1115/1.4023826

Han, J. C. (2018). Advanced Cooling in Gas Turbines 2016 Max Jakob Memorial Award Paper. *Journal of Heat Transfer*, *140*(11). https://doi.org/10.1115/1.4039644

Han, J. C., Dutta, S., & Ekkad, S. (2012). *Gas Turbine Heat Transfer and Cooling Technology* (2nd ed.). CRC Press. https://doi.org/10.1201/b13616

Han, J. C., & Wright, L. M. (2006). *Enhanced Internal Cooling of Turbine Blades and Vanes*.

Han, J. C., Zhang, L., & Ou, S. (1993). Influence of Unsteady Wake on Heat Transfer Coefficients from a Gas Turbine Blade. *Journal of Heat Transfer*, *115*.

Hoffs, A., Drost, U., & Bölcs, A. (1996, June 10). Heat Transfer Measurements on a Turbine Airfoil at Various Reynolds Numbers and Turbulence Intensities Including Effects of Surface Roughness. *Volume 4: Heat Transfer; Electric Power; Industrial and Cogeneration*. https://doi.org/10.1115/96-GT-169

Horbach, T., Schulz, A., & Bauer, H.-J. (2011). Trailing Edge Film Cooling of Gas Turbine Airfoils—External Cooling Performance of Various Internal Pin Fin Configurations. *Journal of Turbomachinery*, *133*(4). https://doi.org/10.1115/1.4002964

Hrycak, P. (1983). Heat Transfer from Round Impinging Jets to a Flat Plate. *International Journal of Heat and Mass Transfer*, *26*(12), 1857–1865. https://doi.org/10.1016/S0017-9310(83)80156-2

Hrycak, P., Lee, D. T., Gaunter, J. W., & Livingood, J. N. B. (1970). Experimental Flow Characteristics of a Single Turbulent Jet Impinging on a Flat Plate. *NASA TN D-5690*.

Hwang, J.-J., & Lu, C.-C. (2001). Lateral-Flow Effect on Endwall Heat Transfer and Pressure Drop in a Pin-Fin Trapezoidal Duct of Various Pin Shapes. *Journal of Turbomachinery*, *123*(1), 133–139. https://doi.org/10.1115/1.1333093

Hwang, J.-J., & Lui, C.-C. (1999). Detailed Heat Transfer Characteristic Comparison in Straight and 90-deg Turned Trapezoidal Ducts with Pin-Fin Arrays. *International Journal of Heat and Mass Transfer*, *42*(21), 4005–4016. https://doi.org/10.1016/S0017-9310(99)00056-3

Hylton, L. D., Mihelc, M. S., Turner, E. R., Nealy, D. A., & York, R. E. (1983). Analytical and Experimental Evaluation of the Heat Transfer Distribution Over the Surfaces of Turbine Vanes. *National Aeronautics and Space Administration*.

Jambunathan, K., Lai, E., Moss, M. A., & Button, B. L. (1992). A Review of Heat Transfer Data for Single Circular Jet Impingement. *International Journal of Heat and Fluid Flow*, *13*(2), 106–115. https://doi.org/10.1016/0142-727X(92)90017-4

Jiao, L. (2016). *On The Vortex Structures and Flow Characteristics of Circular and Elliptic Jet Impingement Upon Convex Cylinders* [PhD]. Nanyang Technological University.

Johnke, T., & Mast, M. (2002). Power Boosters-Technologies to Enhance Gas Turbine Power Output on Demand. *Siemens Power Journal*.

Kakac, S., Shah, R. K., & Aung, W. (1987). *Handbook of Single-Phase Convective Heat Transfer*. John Wiley & Sons Inc.

Kan, R., Ren, J., & Jiang, H. (2014, June 16). Combined Effects of Perforated Blockages and Pin Fins in a Trailing Edge Internal Cooling Duct. *ASME Turbo Expo 2014: Turbine Technical Conference and Exposition, V05AT12A020*. https://doi.org/10.1115/GT2014-25767

Kays, W. M., Crawford, M. E., & Weigand, B. (2005). *Convective Heat and Mass Transfer* (4th ed.). McGraw-Hill.

Kim, Y., Choi, S. M., Park, H. S., Kim, S. W., Jung, E. Y., Park, J. S., & Cho, H. H. (2019). Heat Transfer Characteristics of the Rib Angle in the Pin-Fin Cooling Combined with Perforated Blockage. *Transactions of the Korean Society of Mechanical Engineers - B*, *43*(7), 453–461. https://doi.org/10.3795/KSME-B.2019.43.7.453

Kumar, B. V. N. R., & Prasad, B. V. S. S. S. (2008). Computational Flow and Heat Transfer of a Row of Circular Jets Impinging on a Concave Surface. *Heat and Mass Transfer*, *44*(6), 667–678. https://doi.org/10.1007/s00231-007-0274-3

Laban, A., Aleyasin, S. S., Tachie, M. F., & Koupriyanov, M. (2019). Experimental Investigation of Nozzle Spacing Effects on Characteristics of Round Twin Free Jets. *Journal of Fluids Engineering, 071201*, *141*(7). https://doi.org/10.1115/1.4041989

Langston, L. S. (2007). Fahrenheit 3,600. *Mechanical Engineering*, *129*(04), 34–37. https://doi.org/10.1115/1.2007-APR-3

Lau, S. C., Cervantes, J., Han, J. C., & Rudolph, R. J. (2008). Internal Cooling Near Trailing Edge of a Gas Turbine Airfoil With Cooling Airflow Through Blockages With Holes. *Journal of Turbomachinery*, *130*(3). https://doi.org/10.1115/1.2775489

Lau, S. C., Cervantes, J., Han, J. C., Rudolph, R. J., & Flannery, K. (2003). Measurements of Wall Heat (Mass) Transfer for Flow Through Blockages with Round and Square Holes in a Wide Rectangular Channel. *International Journal of Heat and Mass Transfer*, *46*(21), 3991–4001. https://doi.org/10.1016/S0017-9310(03)00246-1

Lawson, S. A., Thrift, A. A., Thole, K. A., & Kohli, A. (2011). Heat Transfer from Multiple Row Arrays of Low Aspect Ratio Pin Fins. *International Journal of Heat and Mass Transfer*, *54*(17–18), 4099–4109. https://doi.org/10.1016/j.ijheatmasstransfer.2011.04.001

Lee, J., & Lee, S.-J. (2000). The Effect of Nozzle Configuration on Stagnation Region Heat Transfer Enhancement of Axisymmetric Jet Impingement. *International Journal of Heat and Mass Transfer*, *43*(18), 3497–3509. https://doi.org/10.1016/S0017-9310(99)00349-X

Lim, K. B., Lee, C. H., Sung, N. W., & Lee, S. H. (2007). An Experimental Study on the Characteristics of Heat Transfer on the Turbulent Round Impingement Jet According to the Inclined Angle of

Convex Surface Using the Liquid Crystal Transient Method. *Experimental Thermal and Fluid Science*, *31*(7), 711–719. https://doi.org/10.1016/j.expthermflusci.2006.07.005

Liu, Y. Y., Schekman, S. W., Bhaiyat, T. I., Lu, T. J., & Kim, T. (2022). Impingement Cooling of an Isoflux Flat Plate by Blockage Jet. *Applied Thermal Engineering*, *209*(118239), 1–12. https://doi.org/https://doi.org/10.1016/j.applthermaleng.2022.118239

Long, J., & New, T. H. (2019). Vortical Structures and Behaviour of an Elliptic Jet Impinging Upon a Convex Cylinder. *Experimental Thermal and Fluid Science*, *100*, 292–310. https://doi.org/10.1016/j.expthermflusci.2018.09.002

Lorenz, M., Schulz, A., & Bauer, H.-J. (2010). An Experimental Study of Airfoil and Endwall Heat Transfer on a Linear Turbine Blade Cascade — Secondary Flow and Surface Roughness Effects. *Heat Transfer Research*, *41*(8), 867–887. https://doi.org/10.1615/HeatTransRes.v41.i8.60

Lyall, M. E. (2006). *Heat Transfer From Flow Low Aspect Ratio Pin Fins*. Virginia Polytechnic Institute and State University.

Lyall, M. E., Thrift, A. A., Thole, K. A., & Kohli, A. (2011). Heat Transfer From Low Aspect Ratio Pin Fins. *Journal of Turbomachinery*, *133*(1). https://doi.org/10.1115/1.2812951

Martinez-Botas, R. F., Lock, G. D., & Jones, T. V. (1995). Heat Transfer Measurements in an Annular Cascade of Transonic Gas Turbine Blades Using the Transient Liquid Crystal Technique. *Journal of Turbomachinery*, *117*(3), 425–431. https://doi.org/10.1115/1.2835678

Mayle, R. E., & Dullenkopf, K. (1991). More on the Turbulent-Strip Theory for Wake-Induced Transition. *Journal of Turbomachinery*, *113*(3), 428–432. https://doi.org/10.1115/1.2927892

McNaughton, K. J., & Sinclair, C. G. (1966). Submerged Jets in Short Cylindrical Flow Vessels. *Journal of Fluid Mechanics*, *25*(2), 367–375. https://doi.org/10.1017/S0022112066001708

Metzger, D. E., Fan, C. S., & Haley, S. W. (1984). Effects of Pin Shape and Array Orientation on Heat Transfer and Pressure Loss in Pin Fin Arrays. *Journal of Engineering for Gas Turbines and Power*, *106*(1), 252–257. https://doi.org/10.1115/1.3239545

Metzger, D. E., & Haley, S. W. (1982, April 18). Heat Transfer Experiments and Flow Visualization for Arrays of Short Pin Fins. *Volume 4: Heat Transfer; Electric Power*. https://doi.org/10.1115/82-GT-138

Moon, S. W., & Lau, S. C. (2003). Heat Transfer Between Blockages With Holes in a Rectangular Channel. *Journal of Heat Transfer*, *125*(4), 587–594. https://doi.org/10.1115/1.1576812

Nealy, D. A., Mihelc, M. S., Hylton, L. D., & Gladden, H. J. (1984). Measurements of Heat Transfer Distribution Over the Surfaces of Highly Loaded Turbine Nozzle Guide Vanes. *Journal of Engineering for Gas Turbines and Power*, *106*(1), 149–158. https://doi.org/10.1115/1.3239528

Nguepnang, M. A., Boer, M., & Kim, T. (2016). Stagnation Heat Transfer on a Concave Surface Cooled by Unconfined Slot Jet. *Journal of Thermophysics and Heat Transfer*, *30*(3), 558–566. https://doi.org/10.2514/1.T4793

Ni, M., Zhu, H., & Qiu, Y. (2005). Review of Aero-Turbine Blade Cooling Technologies. *Gas Turbine Technology*, *18*, 25–33.

O'Brien, J. E., & Capp, S. P. (1989). Two-Component Phase-Averaged Turbulence Statistics Downstream of a Rotating Spoked-Wheel Wake Generator. *Journal of Turbomachinery*, *111*(4), 475–482. https://doi.org/10.1115/1.3262296

Otto, M., Gupta, G., Tran, P. K., Ghosh, S., & Kapat, J. S. (2021). Investigation of Endwall Heat Transfer in Staggered Pin Fin Arrays. *Journal of Turbomachinery*, *143*(2). https://doi.org/10.1115/1.4049784

Park, J. S., Jo, Y. H., & Kwak, J. S. (2016). Heat Transfer in a Rectangular Duct with Perforated Blockages and Dimpled Side Walls. *International Journal of Heat and Mass Transfer*, *97*, 224–231. https://doi.org/10.1016/j.ijheatmasstransfer.2016.01.081

Parsons, D., Chatterton, J., & Nicholls, J. (2011). Carbon Brainprint Case Study Ceramic coatings for jet engine turbine blades. *Cranfield University*.

Praisner, T. J., & Smith, C. R. (2006). The Dynamics of the Horseshoe Vortex and Associated Endwall Heat Transfer—Part I: Temporal Behavior. *Journal of Turbomachinery*, *128*(4), 747–754. https://doi.org/10.1115/1.2185676

Priddy, W. J., & Bayley, F. J. (1988). Turbulence Measurements in Turbine Blade Passages and Implications for Heat Transfer. *Journal of Turbomachinery*, *110*(1), 73–79. https://doi.org/10.1115/1.3262170

Quinn, W. R. (2006). Upstream Nozzle Shaping Effects on Near Field Flow in Round Turbulent Free Jets. *European Journal of Mechanics - B/Fluids*, *25*(3), 279–301. https://doi.org/10.1016/j.euromechflu.2005.10.002

Rolls-Royce. (1996). *The Jet Engine* (5th ed.). Rolls-Royce plc.

Sahin, B., Ozturk, N. A., & Gurlek, C. (2008). Horseshoe Vortex Studies in the Passage of a Model Plate-Fin-and-Tube Heat Exchanger. *International Journal of Heat and Fluid Flow*, *29*(1), 340–351. https://doi.org/10.1016/j.ijheatfluidflow.2007.06.005

Schekman, S., & Kim, T. (2017). Thermal Flows Around a Fully Permeable Short Circular Cylinder. *International Journal of Heat and Mass Transfer*, *105*. https://doi.org/10.1016/j.ijheatmasstransfer.2016.09.089

Schobeiri, T., & Pardivala, D. (1992). Development of a Subsonic Flow Research Facility for Simulating the Turbomachinery Flow and Investigating Its Effects on Boundary Layer Transition, Wake Development and Heat Transfer. *Fourth International Symposium on Transport Phenomena and Dynamics of Rotating Machinery*.

Shaikh, A. S. (2018). Development of a γ' Precipitation Hardening Ni-Base Superalloy for Additive Manufacturing. *Department of Industrial and Materials Science Chalmers University of Technology*.

Shakouchi, T., & Kito, M. (2012). Heat Transfer Enhancement of Impinging Jet by Notched – Orifice Nozzle. In *An Overview of Heat Transfer Phenomena*. https://doi.org/10.5772/52029

Shin, S., & Kwak, J. S. (2008). Effect of Hole Shape on the Heat Transfer in a Rectangular Duct with Perforated Blockage Walls. *Journal of Mechanical Science and Technology*, *22*(10), 1945–1951. https://doi.org/10.1007/s12206-008-0736-7

Simpson, R. L. (2001). Junction Flows. *Annual Review of Fluid Mechanics*, *33*(1), 415–443. https://doi.org/10.1146/annurev.fluid.33.1.415

Sulzer. (2019). *Blades equivalent to Siemens V64.3A / SGT-1000 and Ansaldo AE64.3A*.

Sumner, D., Wong, S. S. T., Price, S. J., & Paidoussis, M. P. (1999). Fluid Behaviour of Side-By-Side Circular Cylinders in Steady Cross-Flow. *Journal of Fluids and Structures*, *13*(3), 309–338. https://doi.org/10.1006/jfls.1999.0205

Suo, M. (1978). *Turbine cooling. In Aerothermodynamics of Aircraft Gas Turbine Engines*. Wright-Patterson Air Force Base.

Svensson, K., Rohdin, P., & Moshfegh, B. (2016). On the Influence of Array Size and Jet Spacing on Jet Interactions and Confluence in Round Jet Arrays. *Journal of Fluids Engineering, 081206*, *138*(8). https://doi.org/10.1115/1.4033024

Tanaka, E. (1969). The Interference of Two-Dimensional Parallel Jets : 1st Report Experiments on Dual Jet. *Transactions of the Japan Society of Mechanical Engineers*, *35*(274). https://doi.org/10.1299/kikai1938.35.1257

Tanaka, E. (1974). Interference of Two-Dimensional Parallel Jets - 2. Experiments on the Combined Flow of Dual Jet. *Bull JSME*, *17*(109). https://doi.org/10.1299/jsme1958.17.920

Tarchi, L., Facchini, B., & Zecchi, S. (2008). Experimental Investigation of Innovative Internal Trailing Edge Cooling Configurations with Pentagonal Arrangement and Elliptic Pin Fin. *International Journal of Rotating Machinery*, *2008*, 1–10. https://doi.org/10.1155/2008/109120

Thomas, A. S. W. (1987). The Unsteady Characteristics of Laminar Juncture Flow. *The Physics of Fluids*, *30*(2), 283–285. https://doi.org/10.1063/1.866374

VanFossen, G. J. (1982). Heat-Transfer Coefficients for Staggered Arrays of Short Pin Fins. *Journal of Engineering for Power*, *104*(2), 268–274. https://doi.org/10.1115/1.3227275

Visbal, M. R. (1991). Structure of Laminar Juncture Flows. *AIAA Journal*, *29*(8), 1273–1282. https://doi.org/10.2514/3.10732

Walker, R. E., & Kors, D. L. (2973). *Multiple Jet Study*.

Wang, N., Chen, A. F., Zhang, M., & Han, J. C. (2018). Turbine Blade Leading Edge Cooling With One Row of Normal or Tangential Impinging Jets. *Journal of Heat Transfer*, *140*(6). https://doi.org/10.1115/1.4038691

Wang, X. L., Yan, H. B., Lu, T. J., Song, S. J., & Kim, T. (2014). Heat Transfer Characteristics of an Inclined Impinging Jet on a Curved Surface in Crossflow. *Journal of Heat Transfer, 081702*, *136*(8). https://doi.org/10.1115/1.4027389

Wang, Z. J., & Zhou, Y. (2005). Vortex Interactions in a Two Side-By-Side Cylinder Near-Wake. *International Journal of Heat and Fluid Flow*, *26*(3), 362–377. https://doi.org/10.1016/j.ijheatfluidflow.2004.10.006

Ward-Smith, A. J. (1971). *Pressure Losses in Ducted Flow*. Cambridge University Press.

Westerweel, J. (2000). Theoretical Analysis of the Measurement Precision in Particle Image Velocimetry. *Experiments in Fluids*, *29*(SUPPL. 1). https://doi.org/10.1007/s003480070002

Westerweel, J. (2008). On Velocity Gradients in PIV Interrogation. *Experiments in Fluids*, *44*(5), 831–842. https://doi.org/10.1007/s00348-007-0439-3

Wright, L. M., Fu, W. L., & Han, J. C. (2004). Thermal Performance of Angled, V-Shaped, and W-Shaped Rib Turbulators in Rotating Rectangular Cooling Channels (AR=4:1). *Journal of Turbomachinery*, *126*(4), 604–614. https://doi.org/10.1115/1.1791286

Wright, L. M., & Han, J. C. (2013). *Heat Transfer Enhancement for Turbine Blade Internal Cooling* (1st ed.). American Society of Mechanical Engineer. https://doi.org/10.1115/HT2013-17813

Ye, Y., Li, X., Ren, J., & Jiang, H. (2019). Split of Heat Transfer Regions and Flow Characteristics of Perforated Blockages with Inclined Holes for Trailing Edge Cooling. *Numerical Heat Transfer, Part A: Applications*, *75*(1), 21–39. https://doi.org/10.1080/10407782.2018.1562736

Yeranee, K., Wae-hayee, M., & Nuntadusit, C. (2020). Flow and Heat Transfer of Impinging Jet Array Associated with Entrained Air Ducts. *Applied Thermal Engineering*, *178*, 115541. https://doi.org/10.1016/j.applthermaleng.2020.115541

Yimer, J., Becker, H. A., & Grandmaison, E. W. (1996). Development of Flow from Multiple-Jet Burners. *The Canadian Journal of Chemical Engineering*, *74*(6), 840–851. https://doi.org/10.1002/cjce.5450740605

Yunus A. Çengel, & John M. Cimbala. (2014). *Fluid Mechanics* (3rd ed.). McGraw-Hill.

Yuri, M., Masada, J., Tsukagoshi, K., Ito, E., & Hada, S. (2013). Development of 1600°C-Class High-efficiency Gas Turbine for Power Generation Applying J-Type Technology. *Mitsubishi Heavy Industries Technical Review*, *50*(3).

Zhang, M., Wang, N., & Han, J. C. (2019). Internal Heat Transfer of Film-Cooled Leading Edge Model with Normal and Tangential Impinging Jets. *International Journal of Heat and Mass Transfer*, *139*, 193–204. https://doi.org/10.1016/j.ijheatmasstransfer.2019.04.140